6-25-2018

Development and Life Cycle Assessment of Advanced-Concept III-V Multijunction Photovoltaics

Brittany L. Smith
bls9317@rit.edu

R·I·T

Development and Life Cycle Assessment of Advanced-Concept III-V Multijunction Photovoltaics

by

Brittany L. Smith

A Dissertation
Submitted in Partial Fulfillment of the Requirements
for the Degree of Doctor of Philosophy in Sustainability

Department of Sustainability
Golisano Institute of Sustainability

Author: _____
Sustainability Program

Certified by: _____
Dr. Callie Babbitt
Associate Professor of Sustainability Program

Approved by: _____
Dr. Thomas Trabold
Department Head of Sustainability Program

Certified by: _____
Dr. Nabil Nasr
Assistant Provost and Director, Golisano Institute for Sustainability and CIMS

Rochester Institute of Technology
Rochester, NY
June 25, 2018

Development and Life cycle Assessment of Advanced-Concept III-V Multijunction Photovoltaics

by

Brittany L. Smith

Submitted by Brittany Smith in partial fulfillment of the requirements for the degree of Doctor of Philosophy in Sustainability and accepted on behalf of the Rochester Institute of Technology by the dissertation committee.

We, the undersigned members of the dissertation committee, certify that we have advised and/or supervised the candidate on the work described in this dissertation. We further certify that we have reviewed the dissertation manuscript and approve it as partial fulfillment of the requirements of the degree of Doctor of Philosophy in Sustainability.

Approved by:

Dr. Seth Hubbard _____
Committee Co-Chair and Dissertation Co-Advisor, Date
Rochester Institute of Technology

Dr. Callie Babbitt _____
Committee Co-Chair and Dissertation Co-Advisor, Date
Rochester Institute of Technology

Dr. Gabrielle Gaustad _____
Committee Member, Rochester Institute of Technology Date

Dr. Jing Zhang _____
Committee Member, Rochester Institute of Technology Date

SUSTAINABILITY PROGRAM
ROCHESTER INSTITUTE OF TECHNOLOGY
June 2018

ABSTRACT

Golisano Institute for Sustainability
Rochester Institute of Technology

Degree: Doctor of Philosophy Program: Sustainability

Name of Candidate: Brittany L. Smith

Title: Development and Life Cycle Assessment of Advanced-Concept III-V Multijunction Photovoltaics

III-V semiconductors make for highly efficient solar cells, but are expensive to manufacture. However, there are many mechanisms for improving III-V photovoltaics in order to make them more competitive with other photovoltaic (PV) technologies. One possible method is to design cells for high efficiency under concentrated sunlight, effectively trading expensive III-V material for cheaper materials such as glass lenses. Another approach is to reduce the amount of III-V material necessary for the same power output, which can be achieved by removing the substrate and installing a reflector on the back of the cell, while also adding quantum structures to the cell to permit absorption of a greater portion of the solar spectrum.

Regarding the first approach, this dissertation focused on the development of an InAlAsSb material for a mulitjunction design with the potential of achieving 52.8% efficiency under 500 suns. First, development of a single-junction InAlAs cell lattice-matched to InP was executed as a preliminary step. The InAlAs cell design was optimized via simulation, then grown via metal organic vapor phase epitaxy (MOVPE) and fabricated resulting in 17.9% efficiency under 1-sun AM1.5, which was unprecedented for the InAlAs material. Identical InAlAs cells were grown using alternative MOVPE precursors to study the effects of necessary precursors for InAlAsSb. Fits to experimental device results showed longer lifetimes when grown with the alternative aluminum precursor. InAlAsSb grown using these alternative precursors targeted a 1.8 eV bandgap required for the multijunction design. Ultimately, InAlAsSb material with the desired bandgap was confirmed by photoreflectance spectroscopy.

For the second approach, this dissertation studied the integration of InAs quantum dots (QDs) in a GaAs solar cell in conjunction a back surface reflector (BSR). A quantum dot solar cell (QDSC) with a BSR has the potential to increase short-circuit current by 2.5 mA/cm^2 and also increase open-circuit voltage due to photon recycling. In this study, multiple textured BSRs were fabricated by growing inverted QDSCs on epitaxial lift-off templates and then texturing the rear surface before removing the device from the substrate. Identical cells with a flat BSR served as controls. Optimization of inverted QDSC growth conditions was also performed via a cell design study. Device results showed increased open-circuit voltage with increasing optical path length, and the greatest improvement in sub-band current over a flat BSR control device was 40%.

In the final chapter, a life cycle assessment (LCA) of these technologies was performed to identify the hypothetical optimum at which energy investments in cell performance (such as the two described above) no longer correspond to improvements in the overall life cycle performance of the PV system. Four cell designs with sequentially increasing efficiencies were compared using a functional unit of 1 kWp. The first is a commercially available and has been studied in previous LCAs. The second is the design containing InAlAsSb mentioned above.

The third represents the most material-intensive option, which bonds two substrates to create a five-junction cell. The fourth is a six-junction cell that uses a metamorphic grade between subcells and represents the most energy-intensive option. A thorough literature review of existing LCAs of high-concentration photovoltaic (HCPV) systems was performed, which obviated the need for data on the manufacture of MOVPE precursors and substrates. LCAs for the most common III-V substrate (GaAs) and precursors were executed prior to conducting the HCPV system LCA, due to the absence of detailed information on the life cycle impacts of these compounds in literature. Ultimately, both the cumulative energy demand and greenhouse gas emissions of the HCPV system decreased proportionally with increasing cell efficiency, even for the most energy and material-intensive cell designs. It was found that the substrates and precursors corresponded to less than 2% of system impacts. This implies that current mechanisms to increase cell efficiency are environmentally viable in HCPV applications without the need for material reduction, and would make III-V HCPV more environmentally competitive with dominant silicon PV technologies.

.

ACKNOWLEDGEMENTS

I would first like to thank my co-advisors, both of whom transformed me into the scholar I am today. Dr. Seth Hubbard gave me so many opportunities to learn and challenge myself - none of this would be possible without him. Dr. Callie Babbitt provided guidance since my arrival at RIT and always encouraged me to pursue my interests – thank you, your support is the reason I made it here! Also, my committee members, Dr. Gabrielle Gaustad: thank you for your time, insight, and companionship at conferences. Dr. Jing Zhang, thank you for sharing your time, expertise, and research assistants to help turn research ideas into a reality! And the department head Dr. Tom Trabold, you have been an enormous help and guiding force during all this – thank you.

A special thanks to my NREL collaborators – you helped me direct my research efforts in a wonderfully synergistic and effective direction, and I am so grateful. Especially Kelsey Horowitz and Dr. Robert Margolis, for supporting my research interests and discussing them in context of current events. My NASA collaborators, Jeremiah McNatt and Anna Marie T Pal, who contributed so much towards my work on MOVPE growth and were my main companions in Cleveland, in addition to Dr. David Forbes and Nichole Hoven who got me started at NASA in the first place. Also thank you to my NSTRF mentor, Dr. Geoffrey Landis, who was always supportive of my research interests. I would also like to thank Dr. Eric Hittinger, who transformed my approach to energy policy by example. And Dr. Annick Anctil, thank you for sharing your time and thoughts on how to approach PV sustainability and inviting me to work on the women's PV lunch!

To the Nano-PV lab - thank you for your camaraderie and support. In particular, Dr. Zachary Bittner, thanks for answering my questions, having great taste in food, and even better taste in humor. Dr. Stephen Polly, for being the best teacher around and a good friend. Dr. Michael Slocum, thanks for being so available and efficient. Dr. Yushuai Dai, George Nelson, Elisabeth McClure, and Adam Podell: thanks for both your help and your friendship. Emily Kessler, Kayva Duggimpudi, Adam Bennett, and Andrew Sindermann, thanks for all your hard work, you were truly exceptional and talented undergrads. Also thanks to Dr. Hyun Kum, Dr. Alessandro Giussani, Jim Smith, Elaine Lewis, and Lisa Dammeyer for keeping everything running.

A huge thank you to my sustainability cohort – you know who you are – the economics-homework-pizza-sessions and Mex rituals kept me going. In particular Michele Bustamante, my classmate, roommate, confidante, I feel so lucky to have gone through the Sustainability PhD with you. Also Lourdes Gutierrez and Saloni Vardhan, who were supportive in so many ways. My best friend Anna Cava Grosso, thank you for being so available for phone calls and giving me the idea to join sustainability in the first place: you've created a monster. Also Aditya Bose for being in the room for half those calls, and making me laugh when I needed it most. Thanks to my family for their patience while I completed this degree, dealing with me being so far away and absent at times, and for letting me talk your ears off trying to explain the nuanced world of graduate school. And finally to Abraham White for all your support during my defense and being there for me to see this through to the end.

I am eternally grateful for my funding sources: ARPA-E grant DE-AR0000335 and my NSTRF fellowship (NASA grant NNX15AP53H) which was an honor and made this experience truly exceptional. There are so many people that have been involved along the way, I cannot list them all. To anyone I did not specifically mention, but who helped me achieve this in some way – thank you. I remember you.

TABLE OF CONTENTS

LIST OF FIGURES

LIST OF TABLES

LIST OF ACRONYMS

AM0: air mass 0

AM1.5D: air mass 1.5 direct

AM1.5G: air mass 1.5 global

ARC: anti-reflective coating

BOS: balance-of-system

BSF: back surface field

BSR: back surface reflector

CB: conduction band

CED: cumulative energy demand

CO_2-eq: carbon-dioxide equivalent

DEZn: diethylzinc

Eg: bandgap

ELO: epitaxial lift off

EPBT: energy payback time

EQE: external quantum efficiency

EROI: energy return on investment

FF: fill factor

FKO: Franz-Keldysh oscillations

GHG: greenhouse gas

HCPV: high-concentration photovoltaics

HRXRD: high-resolution x-ray diffraction

IB: intermediate band

IBSC: intermediate band solar cell

III-V: semiconductor materials using elements in groups III and V of the periodic table

IMM: inverted metamorphic

IQE: internal quantum efficiency

I-V: current-voltage

Jsc: short-circuit current

LCA: life cycle assessment

LEIO: low energy interference oscillations

LILT: low-intensity low-temperature

MBE: molecular beam epitaxy

MOVPE, OMVPE, MOCVD: metal organic vapor phase epitaxy, metal organic chemical vapor deposition

QD: quantum dot

QDSC: quantum dot solar cell

PL: photoluminescence

PR: photoreflectance

PV: photovoltaic

SIMS: secondary-ion mass spectrometry

SR: spectral response

SRV: surface recombination velocity

TBAs: tertiarybutylarsine

TDFF: third derivative functional form

TEM: transmission electron microscopy

TMAl: trimethylaluminum

TMIn: trimethylindium

TMSb: trimethylantimony

TTBAl: tritertiarybutylaluminum

UV-Vis: ultra-violet & visible

VB: valence band

Voc: open-circuit voltage

XRD: x-ray diffraction

CHAPTER 1: Introduction

1.1 Motivation

In the photovoltaics community, it is common knowledge that III-V multijunction photovoltaics have the highest efficiencies [1]. This is due to the availability of a wide range of direct bandgaps, where multiple junctions with successively decreasing bandgaps can more effectively split up the solar spectrum and waste less photon energy due to transmission and thermalization. III-V semiconductors also have exceptionally high material quality with few impurities and electronic traps, in addition to the fact that most III-V photovoltaics have direct bandgaps which result in high absorption coefficients. This is illustrated in Figure 1 which depicts the standard commercially available germanium-based triple junction cell on the left, while the right and middle graphs display a black line corresponding to the AM1.5D solar spectrum, which stands for "Air Mass 1.5, Direct" and is defined as the intensity of direct light observed on the earth's surface though an air mass that is 1.5x the thickness of the atmosphere, which is useful for concentrator photovoltaics in most non-equatorial regions. The colored sections of the right-hand graph denote the usable fraction of the spectrum available to each of the subcells, calculated by multiplying the spectrum by ratio of the subcell bandgap to the energy of the wavelength on the x-axis. The difference between the AM1.5D spectrum and cell absorption corresponds to thermalization losses, where the energy is lost as heat in the device (assuming no reflection losses). At the band-edge of each material, its absorption coefficient drops to zero, after which no absorption occurs and which is labeled transmission losses. These are circumvented by adding additional subcells, such that transmission losses only occur after the final subcell. When comparing the single-junction graph with the multi-junction graph, it is evident that multiple junctions reduce both thermalization and transmission losses.

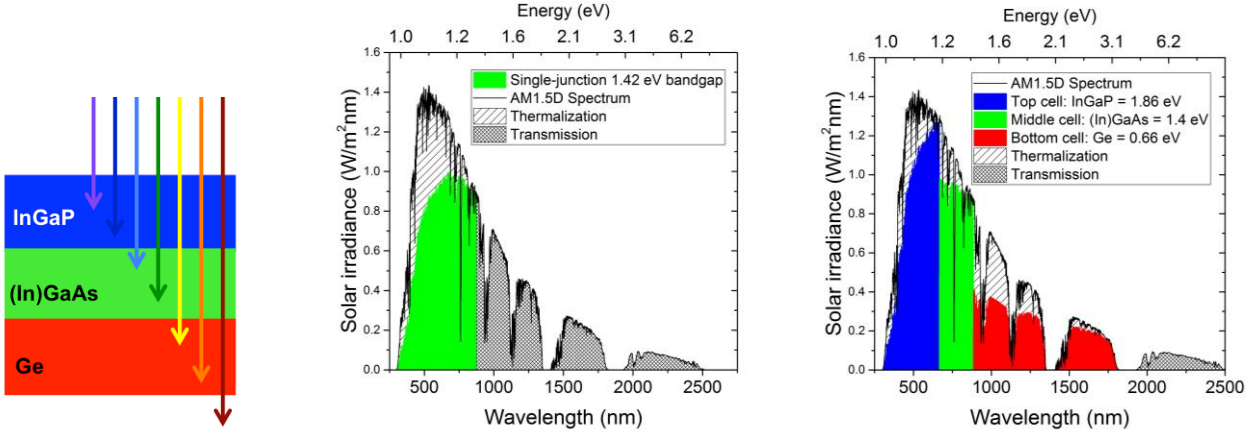

Figure 1: (left) Germanium triple junction schematic, (center) AM1.5D terrestrial solar spectrum overlay with approximate absorption of 1.35eV single-junction, and (right) AM1.5D terrestrial solar spectrum overlay with approximate absorption of germanium-based triple junction

Despite the superior performance of III-V photovoltaics, the National Renewable Energy Laboratory indicates that both cell efficiency and production methods of III-V photovoltaics need improvement in order to be competitive with other terrestrial energy technologies, even when used under highly concentrated sunlight where cell efficiency increases further [2, 3]. To date, the best multijunction III-V photovoltaics have used three junctions, grown on a

germanium or GaAs substrate and sometimes utilizing a metamorphic grade to incorporate additional junctions with differing lattice constants and thus extending the range of available bandgaps. This limits spectrum-splitting to the bandgaps of materials afforded by the substrate lattice constant and the ability to create a successful metamorphic grade, which often means less-than-optimal bandgap combinations. Research published by González et al. [4] demonstrated that the optimal bandgap combination for a triple-junction photovoltaic cell under the terrestrial solar spectrum AM1.5D is 1.74 eV/1.17 eV/0.7 eV, as shown in Figure 2. González et al. argue that such a combination is feasible using materials lattice-matched to an InP substrate, specifically a stack comprised of $In_{0.21}Al_{0.79}As_{0.74}Sb_{0.26}/In_{0.52}Al_{0.33}Ga_{0.15}As/In_{0.53}Ga_{0.47}As$, and could achieve up to 52.8% efficiency under 500 suns AM1.5 based on a predictive drift-diffusion model [4]. Growth of InAlAsSb by molecular-beam epitaxy has been demonstrated with successful composition control, however significant challenges exist for growth by metal organic vapor phase epitaxy (MOVPE) [5-7]. This is a critical issue for photovoltaic applications as MOVPE is a more cost effective method of growing large area III-V devices. Existing reports on InAlAsSb growth by MOVPE have targeted alloys with a composition of $In_{0.34}Al_{0.66}As_{0.85}Sb_{0.15}$, or even lower Sb content [5, 8, 9]. The InAlAsSb material needs to have a higher Sb composition ($In_{0.21}Al_{0.79}As_{0.74}Sb_{0.26}$) to target the 1.74 eV bandgap for photovoltaic applications [10].

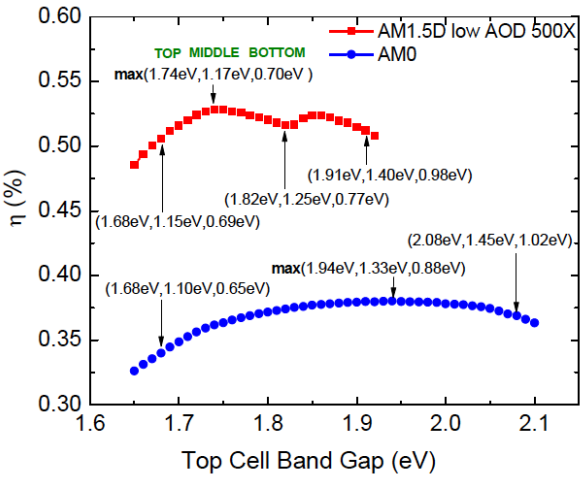

Figure 2: Bandgap optimization modeling for triple junction photovoltaics where η is conversion efficiency (reprinted with permission from [4])

As a separate strategy, quantum structures such as quantum dots (QDs) and quantum wells in photovoltaics can extend the long-wavelength absorption of a solar cell, and enhance both single junction and multijunction cell performance since QDs can increase short-circuit current (J_{SC}) and improve current-matching [11, 12]. QDs are also an avenue to realizing the intermediate band solar cell, which is explained in more detail in Chapter 5 and could exceed conventional single-junction limits with a theoretical maximum efficiency of 44.5% at one sun and over 60% under concentration [13]. However, due to low surface coverage of QDs, many QD layers are necessary to enhance performance. Increasing the QD layers presents significant challenges regarding growth time and strain management, which would negatively impact the open-circuit voltage (V_{OC}). Removal of the substrate and

fabricating a back surface reflector increases absorption both in the QD region and the bulk of the cell, which enables the use of a thinner bulk cell to achieve the same power output. Texturing the back surface to randomize the angles at which the light is reflected can increase the proportion of the light that is totally internally reflected and increase the optical path length through the device, which has been demonstrated in quantum well solar cells [14].

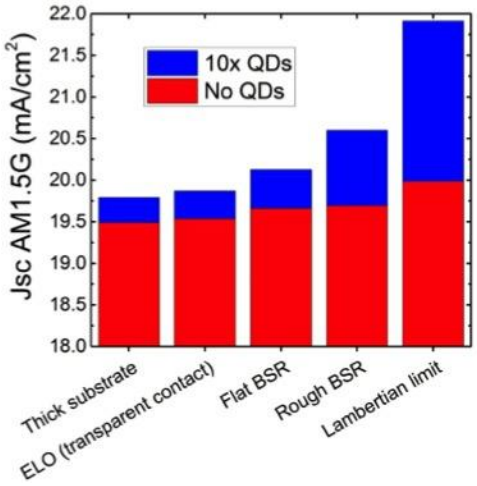

Figure 3: Predicted short-circuit current of a GaAs photovoltaic cell compared to a GaAs cell with InAs QDs as a function of back reflector

Figure 3 illustrates these potential improvements using absorption coefficients for InAs dots in GaAs, calculated via a 8 band k·p simulation [15-17]. The expected J_{SC} of a single-junction GaAs cell is compared to a GaAs cell of the same thickness with 10 layers of InAs QDs by converting the absorption coefficients into photocurrent. Increasing the texture of a back surface reflector improves both the control and QD cell performance, though significantly more improvement is predicted with QDs as the optical path length enhancement approaches the Lambertian limit of $4n^2$ where n is the refractive index of the material [18]. Re-use of the substrate and a thinner cell both represent intensive materials reduction and are significant strategies to improving the techno-economic performance of III-V photovoltaic devices, as outlined by the National Renewable Energy Laboratory [3]. Furthermore, there are significant benefits for space applications in that quantum structures in photovoltaics are known to improve the radiation tolerance of a device, in addition to the fact that thinner devices are less susceptible to radiation damage [19, 20].

Viewing III-V photovoltaic technology from a systems perspective, the application of III-V PV cells in high concentration photovoltaic (HCPV) systems results in a stronger overall life cycle performance, given that less of the expensive III-V material can be used in combination with glass lenses for the same power output. Life cycle assessments (LCAs) for a MOVPE-grown Ge-based triple junction HCPV system have attributed >1% to up to 15% of the cumulative energy demand (CED) to manufacturing the cell itself [21-24]. Existing HCPV LCAs employed liberal assumptions and approximations concerning the cell manufacturing process, which involves specialty chemicals whose manufacture is proprietary in nature [25]. Given the wide discrepancy between previously published results, this research also intends to provide a more precise figure on the contribution of the cell

manufacture to the overall life cycle of the HCPV system. Furthermore, given that III-V cell efficiency is improved by incorporating additional junctions which require metamorphic grades or additional substrates and processing techniques, this implies that further material and energy usage occur during the cell manufacturing stage to achieve marginal efficiency gains. Iterative LCAs could identify a point at which the cell manufacturing process becomes too energy-intensive or impact-intensive such that improvements in cell efficiency no longer correlate to improvements in the overall life cycle of the HCPV system. Furthermore, since photovoltaics are a renewable energy source, LCAs should consider both the energy invested in its manufacture and the GHG emissions that its use is attempting to offset.

1.2 Approach

The goals of this thesis are achieved by pursuing three different trajectories simultaneously. The first involves development of the top cell in the multijunction design on InP, the second involves development of light management textures, and the third investigates the life cycle impacts of multijunction photovoltaics. The structure of the overarching research question based on these trajectories is displayed in Figure 4.

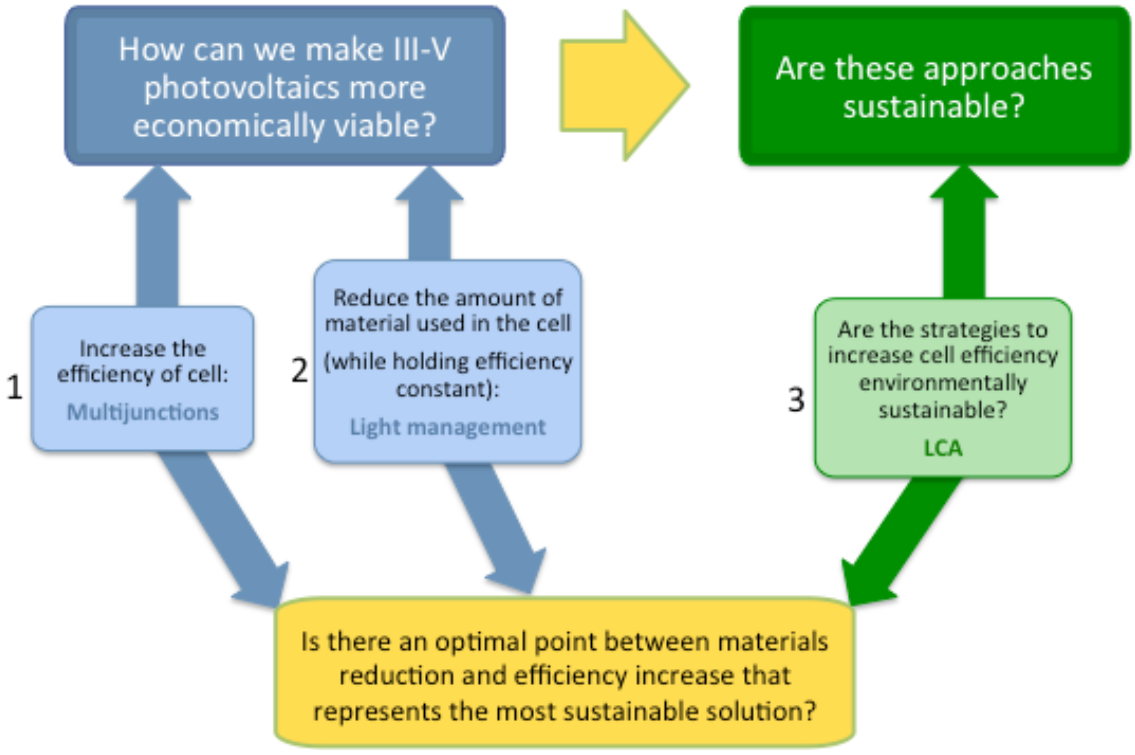

Figure 4: Schematic showing multiple trajectories that all feed into the same overarching research question.

In the first trajectory, initial work focused on development of InAlAs as the starting point for the top cell material InAlAsSb in the lattice-matched triple junction design on InP. This involved bulk material characterization,

optimization of a InAlAs cell design via simulation, fabrication process development, and testing of completed devices. Multiple rounds of devices were fabricated where the InAlAs material was grown with alternative MOVPE precursors in subsequent iterations. Investigation of alternative precursors has been established as necessary to move towards growth of InAlAsSb or any Sb-containing alloy [26]. Development of the InAlAsSb material by MOVPE involved preliminary growth studies comparing precursors and growth temperature. The development of InAlAsSb targeted a specific composition with a high bandgap. For composition verification of the alloy, samples were sent out for analysis by secondary-ion mass spectrometry. For bandgap verification, multiple techniques were investigated including photoluminescence, ultra-violet and visible transmission spectroscopy, and photoreflectance.

For the second trajectory, GaAs solar cells with InAs QDs were used because these quantum dot solar cells (QDSCs) are well-developed and have been extensively characterized which makes it useful as a known material system for a light management study. In order to implement light management in the QDSC, the thin photovoltaic device would need to be removed from its substrate so that free carriers would not be absorbed and lost in the thick substrate. This could be achieved using an epitaxial lift off (ELO) technique which selectively etches away a sacrificial layer between the cell and the substrate, and also permits re-use of the substrate. Access to an ELO process is available through a collaborator, Microlink Devices, Inc. who holds a patent on the technique. A back surface texture was created using a lithography pattern and a crystallographic etchant for AlGaAs, similar to that reported in [14]. Absorption enhancement is quantified by measuring spectral response from fabricated devices and integrating that data past the GaAs bulk bandedge to compare current collected from the QDs for different back surface textures.

The third trajectory aims to provide a more precise figure on the contribution of the cell manufacture to the overall life cycle of the HCPV system. This is achieved by extensive data collection and process modeling of the cell growth and fabrication process, based on patents as well as empirical data in a level of detail heretofore unavailable in literature. By conducting the LCA for multiple existing and proposed advanced III-V photovoltaic designs (including the cell from the first trajectory), this study attempts to evaluate the impact of the most energy-intensive cell designs to see if there is a limit at which the cell impacts start to dominate the overall life cycle of the HCPV system. This is accomplished by comparing metrics such as cumulative energy demand (CED) and greenhouse gas emissions in terms of equivalent kg of carbon dioxide (CO_2-eq).

1.3 Objectives

This research was supported by contributions from many members within the RIT NanoPV research group, and original contributions are listed below as research objectives:

- Optimized $In_{0.52}Al_{0.48}As$ single junction device
- Precursor and growth parameter space in InAlAs and InAlAsSb
- Bandgap measurement of high bandgap $In_{0.21}Al_{0.79}As_{0.74}Sb_{0.26}$
- Increased absorption in quantum-dot solar cell as a function of back surface texture
- LCA of MOVPE precursors and next-generation high-concentration PV

- Determine if a point exists at which cell manufacturing becomes too energy- or impact-intensive such that improvements in cell efficiency no longer correlate to improvements in overall life cycle of HCPV system

1.4 Organization of Dissertation

Chapter 1 briefly describes the motivation behind the research in the dissertation, including the significance of III-V photovoltaic technology and challenges for market penetration. Mechanisms for improving III-V photovoltaic performance are presented, including development of an InAlAsSb material for a mulitjunction design, integration of quantum dots, and light management. The motivation for life cycle assessment of these photovoltaic technologies is also discussed. These individual research trajectories (multiple mechanisms for improvement, and life cycle assessment) are presented in context of the broader research question, which is to identify optimum conditions at which energy investments in cell performance no longer correspond to improvements in the overall life cycle performance of the PV system. Anticipated research outcomes are specified and the organization of the dissertation is described.

Chapter 2 presents background information that will be necessary for understanding the content in the following chapters. This includes background on III-V semiconductor materials and the most prevalent III-V material production process, metal organic vapor phase epitaxy (MOVPE). This chapter also discusses the salient features of basic solar cell operation using illustrative figures such as a generic semiconductor band diagram, a current-voltage measurement from an illuminated solar cell, and spectral response from a solar cell as a function of wavelength.

Chapter 3 discusses the development of a single-junction InAlAs cell lattice-matched to InP as a preliminary goal towards the development of InAlAsSb and as a material with its own merits. A cell design was developed and optimized via simulation, then grown by MOVPE using standard precursors, fabricated and tested. Fits to the experimental data were generated by the same simulation tool to extract device parameters. An anti-reflective coating study was completed which resulted in an unprecedented efficiency measurement. Bulk InAlAs samples were grown using alternative MOVPE precursors in order to prepare for the transition to the InAlAsSb quaternary, and impurity concentrations were analyzed. Another round of InAlAs cells were grown in order compare standard and alternative MOVPE precursors. The experimental results from these cells show the alternative precursor tritertiarybutylaluminum (TTBAl) resulted in improved performance as compared to the industry standard trimethylaluminum. Fits to experimental results indicated longer lifetimes in the TTBAl-InAlAs material caused the improvement.

Chapter 4 focuses on the development and characterization of the InAlAsSb material for the optimized InP-based multijunction design. A tabular summary of an extensive literature review is presented in order to identify the optimal MOVPE growth conditions for InAlAsSb. This informed the subsequent growth of InAlAs, AlAsSb and InAlAsSb with alternative precursors at non-standard temperatures and V/III ratios. Bandgap verification of the resulting InAlAsSb samples was attempted by each photoluminescence, UV-Vis transmission, and photoreflectance spectroscopy. A defect state dominated the photoluminescence measurement, even at low temperature, which motivated the investigation of alternative bandgap measurement techniques. Ultimately, the method of extracting

bandgap from UV-Vis transmission data involved a high degree of uncertainty, and photoreflectance was used for the majority of InAlAsSb samples. The photoreflectance technique was first verified on known binary samples such GaAs and InP, as well as ternary samples such as InGaAs and InAlAs. Ultimately, bandgap measurements extracted from photoreflectance of InAlAsSb samples agreed with quaternary-composition dependent predictive model based on band parameters.

Chapter 5 describes the motivation for quantum structures in photovoltaics in more detail. It quantifies the benefits of a back surface reflector (BSR) for both the quantum structures and the bulk cell. Fabrication process development for a triangular and a rounded BSR is presented, and characterized by multiple reflectance measurements. An initial round of quantum dot solar cells (QDSCs) and identical solar cells with QDs were grown and fabricated with a triangular BSR, as well as a flat BSR to serve as a control, before being lifted off and fabricated for testing. These QDSC results showed a 30% increase in sub-band current for the triangular BSR, though the bulk device performance suffered due to poor QD conditions. A second round of QDSCs were grown with improved QD conditions. Separate samples were fabricated with flat, triangular, and rounded BSRs to compare BSR performance. The rounded BSR showed the highest sub-band current, representing a 40% increase over the flat BSR. Finally, a QDSC cell design study was executed in order to evaluate cell performance dependence on bulk layer thickness, amount of material grown after the QD layers, and the layers inserted between QD layers. It was determined that using a thick n-type emitter produced the highest open-circuit voltage, while the amount of material grown after the QDs was observed to have no effect, and increasing the thickness between QDs layers resulted in improved open-circuit voltage as well. Finally, a two-dimensional BSR was developed and fabricated on ELO devices, and the insertion of a dielectric was also investigated. This resulted in fabrication issues, but device results still showed the highest sub-band current out of all previous QDSCs with BSRs.

Chapter 6 summarizes the existing LCAs of III-V PV and outlines the assumptions employed that warrant further research, specifically the MOVPE precursors and III-V substrates that comprise the cell. The goal, scope, and functional unit of the LCA is defined in order to compare different cell types employed in equivalent HCPV systems. The cells and HCPV systems under analysis are described in detail. Life cycle inventories for MOVPE precursor and substrate manufacturing are presented. The life cycle impacts of the HCPV system containing each cell type are reported for cumulative energy demand and greenhouse gas emissions. Finally, these results are interpreted in the context of previous LCAs, and implications for the technology are discussed.

Chapter 7 presents a summary of the dissertation and outlines potential trajectories for future work.

CHAPTER 2: Background

2.1 III-V semiconductors

III-V photovoltaics are named for the groups in which the comprising elements occur in the periodic table. A group III atom always bonds to a group V atom, making the ratio of group III elements to group V elements 1:1 in any given material. The possible binary alloys (one group III element and one group V element) are shown as circular data points in Figure 5. These binaries have fixed 1:1 compositions, fixed lattice constants, and fixed bandgap. The lines connecting these binary endpoints represent ternary alloys, which vary compositionally between the two binary endpoints, while quaternary alloys occur in any space delineated by multiple binary endpoints. Ternary and quaternary alloys are pseudobinary in that they still retain the 1:1 group III to group V ratio, so composition nomenclature always refers to the fraction within the group, such as $In_xAl_{1-x}As_ySb_{1-y}$.

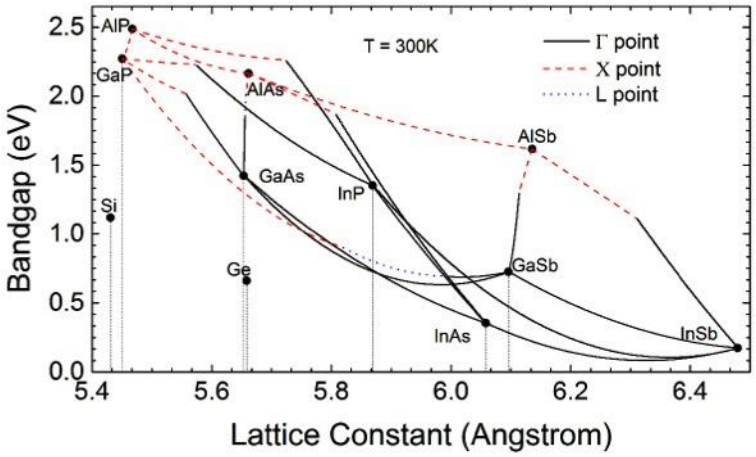

Figure 5: Γ, X, and L band transitions shown as a function of lattice constant for ternary alloy lines between binary endpoints

The majority of materials shown in Figure 5 have direct bandgaps labeled as Γ-points. These Γ-points, and other "critical points" such as the X-points and L-points shown in Figure 5, correspond to points of high symmetry in the Brillouin zone for a given crystal lattice. The Brillouin zone is the smallest repeating unit of a crystal in reciprocal space. For face-centered-cubic (FCC) crystals such as GaAs, the critical points of its Brillouin zone (shown in Figure 6) refer to the center of the Brillouin zone (Γ), the center of a hexagonal face, and the center of a square face. Plotting these critical points against the valence and conduction bands of a given material, referred to as an E-k diagram, display the critical point transitions in a way that is quantifiable. An example is depicted in Figure 6 for GaAs. Direct bandgaps occur when the valence band maxminum and conduction band minimum occur in the same location in reciprocal space. Transitions can occur between other locations in reciprocal space, as well as between the multiple valence bands which are labeled V1-V3 in Figure 6.

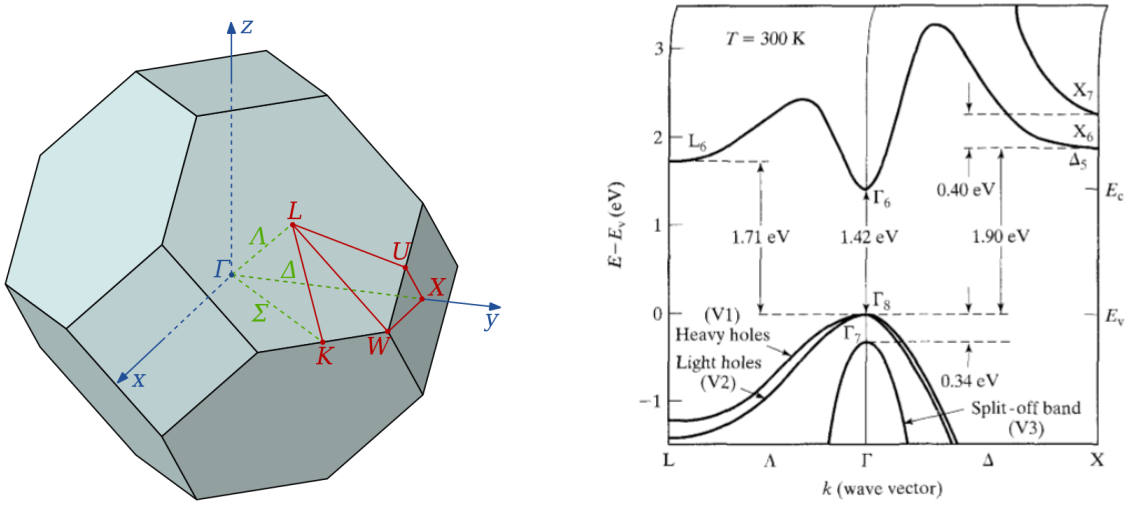

Figure 6: (left) Brillouin zone for an FCC crystal (public domain [27]), (right) E-k diagram for GaAs ([28], reprinted with permission)

2.2 III-V crystal growth

To grow a III-V semiconductor device, a bulk binary crystal is used as a crystal lattice template (germanium can also be used, and silicon somewhat less effectively) referred to as a substrate. This process of growth of a crystalline layer on a crystalline substrate is referred to as epitaxy. The highest throughput and most commercially used method of III-V growth is metal organic vapor phase epitaxy. The "metal organic" term refers to compounds such those shown in Figure 7 where organic ligands or hydrogen atoms have been attached to group III or group V elements. These precursors are typically stored as a liquid and are transported into the growth chamber using hydrogen as a carrier gas. The growth chamber contains a substrate at a high temperature where precursors epitaxially deposit the group III or group V atom and the severed organic ligands react with each other and are pumped away. Equation **1** below shows an example of such a reaction.

$$AsH_{3\,(g)} + Al(CH_3)_{3\,(g)} \rightarrow AlAs_{(s)} + 3CH_{4\,(g)} \qquad \text{Equation 1}$$

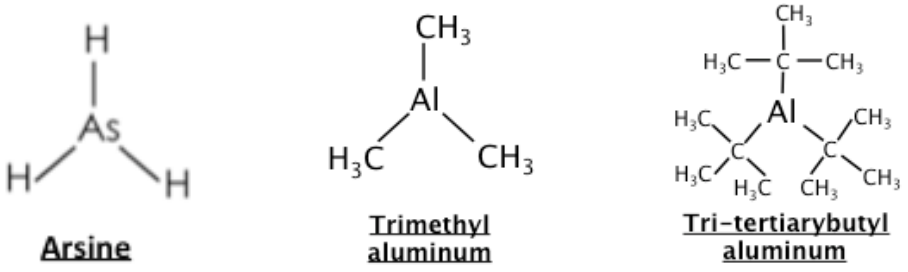

Figure 7: Schematic of III-V precursors with organic ligands

Several MOVPE growth conditions can affect the quality of a given material, such as growth temperature, growth rate, reactor pressure, carrier gas flow, and V/III ratio which refers to the molar ratio of group V gases to group III gases. The appropriate ranges for these conditions vary depending on the epitaxial material and reactor configuration. Two different reactors have been used for the material developed in this thesis. The first, where the majority of samples were developed, was a rotating disk Veeco D125 3x2" multiwafer LDM MOVPE reactor located at the NASA Glenn Research Center. Growth on this reactor typically occurred at 60 torr using a rotation of 1000 rpm. Due to the high-speed rotating disk providing the mechanism for uniform laminar flow and preventing backflow, the rotation, pressure, and carrier gas flow could not be altered without significant recalibration [29]. Over the course of this dissertation, an MOVPE reactor was installed at RIT, which was used for samples occurring later in the dissertation. This reactor was a 3x2" multiwafer Aixtron close-coupled showerhead MOVPE (CCS-MOVPE) reactor. The close-coupled showerhead permits greater variation for pressure and carrier gas flow, since its mechanism for reducing backflow is reduction in reactor height [29]. Pressure on the CCS-reactor was typically kept between 50 to 100 mbar, and rotation was kept at 50 rpm. For further information, the concepts behind MOVPE growth, relevant parameters, and reactor configurations can be found in references [30-32].

2.3 Solar Cells

A band diagram of a representative single-junction solar cell under illumination is shown in Figure 8, where the emitter is doped with electrons (n-type), the base is doped with holes (p-type) and the junction occurs in the space charge region. Incident light absorbed in the material generates electron-hole pairs (carriers) that are separated by energy equivalent to the energy of the photon that generated them, with electrons occurring in the conduction band and holes occurring in the valence band. This occurs for light with energy greater than the bandgap (E_g) which is defined as the energetic difference between the valence band (VB) and the conduction band (CB), while photons with lower energies are transmitted through the cell and lost. Electron-hole pairs that have significantly greater energy than the bandgap relax to their respective bands quickly such that any energy in excess of the bandgap is lost as heat, hence this loss is known as thermalization.

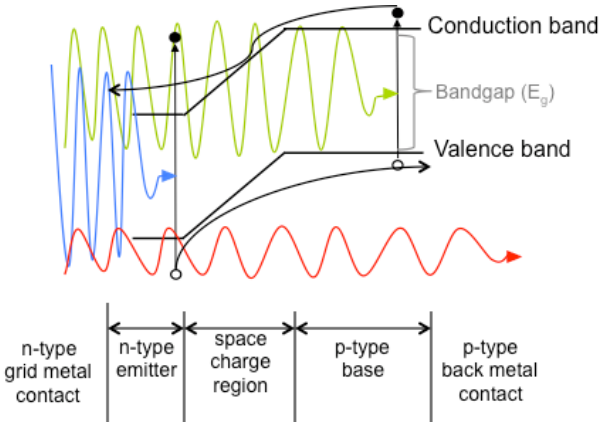

Figure 8: Representative band diagram of a single junction *nip* solar cell

If one assumes that all photons with energy greater than the bandgap get absorbed and converted into carriers, and that all carriers are collected, a maximum efficiency can be calculated for a given bandgap. This was executed by Shockley and Queisser in 1961 in a detailed balance model that accounts for thermodynamic limits by incorporating both absorption and emission in a solar cell [33]. This model assumes both the sun and solar cell to be blackbody radiators at 6000K and 300K, respectively, and uses the solar radiance calculated from the angle of the Sun incident on Earth. The maximum efficiency from this calculation is 31% for a bandgap of approximately 1.2 eV under this idealized 1-sun condition. Multijunction solar cells can exceed this single-junction detailed balance limit by stacking multiple bandgaps, typically the largest first to absorb the highest energy photons and minimize thermalization losses, followed by lower bandgaps that absorb photons that would otherwise be lost to transmission. These cells are stacked in series such that the voltage of each cell adds to the total, while the current is limited by whichever sub-cell generates the least current. For example, the InGaP/GaAs/InGaAs inverted metamorphic triple junction cell is commercially available and achieved 37.9% efficiency under AM1.5G manufactured in a laboratory, which clearly exceeds detailed balance limit for a single junction [34].

The portion of light that gets converted into current within the solar cell is characterized by a measurement known as spectral response (SR), which measures the current generated by the solar cell in comparison to the power incident on the solar cell as a function of wavelength. Integration of the spectral response with respect to the solar spectrum corresponds to the photocurrent generated by the device, or short-circuit current under illumination (J_{SC}). Spectral response can be converted to external quantum efficiency (EQE), which represents the ratio of electrons generated per incident photon, by Equation 2. EQE can be converted to internal quantum efficiency (IQE) using reflectance data and Equation 3, where IQE represents the number of electrons generated for every photon that is absorbed. A representative graph of EQE and IQE of a typical solar cell is shown in Figure 10, where the difference between the IQE and EQE is proportional to the reflectance of the solar cell. Short wavelength losses are primarily due to thermalization, though front surface recombination is also responsible for significant short-wavelength losses. QE improves nearest to the bandedge, though some recombination losses occur throughout the spectrum, after which QE drops after the bandedge due to transmission.

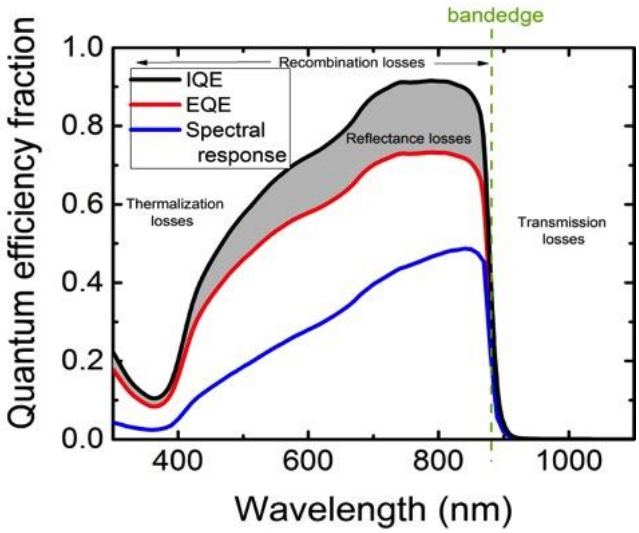

Figure 9: Representative EQE and IQE curves as a function of wavelength

$$EQE(\lambda) = \frac{hc}{q\lambda} SR(\lambda) \quad \text{Equation 2}$$

$$IQE(\lambda) = \frac{EQE(\lambda)}{1-R(\lambda)} \quad \text{Equation 3}$$

Solar cell performance is characterized by measuring a current-voltage (I-V) sweep under illumination, referred to hereafter as light I-V. A representative light I-V curve is shown in Figure 10. The open-circuit voltage (V_{OC}) is the measured potential difference across the two terminals of a solar cell when no current is flowing [35]. The V_{OC} can be used contributes to a useful parameter referred to as the bandgap-voltage offset (W_{OC}), which is equal to the V_{OC} of a device subtracted from its bandgap (E_g), as shown in Equation **4**. W_{OC} is a useful metric to compare solar cells of different materials because it is generally independent of bandgap within the range of 0.67 to 2.1 eV [36] . Using the detailed balance model to solve for the ideal 1-sun W_{OC} across this range produces a roughly constant value of 0.25, assuming only radiative recombination is occurring in the device [36].

$$W_{oc} = E_g/q - V_{oc} \quad \text{Equation 4}$$

The short-circuit current is the photocurrent generated due to the spectral response of the cell, described previously. Multiplying current and voltage calculates the power output of the cell, and the point at which this curve reaches a maximum is referred to as the maximum power point (MPP). Another metric of cell quality is to divide the MPP by the product $J_{SC}V_{OC}$. This metric is referred to as the fill factor (FF) and is generally used to describe the "squareness" of the I-V curve [35]. Finally, power conversion efficiency of the solar cell is calculated by dividing the product $J_{SC}V_{OC}FF$ by the incident power on the cell, which varies depending on the solar spectrum in use.

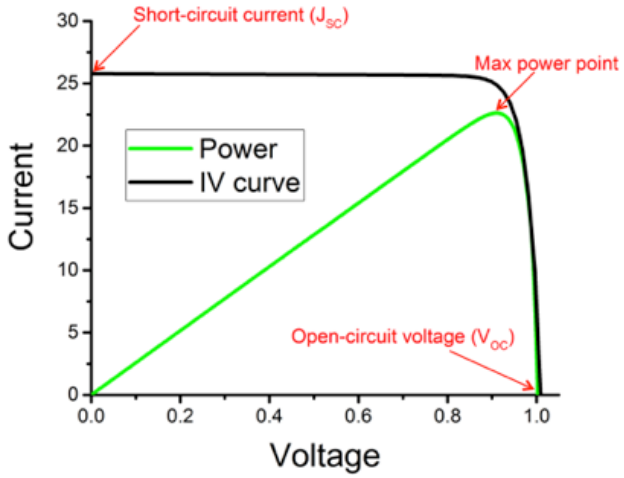

Figure 10: Representative light I-V curve of a solar cell

CHAPTER 3: Development of single-junction InAlAs photovoltaic cell lattice-matched to InP

3.1 Motivation

InAlAs has conventionally been used as a wide bandgap barrier material in optoelectronics lattice-matched to InP because of its 1.45 eV bandgap, however, it has undergone little development for photovoltaic (PV) applications [37, 38]. A small number of InAlAs photovoltaic cells have been studied under lattice-matched conditions to InP, lattice-matched to an engineered substrate, or metamorphically graded on a GaAs substrate [39-42]. When lattice-matched to InP, band parameters predict $In_{0.52}Al_{0.48}As$ to have a bandgap of 1.437 eV, though it has been reported to vary up to 100 meV due to tetragonal distortion that can occur in layers less than 2 μm thick that are not precisely lattice-matched [43, 44]. This material could comprise the top cell of an all-lattice-matched InP-based triple junction device, however detail balance calculations predict the maximum efficiency of an InAlAs/InGaAsP/InGaAs (1.47 eV/1.06 eV/0.74 eV) device is only 46% under 100 suns AM1.5 [40]. In order to increase efficiency, the top cell bandgap must be increased into the 1.7-1.8 eV range. Adding antimony, the quaternary alloy $In_{0.21}Al_{0.79}As_{0.74}Sb_{0.26}$ has a direct bandgap of 1.74 eV and is lattice-matched to InP [10]. A triple junction cell with InAlAsSb/InGaAsP/InGaAs (1.74 eV/1.17 eV/0.7 eV) subcells lattice matched to InP could achieve up to 52.8% under 500 suns AM1.5 using a model incorporating radiative efficiency which provides a more realistic estimate than typical detailed balance calculations [4].

Furthermore, $In_{0.37}Al_{0.63}As$ lattice-matched to an engineered substrate with a lattice constant of 5.80 Å has a bandgap of 1.93 eV [41]. This substrate has been experimentally demonstrated by growing a strained layer of InGaAs with a 5.80 Å lattice constant on InP, then removing the InP substrate and transferring the InGaAs layer to a glass substrate [41]. This virtual substrate can then be used as a crystalline template on which to grow a triple junction cell. The proposed triple junction InAlAs/InGaAsP/InGaAs (1.93 eV/1.39 eV/0.94 eV) is predicted to have an efficiency of 40.4% under 1-sun AM1.5 and 51.8% under 100-suns [45]. Development of InAlAs lattice-matched to InP is a useful starting point to develop InAlAsSb lattice-matched to InP as well as InAlAs with alternative lattice constants.

Additionally, InAlAs lattice-matched to InP could be a good candidate for low-intensity low-temperature (LILT) applications that require high radiation tolerance. Single-junction silicon or GaAs cells have previously been studied for LILT applications; triple-junction solar cells have been studied as well but suffer degraded performance if used over a wide range of temperatures which is problematic for distances >3 AU (astronomical units) [46, 47]. The bandgap of InAlAs lattice-matched to InP (1.4-1.5 eV) is low enough to make it useful for LILT applications as a single-junction solar cell. It could also be a good candidate for tandem cells which have previously been studied for LILT applications [47]. The radiation tolerance associated with InP-based materials makes this cell an even more attractive candidate for LILT applications such as missions to Jupiter which would encounter significant radiation [48].

3.2 Design/Development using industry standard MOVPE precursors

3.2.1 Cell design and optimization via simulation

Initial design considerations focused on comparing InAlAs cells from literature. The highest performing cell was an n-on-p device with a 200 nm emitter and a 1500 nm base, with extracted lifetimes used for simulations in Table 1 [40]. Bulk layers of doped InAlAs were grown by MOVPE to inform cell design, and results from Hall effect measurements are also shown in Table 1. Thicknesses for the final design were determined based on these mobilities and other parameters in Table 1, by iterative simulations using a one-dimensional minority carrier drift/diffusion model [40, 49]. The optimized cell structure is shown in Table 2. A 50 nm intrinsic region (i-region) was included between the emitter and base in order to prevent diffusion and compensation.

Table 1
Input Parameters for Design Simulations

Parameter	Value	Reference
4.5 x 10^{17} cm^{-3} p-InAlAs hole mobility	27 $cm^2V^{-1}s^{-1}$	measured
2 x 10^{18} cm^{-3} n-InAlAs electron mobility	905 $cm^2V^{-1}s^{-1}$	measured
Emitter minority carrier lifetime – holes (extracted from EQE)	400 picoseconds	[40]
Base minority carrier lifetime – electrons (extracted from EQE)	4 nanoseconds	[40]
n, k optical constants	See reference	[50]

Table 2
Optimized InAlAs Solar Cell Design

	Thickness (nm)	Type	Doping (cm^{-3})	Layer
$In_{0.53}Ga_{0.47}As$	20	n+	5 x 10^{18}	Contact
InP	10	n+	5 x 10^{18}	Etch stop
$In_{0.35}Al_{0.65}As$	15	n+	3 x 10^{18}	Top window
$In_{0.52}Al_{0.48}As$	75	n	1 x 10^{18}	Emitter
$In_{0.52}Al_{0.48}As$	50	i	-	Intrinsic
$In_{0.52}Al_{0.48}As$	1500	p	3 x 10^{17}	Base
$In_{0.52}Al_{0.48}As$	200	p	2 x 10^{18}	BSF
InP		p		Substrate

Strained InAlAs was selected for the top window due to the limited availability of high bandgap InP lattice-matched materials. Alternatives include AlAsSb or InAlAsSb, however these materials need further material development before they can be grown in high quality by MOVPE and do not offer as large of a valence band offset as strained InAlAs [51]. The strained $In_{0.35}Al_{0.65}As$ window is predicted to have a bandgap of 1.754 eV via interpolation of parameters reported by Vurgaftman et al., accounting for bowing and strain shifts [44]. The interpolation indicates that the conduction band of the $In_{0.35}Al_{0.65}As$ window is offset from the conduction band of the emitter by 256 meV and the valence band is offset by 61 meV. This is an adequate barrier for holes in the window layer given that the emitter is n-type, and the electric field of 17.6 kV/cm in the window layer acts as passivation. Since the selected window is strained, defects could potentially occur in the window/emitter interface. Such defects would increase the surface recombination velocity (SRV), which degrades quantum efficiency. Defects may occur once the critical thickness of a strained layer is exceeded and the layer begins to relax. The maximum critical thickness for the nominal material is 9.1 nm as predicted by Mathews and Blakeslee [52]. Given that the Mathews-Blakeslee limit is known to produce conservative estimates of critical thickness, and the window layer is on the order of the critical thickness, it can be assumed that the window is in the pseudomorphic regime and the density of misfit dislocations at the interface is low. Previous work on an $In_{0.3}Al_{0.7}As$ window for InP-based materials reported an SRV below 200 cm/s, which indicates defects are not excessive [51]. In order to prevent defect formation in the optically active regions of the cell, $In_{0.52}Al_{0.48}As$ with a doping of 2 x 10^{18} cm^{-3} was employed as a back surface field (BSF) between the base and the substrate rather than a strained rear window. Since previous reports were unable to remove the contact layer without degrading cell performance due to rapid oxidation of the high-aluminum content window, an InP etch stop layer was added to the design to protect the window [53]. One could conceivably etch the contact layer and attempt to deposit an anti-reflective coating (ARC) immediately to

minimize window oxidation, though some oxidation may still occur. However, incorporating an InP etch stop into the design permits the selective etch of the contact layer without exposing the window.

To quantify the improvement from reducing absorption losses, the simulation of a device retaining the 20 nm InGaAs contact layer was compared to the simulation of a device with an InP etch stop, and also compared to a device with neither contact layer nor etch stop. Sentaurus Device™ (a physics-based finite-element device simulation package by Synopsys, Inc.) was used to simulate AM1.5G I-V performance, by solving Poisson's equation and drift-diffusion equations for the PV device design. The simulations used most parameters from Table 1 except minority carrier lifetimes. Lifetimes were calculated from the electron effective mass in InAlAs and a mid-gap electron trap with low density (1×10^{14} cm^{-3}) to approximate a high quality cell, which corresponded to lifetimes on the order of 80 nanoseconds [50, 54]. Figure 11 shows light-IV simulations comparing devices with a top layer of either 20 nm InGaAs, 10 nm InP, or 15 nm $In_{0.35}Al_{0.65}As$, each with an optimized Si_3N_4 anti-reflective coating. The short-circuit current (J_{sc}) for a device with an InGaAs cap is 18.3 mA/cm^2, while the InP cap has a J_{sc} of 22.1 mA/cm^2, and the device with the exposed $In_{0.35}Al_{0.65}As$ window has a J_{sc} of 24.6 mA/cm^2. This represents a 21% relative increase in efficiency when using an InP cap rather than InGaAs, and an 11% increase when removing the InP cap from the $In_{0.35}Al_{0.65}As$ window. These simulation results confirm that it is advantageous to remove the InGaAs layer and include the InP etch stop in order to protect the high-aluminum content window from oxidation. Furthermore, the simulation results with the InP etch stop can serve as an ideal performance benchmark for the design in Table 2, with a J_{sc} of 22.1 mA/cm^2, an open-circuit voltage (V_{oc}) of 1.00 V, and an efficiency of 19.2% under 1-sun AM1.5G with an 87% fill factor. Removing the InP etch stop immediately before depositing the ARC could improve the device performance further, representing another 11% increase in 1-sun AM1.5G efficiency of 21.4%.

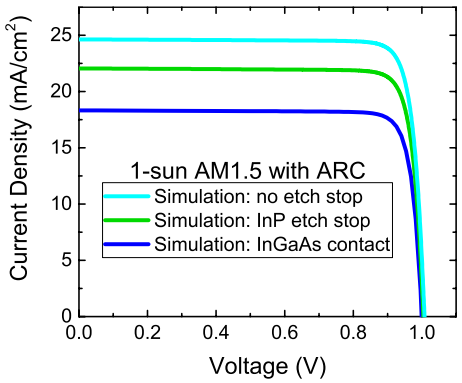

Figure 11: Simulated light-IV results of InAlAs cells with low trap density to establish a benchmark of "ideal" performance, comparing three cells based off the structure shown in Table II: "InGaAs contact" has no InP etch stop but retains the 20 nm InGaAs contact layer between grid fingers, "InP etch stop" removes the 20 nm InGaAs contact between grid fingers but retains the 10 nm InP etch stop, and "No etch stop" has neither InGaAs nor InP between the grid fingers.

3.2.2 Cell growth, materials characterization, and fabrication

InAlAs solar cells were grown on two InP substrates in a Veeco D125 3x2" MOVPE reactor at 60 torr using a rotation of 1000 rpm. The metalorganic precursors were trimethylindium (TMIn), trimethylaluminum (TMAl), and

arsine, doped with disilane for n-type and diethylzinc for p-type. TMIn was flowed at a rate of 39.4 μmol/min, TMAl at 35.5 μmol//min, and arsine at 1020 μmol/min, which corresponds to a V/III ratio of 100 and resulted in a growth rate of 1.94 μm/hr. The emitter was grown at 610°C because silicon incorporation in InAlAs decreases significantly with temperature, whereas the base was grown at 580°C in order to maintain p-dopant control. Devices were grown on InP:Zn (100) oriented substrates with a 2° offcut towards (110). A schematic and photograph of a fabricated devce are shown in Figure **12**.

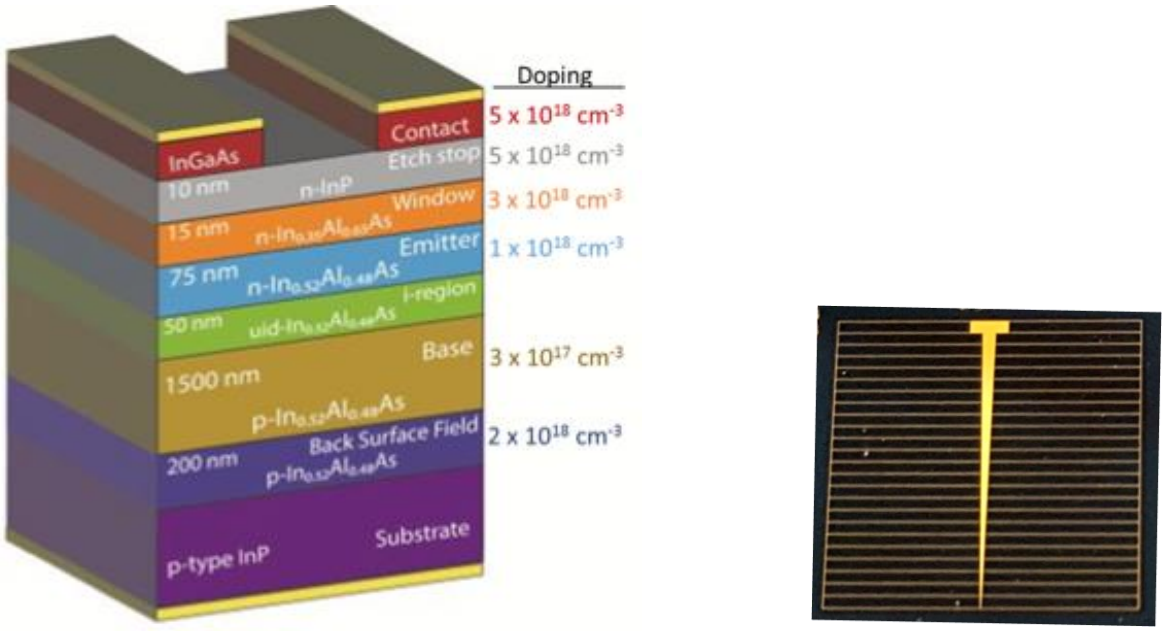

Figure 12: (a) Schematic of single-junction InAlAs device design with InGaAs underneath metal only (b) Photograph of fabricated 1 x 1 cm^2 InAlAs solar cell with ARC.

High resolution x-ray diffraction (HRXRD) of the window layer indicates a composition of $In_{0.34}Al_{0.66}As$, which is a slight deviation from the nominal design, but is expected to have little impact overall. HRXRD of the solar cell indicates that the base was compressively strained by 620 ppm to the substrate, which corresponds to a slightly In-rich layer consisting of $In_{0.53}Al_{0.47}As$. The composition-dependent bandgap relation for InAlAs indicates such an alloy should have a bandgap of 1.42 eV [44]. Electroluminescence shows a peak at 1.40 eV which is lower than expected and may include low-energy emission from the base which was grown at a lower temperature. InAlAs grown below 615°C is known to exhibit a significant degree of phase separation, where regions of InAs and AlAs occur separately in the epilayer [55]. Studies have shown phase separation in InAlAs grown at low temperatures can lower the bandgap as much as 290 meV [55]. To investigate if phase separation is observed in the InAlAs grown for this study, a sample was shipped to Andrew Norman at the National Renewable Energy Laboratory for transmission electron microscopy (TEM) analysis. A representative TEM image from this sample is shown in Figure **13**, which is a 110 cross-section of the InAlAs sample imaged using a -220 dark field. The fringes of dark and light contrast represent compositional variation which indicates the phase separation is likely the cause of bandgap reduction.

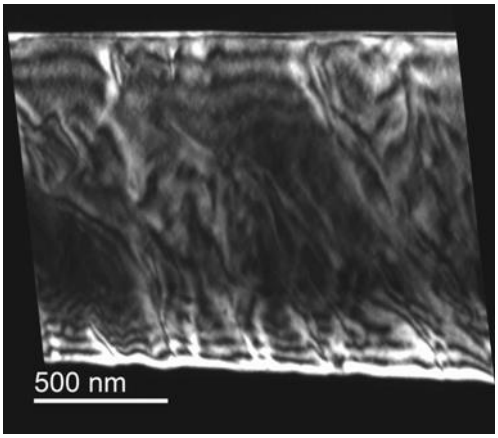

Figure 13: 110 cross-sectional TEM of InAlAs grown at 580ºC using -220 dark field, contrast fringes due to compositional variation.

Solar cells were fabricated using Au/Zn/Au as the p-type contact and Au/Ge/Ni/Au as the n-type contact. Cells were 1 cm by 1 cm with a grid finger spacing of 500 μm and 4% grid shadowing. A 1:1:38 mixture of H_3PO_4:H_2O_2:H_2O was used as a mesa-etchant as well as a contact etchant because it does not etch InP and also results in more uniform InAlAs sidewalls than HCl-based etchants. The mesa was etched approximately 700 nm into the base in order to isolate the junction. A 1:1:2 mixture of HCl:H_3PO_4:CH_3COOH (acetic acid) was used as a selective etchant of the InP etch stop layer, with the acetic acid acting to dilute the etchant to increase etch uniformity and precision for the thin etch stop. This etchant exhibited 6:1 selectivity to InP over $In_{0.52}Al_{0.48}As$. This etchant was used to selectively remove the InP etch stop on one of the substrates immediately before depositing an ARC. A dual-layer ZnS/MgF_2 ARC was deposited by thermal evaporation, using 46 nm/97 nm respectively for the cells retaining the InP etch stop, and 49 nm/107 nm respectively for the cell with the etch stop selectively removed. The thicknesses for the ARC were optimized using the optical software TFCalc by minimizing reflectance in the wavelength range of interest (below the nominal bandgap of InAlAs) given the optical constants of the topmost layers (InP and $In_{0.35}Al_{0.65}As$, respectively).

3.2.3 Experimental device results and fitting

Experimental light-IV results under 1 sun AM1.5G illumination are shown in Figure **14**, summarized in Table 3, and published in [56]. Light-IV was measured in a two-zone TS Space Systems solar simulator calibrated with $InGaP_2$ and GaAs reference cells, which were calibrated to AM1.5G by the National Renewable Energy Laboratory. A total of 7 cells were measured on the two wafers. Light-IV of the best performing cell from each wafer is shown in Figure **14**(a). The best cell from the wafer that retained the InP etch stop had an efficiency of 17.1% under 1-sun AM1.5G, which corresponds to an AM0 efficiency of 14.7%. The average AM1.5G efficiency for the wafer was 16.7% with a standard deviation of 0.5%. The best cell from the wafer that had the InP etch stop selectively removed had an efficiency of 17.9% under 1-sun AM1.5G. The average efficiency for the wafer was 17.2% with a standard deviation of 0.5%. The reflectivity of the ARC is not identical between the two wafers due to non-uniformity in ZnS deposition, resulting in higher reflectance from the cell with the InP etch stop. However, a simple calculation confirms that if the reflectivity of the two wafers were identical, the cell without the etch stop would still exhibit 4% higher current. This is also evident in the internal quantum efficiency (IQE) data, shown below in Figure **15**(b).

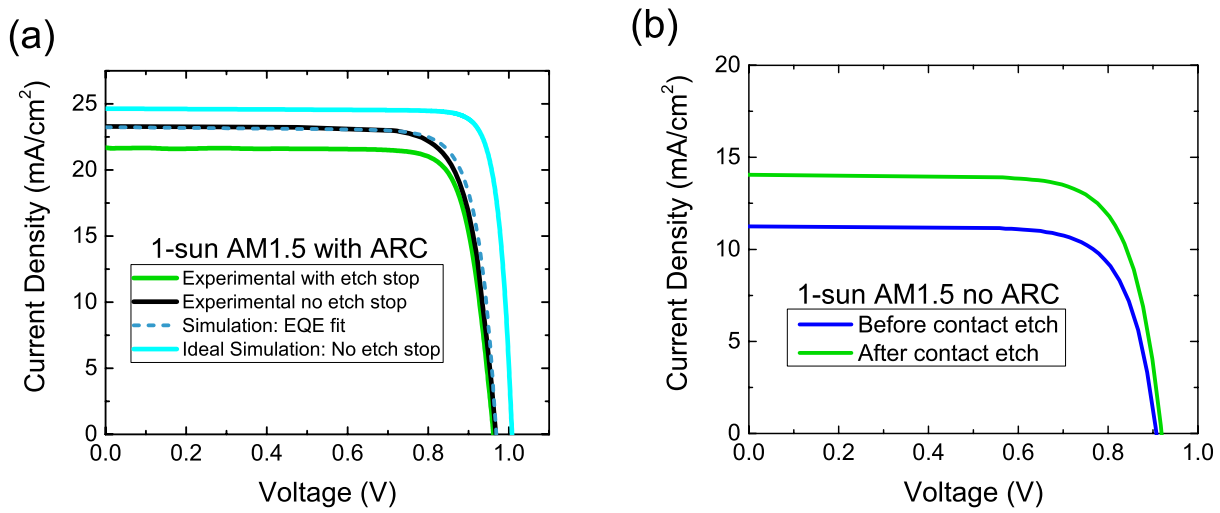

Figure 14: (a) Experimental light-IV of best performing cells, a simulated fit to experimental light-IV from best cell with no etch stop generated using lifetimes extracted from a fit to experimental EQE data, and the "benchmark" simulated light-IV curve shown in Figure 11 with no InP etch stop (b) Experimental light-IV results from a cell before and after contact etch agree with predicted 21% J_{SC} increase.

Figure 14(a) includes two simulated IV curves, one is the ideal simulation of an InAlAs cell with no etch stop as shown in Figure 11, while the other simulation is intended to be a fit to experimental data from the best cell with no InP etch stop. The light-IV fit was generated using minority carrier lifetimes calculated by fitting experimental EQE results, and assumed an InAlAs bandgap of 1.437 eV in order to approximate the band edge seen in the EQE. Experimental light-IV measurements of a different cell on a wafer that retained the InP etch stop are shown in Figure 14(b) before and after contact etch without an ARC. This illustrates that the contact etch results in a 24% relative increase in J_{SC}, which is consistent with the current enhancement predicted via simulation in Figure 11.

Table 3
Experimental light-IV results compared to simulation

	J_{sc} (mA/cm^2)	Voc (V)	FF (%)	Efficiency (%)
Best cell without etch stop (ARC) AM1.5	23.3	0.97	79	17.9
Best cell with etch stop (ARC) AM1.5	21.7	0.96	82	17.1
Best cell with etch stop (ARC) AM0	25.5	0.96	82	14.7
EQE fit simulation without etch stop (ARC) AM1.5	23.2	0.97	81	18.3
Ideal simulation without etch stop (ARC) AM1.5	24.6	1.00	87	21.4
Before contact etch (no ARC) AM1.5	11.3	0.91	75	7.7
After contact etch (no ARC) AM1.5	14	0.92	75	9.7

Spectral response (SR) was measured using an Oriel IQE200 monochromator and a Stanford Research SR570 preamplifier coupled to a SR830 lock-in amplifier. External quantum efficiency (EQE) data from the best cell without an etch stop is presented in Figure 15(a). Losses at short wavelengths are not excessive which indicates the strained window is successfully passivated. At long wavelengths, the EQE extends roughly 70 nm past the band edge. The presence of this tail is assumed to be an effect of phase separation in the base as described in the experimental section [55]. Figure 15(a) also shows a fit to the EQE data, where minority carrier lifetimes were adjusted in the device simulation software Sentaurus to approximate the experimental data. The fit used minority

carrier lifetimes of 400 ps in emitter and 9 ns in the base, which correspond to minority carrier diffusion lengths of 170 nm and 4.6 μm respectively, though the diffusion length calculated for the base is slightly overestimated due to EQE tailing. It is more reasonable to state the diffusion lengths are at least twice the thickness of their respective layers. In order to fit the experimental data, a bandgap of 1.437 eV defined within the model provided a reasonable approximation of both the current collection observed near the band edge and the open circuit voltage as shown in Figure 14(a). In order to approximate the experimentally-observed band tailing in the model, the extinction coefficient used for InAlAs was iteratively increased above the band gap. The IQE data shown in Figure 15(b) illustrates the inherent device improvement when removing the InP etch stop, regardless of ARC efficacy. IQE should be able to approach 100% in high-quality device, the losses observed may be due to recombination occurring at interfaces or may be the result of insufficient diffusion lengths.

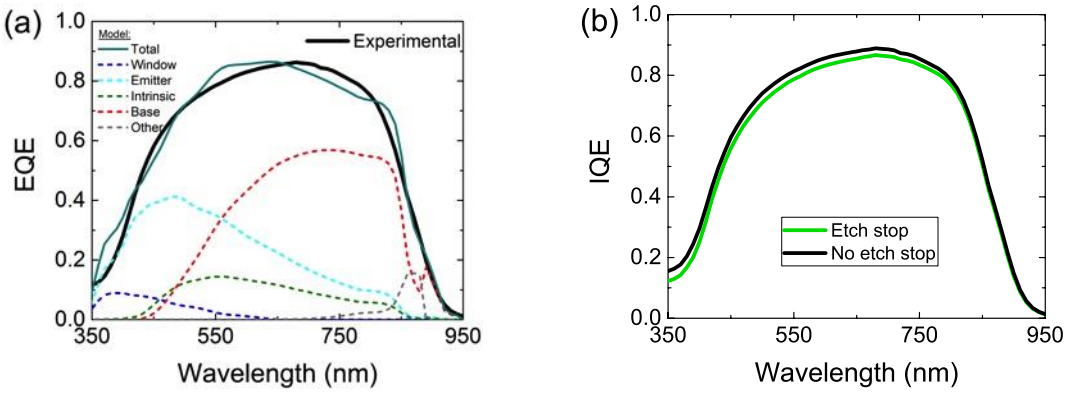

Figure 15: (a) Experimental EQE data from best performing cell with no etch stop (with ARC) and simulated fit to EQE data generated by adjusting lifetimes to approximate experimental results. The simulated fit used minority carrier lifetimes of 0.4 ns in the emitter and 9 ns in the base. Individual layer contributions of simulated fit are shown as dashed lines. (b) Internal quantum efficiency (IQE) data from the best cell of each wafer: enhanced short wavelength response is observed upon etch stop removal.

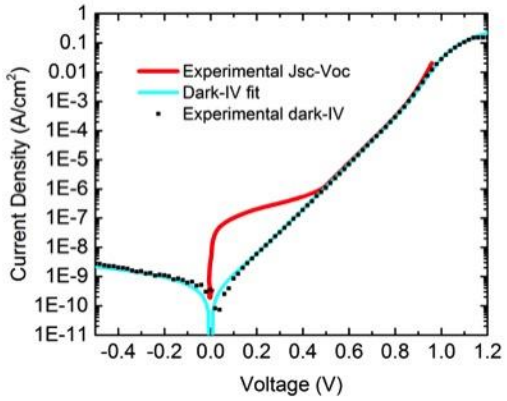

Figure 16: Experimental and fitted dark-IV data using a two-diode model, and experimental J_{sc}-V_{oc} data to extract series and shunt resistance.

Dark current-voltage (dark-IV) and J_{sc}-V_{oc} data are shown in Figure **16**. A fit to a two-diode equation (Equation 5) indicates ideality factors (n) of 1 and 2.15, respectively. The n=1 region occurs near the reported Voc which implies even at 1-sun the device is beginning to operate in the radiatively limited regime. The extracted dark series resistance was 0.74 ohms/cm^2 and the shunt resistance was 2.0 x 10^8 ohms/cm^2. Series resistance was also calculated using the J_{SC}-V_{OC} and light I-V data as published in [57], which corresponds to a 1-sun illuminated series resistance of 1.25 ohms/cm^2. The series resistance is higher than desired and could be reduced by increasing the thickness of the grid fingers. The shunt resistance value is notably high, comparable with other well-developed III-V devices such as GaAs which implies there are few bulk shunt defects occurring in the epitaxial layers. The dark currents for this fit were J_{01}=7.8 x 10^{-19} A/cm^2 and J_{02}=1.5 x 10^{-10} A/cm^2, respectively. An ideal J_{01} for InAlAs calculated from experimental mobility values and bandgap, nominal doping, effective masses from literature, and the diffusion lengths extracted above is 8.6 x 10^{-20} A/cm^2. The experimental J_{01} is less than an order of magnitude greater than this value and would improve with material quality. Furthermore, the experimental dark current density is two orders of magnitude greater than typically seen from the highest performing GaAs solar cells, which implies the InAlAs material quality has room for improvement compared to well-developed III-V materials [58].

$$J_{dark} = J_{01}\left(e^{\frac{q(V-JR_{series})}{n_1 kT}} - 1\right) + J_{02}\left(e^{\frac{q(V-JR_{series})}{n_2 kT}} - 1\right) + \frac{V-JR_{series}}{R_{shunt}} \qquad \textbf{Equation 5}$$

3.2.4 Further design optimization

The minority carrier lifetime extracted from the base Figure **15**(a) differs from the lifetime used when initially designing the device, which was determined from the reference in Table 1. Using the lifetimes from Figure **15**(a) as inputs, simulations indicate that using a 3.5 µm base would be 19% efficient under AM1.5G with an ARC and no etch stop. This would be directly achievable given that the material quality and the ability to deposit an ARC immediately after removing the etch stop to prevent oxidation of the window have both already been demonstrated in this study. An experimental demonstration of this re-optimized cell design would further establish InAlAs as a qualified option for the top-cell applications described in the introduction.

3.2.5 Anti-reflective coating study

An earlier iteration of devices with an InP etch stop had an ARC of 75 nm of Si_3N_4 deposited via plasma enhanced chemical vapor deposition (PECVD). This was observed to degrade the V_{OC} and the overall light-IV performance, as shown in Figure **17**(a). Light-IV parameters are tabulated in Table 4. The deposition temperature for the ARC was 350ºC. Possible explanations for degradation include front contact eutectic diffusion into the junction, damage to the InAlAs window, or a surface interaction between the InP etch stop and the Si_3N_4 PECVD mechanism. In order to isolate the cause of degradation, the Si_3N_4 was selectively removed using hydrofluoric acid. The removal of Si_3N_4 did not result in any V_{OC} recovery which indicates degradation is not due to a surface mechanism, however the fill factor did recover. An annealing test of an alternate cell at 350ºC showed a similar degradation of V_{OC} as seen in Figure **17**(b). This indicates the degradation may be the result of eutectic diffusion or damage to the highly

strained window layer. This prompted consideration of alternate ARCs at lower deposition temperatures, ultimately leading to the dual layer ZnS/MgF_2 deposited by thermal evaporation as reported in section 3.2.3.

Table 4
Experimental Light-IV Parameters from ARC Study

AM1.5G light-IV results	J_{sc} (mA/cm^2)	Voc (V)	FF (%)	Efficiency (%)
Before ARC	14.05	0.92	75	9.7
With ARC	17.93	0.62	71	8.1
ARC Removed	12.4	0.62	75	5.8
Before anneal (no ARC)	13.8	0.91	70	8.8
After anneal (no ARC)	12.6	0.43	55	3.0

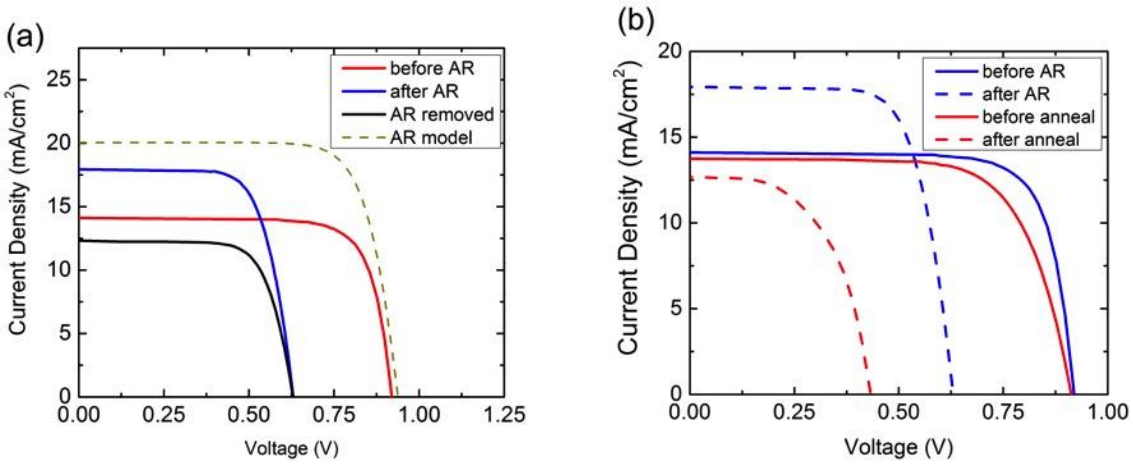

Figure 17: (a) Light-IV measurements of a cell before ARC, with a Si_3N_4 ARC, and after the ARC was removed, including a model of expected performance with ARC (b) Light IV measurements of the cell in (a) before ARC and with Si_3N_4 ARC compared to an alternate cell (red) before and after annealing at 350°C

3.3 Development using alternative MOVPE precursors

3.3.2 Motivation

In general, MOVPE growth of aluminum-containing alloys such as AlGaAs and InAlAs often suffers from unintentional incorporation of impurities such as carbon and oxygen. Carbon is inherent to the MOVPE process as the metalorganic sources contain methyl- or ethyl- organic ligands. Oxygen is a particular problem for aluminum containing materials due to the high Al-O bond strength. Oxygen creates deep traps and deteriorates carrier lifetime, while carbon is a shallow acceptor which can increase background carrier concentration [59]. Minimizing the C and O impurity background using optimized epitaxial growth conditions is well-documented for AlGaAs [60-62] with the growth temperature and V/III ratio among the strongest process variables that control the carbon and oxygen impurity levels.

Alternative precursors allow for some variety in growth conditions, which may prove advantageous for material quality or device performance. Alternative precursors with lower pyrolysis temperatures also enable a reduction in growth temperature and increased material efficiency [63]. Lower pyrolysis temperatures will be significant later in

this research trajectory since growth of InAlAsSb may require lower growth temperatures in order to incorporate antimony into the crystal lattice [64].

Arsine (AsH_3) and TMAl are the industry-standard precursors for As and Al respectively, however the alternative precursors tertiarybutylarsine (TBAs) and tritertiarybutyl aluminum (TTBAl) pyrolize at lower temperatures than their standard counterparts [65, 66]. TBAs is well-studied in literature and has produced higher quality materials at lower growth temperatures and V/III ratios as compared to arsine [67, 68]. Use of TBAs for other materials systems (such as AlGaAs) has resulted in lower carbon and oxygen impurity concentrations as compared to arsine [63, 69]. As for the aluminum sources, TMAl is well-studied in literature but TTBAl is less common. Given the dearth of literature on TTBAl, this research appears to be the first using such a growth configuration for InAlAs. TTBAl has previously been utilized in other materials systems (such as AlGaSb and AlGaAs) to replace TMAl with the effect of comparatively reducing carbon and oxygen incorporation and background doping levels [70, 71].

3.3.3 Impurity incorporation study

An initial study of bulk unintentionally doped InAlAs was conducted in order to identify the best precursors and find the optimum growth conditions in order to produce the highest quality epitaxial layers. For this study, the V/III ratio, growth temperature, and growth rate were varied for each given set of precursor combinations (out of four possible configurations). Unintentionally doped InAlAs epitaxial layers were grown on InP substrates in a 3x2" Veeco D125LDM multiwafer MOVPE reactor. Trimethylindium was the indium precursor while the aluminum precursor was either TMAl or TTBAl and the arsenic source was either arsine or TBAs. The growth parameters were varied in multilayer samples. The growth temperature was varied between 520-650°C, the V/III ratio was varied between 5 and 115, and the growth rate was varied between 1.5 – 6.0 μm/hr. Carbon and oxygen impurities were measured as a function of depth by secondary ion mass spectrometry (SIMS). The composition of each InAlAs sample was verified by high-resolution x-ray diffraction rocking curves using (004) reflection.

3.3.3.1 Arsenic Precursors

To compare the arsenic precursors, InAlAs samples were first grown using TMAl with arsine, then using TMAl with TBAs. Figure 18 and Figure 19 display impurity concentrations (oxygen and carbon, respectively) as a function of the V/III ratio. Each data set in Figure 18 and Figure 19 is named by growth temperature in degrees Celsius, a relative growth rate ("gr1" denotes twice the growth rate of "gr0.5"), and precursor (either arsine or TBAs). Data points for arsine growths are solid, while data points for TBAs are open symbols.

Oxygen levels in the InAlAs samples vary from 10^{16}-10^{18} cm^{-3} as shown in Figure 18. Holding all else constant, the samples show decreasing oxygen concentration as V/III ratio increases. The oxygen concentrations do not appear conclusively dependent on precursor type. Figure 18 illustrates that some arsine growths exhibit higher oxygen levels than TBAs growths even when the arsine growths have higher V/III ratios. Figure 19 shows carbon concentrations in InAlAs samples as a function of V/III ratio. Carbon concentrations are seen to vary from 10^{16} to 10^{17} cm^{-3}. Similar to Figure 18, samples exhibit decreasing carbon content with increasing V/III ratio. A TBAs

sample grown at 525ºC with a V/III ratio of 20 does not follow the general trend, however this sample also had a decreased growth rate which may be a confounding variable. There appears to be a distinction between carbon levels corresponding to precursor type: carbon levels in the arsine samples were all exceptionally low. Arsine samples with a V/III ratio greater than 25 exhibited carbon concentrations below 10^{16} cm^{-3}, which is below the detection limit of the SIMS instrument. Therefore, those arsine samples are not included in Figure 19.

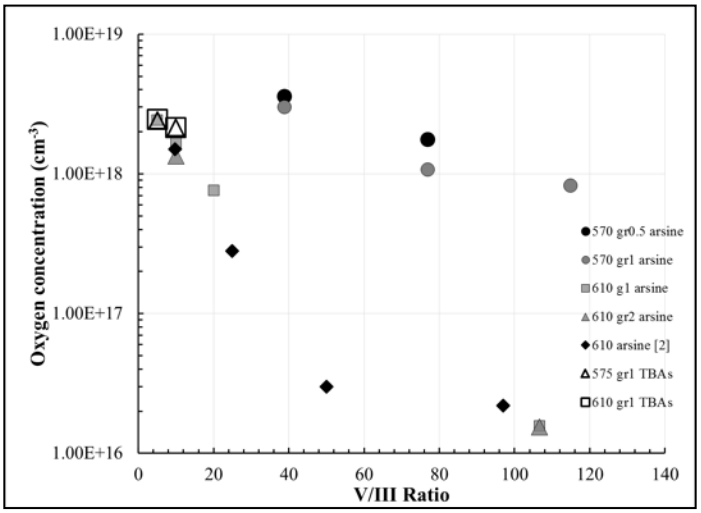

Figure 18: Oxygen impurity concentration in InAlAs as a function of V/III ratio, comparing arsenic precursors.

The trend of decreasing carbon with V/III ratio is expected and has been previously demonstrated for AlGaAs with AsH_3 [69]. As V/III increases, more atomic hydrogen is present from the decomposition of AsH_3 to form CH_4 and scavenge the carbon prior to incorporation. The trend of decreasing carbon with increasing V/III ratio is also present in the TBAs-grown samples which implies that a sufficient reaction pathway exists with TBAs to remove methyl radicals. The carbon measured in the epitaxial layers is notably higher when comparing the TBAs-grown samples to the AsH_3-grown samples. This suggests that the AsH_3 decomposition is more effective than TBAs most likely due to the higher amount of hydrogen available from AsH_3 compared to TBAs.

At temperatures above 400ºC, the main decomposition products from TBAs are C_4H_{10} and H_2 — whereas at slightly higher temperatures, AsH_3 has also been detected as a decomposition product [72]. This is critical to explain the V/III ratio dependence. Since TBAs decomposition above 400ºC produces AsH_3 as a byproduct, the further decomposition of this AsH_3 provides the requisite mechanism to remove carbon from the InAlAs epilayer. Both Figure 18 and Figure 19 display some dependence on growth rate. Samples tend to exhibit decreased impurities with increased growth rate, holding all else constant (growth temperature and V/III ratio). It should be noted that this trend does not hold as a rule for all samples.

Figure 20 and Figure 21 display impurity concentrations as a function of growth temperature. Again, AsH_3 data points are solid and TBAs data points are open symbols. Figure 20 and Figure 21 illustrate more clearly that both oxygen and carbon impurity concentrations respectively decrease with increasing growth temperature. For each V/III value, identified by symbol type in Figure 20, the oxygen level decreases with increasing temperature. In

addition, the TBAs-based InAlAs layers exhibit an elevated oxygen level compared to AsH_3, though s single outlier is observed at 650°C (V/III=39). Figure 21 shows that when using TBAs, carbon decreases markedly as temperature increases. The limited data points for AsH_3 result from the fact that most arsine InAlAs samples exhibit carbon levels below the SIMS detection limit.

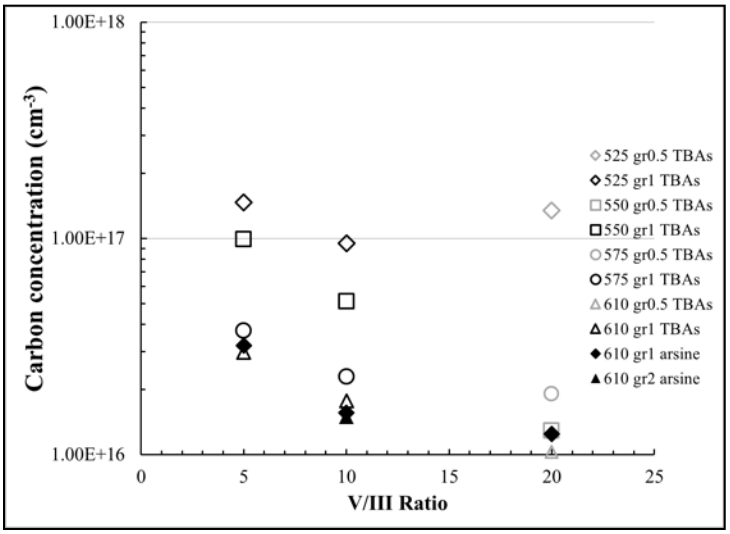

Figure 19: Carbon impurity concentration in InAlAs as a function of V/III ratio, comparing arsenic precursors.

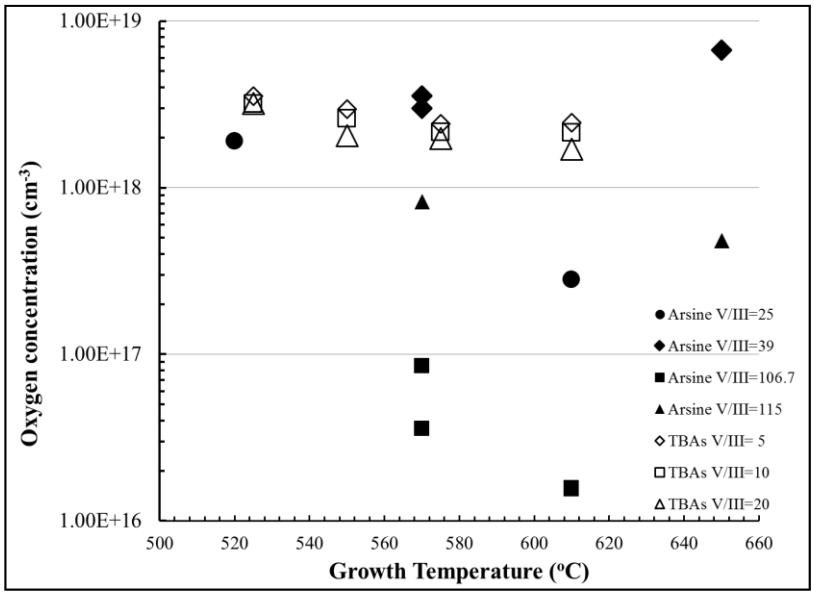

Figure 20: Oxygen impurity concentration in InAlAs as a function of growth temperature, comparing arsenic precursors

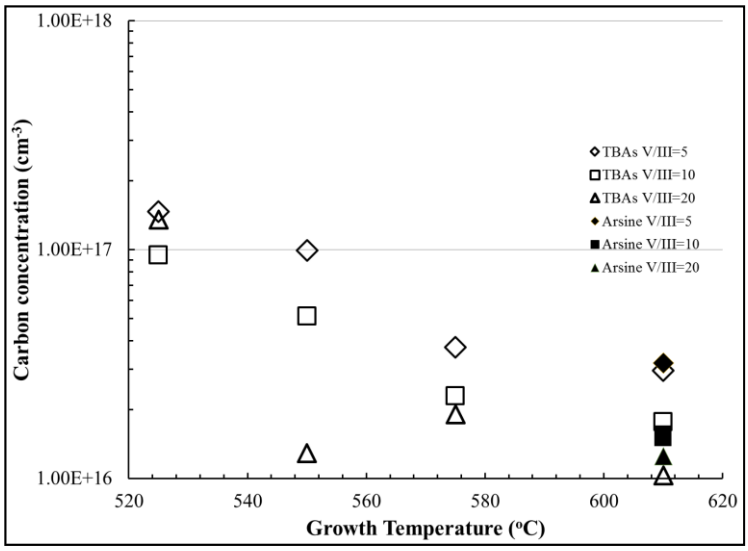

Figure 21: Carbon impurity concentration in InAlAs as a function of growth temperature, comparing arsenic precursors

3.3.3.2 Aluminum Precursors

In order to compare the aluminum precursors, InAlAs layers were grown using arsine with TMAl, then using arsine with TTBAl. Using the combination of TMIn, TTBAl, and AsH_3, two layers of InAlAs were grown at 610°C with V/III ratios of 90 and 13.5. Figure 22 displays a comparison between the oxygen impurity concentrations for the two aluminum precursors. TMAl data points are solid while TTBAl data points are open symbols. All data in Figure 22 were taken from samples grown at 610°C. Figure 22 shows that oxygen incorporation is virtually independent of the V/III ratio for the TTBAl precursor combination, with a value of 0.9 – 1.2 x 10^{17} cm^{-3} across the V/III ratio range. For InAlAs grown using TMAl, oxygen levels decrease with increasing V/III ratio.

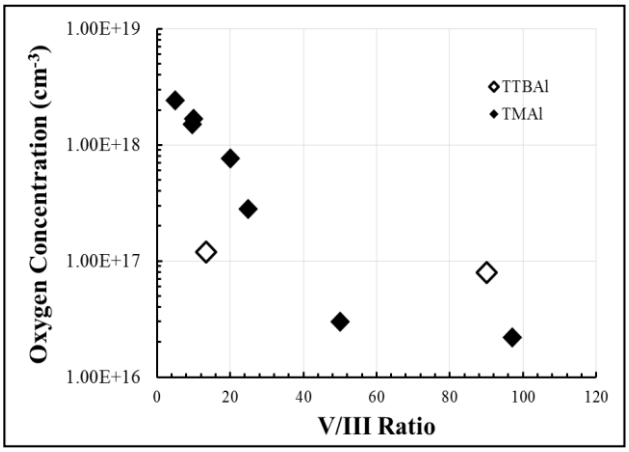

Figure 22: Oxygen impurity concentration in InAlAs as a function of V/III ratio, comparing aluminum precursors.

Furthermore, SIMS measurements of the TTBAl samples indicate a low carbon background, quite close to the detection limit of the SIMS. Carbon levels in TTBAl samples are also essentially independent of V/III ratio between values of 13.5 to 90, measured at 10^{16} cm^{-3} for both conditions. The lack of carbon dependence on V/III ratio can be explained by the elimination of the methyl radical by using TTBAl in place of TMAl. The decomposition products of TTBAl that include carbon are less likely to react with Al, unlike the methyl radicals originating from TMAl. Therefore, less carbon is incorporated into the solid even at low V/III ratios. TMAl, by comparison, incorporates more carbon as V/III ratios decrease: see Figure 19.

While it appears that the TTBAl causes significantly less impurities than TMAl, one must consider the actual aluminum composition of the InAlAs. TTBAl resulted in a low incorporation of Al compared to TMAl and these layers had an Al composition of only 0.30 while the TMAl samples had Al = 0.50. An increase in aluminum composition in AlGaAs is known to increase oxygen [62, 70] so the absolute oxygen levels cannot be directly compared. The same caution should be applied to comparing carbon levels as well. However, the constant impurity levels in TTBAl samples as a function of V/III is remarkable and may be beneficial for use in growth of antimonides which require a low V/III [64].

3.3.4 Cell growth and fabrication

The alternate precursors were used to grow identical device structures at conditions optimized for each precursor in order to achieve comparable dopant concentrations and then underwent fabrication in parallel. Epitaxial layers were grown in a Veeco D125 3x2" MOVPE reactor. InAlAs samples were grown using the precursor combinations outlined in Table 5, with all samples using the industry standard trimethylindium (TMIn). InAlAs growths targeted InP lattice-matched compositions, where x=0.48 for $In_{1-x}Al_xAs$. The device structure for the InAlAs photovoltaic devices in this study has already been shown in Table 2 in section 2.2. Layers below the window were grown at 580°C to maintain p-dopant control, while the window and upper layers were grown at 610°C.

Table 5
Precursor Description of Devices

	Indium	Aluminum	Arsenic
Cell 1	TMIn	TMAl	Arsine
Cell 2	TMIn	TTBAl	Arsine
Cell 3	TMIn	TTBAl	TBAs

Growing InAlAs at lattice-matched conditions required a higher aluminum to indium molar ratio when using TTBAl as opposed to TMAl. This has previously been attributed to a reduced sticking coefficient of TTBAl caused by the steric effects of the larger organic ligands [70, 73]. Following the completion of all three cell growths, it was noted that the injection mass flow controllers lost calibration following any growth that used TTBAl and the p-dopant diethylzinc (DEZn) in the same layer. A white solid deposit was observed on the inside of the stainless steel gas lines. This indicates a pre-reaction occurring between the two gases before deposition. Future development could consider an alternative p-type dopant such as CCl_4 in order to avoid degradation of the MOVPE system. Dopant flows for the final cells are shown in Table 6, and were selected based on prior doping calibrations. This

table displays the dopant molar flow divided by the total group-III elements molar flow in order to account for growth rate. The fact that more DEZn was flowed for cell 3 indicates that this cell may exhibit more pronounced effects from the prereaction. However, mobilities measured by Hall effect for doping calibrations were roughly comparable for all three cell types.

Table 6
Dopant-To-Group-III Molar Ratio

	N-TYPE (DISILANE)	P-TYPE (DEZN)
Cell 1	410 ppm	205 ppm
Cell 2	235 ppm	392 ppm
Cell 3	35 ppm	5570 ppm

A device from cell 1 and a device from cell 2 were sent out for depth profiling by SIMS. This analysis was intended to confirm impurity incorporations when using either precursor. The results are shown below in Figure 23 and impurity measurements are tabulated in Table 7. The concentration of carbon in either sample was below the detection limit of the SIMS measurement (4.0 x 10^{15} atoms/cm^3). The oxygen content in the TTBAl sample is below the detection limit of SIMS (6.0 x 10^{15} atoms/cm^3) however the TMAl sample has increased oxygen content throughout, at 7.0 x 10^{15} atoms/cm^3 in the base and two orders of magnitude greater in the back surface field (BSF).

Table 7
Impurity concentrations in InAlAs cells measured by SIMS

	Carbon (atoms/cm^3)	Oxygen (atoms/cm^3)
TMAl-InAlAs	At Limit	7.0 x 10^{15}
TTBAl-InAlAs	At Limit	At Limit
Detection Limit	4.0 x 10^{15}	6 x 10^{15}

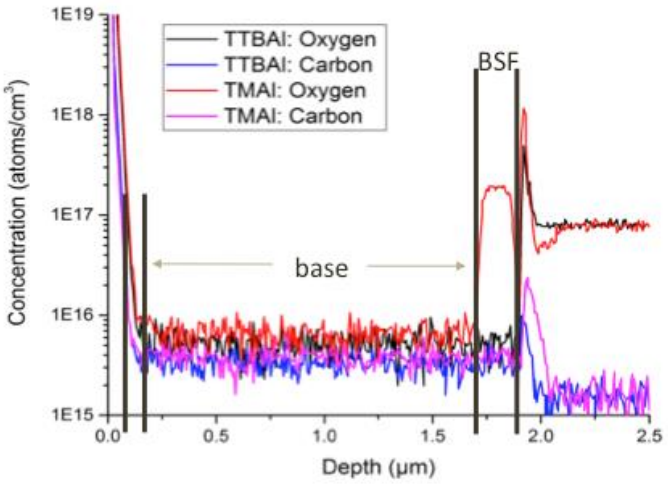

Figure 23: Secondary-ion mass spectrometry data on impurity concentrations in two different InAlAs cells, one grown with TMAl and the other with TTBAl.

Solar cells were fabricated in the same manner as section 2.2, using Au/Zn/Au contacts to the p-InP substrate and Ge/Au/Ni/Au contacts to the InGaAs contact layer. Devices were isolated with a 1:1:38 H_3PO_4:H_2O_2:H_2O wet mesa etch, in addition to a 1:1:2 HCl: H_3PO_4:CH_3COOH etch to remove the InP etch stop. Afterwards, the contact layer was removed between grid fingers with the H_3PO_4:H_2O_2:H_2O etch. Each wafer contained an array of 1x1 cm^2 solar cells with grid finger shadowing of 4%. One-sun AM1.5 illuminated IV measurements were performed with a two-zone TS Space Systems solar simulator with a Keithley 2440 Source Measure Unit (SMU). The simulator was calibrated using $InGaP_2$ and GaAs reference solar cells calibrated to AM1.5G by NREL. Spectral response (SR) was measured using an Oriel IQE200 monochromator and a Stanford Research SR570 preamplifier coupled to a SR830 lock-in amplifier. Dark-IV measurements were performed using a Keithley 2400 SMU.

3.3.5 Device results

Experimental light-IV measurements under 1-sun AM1.5 from the champion cell from each wafer are shown in Figure 24 and parameters are tabulated in Table 8. From this table, it is clear that cell 1 (TMAl+Arsine) has the best V_{oc} and fill factor (FF), while cell 2 (TTBAl+Arsine) has the highest J_{sc} and the highest efficiency. Since cell 3 had ~14X higher mole fraction of DEZn in the gas phase (as compared to cell 2), it is important to note that the performance of cell 3 may have been more severely affected by the homogenous gas phase TTBAl-DEZn reaction.

Dark IV data for all three cells are shown in Figure 25. This data was fit to a two-diode model (or one diode where appropriate) and parameters extracted from the model are shown in Table 9.. Cell 1 is the only device that displayed both an n=1 and an n=2 region. This is indicative of higher quality material, such that this is the only device that is radiatively limited in the n=1 section near V_{oc}. Cells 2 and 3 have ideality factors approximately n=2 which indicates these devices are dominated by recombination in the space charge region.

Series and shunt resistance were extracted from dark-IV data. All cells had acceptable series resistance (R_{series}) for 1-sun operation, though R_{series} for cell 3 was noticeably greater which is reflected in its low fill factor. The shunt resistance (R_{shunt}) is a typical magnitude for all cells however cell 2 has an order of magnitude lower shunt resistance than cell 1 which is consistent with its lower fill factor. An ideal dark current (J_{01}) for this material is 1.2 x 10^{-16} mA/cm^2, calculated from experimental mobility values and bandgap, nominal doping, effective masses from literature, and diffusion lengths extracted from experimental data via a Hovel-Woodall model [49, 74]. The J_{01} for cell 1 is three orders of magnitude greater than the ideal J_0 in the n=1 diode region, which is reflective of high material quality. The J_{01} of cells 2 and 3 are masked by the second diode region given the ideality factors greater than 2 indicating recombination in the space charge region and elsewhere in the device.

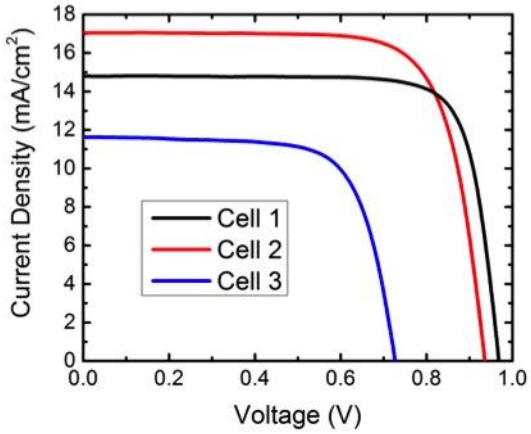

Figure 24: Light-IV experimental results under 1-sun AM1.5 for InAlAs cells grown with alternate precursors (no ARC)

Table 8
Experimental Light-IV Parameters per Precursor Configuration

	J_{sc} (mA/cm^2)	V_{oc} (V)	FF (%)	η (%)
Cell 1	14.8	0.97	80	11.5
Cell 2	17.1	0.94	75	12.0
Cell 3	11.6	0.73	72	6.1

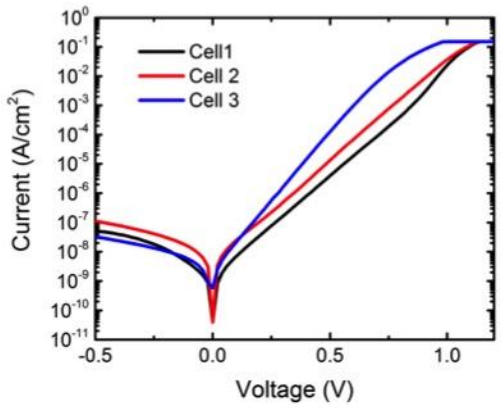

Figure 25: Dark-IV experimental results from InAlAs cells grown with alternate precursors

Table 9
Dark IV Parameters from Experimental Data

	R_{SERIES} (Ω)	R_{SHUNT} (Ω)	J_0 (mA/cm^2)	n
Cell 1	0.51	7.0×10^7	1.8×10^{-13}	1.2
			1.5×10^{-6}	2.5
Cell 2	0.45	7.12×10^6	3.1×10^{-6}	2.3
Cell 3	1.23	2.03×10^7	2.5×10^{-6}	1.8

External quantum efficiency (EQE) and internal quantum efficiency (IQE) data are shown in Figure 26. A Hovel-Woodall model [49] was used to simulate EQE results and extract minority carrier diffusion lengths, which are tabulated in Table 10. EQE simulations are shown in Figure 27. From the IQE data, it is evident that cell 2 has a greater overall spectral response than cell 1, which corresponds to a higher J_{sc} due to its superior carrier collection. Cells 2 and 3 both have significantly better collection than cell 1 in the window and emitter, as seen at lower wavelengths. Despite possible pre-reactions between TTBAl and DEZn in the gas phase, cell 2 appears to have better collection in the base than both cells 1 and 3. This would seem to indicate that the pre-reaction is limited to the gas phase and does not extend to gas-to-solid incorporation. This could be due to the ~14x increase in DEZn molar flow used in this device as compared to cell 2. The higher degree of pre-reaction could have degraded the base minority carrier properties, as evidenced in Table 10.

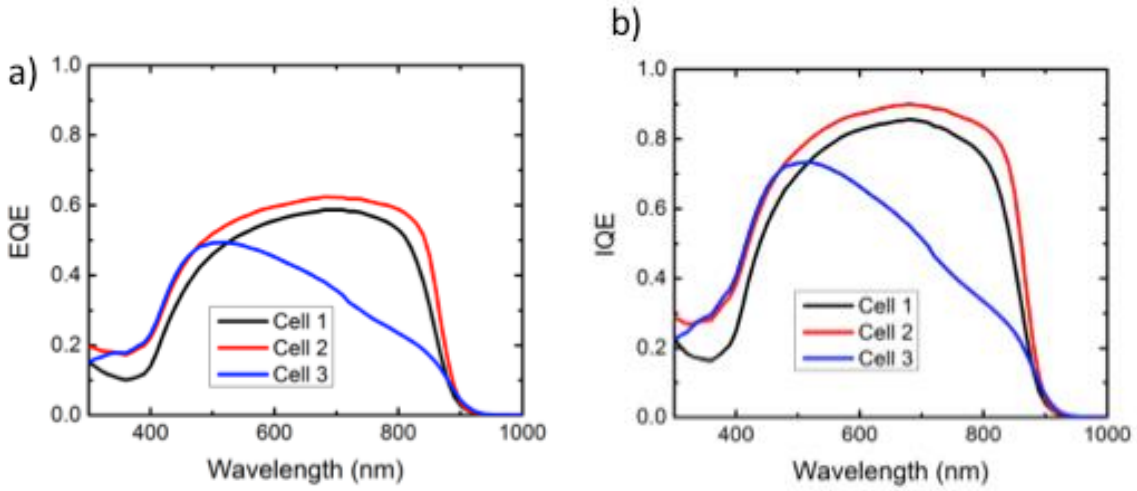

Figure 26: a) external quantum efficiency and b) internal quantum efficiency of InAlAs cells as a function of precursor combination

Table 10
Minority Carrier Diffusion Lengths

	Multiple of emitter thickess (75 nm)	Multiple of base thickness (1.5 µm)
Cell 1	>2x	>2x
Cell 2	>>2x	>>2x
Cell 3	>>2x	0.05x

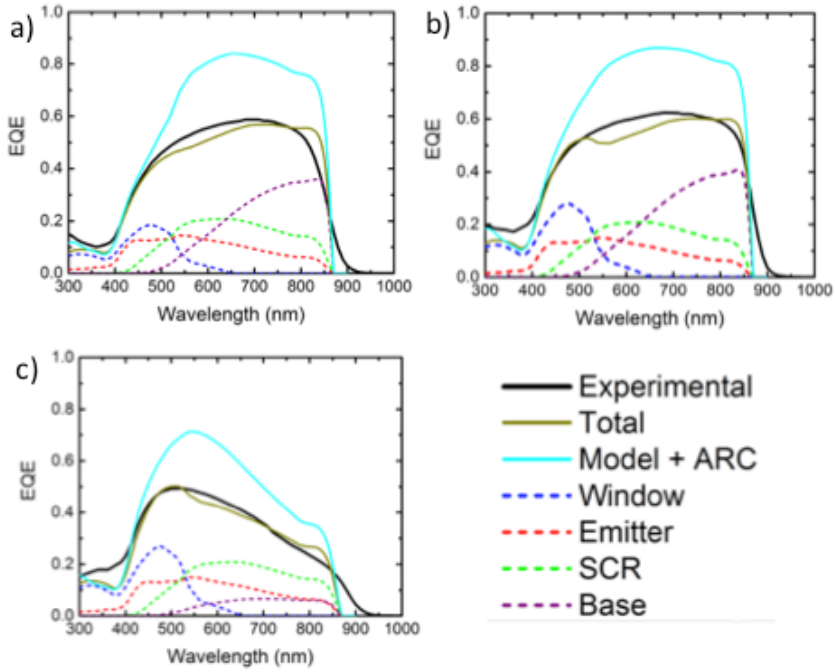

Figure 27: Results from modified Hovel-Woodall model for alternate precursor InAlAs cells: a) cell 1, b) cell 2, and c) cell 3.

The diffusion lengths shown in Table 10 validate the layer thicknesses in the cell design. Diffusion lengths in cells 1 and 2 (and emitter diffusion length in cell 3) are more than twice the thicknesses of their respective layers which implies high collection. Cell 2 and 3 both have greater emitter diffusion lengths than cell 1 which indicates InAlAs growth with TTBAl results in greater minority carrier diffusion lengths in n-type material. Cell 2 has a greater base diffusion length of cell 1 which indicates that TTBAl also results in greater diffusion lengths in p-type InAlAs. Though, it should be noted that the diffusion lengths from the base are slightly overestimated as a result of the EQE tailing past 900 nm. This tail is assumed to be caused by phase separation in the material which creates regions with a lower bandgap, often seen in MOVPE-InAlAs grown at lower temperatures [55]. If InAlAs grown with TTBAl is more prone to ordering than InAlAs grown with TMAl, this may explain the increased spectral response of cell 2 and could be analyzed by TEM to compare to the existing images of TMAl-InAlAs.

3.3.6 Conclusions

A single-junction $In_{0.52}Al_{0.48}As$ solar cell design lattice-matched to InP was developed by leveraging existing device results in literature, in-house bulk material characterization, and physics-based device simulations. This design built off of previous InAlAs solar cells in literature by incorporating a protective etch stop above the high-aluminum content window to prevent the window from oxidizing. This etch stop could then be selectively removed immediately before depositing an ARC. A material-specific etch process was developed for the proposed design. This design was then grown by MOVPE using industry-standard precursors, fabricated, and tested. Device results showed 17.9% efficiency under 1-sun AM1.5 with an ARC which represents a significant improvement over previous single-junction $In_{0.52}Al_{0.48}As$ solar cell efficiencies in literature [40]. EQE data was fit using physics-based device simulation software and indicated the diffusion lengths in the emitter and base were greater than twice the respective thickness of the emitter and base, while the base diffusion length in particular represented a significant increase over previous diffusion lengths reported for comparable p-type InAlAs [40]. Based on these extracted diffusion lengths, a further optimized device design is proposed for any future research efforts on this material. Cross-sectional TEM of the device was executed by collaborators at NREL and indicated significant compositional fluctuation throughout the base of the device, which has been previously reported to lower the effective bandgap of $In_{0.52}Al_{0.48}As$ [55]. This phase separation provides a consistent explanation for the long-wavelength tail observed in the EQE results from the device. Work on the single-junction InAlAs device also involved development of an anti-reflective coating. Initial depositions of Si_3N_4 by PECVD were determined to excessively heat the device and degraded performance, so a dual layer ZnS/MgF_2 ARC was developed by thermal evaporation and resulted in targeted device enhancement.

Further $In_{0.52}Al_{0.48}As$ materials development considered the use of alternative MOVPE precursors as an initial step towards incorporation of antimony into the alloy. Bulk material was grown using alternative aluminum and arsenic precursors and compared to material grown with industry-standard precursors, where the industry standards were TMAl and arsine, while the alternatives were TTBAl and TBAs. Each aluminum precursor is used in conjunction with each arsenic precursor in order to compare all possible precursor combinations. Multiple sets of samples were grown with either precursor with varying growth conditions such as growth temperature, growth rate,

and V/III ratio. These bulk materials were sent out for analysis by SIMS to quantify impurity concentrations of carbon and oxygen. When comparing arsenic precursors, impurity concentrations measured by SIMS decrease as the V/III ratio increases, for both arsine and TBAs growths. Impurities also decrease as growth temperature increases. Oxygen incorporation associated with arsine is comparable to that of TBAs, whereas carbon incorporation is definitively less for arsine as compared to TBAs under the conditions studied. When used in conjunction with arsine, the aluminum precursors under investigation behave differently. TMAl exhibits an inverse impurity dependence on V/III ratio while TTBAl growths did not exhibit such a dependence, impurity concentrations remained virtually constant regardless of V/III ratio. The impurity independence of TTBAl at low V/III ratios make it a desirable candidate for other alloys that may require low V/III ratios, such as antimony-containing alloys.

Finally, single-junction $In_{0.52}Al_{0.48}As$ solar cells were grown using the alternative precursors and fabricated in parallel to devices grown with the standard precursors to control for variation in fabrication runs. Three devices were compared, the first using TMIn/TMAl/arsine, the second TMIn/TTBAl/arsine, and the third TMIn/TTBAl/TBAs. Growth of doping calibrations for each device were necessary, and the dopant flow information indicates a pre-reaction between TTBAl and DEZn, the effects of which are more pronounced when using TBAs because of the need for increased dopant flow. This was apparent in the device results as well, where the TBAs device showed only 6% efficiency under 1-sun AM1.5 without an ARC, while the first two cells showed 11.5% efficiency and 12% efficiency, respectively. Devices grown with TMAl had a higher V_{oc}, a lower dark current, and a two diode region dark-IV curve which reflects better material quality. However, cells grown with TTBAl show enhanced J_{sc} and spectral response as compared to those grown with TMAl. Devices grown with TTBAl show exceptional carrier lifetimes throughout the device due to significant improvements in diffusion length even though this device was affected by the prereaction, and would benefit from time-resolved photoluminescence measurements to empirically verify lifetimes in future work.

CHAPTER 4: Development of bulk InAlAsSb lattice-matched to InP

4.1 Motivation

Development of multijunction III-V photovoltaics has typically been executed on a germanium or GaAs substrate, sometimes utilizing a metamorphic grade in order to incorporate cells with differing lattice constants. Therefore, the spectrum-splitting enabled by use of multiple junctions is limited to the bandgaps of materials afforded by the lattice constant of the substrate and/or the ability to create a successful metamorphic grade. Lattice-matched cells have improved material quality compared to cells grown on a metamorphic grade, and are less material-intensive, given the additional time, energy, and material consumed to grow a metamorphic grade. Lattice-matched multijunction cells are also advantageous for space applications in that they require less panel support than metamorphic cells, which are subject to device cracking due to mechanical and thermal stresses [75]. This corresponds to lower mass-specific power, which is a critical metric for space photovoltaics.

Assuming one is limited to lattice constants available from binary substrates such as GaAs or InP, there exists a finite optimum for a multijunction cell configuration. In the case of InP, a triple junction cell with $In_{0.21}Al_{0.79}As_{0.74}Sb_{0.26}$/InGaAsP/InGaAs (1.74 eV/1.17 eV/0.7 eV) subcells lattice matched to InP could achieve up to 52.8% under 500 suns AM1.5 based on a predictive drift-diffusion model [4]. This model uses a radiative efficiency parameter to account for nonradiative recombination and approximate realistic material quality. This deviates from the typical detailed balance model, which assumes that all recombination is radiative. The top cell would use a quaternary alloy $In_{0.21}Al_{0.79}As_{0.74}Sb_{0.26}$ which has a direct bandgap of 1.74 eV and is lattice-matched to InP [10]. A similar multijunction design optimized for the AM0 spectrum with a $In_{0.3}Al_{0.7}As_{0.83}Sb_{0.17}$ top cell is predicted to achieve 37.1% efficiency under 1-sun AM0 [4]. This design is especially promising for space applications in that InP is known to be more radiation tolerant, which corresponds to increased device longevity and the potential for reduced shielding, enabling greater mass-specific power [48, 76].

The alloy InAlAsSb is generally of interest for optoelectronic and electronic devices as a direct, high bandgap material that is lattice-matched to InP, however limited materials development exists to date. Growth of InAlAsSb by molecular-beam epitaxy has been demonstrated with successful composition control, however significant challenges exist for MOVPE growth of InAlAsSb [5-7]. This is a critical issue for photovoltaic applications as MOVPE is a more cost effective method of growing large area III-V devices. Existing reports on InAlAsSb growth by MOVPE have targeted alloys with a composition of $In_{0.34}Al_{0.66}As_{0.85}Sb_{0.15}$, or even lower Sb content [5, 8, 9]. For photovoltaic applications, the InAlAsSb material needs to have a higher Sb composition ($In_{0.21}Al_{0.79}As_{0.74}Sb_{0.26}$), which is the goal of this research.

4.2 MOVPE Growth of InAlAsSb

4.2.1 Literature review of antimonide growth

The quaternary InAlAsSb material identified for a top cell in Chapter 1 represents a significant undertaking due to the known challenges of antimonide growth [26]. A literature review of MOVPE growth of related antimonide alloys was conducted in order to inform experimental growth effort towards InAlAsSb. Often antimonides have low

melting temperatures (such as InSb which melts at 525°C) so growth temperatures must be kept low [64]. Most ternary and quaternary materials made from antimonides are thermodynamically unstable and tend to show different forms of phase separation and ordering, which requires growth to be performed at low temperatures between 350°C and 600°C [26]. It is hypothesized that antimony causes localized melting in the lattice which enhances the occurrence of phase separation [26]. Furthermore, the size of the Sb atom contributes to its low vapor pressure and solubility, which corresponds to surfactant-like behavior and causes additional phase separation. This occurs because all the antimony precursor that reaches the surface and decomposes will stay on the surface, and any excess that does not get incorporated into the lattice will sit on top of the semiconductor and form a separate elemental phase due to low solubility [64]. The low vapor pressure of antimonides requires that any Sb-based lattices be grown at an V/III ratio close to one, where any deviation from unity will result in Sb or group III metal deposits on the surface since group III metals are also not soluble in the semiconductor, so any excesses will appear on the surface as a separate phase [64].

Since antimonides have low melting points, this precludes the use of certain precursors since some precursors do not decompose significantly at temperatures below the melting point of the antimonide alloy, such as trimethylantimony (TMSb) which does not decompose until almost 500°C. A partial solution is to use large V/III gas phase ratios, however this has other drawbacks with regards to surfactant behavior and phase separation [64]. However, the commercial demand for InSb led to the development of trisdimethylaminoantimony (TDMASb) as a substitute for the TMSb precursor, since it has a lower decomposition temperature [64]. Similarly, growth temperatures below 600°C are inadequate for the most widely used Al precursor, trimethyl-aluminum (TMAl), and so alternative precursors such as triethylaluminum (TEAl), trimethylamine-alane (TMAA), tritertiarybutylaluminum (TTBAl), or dimethylethylamine alane (DMEAA) have been proposed. However, TEAl and TTBAl have the disadvantage of very low vapor pressures which correspond to low growth rates.

Table 11: Literature review of precursor interactions intended for InAlAsSb growth

	TMAl	**TTBAl**	**DMEAA (EDMAA)**	**TMAA**	**TEAl**
TMSb	More significant pre-reaction than with TMSb+TTBAl [77]	Pre-reactions [26]	Severe pre-reactions [26]		
TESb		Al memory effect [78, 79]	None noted [80, 81]	None noted [82, 83]	
TDMASb		Severe pre-reactions [78]	Severe pre-reactions [26]		
TMIn		None observed [66]	Pre-reactions [64]		
TBAs	Pre-reactions above 625°C [84]				

Table 11 reports all possible combinations of common alternative precursors used for antimonide growth, tabulating any observed issues or prereactions where available in references. DMEAA, TTBAl, and TDMASb all decompose at temperatures below 400°C, but tend to exhibit severe prereactions and predeposition both in the hot reactor or in the cold pipelines [26]. DMEAA and trimethylindium (TMIn) have been observed to react spontaneously in the pipelines of an MOVPE reactor and therefore should only be used in the same experiment

provided they use separate lines into the reactor [64]. DMEAA with TMSb also leads to severe prereactions in the gas phase, in situations where the temperature is greater than ~100°C [26]. Experimentally, it has been determined that when using DMEAA as a precursor for growth of (AlGa)Sb, Al-content in the solid was found to be zero up to a gas-phase concentration of 35% [26]. This has been attributed to the complete loss of the DMEAA due to pre-reactions and predeposition before reaching the wafer. Predeposition occurred right at the inlet of the precursors into the reactor where the temperature is still low, and data indicates both TMSb and TEGa participated in prereactions with DMEAA [26]. It should be noted that TESb with DMEAA has been observed to not offset the Al content in the solid, though this might be attributed to the reactor set-up in the particular research effort [26].

Carbon and oxygen are considered major defects in semiconductors, since they often function as p-type impurities [64]. If it were stable, stibine (SbH_3) would be a desirable prescursor because of the H-radicals it supplies via hydride pyrolysis which reduce the C and O background levels [26]. Unfortunately, stibine is unstable at room temperature and cannot provide this function. Similarly, it has been observed that using trimethylarsenic (TMAs) instead of arsine (AsH_3) results in high levels of carbon impurities [64]. Furthermore, oxygen defects are particularly problematic in the presence of aluminum, which is very reactive with oxygen. It has been reported that DMEAA produces the most oxygen defects [26]. However, it has been reported in [64] that using TMAA and TESb as precursors have the best reported oxygen value for AlSb growth by MOVPE.

More specifically, all existing reports of InAlAsSb by MOVPE have use the most standard precursors for each element, TMIn, TMAl, TMSb, and arsine. Chang et al. [8] used a very low arsine flow relative to other gases, particularly in comparison to [5]. Ostensibly, the authors in [8] achieved the nominal quarternary composition $In_{0.34}Al_{0.66}As_{0.85}Sb_{0.15}$. The authors observed that lattice-mismatch decreased with increasing arsine flow until an optimum value, at which point mismatch began increasing again with increasing arsine flow. Yokoyama et al., however, were not able to get more than 2% Sb to incorporate into the solid [5]. The authors held all other gas flows constant and gradually increased Sb flow during sample growth, but a corresponding shift in solid-phase composition was not observed. The authors concluded that the decomposition of TMAl is suppressed by TMSb injection, and further research on AlAsSb indicated that excess Sb on the growth surface suppresses the decomposition of TMAl [5].

4.2.2 Experimental development of InAlAsSb

Given that high-quality InAlAs had already been demonstrated on the Veeco D125 MOVPE reactor at NASA Glenn Research Center, the initial trajectory of InAlAsSb development was to begin with the optimum growth conditions for InAlAs and modify to facilitate Sb-incorporation. The majority of InAlAs development had used the industry standard precursors of TMIn, TMAl, and arsine. TMSb was selected as the antimony precursor. Sb incorporation was observed to increase at lower growth temperatures and lower V/III gas ratios which is consistent with literature. Figure 28 plots Sb solid incorporation verified by secondary-ion mass spectrometry (SIMS) as a function of Sb-vapor fraction, with multiple data sets that represent different growth temperatures all using a V/III ratio of approximately 5. Samples with Sb vapor fractions approaching unity show Sb solid incorporation is limited to about 4% even with a significant TMSb overpressure. It is clear in the abundance of samples grown at 550°C, Sb

solid incorporation increases at a linear rate which does not approach adequately high concentrations as the Sb vapor fraction nears unity. There is also a trend with decreasing Sb-incorporation as growth temperature increases and all other growth conditions are held constant, which is the case for one data set at a 0.8 Sb vapor fraction.

The majority of samples exhibited poor surface morphology which has mitigated by others by reducing V/III ratio and growth temperature [64]. Lower growth temperatures and V/III ratios were made feasible by replacing arsine with TBAs since arsine pyrolysis is significantly less efficient below 550ºC which necessitates a higher V/III ratio. However, surface morphology still remained relatively poor after switching to TBAs. Energy dispersive x-ray spectroscopy (EDS) was a useful tool for analysis of surface features in order to determine which materials were depositing on the surface. Figure 29 displays a scanning electron microscope (SEM) image of an InAlAsSb surface and EDS maps of the SEM image for each of the constituent elements In, Al, As, and Sb. The maps were recorded using a 25 kV accelerating voltage. This sample was grown at 610ºC using TMIn, TMAl, TBAs, and TMSb. It is evident in the maps that the surface morphology is comprised mainly of antimony and to a lesser extent, indium. Over time, it was observed that growth of InAlAsSb with these precursors resulted in white deposits observed in the reactor lines which were determined to be the result of TMAl pre-reacting with TMSb. TTBAl was readily available so the TMAl source was replaced with TTBAl and no deposits or pre-reactions were observed.

Given the limitations observed by approaching InAlAsSb growth from the InAlAs ternary, the AlAsSb ternary was developed as an alternate route to InAlAsSb. It was similarly observed that TMAl/TBAs and TTBAl/arsine produced poor surface morphology while TTBAl/TBAs created specular surfaces as shown in Figure 30. Extensive literature available on MOVPE growth of AlAsSb indicate low growth temperatures and V/III = 1 are optimal conditions for AlAsSb on InP [85, 86]. Good quality epitaxial layers of AlAsSb were achieved using these growth conditions and the TTBAl/TBAs/TMSb precursors. By marginally increasing TMIn flow, it was identified that a growth temperature of 505ºC and V/III = 5 facilitated growth of high-Sb content InAlAsSb. Details on growth of samples with high Sb-concentration are available in [77].

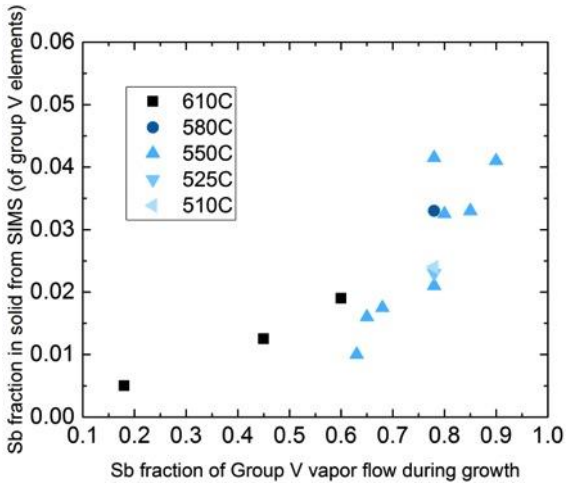

Figure 28: Data from InAlAsSb samples analyzed by SIMS, Sb solid content as a function of Sb vapor fraction during growth.

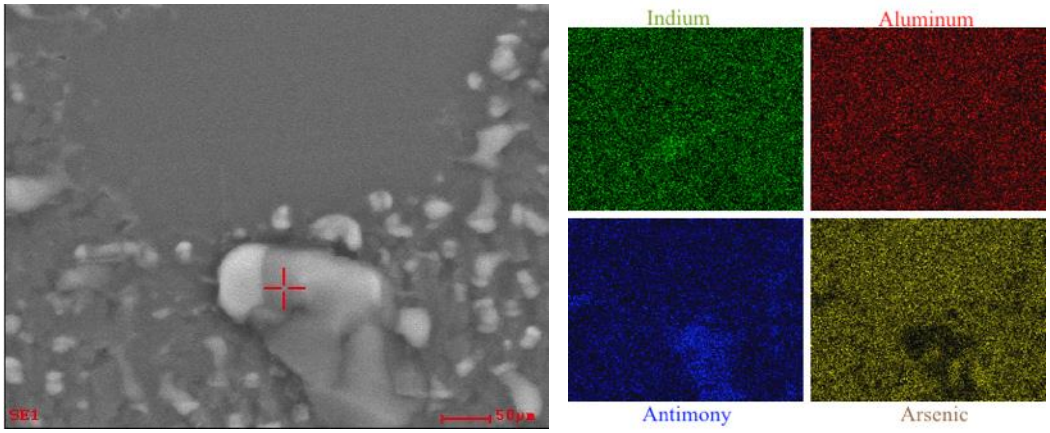

Figure 29: SEM image and EDS elemental maps of InAlAsSb surface morphology grown with TMIn, TMAl, TBAs, and TMSb (sample number 13A164)

Figure 30: AlAsSb samples under 200x magnification Nomarski microscope, grown with different precursors

4.3 Bandgap measurement

In order to verify the composition of InAlAsSb samples, a combination of characterization techniques were used. One way to verify composition is secondary-ion mass spectrometry (SIMS); however SIMS is a destructive technique and is not available in-house, which makes it prohibitively expensive. Alternatively, high-resolution x-ray diffraction and some form of bandgap verification could together provide enough information to determine composition, in addition to providing vital information on strain and optical transitions. A number of techniques are potentially viable methods of bandgap verification, including photoluminescence, photoreflectance, or ultra-violet to visible (UV-Vis) transmission spectroscopy. The benefits and drawbacks of these bandgap measurement techniques will be further discussed in this section.

4.3.1 Photoluminescence

Photoluminescence (PL) is a useful technique for measuring the bandgap of a semiconductor in that it is a non-destructive and contactless method, where carriers are excited by a laser rather than by current injection. A laser with a photon energy larger than the bandgap in the sample of interest is used to generate electron-hole pairs in the sample, which then relax to the lowest possible energy state and recombine. Photoluminescence represents the portion of that recombination which is radiative, though some portion also may occur which is non-radiative. InAlAsSb photoluminescence was measured using a 50 mW 532 nm argon ion laser chopped at a frequency of 257 Hz, a Horiba iHR320 monochromator, Stanford Research 830 lock-in amplifier, and silicon photodiode detector.

In order to verify the accuracy of PL assessment of bandgap, PL was measured on multiple bulk InAlAsSb samples which had composition already determined by SIMS. The layer structures of the samples are shown in Table 12. Figure 31 shows room-temperature PL data from bulk InAlAsSb grown by MOVPE with compositions of $In_{0.10}AlAsSb_{0.48}$ and $In_{0.19}AlAsSb_{0.32}$. These compositions should correspond to bandgaps of 1.98 eV and 1.75 eV respectively as predicted by [10]. However, the PL observed from these samples consists of multiple peaks occurring more than 300 meV below the predicted bandgaps. The room temperature PL peak parameters from these two samples are reported in Table 13. The $In_{0.10}AlAsSb_{0.48}$ displays peaks peaks at 1.33 eV and 1.39 eV. The 1.33 eV peak approximates the direct bandgap of InP and could originate from the substrate since the InAlAsSb epilayer is relatively thin. The 1.39 eV peak does not correspond to any known optical transitions in InP or InGaAs, so it can be assumed that this PL emission originates from the InAlAsSb layer. The PL emission peak from the $In_{0.10}AlAsSb_{0.48}$ sample is more than 500 meV lower than the predicted direct bandgap given the InAlAsSb composition. This behavior has also been observed in PL measurements of InAlAsSb grown by molecular beam epitaxy (MBE), where studies indicate the PL is dominated by excitonic recombination due to compositional fluctuation of the quaternary [6]. The room temperature PL from the $In_{0.19}AlAsSb_{0.32}$ sample shows peaks at 1.39 and 1.42 eV. The absence of a 1.33 eV peak from InP is explained by the thickness of the $In_{0.19}AlAsSb_{0.32}$ epilayer. This sample emits approximately 300 meV below its predicted bandgap, and the presence of multiple peaks is indicative of compositional quaternary fluctuation.

Table 12: Structures of samples used for PL measurements

$In_{0.10}AlAsSb_{0.48}$ structure	**$In_{0.19}AlAsSb_{0.32}$ structure**	**$In_{0.62}AlAsSb_{0.059}$ structure**	**$In_{0.51}AlAsSb_{0.022}$ structure**
			InP cap (50 nm)
InP cap (10 nm)		InP cap (10 nm)	InGaAs (25 nm)
InAlAsSb (250 nm)	InAlAsSb (750 nm)	InAlAsSb (100 nm)	InAlAsSb (950 nm)
InGaAs (10 nm)	InGaAs (10 nm)	InGaAs (10 nm)	InGaAs (25 nm)
InP buffer (100 nm)	InP buffer (100 nm)	InP buffer (100 nm)	InP buffer (100 nm)
Semi-insulating InP substrate	Semi-insulating InP substrate	Semi-insulating InP substrate	Semi-insulating InP substrate

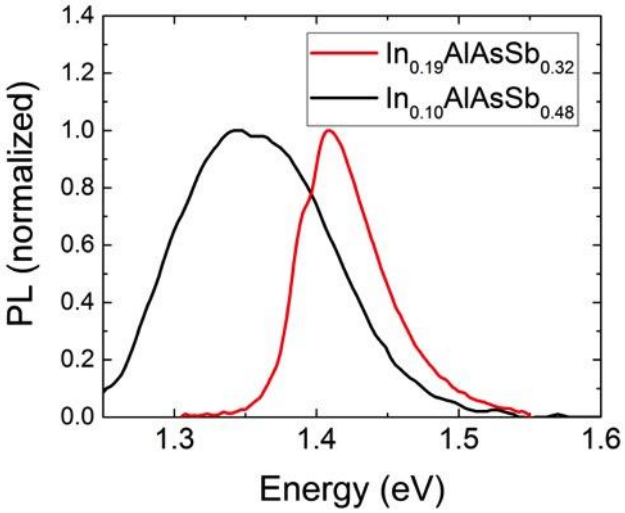

Figure 31: Room temperature PL of MOVPE-InAlAsSb with compositions $In_{0.10}AlAsSb_{0.48}$ and $In_{0.10}AlAsSb_{0.48}$ verified by SIMS (sample numbers 15A040 and 15A058, respectively)

Table 13: Peak parameters from room temperature PL of MOVPE-InAlAsSb

Peak	Peak position	FWHM	Normalized intensity	Predicted bandgap at RT [10]
$In_{0.10}AlAsSb_{0.48}$ peak 1	1.33 eV	80 meV	0.28	
$In_{0.10}AlAsSb_{0.48}$ peak 2	1.39 eV	150 meV	0.93	1.98 eV
$In_{0.19}AlAsSb_{0.32}$ peak 1	1.39 eV	60 meV	0.35	
$In_{0.19}AlAsSb_{0.32}$ peak 2	1.42 eV	100 meV	0.71	1.75 eV

Temperature-dependent PL was measured on the $In_{0.10}AlAsSb_{0.48}$ sample in order to determine if a 1.98 eV transition is evident at lower temperature. PL was measured every 20 K between 100 and 280 K. The data is shown in Figure 33, each spectrum is normalized and vertically shifted, and fit to Gaussians using the code developed in [87]. No peak was observed at high energies, though it was observed that the 1.39 eV peak decreased in intensity with respect to the 1.33 eV peak as temperature decreased. Furthermore, a 1.25 eV peak emerged below 140K which is not a known transition of InP or InGaAs. The presence of this low energy peak at low temperatures may be similar behavior of that reported in [6], where carriers with less thermal energy are unable to diffuse to the deepest localized potential minima. However, unlike the data in [6], the temperature dependent PL peaks do not show a characteristic S-shift in peak energy indicative of compositional fluctuation. This may imply that MOVPE-grown InAlAsSb has less compositional variation than MBE-InAlAsSb, or perhaps higher Sb-content InAlAsSb displays less compositional fluctuation given that the sample in [6] had a composition of $In_{0.31}Al_{0.69}As_{0.82}Sb_{0.18}$.

Low temperature PL at 10 K was measured for a number of InAlAsSb samples with differing composition; structures are all included in Table 12. The 2.2% Sb sample was grown using TMIn, TMAl, arsine, and TMSb at 610°C with a V/III = 5 and Sb vapor fraction of 0.77. The 6% Sb sample used TMIn, TTBAl, TBAs, and TMSb at 520°C, a V/III ratio = 1, and a Sb vapor fraction of 0.57. The 32% and 48% Sb samples were grown using TMIn, TTBAl, TBAs, and TMSb at 505°C, a V/III ratio of 5, and a Sb vapor fraction of 0.7 and 0.8 respectively. The PL is

shown in Figure 32 and peak parameters are tabulated in Table 14, along with the expected bandgap predicted by [10]. The experimental PL peaks loosely follow a trend with composition, where the high Sb samples show higher energy peaks than the low PL samples. However, the 2.2% Sb sample is predicted to have a higher bandgap than the 6% Sb sample yet is PL peak is at a lower energy. Similarly, the 48% Sb sample is expected to have a higher bandgap than the 32% Sb sample, but the 32% sample shows multiple peaks, one of which is higher energy than any in the PL from the 48% sample. Furthermore, all PL peaks occur at least 100 meV lower than a rough estimation of the expected PL emission at 10 K for a given composition. InP is expected to luminesce at 1.41 eV at 10 K, which could be the origin of both the peaks occurring near this value in the 32% and 48% samples [88]. The single PL peak from lowest (2.2%) antimony sample occurs at 1.30 eV; a similar peak is also present in the 6% sample though is not approximated well by a Gaussian on the low-energy end. This is similar to the observation reported in [6], where PL from InAlAsSb at low temperatures exhibited a low-energy tail when compared to a Gaussian. This was assumed to result from carriers having insufficient thermal energy to diffuse to spatially-localized potential minima.

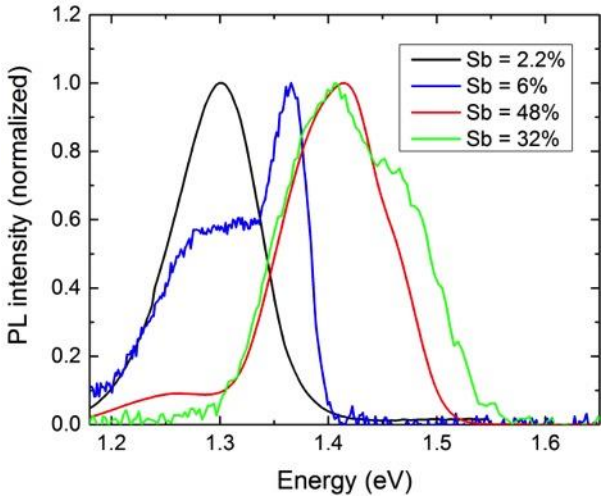

Figure 32: Photoluminescence measure at 10 K from MOVPE-InAlAsSb samples with varying Sb-content (sample numbers 13A235, 14A350, 15A040, and 15A058)

Table 14: Peak parameters from 10K PL of MOVPE-InAlAsSb

Peak	Peak position	FWHM	Normalized intensity	Predicted bandgap at room temperature [10]
$In_{0.10}AlAsSb_{0.48}$ peak 1	1.25 eV	90 meV	0.086	
$In_{0.10}AlAsSb_{0.48}$ peak 2	1.41 eV	110 meV	1	
$In_{0.10}AlAsSb_{0.48}$ peak 3	1.47 eV	25 meV	0.075	1.98 eV
$In_{0.19}AlAsSb_{0.32}$ peak 1	1.40 eV	110 meV	0.95	
$In_{0.19}AlAsSb_{0.32}$ peak 2	1.48 eV	75 meV	0.48	1.75 eV
$In_{0.62}AlAsSb_{0.059}$ peak 1	1.32 eV	150 meV	0.61	
$In_{0.62}AlAsSb_{0.059}$ peak 2	1.37 eV	40 meV	0.58	1.44 eV
$In_{0.52}AlAsSb_{0.022}$	1.30 eV	100 meV	1	1.45 eV

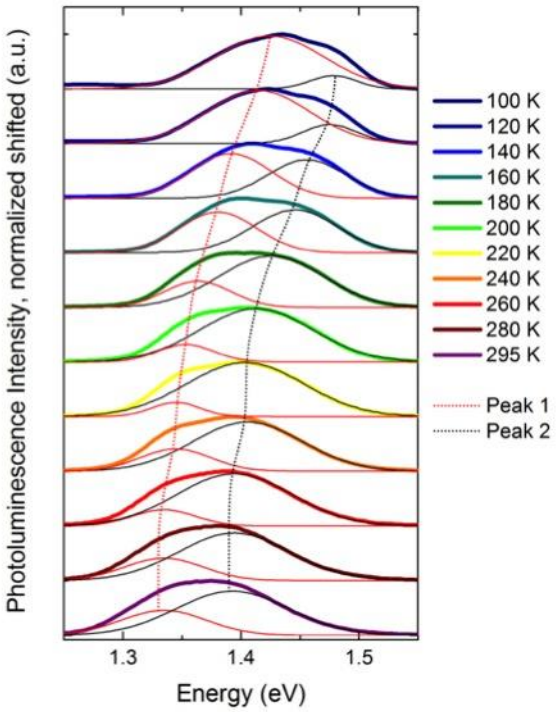

Figure 33: Temperature-dependent photoluminescence of $In_{0.10}AlAsSb_{0.48}$. Each spectrum is normalized and vertically shifted. (sample number 15A040)

4.3.2 UV-Vis-NIR Transmission Spectroscopy

A different method of verifying bandgap was proposed to measure transmission through the epitaxial layer of interest. For a given bandgap, a white light source should reflect off the sample to some degree, with the remaining light either absorbing or transmitting through the sample if the photon has an energy greater or lower than the bandgap, respectively. This requires removal of the epitaxial layer from the substrate so that light passing through the layer of interest only. This was achieved by growing a thin InGaAs layer on the InP substrate before the InAlAsSb epilayer and bonding the sample epitaxial-side-down to a glass slide. KMPR photoresist was applied via pipette to bond the sample, then hard baked on a hot plate at 130°C for 20 minutes. The slide with sample was then placed into into hydrochloric acid for an hour or more to significantly over-etch the 350-µm-thick InP substrate at an etch rate of 6 µm/minute, where the InGaAs layer served as an etch stop. Transmission was measured with a Perkin Elmer LAMBDA 950 spectrophotometer with a silicon detector and tungsten halogen lamp as a light source.

This process was executed for multiple known samples first in order to establish validity as a method of bandgap measurement. The known samples used were InGaAs lattice-matched to InP and an InAlGaAs sample which showed photoluminescence at 1.0 eV. The sample structures are shown in Table 15. The transmission data from these samples is shown in Figure 34(a). Figure 34(a) also includes transmission data from a blank glass slide, as well as a glass slide that has been coated with s1813 photoresist and hard-baked. The InGaAs transmission drops to 30% at the bandedge of approximately 0.75 eV which is near the nominal bandgap of $In_{0.53}Ga_{0.47}As$ lattice matched to InP. Transmission drops below 10% at approximately 2.0 eV which is consistent with the absorption

edge of the resist as evidenced by the data from the resist-only glass slide in the same plot. A transmission measurement is also shown for the same sample before it was removed from the InP substrate. A 0.75 eV bandedge is still observed since any light with energy below 1.34 eV is not absorbed by the InP substrate. For the InAlGaAs sample, transmission drops to approximately 35% at 1.0 eV which is consistent with PL data measured from the same sample. A step at near 1.4 eV occurs in both the InGaAs and InAlGaAs transmission measurements and is assumed to be an artifact from the instrument.

Table 15: Layer structure of samples used to validate UV-Vis transmission as bandgap measurement, InP substrates and buffers removed by selective etch.

InGaAs structure	InAlGaAs structure
InP cap (15 nm)	InP (50 nm)
InGaAs (2000 nm)	InAlGaAs (3000 nm)
InP buffer (200 nm)	InGaAs (50 nm)
InP substrate	InP substrate

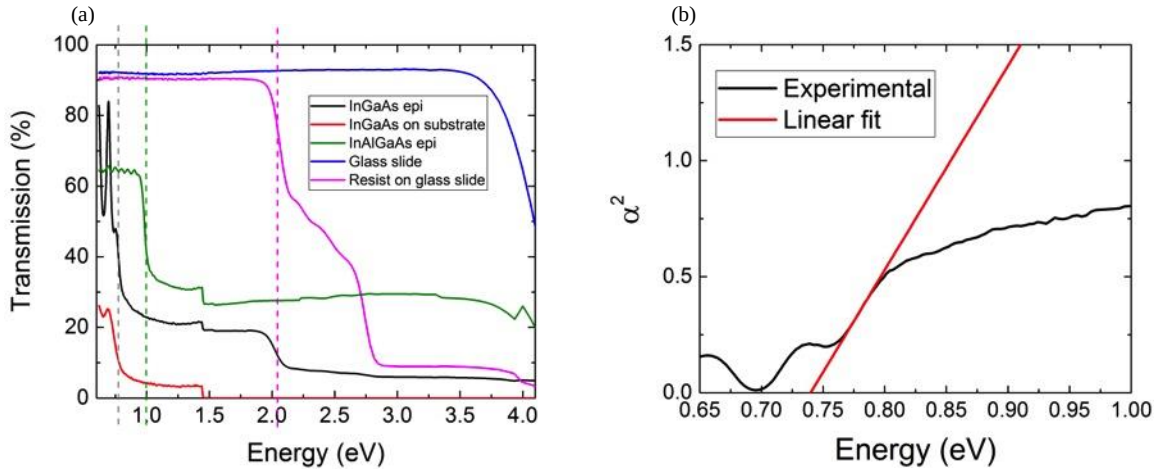

Figure 34 (a) Transmission spectroscopy data through 2 μm of InGaAs and 3 μm of InAlGaAs adhered to glass slides (sample number 12A104 and 13A022 respectively) in addition to control measurements of a blank glass slide and a glass slide with photoresist. (b) A linear fit to α^2 calculated from InGaAs transmission data: x-intercept corresponds to bandgap E_g of 0.74 eV

A quantitative method of extracting bandgap from transmission data was employed on the InGaAs sample to demonstrate accuracy. This method is feasible for semiconductors with a direct bandgap and can be found in [89], where the bandgap E_g is related to the absorption coefficient α as shown by:

$$\boldsymbol{\alpha(hv) = C(hv - E_g)^{\frac{1}{2}}} \qquad \textbf{Equation 6}$$

Plotting α^2 as a function of hv yields a linear region near the band-edge of the sample, to which a line can be fit where the x-intercept of the line corresponds to the bandgap of the sample. The absorption coefficient can be calculated from transmission data if the thickness of the sample is known via a quantity called absorbance. The relation of absorbance, A, to the absorption coefficient α is shown in:

$$A = \alpha * d * \log(e) \qquad \textbf{Equation 7}$$

where d is the thickness of the absorbing layer. Absorbance, A, can be calculated from transmission, T, and reflectance, R, via Equation 8. This method is demonstrated for InGaAs in Figure 34(b) where the x-intercept occurs at 0.74 eV, which corresponds to the expected bandgap. The linear fit for the InGaAs sample had an $R^2 = 99.94$.

$$A = \log\left(\frac{1}{T+R}\right) \qquad \textbf{Equation 8}$$

A number of InAlAsSb samples were grown specifically for transmission measurements. The sample structures are shown below in Table 16. All of these samples had Sb incorporation around 2% which corresponds to an estimated bandgap around 1.44 eV. Transmission data is shown in Figure 35(a). Visually, all samples appear to exhibit a bandedge near 1.5 eV though the drop off is very gradual for some of the samples, particularly the thinnest sample. Furthermore, since the interference fringes appear to damp slowly (as compared to a sharp drop off in the control samples), this confounds the linear fitting method. Linear fits to the α^2 values extracted from sample D are shown in Figure 35(b). The R^2 values for the linear fits D1 and D2 were 99.93 and 99.94, respectively. Due to the ambiguity of extracting bandgap from this data, alternative methods of bandgap verification were then investigated.

Table 16: Layer structure of InAlAsSb samples measured by UV-Vis transmission, InP substrates and buffers removed by selective etch.

A	B	C	D
	InP cap (30 nm)	InP cap (50 nm)	InP cap (50 nm)
InP cap (50 nm)	InGaAs (25 nm)	InGaAs (25 nm)	InGaAs (25 nm)
InAlAsSb (500 nm)	InAlAsSb (1000 nm)	InAlAsSb (1000 nm)	InAlAsSb (950 nm)
InGaAs (50 nm)	InGaAs (25 nm)	InGaAs (25 nm)	InGaAs (25 nm)
InP buffer (100 nm)	InP buffer (100 nm)	InP buffer (100 nm)	InP buffer (100 nm)
InP substrate	InP substrate	InP substrate	InP substrate

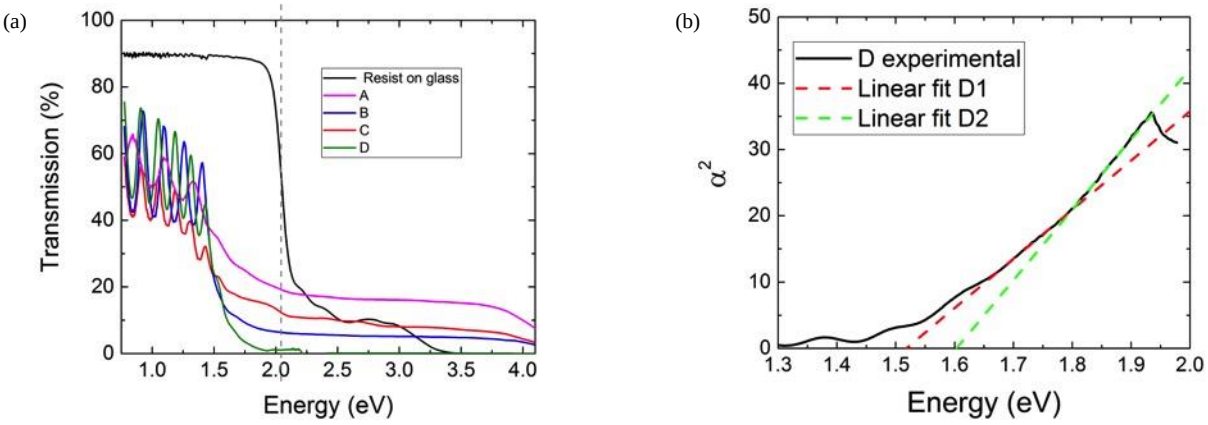

Figure 35: (a) Transmission data through 0.5-1.0 µm InAlAsSb layers and thin InGaAs etch stop (samples 13A212, 13A226, 13A227, and 13A235 respectively) (b) Linear fits to α^2 calculated from sample D transmission data: x-intercepts corresponds to bandgap E_g of 1.52 eV or 1.60 eV

4.3.3 Photoreflectance

Photoreflectance (PR) represents another alternative method to measure bandgap. Photoreflectance is a modulation spectroscopy technique which uses a chopped laser while detecting reflectance off the sample from a white light source. A change in the reflectance of the white light is observed when the chopped laser is incident, due to photogeneration of electrons near the sample surface, which reduces the existing electric field attributed to dangling bonds at the surface [90]. This change in electric field produces a change in the dielectric function of the material in that it accelerates the electrons into the conduction band over a small, finite range of reciprocal space (rather than being a direct vertical transition at a single point in reciprocal space), as depicted in Figure 36 [91]. This acceleration will be used to extract the value of transition occurring at the critical point in question, and is described mathematically in the following section.

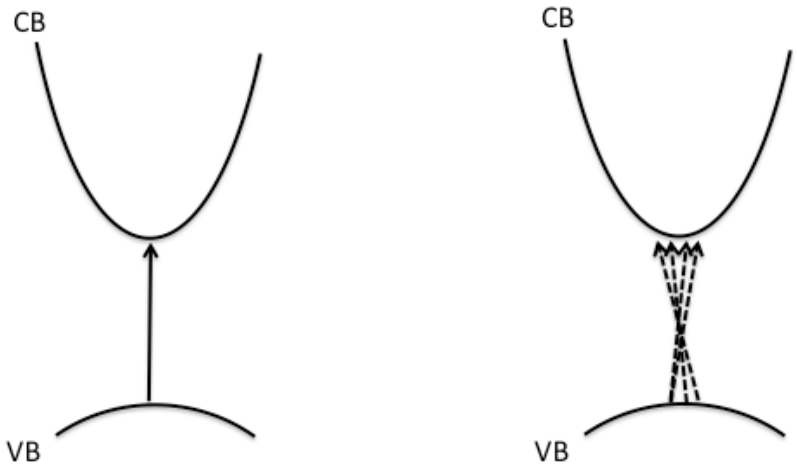

Figure 36: Band transitions with (left) and without (right) application of electric field [91]

The setup used for photoreflectance measurements is shown in Figure 37. A 20 W quartz tungsten halogen (QTH) broadband lamp was used as white light source connected to a fiber. The fiber was attached to a collimator lens which was placed incident on the sample at 90^{o} with respect to the monochromator slit entrance. The 514.5 nm 50 mW argon ion laser was positioned to be incident on the sample near normal so that any PL emission would not be collected by the monochromator. The laser beam and white light are positioned to be incident at the same spot on the sample, and the laser is defocused so that it is larger than the white light spot from the fiber. The white light is reflected off the sample and through a monochromator onto a silicon detector. The detector receives both the static and modulated reflectance as a function of wavelength ($I_0(R+\Delta R)$), which are respectively extracted as a DC-signal ($I_0(R)$) by a digital multi-meter, and as an AC signal ($I_0(\Delta R)$) by a lock-in amplifier phase-locked to the laser chopper. The lock-in amplifier multiplies the input signal by the reference signal from the laser chopper and integrates this over a period of time, such that any signal that is not occurring at the chopper frequency is attenuated close to zero. The integration time is controlled manually, typically 1 second depending on signal-to-noise ratio. Similar to the PL setup, the laser was chopped at 257 Hz, and a Keithley DMM and Stanford SR830 lock-in amplifier were used in addition to the Horiba iHR320 monochromator and a silicon point detector.

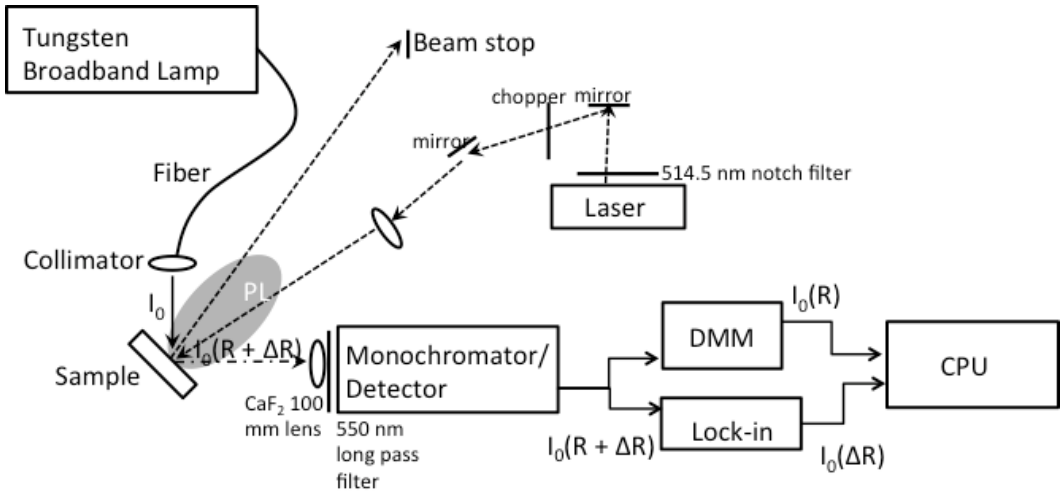

Figure 37: Photoreflectance measurement setup

To demonstrate the functionality of PR for a known material, PR of a blank semi-insulating InP substrate is shown in Figure 38a). The experimental data is the result of dividing the modulated reflectance by the static reflectance, reported as ΔR/R. The change in reflectance data is normalized by the reflectance data so that it produces a useful relation to the change in the dielectric function $\Delta\varepsilon$, shown in Equation 9, where *a* and *b* are Seraphin coefficients and $\Delta\varepsilon_1$ and $\Delta\varepsilon_2$ are changes in the real and imaginary parts of the dielectric function. If absorption is not significant, the *b* term can be neglected and the data is considered to be proportional to only the real part of the dielectric function [90].

$$\frac{\Delta R}{R} = a\Delta\varepsilon_1 + b\Delta\varepsilon_2$$

Equation 9

The normalized modulated reflectance data was determined to represent the real part of the third derivative of the dielectric function, and a third-derivative functional form (TDFF) was developed in [91, 92] to fit experimental data and extract the values of critical points. This is represented by the equation:

$$\frac{\Delta R}{R} = \Re\left[Ce^{i\Theta}\left(E - E_g + i\Gamma\right)^{-n}\right]$$

Equation 10

referring to the real component of an oscillator where C represents an amplitude factor, θ is a phase factor, E_g is the critical point corresponding to an optical transition, Γ is a broadening factor, and n is a factor representing the dimensionality, or confinement, of the band transition. The *n* parameter is dependent on the dimensionality of the sample in question, as defined in Equation 11 where *d* is the available dimensions in the structure, and largely affects the observed broadening factor (increasing with dimensionality). It is equal to 5/2 for the work considered here given that all experimental data is taken from bulk epitaxial films.

$$n = 4 - \frac{d}{2}$$ Equation 11

Fits to experimental data were achieved in this work using the code available from [93]. A fit to a single TDFF gives the critical point E_g at 1.343 eV, with a 95% confidence interval within ±0.001 eV. This corresponds to the direct bandgap of InP [94]. Figure 38(b) shows PR data from a 1500 nm unintentionally doped (uid) layer of InAlAs grown by metal organic vapor phase epitaxy (MOVPE) on an n-doped InP buffer layer on an n-type InP substrate. When fit to a TDFF, the PR signal corresponds to a critical point of 1.447 eV and a 95% confidence interval within ±0.006 eV, which approximates the expected direct bandgap for $In_{0.52}Al_{0.48}As$ [43].

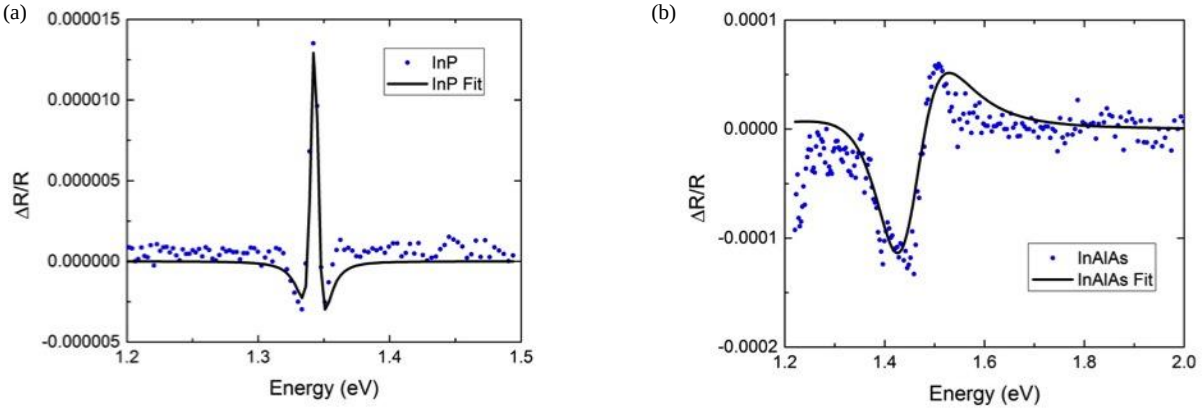

Figure 38: Photoreflectance of (a) InP:Fe substrate and (b) bulk undoped InAlAs

PR data from a series of InAlAsSb samples grown by molecular beam epitaxy (MBE) with compositions verified by SIMS are shown in **Figure 39**. These MBE samples are nominally single 1000 nm epilayers of InAlAsSb on InP substrates with 6.6% Sb content, 17.6% Sb content, and 26.4% Sb content. Two samples are nominally the same Sb composition (17.6%) but were grown at different temperatures. The highest energy oscillation in each sample is associated with the direct bandgap of the InAlAsSb epilayer. These values are tabulated in Table 17. The bandgap transitions shown in green have been fitted using the TDFF equation described above. Lower energy oscillations are attributed to interference effects from interfaces in the sample, referred to as low energy interference oscillations (LEIOs). LEIOs have been fitted in black using the functional form developed in reference [95] which is dependent on the thickness of the epilayer. This form is shown by:

$$\frac{\Delta R}{R} = L_1 + L_2 e^{-yk} \cos(yn + \delta) + L_3 e^{-2yk}$$ **Equation 12**

where $L_{1,2,3}$ are coefficients with Lorentzian forms, δ is a phase factor, n is the refractive index, k is the extinction coefficient, and y is the effective thickness as defined by:

$$y = 2d\cos(\theta_r)\frac{2\pi}{\lambda}$$ **Equation 13**

where d is the layer thickness, θ_r is the angle of refraction, and λ is the wavelength. The value used for d is reported in Table 17 and is compared to the nominal thickness of the sample targeted during growth or verified by ellipsometry where available. The agreement between the nominal layer thickness and the value used for LEIO fitting confirm the origin of these features. It should be noted that the scan time required for good data resolution often resulted in some drift of the signal which is not accounted for in either of the modelling functions. Given the drift in the signal, and the clear presence of smaller peaks within the LEIO fringes, the R^2 values of the LEIO fits are rather low. However, the agreement between the PR results and the bandgaps predicted by [10] demonstrate PR as a valuable technique for verifying InAlAsSb bandgap.

Table 17: MBE-InAlAsSb samples and bandgap measurements

Sample	PR E_g	95% Confidence Interval	Predicted E_g [10]	LEIO thickness	LEIO R^2	Ellipsometry (or nominal) thickness
Sb = 6.6%	1.452 eV	±0.013 eV	1.44 eV	1500 nm	19.64%	(1000 nm)
Sb = 17.6% T= 375ºC	1.562 eV	±0.017 eV	1.48 eV	950 nm	71.20%	943 nm
Sb = 17.6% T= 325ºC	1.621 eV	±0.007 eV	1.48 eV	830 nm	14.54%	(1000 nm)
Sb = 26.4%	1.762 eV	±0.043 eV	1.74 eV	1020 nm	69.94%	(1000 nm)

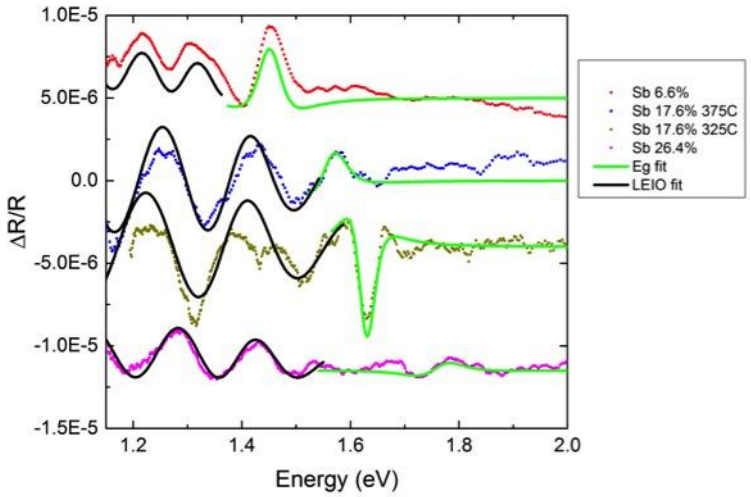

Figure 39: Photoreflectance of MBE-grown InAlAsSb bulk epilayers

PR measurements of MOVPE-InAlAsSb samples are shown in **Figure 40**. Compositions of these samples have been verified by SIMS. The data in **Figure 40**(a) is from 100 nm of $In_{0.62}Al_{0.38}As_{0.94}Sb_{0.06}$ on 10 nm of InGaAs grown on a semi-insulating InP substrate after a 100 nm InP buffer layer. The first six extrema in the experimental

data have a regular period of 0.02 eV and appear to belong to a continuous oscillation. These features are suggestive of Franz-Keldysh oscillations (FKOs), which result from an electric field present in the sample. FKOs have regular periodicity and occur only at energies higher than the critical point (band transition). As such, these first six extrema are assumed to result from the direct bandgap of InP and its subsequent higher energy FKOs. These features were fit using least-squares to Equation 14 taken from reference [96]:

$$\frac{\Delta R}{R} = \Re\left[\frac{Ce^{i\Theta}}{(E-i\Gamma)^2}\, H(z)\right] \qquad \text{Equation 14}$$

where all of the variables have been used previously in earlier equations except *H(z)* which is defined as the electro-optic function for a three dimensional critical point. *H(z)* is defined by:

$$H(z) = 2\pi\left\{e^{-i\left(\frac{\pi}{3}\right)}A_i'(z)A_i'\left[ze^{-i\left(\frac{2\pi}{3}\right)}\right] + ze^{-i\left(\frac{2\pi}{3}\right)}A_i(z)A_i[ze^{-i\left(\frac{2\pi}{3}\right)}]\right\} + i\sqrt{z} \qquad \text{Equation 15}$$

where A_i is the Airy function, A_i' is its derivative, and z is defined as:

$$z = \left[\frac{(E_0-E)}{\hbar\varphi} + i\frac{\Gamma}{\hbar\varphi}\right] \qquad \text{Equation 16}$$

where $\hbar\varphi$ is defined as the electro-optic energy, which is dependent on Planck's constant $\hbar$, the magnitude of the electric field, the electronic charge, the reduced effective mass, and the energy of the critical point E_0. The fit to the FKOs calculates the critical point to be 1.343 eV which is consistent with the InP bandgap and corresponds to a field magnitude on the order of 10^6 V/m which is consistent with an unintentionally doped epitaxial layer on a semi-insulating substrate.

There are two remaining features occurring around 1.43 and 1.5 eV which are assumed to be the split-off transition in InP and the direct bandgap of the InAlAsSb epilayer, respectively. These features are clearly separate from the FKOs at lower energies since the period of the extrema becomes irregular and the oscillator no longer appears to be continuous, which indicates a point of origin from a different depth in the sample. These transitions were each fit with the TDFF defined previously. The critical point for each transition was determined to be 1.437 eV and 1.492 eV, respectively. These two TDFFs are summed and plotted in red in **Figure 40**(a). These critical points are tabulated and compared to predicted values in Table 18. The $In_{0.62}Al_{0.38}As_{0.94}Sb_{0.06}$ epilayer is expected to have a bandgap of 1.44 eV according to [10]. This is relatively good agreement with the critical point extracted from PR, where the fit to the 1.492 eV critical point has a 95% confidence interval between 1.479 and 1.502 eV. The 1.437 eV critical point is likely to be the split-off transition of InP, since this transition is known to exhibit an enhanced PR signal with the inclusion of an InGaAs layer [97].

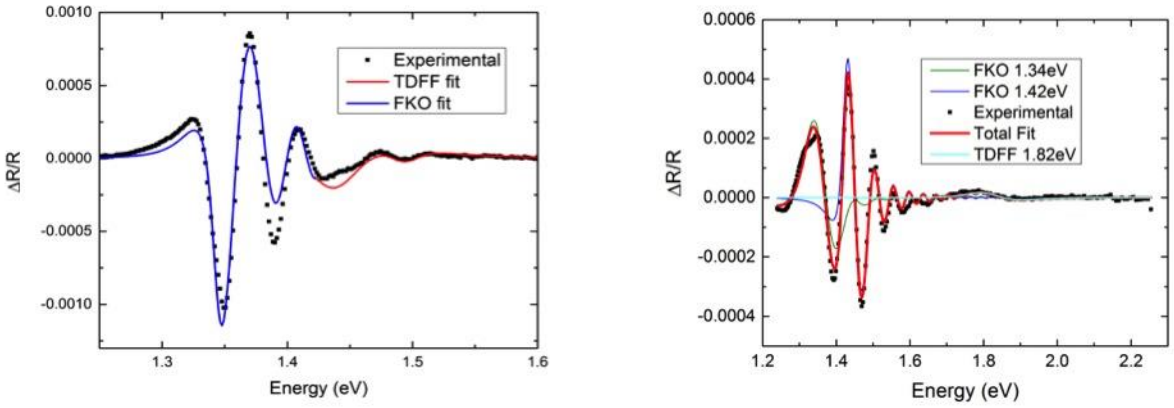

Figure 40: Photoreflectance of MOVPE-InAlAsSb: (a) $In_{0.62}AlAsSb_{0.059}$ (b) $In_{0.10}AlAsSb_{0.48}$

Table 18: PR critical points from MOVPE-InAlAsSb

	Predicted Bandgap (eV)[10]	**TDFF critical point (eV)**	**95% Confidence Interval**	**InP split-off (eV)**	**InP Gamma (eV)**
$In_{0.62}AlAsSb_{0.059}$	1.44	1.492	±0.013 eV	1.42	1.34
$In_{0.10}AlAsSb_{0.48}$	1.98	1.822	±0.149 eV	1.42	1.34

Figure 40(b) displays photoreflectance data from 250 nm of $In_{0.10}Al_{0.90}As_{0.52}Sb_{0.48}$ on 10 nm of InGaAs grown on a semi-insulating InP substrate after a 100 nm InP buffer. There appears to be two sets of FKOs originating from InP, one associated with the bandgap 1.34 eV and the other associated with the split off transition 1.42 eV. Given that InGaAs is known to enhance the split off transition, it is assumed that these FKOs are originating from different depths in the sample. The FKOs associated with the split-off transition originate from the InP buffer layer immediately below the InGaAs layer, and the FKOs associated with the gamma-point transition originate from the InP substrate. Finally, the high-energy oscillation is assumed to correspond to the direct bandgap of the $In_{0.10}Al_{0.90}As_{0.52}Sb_{0.48}$ epilayer, which is expected to have a bandgap of 1.98 eV according to [10]. The critical point extracted from this oscillation once fitted by the TDFF is 1.82 eV, which is within a reasonable approximation of the predicted value.

4.4 Conclusions

An extensive literature review, composition analysis, and surface characterization contributed to the development of InAlAsSb growth by MOVPE. This work informed the growth conditions necessary for compositional control and high-Sb content InAlAsSb. Specifically, this included low growth temperatures and low V/III ratios, which necessitated the use of alternative precursors with low pyrolysis temperatures to be substituted in the place of more standard industry precursors that have higher pyrolysis temperatures. Use of these alternative precursors resulted in both higher incorporation of Sb and mitigated surface morphology issues.

Multiple bandgap characterization techniques including photoluminescence, UV-Vis transmission, and photoreflectance spectroscopy were used to evaluate InAlAsSb samples. Temperature-dependent photoluminescence measurements were dominated by an excitonic defect peak which has been attributed to compositional fluctuation in the alloy [6]. UV-Vis transmission spectroscopy showed potential as a viable technique, however more samples with verified bandgap would need to be analyzed to remove ambiguity of location for the linear fit to absorbance data. Photoreflectance proved to be the most promising technique, where spectroscopic features were consistently evident in origin. Measurements of multiple known-composition InAlAsSb samples corresponded to bandgap values predicted by [10] for the given composition. Photoreflectance was used to verify a 1.82 eV bandgap on an InAlAsSb sample which nearly approximated the target composition for the top cell in a InP-lattice-matched triple junction solar cell. Furthermore, photoreflectance was used on MBE-grown InAlAsSb from collaborators to assist in an MBE growth temperature study and informed collaborator's subsequent annealing experiments.

CHAPTER 5: Light management in quantum dot solar cells via back surface reflector

5.1 Motivation

Quantum structures can be used to extend the absorption range of a solar cell, in that they typically have a smaller bandgap than the host material (the bulk of the solar cell), and in this way reduce transmission losses, as displayed on the left in **Figure 41**. The right side of **Figure 41** shows a band structure of a typical *p-i-n* diode with repeating quantum structures occurring in the i-region. This allows absorption of lower-energy photons (lower than Eg) which can then contribute to the photocurrent of the cell assuming carriers are able to be collected from these confined states.

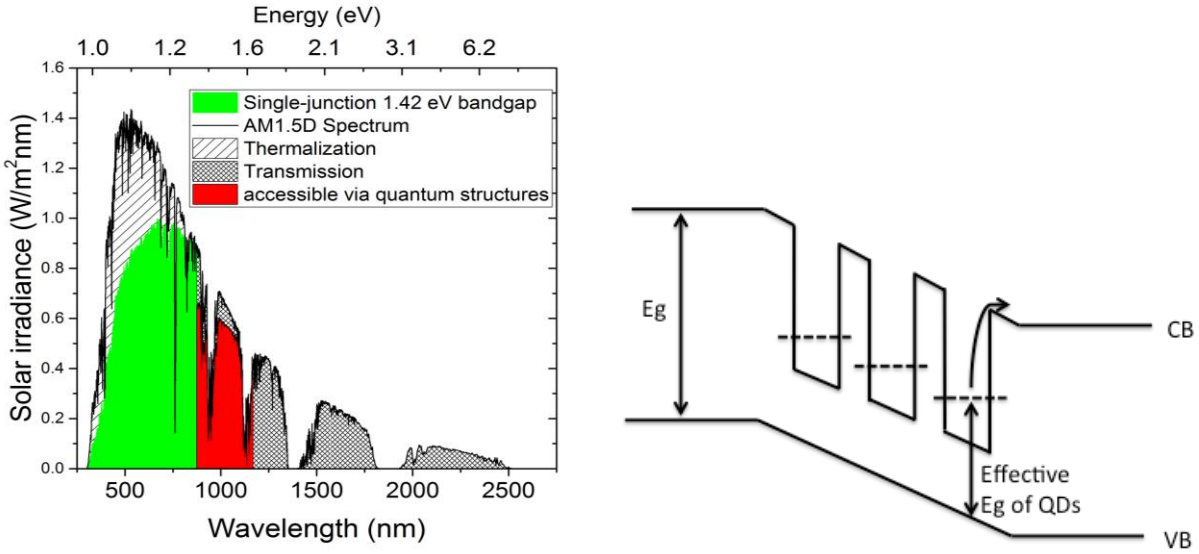

Figure 41: (left) absorption extension by quantum structures, (right) Band structure of a *p-i-n* diode with quantum confined structures in the i-region

Quantum dot solar cells (QDSCs) also represent an avenue to achieving the intermediate band solar cell (IBSC), where QD wavefunctions overlap to form an intermediate band of states between the conduction band and valence band of the host cell as shown on the left in **Figure 42**. This would effectively permit a single-junction cell to capture three optical transitions, as depicted on the right of **Figure 42**, and relies a two-step photon absorption (TSPA) process where a photon excites a carrier from the valence band (VB) to the intermediate band (IB), and a second, lower energy photon excites the carrier into the conduction band (CB). Because of this TSPA process, the IBSC is predicted to exceed conventional single-junction limits with a theoretical maximum efficiency of 44.5% at one sun and over 60% under concentration [13].

Quantum dots (QDs) in photovoltaics can enhance both single junction and multijunction cell performance, since QDs can increase short circuit current (J_{sc}) and improve current-matching [11, 12]. InAs QDs in GaAs are well-developed and have been extensively characterized which makes them a useful, known material system for this study. A GaAs cell with InAs QDs could approach a theoretical maximum of 38% efficiency [13]. The efficiency of

a single-junction GaAs cell has been shown to increase by 0.5% with the addition of 40 layers of QDs as compared to a control [12]. Additional QD layers would be necessary to further increase performance, due to low surface coverage of QDs. Furthermore, to achieve the IBSC, the QD density would need to approach $10^{12}/cm^2$ in order to overcome recombination and have a net positive generation rate [98]. However, increasing the QD layers presents significant challenges regarding growth time and strain management, which would negatively impact the open circuit voltage (V_{oc}).

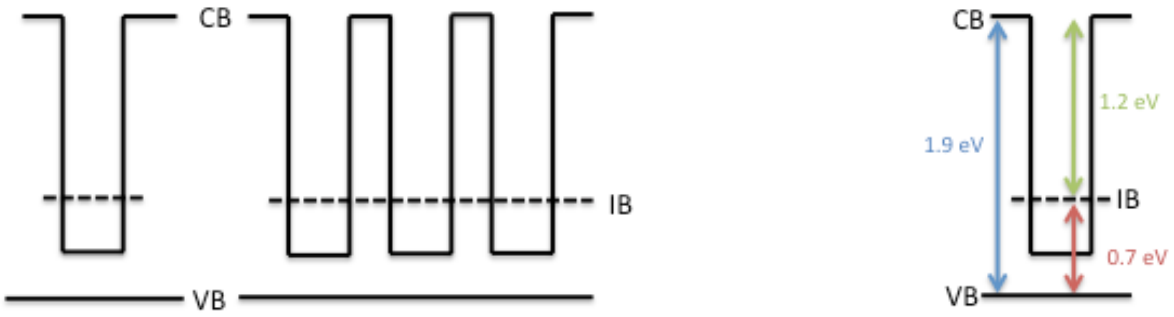

Figure 42: (left) Intermediate band creation in IBSC, (right) two-step photon absorption in IBSC

Light management represents a feasible alternative to increase absorption in the QD region of the cell, where texturing or a reflective material is used on either the front or rear surface of the device to effectively "trap" light in the cell and increase the optical path length. This would require the thin photovoltaic device to be removed from its substrate so that free carriers would not be absorbed and lost in the thick substrate, as represented by the schematic in Figure 43. This could be achieved using an epitaxial lift off (ELO) technique which selectively etches away a sacrificial layer between the cell and the substrate, and also permits re-use of the substrate. Historically, ELO technology has been applied to single junction and multijunction cells [99].

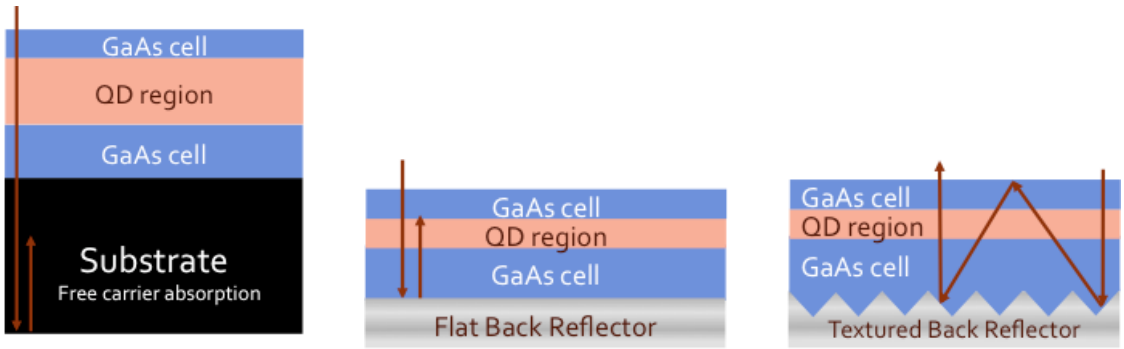

Figure 43: Schematics comparing optical path length for different back surface reflector configurations including devices left on a thick substrate.

Light management would not only increase absorption in the QD region, but would also enable the use of a thinner GaAs bulk cell to achieve the same power output. Re-use of the substrate and a thinner GaAs cell both

represent intensive materials reduction and are significant strategies to improving the techno-economic performance of III-V photovoltaic devices, as outlined by the SunShot roadmap available from the National Renewable Energy Laboratory [3]. Furthermore, there are multiple benefits for space applications in that QDs are known to improve the radiation tolerance of a device, in addition to the fact that thinner devices are less susceptible to radiation damage [19, 20].

Light management in quantum dot solar cells (QDSCs) has been reported using plasmonics as well as gold back surface mirrors, as represented by the flat back reflector schematic in Figure 43 [100, 101]. Using a texture to randomize the angles at which the light is reflected can increase the proportion of the light that is totally internally reflected and increase the optical path length, such as the texture shown in the schematic in Figure 43. Use of such textures has the potential to increase the optical path length by a factor of $4n^2$ where n is the refractive index of the material as originally published in [18]. Similar studies on multiple quantum well solar cells have published results using a crystallographic etch to create either a periodic or random texture in the rear of the cell and report a 480% increase in optical path length as compared to a cell with no rear reflector [14, 102].

5.2 Quantum dot solar cells with back surface reflector

5.2.1 Quantum Dot Growth

The quantum dots in this section were grown using the Stranski-Krastanov (S-K) growth regime, where the QD material must have a lattice-mismatch compared to the substrate such that there is adequate strain between the two materials [103]. As the QD material is epitaxially deposited, it will first form a thin wetting layer (WL) on the substrate. The WL will eventually reach a critical thickness (dependent on the mismatch of the materials involved, among other factors) where the stress in the WL generates enough surface tension that islands form on top of the WL [104, 105]. An example atomic force microscopy (AFM) image is shown on the left side of Figure 44, where typical dot height, diameter, and densities are on the order of 2 nm, 15 nm, and 10^{10} cm^{-3}, respectively. Photoluminescence of the same sample is shown on the right side of Figure 44, and the layer structure of the sample is reported in Table 19.

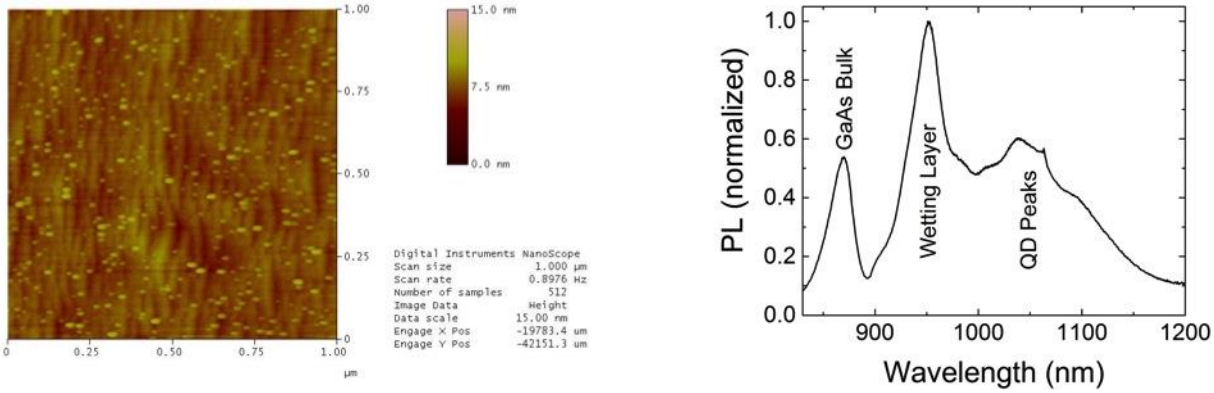

Figure 44: (left) AFM image of 5 layer QD test structure grown with conditions used in solar cell superlattice (right) room temperature PL of the same 5 layer test structure

Quantum dot test structures are typically grown on 2-inch GaAs substrates with a 2 degree offcut towards (110), though 4-inch substrates will also be discussed later in this chapter. Growth precursors are trimethylgallium, trimethylindium (TMIn), arsine, and phosphine. Material before the dots is typically grown at 630°C while material after the dots was grown at 580°C. The bulk of the structure is grown with a V/III ratio of 45 and a growth rate of 2 μm/hr. QDs were grown at a V/III ratio of 80, where TMIn and arsine were flowed for approximately 30 seconds before a growth pause of 60 seconds, resulting in approximately 2 monolayers of QD height. Strain balancing in the 12 nm superlattice period was achieved by growing a 4 nm GaAs spacer on top of the QDs and wetting layer, then a layer of GaP with approximately 1 nm thickness optimized by a similar procedure as described in [106], followed by another 4 nm GaAs spacer on which to grow the next QDs. Samples from two different MOVPE reactor configurations will be included in this chapter, and it will help to clarify now that pressure and carrier gas flow are variables only for the CCS reactor, and not the rotating disk reactor.

Table 19: Layer structure for QD test structures analyzed by AFM, XRD, and PL

*pressure and carrier gas flow are variables for material grown on CCS-MOVPE only

Material	Thickness (nm)	Layer	Repeats	Temperature	Pressure* (mbar)	Carrier Gas Flow* (liters per minute)
InAs	1.8 ML	Surface QDs for AFM		460 C	50	14,000
GaAs (HT)	4.6	buffer		580 C	100	6,000
GaAs (HT)	4.6	surface for next QDs	5x	580 C	100	6,000
GaP	1	strain-balancing layer	5x	580 C	100	6,000
GaAs (HT)	3.7	high-temp cap	5x	580 C	100	6,000
GaAs (LT)	3	low-temp cap	5x	460 C	50	14,000
InAs	1.8 ML	QDs	5x	460 C	50	14,000
GaAs	200	buffer		630 C	100	6,000
GaAs	375,000	substrate				

5.2.2 Back surface reflector development

The back surface texture was first developed in GaAs using a 1:1:75 solution of $NH_4OH:H_2O_2:H_2O$, as reported in [14]. Positive photoresist was applied to a 4-inch diameter GaAs wafer and exposed through a dark field photolithography mask with 2 μm spaces separated by 4 μm of chrome, creating a sample as depicted in the first line of Figure 45. The orientation of the mask with respect to the wafer flat was aligned to create a v-groove etch along the length of the 2 μm spaces. The correct orientation depends on if the wafer manufacturer used US (United States) or EJ (European-Japanese) orientation, which are oriented orthogonally to each other, and the major flat is along [01-1] and [0-1-1], respectively [107]. The lines in the mask are aligned perpendicular to the major flat for US wafers, or parallel to the major flat for EJ wafers. Once oriented correctly, an anisotropic etchant can be used to preferentially etch in the <111> direction to create a v-groove etch [108, 109].

The 2-μm-thick lines of exposed GaAs were etched in the 1:1:75 solution of $NH_4OH:H_2O_2:H_2O$ for multiple etch times. Cross-sectional scanning electron microscopy (SEM) images are shown in Figure 46 for 14 minutes, 16 minutes, and 19 minutes etch time. The 14 minutes etch still displays a flat surface at the bottom of the v-groove,

whereas the 19 minute etch exhibits a perfect v-groove in the trenches, however the tops of the v-grooves have been rounded out by undercutting of the photoresist. All etches exhibited a 6 μm period. The 14 minute etch exhibits a 1.6 μm pitch, while the 19 minute etch exhibits a 1 μm pitch.

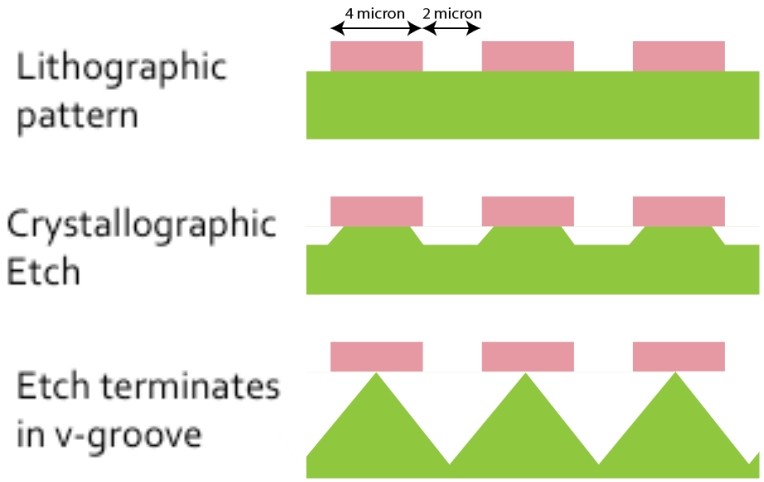

Figure 45: Schematic of lithography and etch process to create back surface texture, where the pink represents protective photoresist and the green is the GaAs substrate.

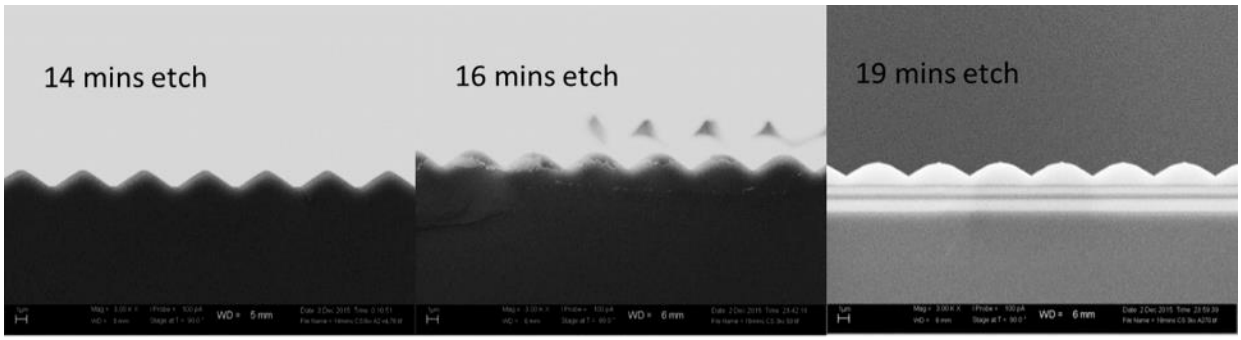

Figure 46: SEM image of textured GaAs: all etches exhibit 6 μm period, 14 minute etch exhibits 1.6 μm pitch, 19 minute etch exhibits 1 μm pitch.

These textures were characterized using a VASE ellipsometer to measure specular reflectance as a function of wavelength, using an angle of incidence = 15° to normal. Reflectance data for multiple etch times is shown in Figure 46. This data indicates that specular reflectance decreases as etch time decreases, which is a useful metric in that it indicates more scattering is occurring. The less specular reflectance a texture exhibits, the longer the corresponding optical path length in a device.

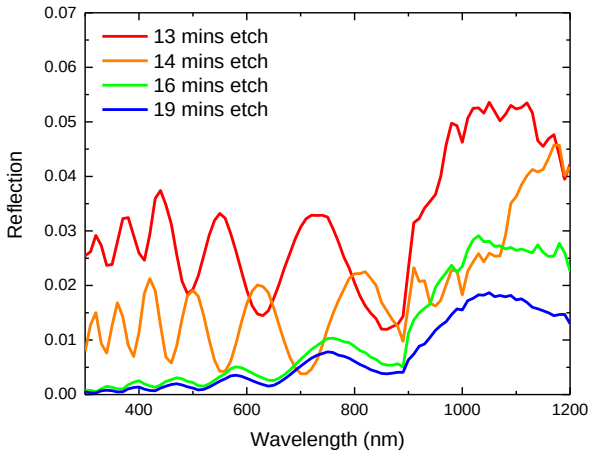

Figure 47: Specular reflectance as a function of wavelength for multiple etch times, using a 15° angle of incidence.

Reflectance was also measured as a function of detection angle, using an angle of incidence = 10° to normal. The measurement setup and data is shown in Figure 47 for the 13 minute etch and the 19 minute etch. The triangular texture (13 minute etch) exhibits more interference fringes as compared to the rounded texture (19 minute etch). The interference fringe frequency observed in this data exhibits significant wavelength dependency, which suggests a diffraction effect occurring off the grating-like periodic texture. Furthermore, the angle for total internal reflection (TIR) in GaAs is 16.6°, and the amount of light reflected below this angle is greater for the rounded texture. More specifically, 15.4% is reflected below the TIR angle for the triangular texture, whereas 39.7% of light is reflected below the TIR angle for the rounded texture.

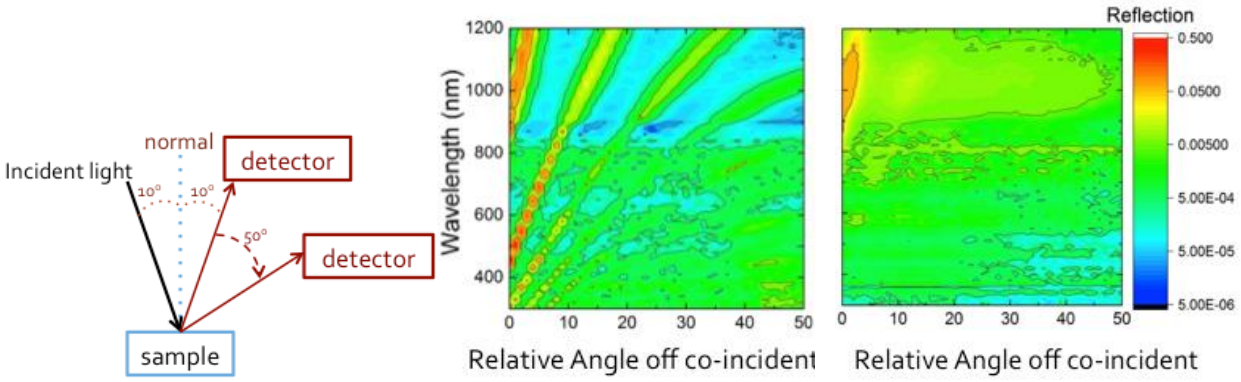

Figure 48: (left) Angle-dependent reflectance measurement setup, (right) Angle-dependent reflectance off the 14 minute etch (left) and the 19 minute etch (right), using a 10° angle of incidence

5.2.3 Device results

5.2.3.1 PIN cells

For the first iteration of QDSCs with back surface reflectors, epitaxial layers were grown in a Veeco D125 rotating-disk MOVPE reactor located at NASA Glenn Research Center. Two *pin* GaAs cells with a 10 layer QD superlattice and two baseline *pin* GaAs cells without QDs were grown inverted on substrates with epitaxial lift off

(ELO) layers. *PIN* cell configurations were grown given the available ELO templates from our collaborator, Microlink Devices, which already incorporated an inverted p-type window and contact layer intended for front metallization after lift off. A basic schematic for the ELO template is shown below in Figure 49. AlAs was used as the sacrificial etch layer to detach the substrate after the rear of the cell has been metallized and attached to a rigid handle. The ELO substrates were 4-inch diameter unintentionally doped (uid) GaAs with a 6 degree offcut towards (110).

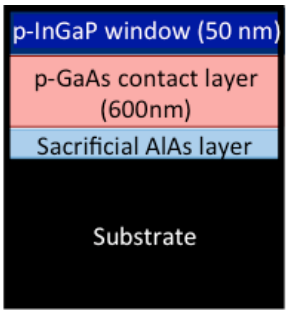

Figure 49: Basic schematic of ELO template provided by collaborators, Microlink Devices

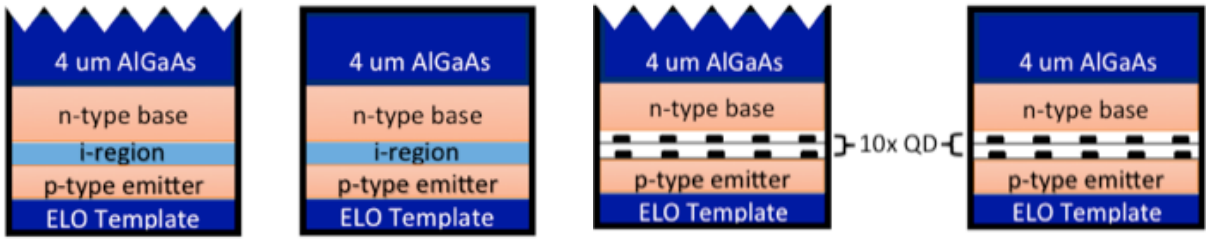

Figure 50: Schematic of GaAs baseline cells and QD cells: one of each has a textured BSR and the other has a flat BSR

Rough schematics for the GaAs cells in this study are shown in Figure 50, while full cell details are reported in Table 20. The cells had a *pin* configuration, with an InGaP window and back surface field. The *pin* design was selected due to the availability of p-type epitaxial lift off templates provided by our collaborator Microlink Devices Inc. The emitter was 500 nm thick and the base was 2000 nm thick in order for the cell to be relatively optically thick. The control cells had a 180 nm i-region which corresponds to the thickness of the 10 layer QD superlattice in the QD cells. The material before and after the QDs was grown at 620ºC, while the QDs were grown at 460ºC and are approximately 1.8 monolayers in height. GaAs QD cell growth on this reactor has been described previously in references [105, 106]. For back patterning, 4 µm of $Al_{0.15}Ga_{0.85}As$ were grown on the back of the cells. One baseline cell and one QDSC were textured with the triangular pattern as a back surface reflector (BSR), leaving one baseline and one QDSC as controls with a flat BSR. All four cells had Cr/Au deposited as the rear reflective material which was then attached to a rigid polyethylene terephthalate handle. The solar cell was then epitaxially lifted off from the substrate by etching the sacrificial AlAs layer in an HF-acid solution. Lithography was applied to the now-exposed front side of the solar cell in order to metallize 0.5 x 0.5 cm^2 cells across the wafer using p-type contact

metallization. Devices were mesa-etched so both the front and back contact were accessible from the front surface of the wafer.

Table 20: Detailed structure of PIN cells: (left) QDSCs, (right) baseline

Material	Thickness (nm)	Type	Doping (cm^{-3})	Layer
GaAs	500	p++	4×10^{18}	Contact
GaAs	100	p+	2×10^{18}	Contact
$In_{0.5}Ga_{0.5}P$	50	p+	2.1×10^{18}	Top window
GaAs	500	p	1.2×10^{18}	Emitter
GaAs	33	i	-	Intrinsic
InAs	1.8 ML	i	-	10x
GaAs (LT)	3	i	-	10x
GaAs (HT)	3.7	i	-	10x
GaP	1	i	-	10x
GaAs (HT)	4.6	i	-	10x
GaAs	33	i	-	Intrinsic
GaAs	2000	n	1.6×10^{17}	Base
$In_{0.5}Ga_{0.5}P$	50	n	2.9×10^{18}	BSF
GaAs	10	n	2×10^{18}	Cap
$Al_{0.15}Ga_{0.85}As$	4000	n	5×10^{19}	Back Contact
GaAs	5	n	5×10^{19}	Cap
Cr/Au	500			Back Contact

Material	Thickness (nm)	Type	Doping (cm^{-3})	Layer
GaAs	500	p++	4×10^{18}	Contact
GaAs	100	p+	2×10^{18}	Contact
$In_{0.5}Ga_{0.5}P$	50	p+	2.1×10^{18}	Top window
GaAs	500	p	1.2×10^{18}	Emitter
GaAs	181	i	-	Intrinsic
GaAs	2000	n	1.6×10^{17}	Base
$In_{0.5}Ga_{0.5}P$	50	n	2.9×10^{18}	BSF
GaAs	10	n	2×10^{18}	Cap
$Al_{0.15}Ga_{0.85}As$	4000	n	5×10^{19}	Back Contact
GaAs	5	n	5×10^{19}	Cap
Cr/Au	500			Back Contact

5.2.3.1.1 QD calibration on 2-inch substrates; QDSCs on 4-inch substrates

After growth of the QDSCs shown in Figure 50, it was noted there had been a discrepancy between the thickness and offcut of the substrates used to calibrate the QDs as compared to the substrates used for the ELO devices. The QDs had been calibrated on 2-inch substrates with a 2 degree offcut, which are typically around 325 μm thick, as shown and described in Figure 44. The ELO templates provided by our collaborators were on 4-inch substrates with a 6-degree offcut, and are typically 675 μm thick. Calibrating QDs on a thinner substrate creates larger dots on thicker substrates because the effective growth temperature is higher. Growth on an increased offcut also results in larger diameter QDs, which alters strain management in the device [105]. Ultimately, this knowledge informed the interpretation of results below.

5.2.3.1.2 Results

The discrepancy described in the previous section resulted in external quantum efficiency (EQE) data from the bulk devices as shown in the inset in Figure 51. Spectral response data was taken with an Oriel IQE200 monochromator and a Stanford Research SR570 preamplified coupled to a SR830 lock-in amplifier. Results for the baseline cells show the material is high quality however the QD devices show degradation in the base. Strain from the increased QD size has resulted in defects propagating through the thick base and causing reduced diffusion lengths, which were fit via a Hovel-Woodall model and are reported in Table 21 [49]. Despite the degraded bulk response, the textured BSR shows increased sub-bandgap absorption as compared to the flat BSR, as shown in Figure 51. By integrating the QE past 880 nm, the short-circuit current (J_{sc}) is calculated to be 0.38 mA/cm^2 for the flat BSR and 0.57 mA/cm^2 for the textured BSR, which represents a 30% increase. Assuming the flat BSR

increases the optical path length (OPL) by a factor of 2, the textured BSR represents an increase in the OPL by a factor of 2.6. However, the flat BSR performances falls short of the predicted sub-band current shown in Figure 3, which implies either non-ideal reflectivity of the rear metal contact, or QD recombination, size, and/or coverage issues. It is evident in the EQE that the textured BSR decreases the degree of destructive interference that occurs from the cavity modes of the light in the thin cell. The decreased amplitude of the fringes in the sub-band EQE data for the QDSC with a textured BSR contributes to the gain in current.

Table 21
Minority Carrier Diffusion Lengths

	Emitter	Base
Flat BSR QD	800 nm	130 nm
Flat BSR Baseline	800 nm	>4000 nm

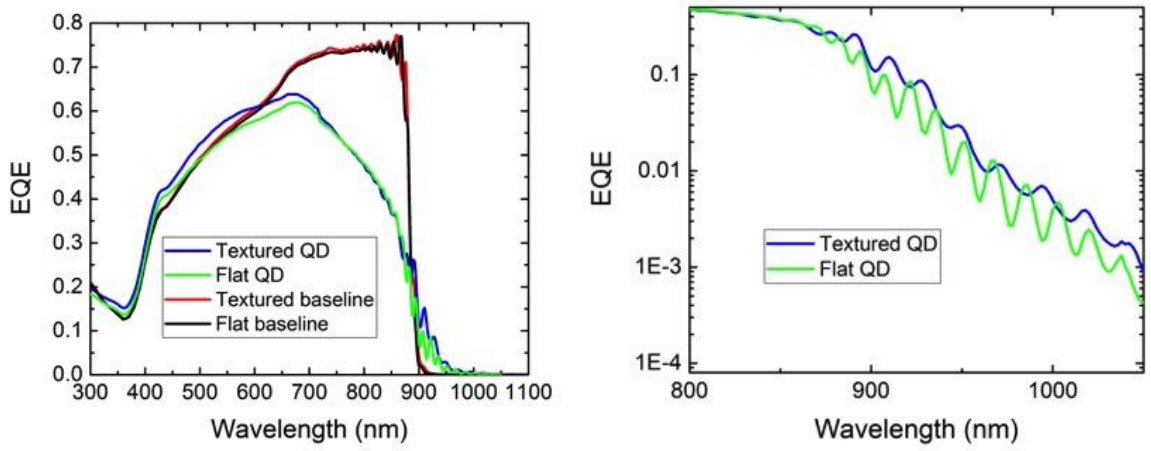

Figure 51: Sub-bandgap EQE for the QD cells: textured BSR shows a 30% increase in absorption compared to flat BSR. Inset: bulk EQE shows base degradation in QD cells as compared to baseline cells.

Electroluminescence (EL) data for each of the cells is shown in Figure 52. Electroluminescence (EL) was measured with Ocean Optics Near-Infrared (NIR512) spectrometer. The strong emission past 1000 nm gives a clear indication of the presence of QDs. The oscillations in the electroluminescence emission exhibit a more regular frequency and result from cavity modes in each of the devices, as opposed to the diffraction fringes observed in Figure 46 which were measured directly off the back side of the texture rather than first traveling through the cavity of a device to a rear texture. The amplitude of the fringes is lower for the textured BSR as compared to the flat BSR, similar to the effect observed in the sub-band EQE. The spacing of fringes from the flat BSR corresponds to a cavity of 6 μm which approximates the device thickness including the BSR. The fringe spacing for the textured BSR corresponds to a cavity of 4.5 μm which is likely occurring at the flat surfaces at the base of the v-grooves, observable in Figure 46. It is possible that the effective cavity depth has some effect on device metrics which could be ascertained by further analysis of the optical absorption in the BSR material or experimental BSR development where AlGaAs is intentionally overgrown to keep the effective cavity constant after etch.

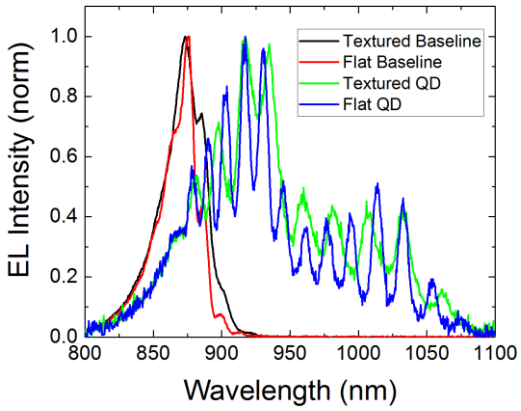

Figure 52: Electroluminescence from the four cells shown in Figure 50: strong emission past 1000 nm indicates QDs in i-region, multiple oscillations correspond to cavity modes and cavity thickness.

5.2.3.2 NIP cells

A second round of devices was grown in order to use optimal QD conditions for 4-inch substrates, which involved decreasing the InAs flow time and adjusting the GaP strain balancing layer accordingly. Details for the growth conditions and structure for these devices are reported in Table 22. Standard precursors were used and diethylzinc and disilane were used as dopants. An *nip* design was intentionally developed and n-type ELO templates were created by our collaborator Microlink Devices, Inc. The *nip* design was specifically chosen in order to facilitate high dopant concentrations (on the order of 1 x 10^{19} cm^{-3}) in the back surface p-AlGaAs layer to enable good contact to the device, since silicon behaves as an amphoteric dopant in n-AlGaAs above ~5 x 10^{18} cm^{-3}. At this point in the project, the 3x2" Aixtron close-couple showerhead MOVPE (CCS-MOVPE) reactor located at RIT had become operational and all following devices were grown on this reactor. GaAs cells with a 10 layer QD superlattice and an InGaP window and back surface field were grown inverted on substrates on top of sacrificial ELO layers and an n-type GaAs contact. The emitter was 50 nm thick and the base was 2000 nm in order for the cell to be an optically thick absorber. The bulk of the cell was grown at 100 mbar, while the QDs and LT GaAs were grown at 50 mbar, as was the p-type InGaP BSF. GaAs QD cell growth conditions have also been described previously in reference [110]. Strain balancing in the superlattice was achieved by growing a 4 nm GaAs spacer on top of the QDs and wetting layer, a layer of GaP with an optimized thickness as described in [106], and another 4 nm GaAs spacer on which to grow the next QDs. For back patterning, 4 μm of AlGaAs were grown on the back of the cells.

A schematic of cells in this study are shown in Figure 53. One cell was fabricated with a flat back surface to act as a mirror, while the other two were textured on the rear surface. All three cells had Cr/Au deposited as the rear reflective material, and was then attached to a rigid polyethylene terephthalate handle. The solar cell was then epitaxially lifted off from the substrate by etching the sacrificial AlAs layer in an HF-acid solution. Lithography was applied to the now-exposed front side of the solar cell in order to metallize 0.5 x 0.5 cm^2 cells across the wafer using n-type front contact metallization. Devices were mesa-etched so both the front and back contact were accessible from the front surface of the wafer. Figure 54 shows cross-sectional SEM images of the rear surface textures on the

cells depicted in Figure 53. The left image represents the 14 minutes etch, which displayed a period of 6 um and a pitch of 2.5 um. The right image is of the 19 minutes etch, which displayed a period of 6 um and a pitch of 2 um. The difference in pitch from the original BSR development may possibly be attributed to the etch rate of 1:1:75 $NH_4OH:H_2O_2:H_2O$ in GaAs versus $Al_{0.15}Ga_{0.85}As$.

Table 22: Growth conditions and solar cell design for NIP back reflector QDSCs

	Thickness (nm)	Type	Doping (cm^{-3})	Layer	Temperature (C)	Pressure (mbar)	Carrier Gas Flow (liters per minute
GaAs	500	n++	6×10^{18}	Contact	630	100	6000
GaAs	50	n+	5.8×10^{18}	Contact	630	100	6000
$In_{0.5}Ga_{0.5}P$	50	n+	3.2×10^{18}	Top window	630	100	6000
GaAs	50	n	1.6×10^{18}	Emitter	630	100	6000
GaAs	33	i	-	Intrinsic	630	100	6000
InAs	1 ML	i	-	10x	440	50	14000
GaAs (LT)	3	i	-	10x	440	50	14000
GaAs (HT)	3.7	i	-	10x	570	100	6000
GaP	1	i	-	10x	570	100	6000
GaAs (HT)	4.6	i	-	10x	570	100	6000
GaAs	33	i	-	Intrinsic	595	100	6000
GaAs	2000	p	5.6×10^{16}	Base	595	100	6000
$In_{0.5}Ga_{0.5}P$	50	p	2.1×10^{18}	BSF	595	50	6000
$Al_{0.15}Ga_{0.85}As$	4000	p	6×10^{18}	Back Contact	595	100	6000
Cr/Au	500			Back Contact	595	100	6000

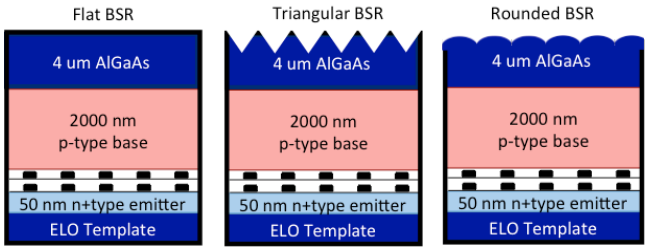

Figure 53: Schematic of GaAs QD solar cells with 3 different back surface reflectors: a flat mirror, a periodic triangular texture, and a periodic rounded texture

QD test structures like those described in Table 19 were grown in order to characterize dot size and density. These test structures were grown with conditions identical to the dots embedded in the cells for this study. Atomic force microscopy (AFM) images were taken of the surface layer of dots and analyzed to calculate a density of ~3 x 10^{10} dots/cm^3, where the average height and diameter were 2 and 21 nm, respectively. The dot size and density are consistent with previously successful studies and exhibit low coalescence which would degrade V_{oc} [12, 101]. Photoluminescence data showed a peak at 870 nm from GaAs, 950 nm from the wetting layer (WL) and emission above 1000 nm from the ground state and excited states of the QDs. These peaks are consistent with previous emission results from InAs dots in GaAs, both experimental and theoretical [12, 15-17, 101, 105, 106, 111, 112].

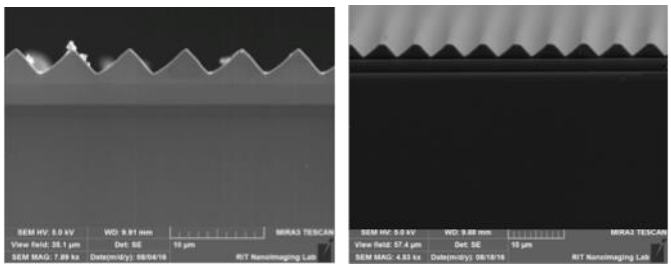

Figure 54: Cross-sectional SEM images of cells after texturing for BSRs: left is "triangular" with 6 μm period and 2.5 μm pitch, right is "rounded" with 6 μm period and 2 μm pitch.

Devices were lifted off and fabricated by collaborators at Microlink Devices, Inc. Spectral response data was taken with an Oriel IQE200 monochromator and a Stanford Research SR570 preamplified coupled to a SR830 lock-in amplifier. EQE data below the GaAs band edge is shown in Figure 55. The sub-band current calculated from integrating the spectral response is tabulated in Table 23. The current from the rounded texture BSR represents a 40% increase over the current from the flat BSR. Assuming the flat BSR corresponds to an optical path length equal to 2, this indicates the optical path length using the rounded BSR approaches 2.8. However, given that an upright cell with no back reflector from a previous experiment showed a sub-band current of 0.26 mA/cm^2, it appears a flat BSR corresponds to less than 2 passes. This may be due to non-ideal reflectivity of the rear metal contact. Furthermore, cavity-mode oscillations are absent from this data which are typically observed in thin devices with BSRs and were present in the previous round of devices [101]. This is another indication that the back contact reflectivity is degraded in some way. It should also be noted that the rounded texture exhibits the greatest EQE near the GaAs band-edge which accounts for its increased sub-band current.

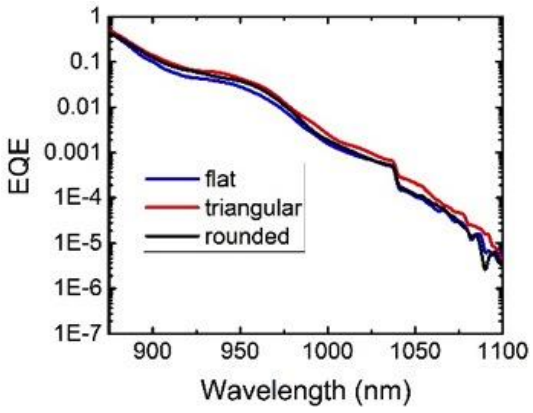

Figure 55: Sub-band EQE from GaAs QDSCs with different back reflectors: rounded texture shows highest EQE near GaAs band edge

Table 23: INTEGRATED SUB-BAND SPECTRAL RESPONSE

Device	Current (mA/cm^2)
Flat BSR	0.43
Triangular BSR	0.53
Rounded BSR	0.60

One-sun AM0 illuminated current-voltage (light I-V) measurements were performed with a two-zone TS Space Systems solar simulator with a Keithley 2440 Source Measure Unit (SMU). The results are shown in Figure 56 and the device parameters are tabulated in Table 24. Short-circuit current (J_{SC}) is expected to follow a similar trend as integrated QE with respect to BSR type, however any statistically significant trend is masked by cross-wafer variability. However, the open-circuit voltage (V_{OC}) increases with increasing back surface texture, which is anticipated due to enhanced photon recycling with an improved back reflector. This can be investigated via injection-current-dependent electroluminescence such as in [113].

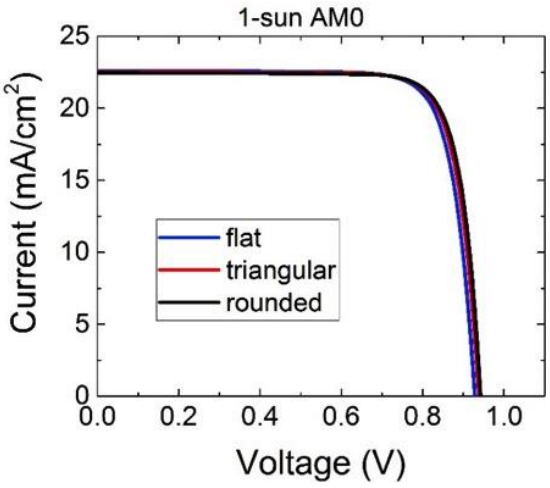

Figure 56: 1-sun AM0 light I-V measurements of *nip* ELO QDSCs with different BSR types: J_{SC} trend masked by cross-wafer variability; V_{OC} trend with BSR type.

Table 24: Light I-V parameters from ELO QDSCs by BSR type

1-sun AM0	J_{sc} (mA/cm^2) Avg (St. Dev)	V_{oc} (V)	FF (%)	Eff (%)
Flat	22.49 (0.26)	0.93	77	11.86
Triangle	22.44 (0.09)	0.94	80	12.38
Rounded	22.36 (0.08)	0.94	81	12.49

5.3 QDSC Design Study

Upright solar cell designs were evaluated to optimize the growth of inverted QDSCs and mitigate potential sources of degradation. The two configurations used for this evaluation are shown in Figure 57. The first configuration is an n+ip solar cell, as shown on the left in Figure 57. Previous studies have shown the n+ip upright cell design is highly sensitive to the inclusion of QDs due to the lower hole lifetime in the n+ emitter caused by residual strain, even with a 100 nm emitter [114]. For this experiment, a 500 nm 10^{18} cm^{-3} n-emitter and 2 µm p-base were selected. This design was intended to clearly show any effects of degradation resulting from the emitter being grown after the QD region, where defects from the strained QDs could potentially propagate upward through subsequent epitaxial material. In this case where the cell is grown upright, this would be seen in the emitter. Three

iterations of this design were grown: 1) a control without QDs, 2) a QDSC, and 3) a second QDSC which was annealed for two hours at 620°C after the growth of the InGaP window under a phosphine flow of 1 mmol/min at a pressure of 100 mbar. The two-hour anneal was intended to assess the impact of high growth temperature for material grown after QDs.

The second configuration was intended to evaluate performance for an inverted growth configuration as would be seen on an ELO device. This configuration maintains the nip polarity but utilizes a nip+ structure, enabling the growth of a 2 µm 10^{17} cm^{-3} n-emitter, as shown on the right in Figure 57. Three iterations of this design were grown: 1) a control without QDs, 2) a QDSC with a 12 nm QD superlattice period, and 3) a second QDSC with a 20 nm QD superlattice period. The device with an increase superlattice period was intended to determine if barrier thickness would mitigate QD-induced degradation of the thick emitter grown after the QDs. This study also provides information about the impact of total material thickness grown after QDs.

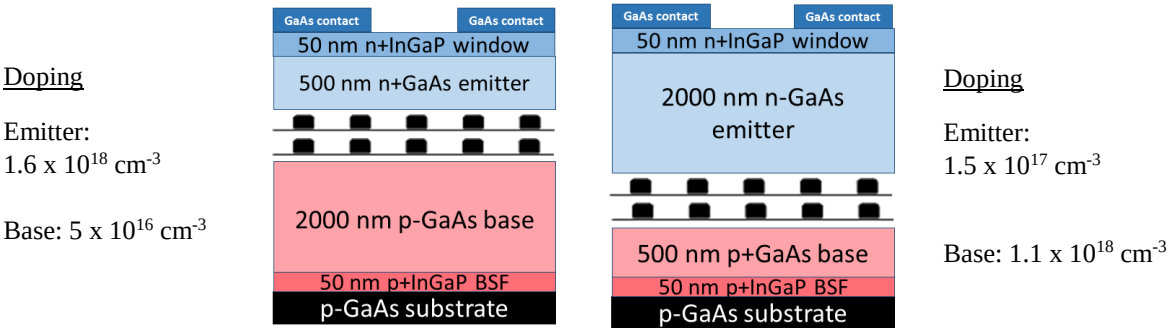

Figure 57: Schematic of upright GaAs designs to evaluate inverted-ELO cell performance. Left design tests thickness grown after QDs and right design tests impact of ELO. A duplicate of the left design was annealed to determine effects of thermal budget, and a duplicate of the right design included thicker superlattice period to determine strain effects from QD region.

Epitaxial layers were grown in a 3x2" Aixtron CCS-MOVPE reactor located at RIT. Six different cells were grown in total. These cells were grown on 2" p-GaAs substrates with a 2 degree offcut towards (110). Growth precursors were trimethylgallium, trimethylindium (TMIn), arsine, and phosphine while disilane and diethylzinc were used as dopants. Material before the dots was grown at 650°C while material after the dots was grown at 620°C. The bulk of the cell was grown at 100 mbar with a V/III ratio of 45, a total gas carrier flow of 6 lpm, and a growth rate of 2 µm/hr. An exception is p-type InGaP, which was grown at 50 mbar, total carrier gas flow of 12 lpm, with a V/III ratio of 95 at 620°C. Growth rate, surface morphology, and strain during growth were monitored by in-situ reflectance and curvature measurements.

QDs were grown at 450°C at a pressure of 50 mbar, a V/III ratio of 80, and a total carrier gas flow of 14 lpm. Specifically, the QDs used a TMIn flow of 1.92 µmol/min, and an arsine flow of 0.15 mmol/min. TMIn and arsine were flowed for 28.6 seconds before a growth pause of 60 seconds, resulting in approximately 2 monolayers of QD height. Strain balancing in the 12 nm superlattice period was achieved as described previously, by growing a 4 nm GaAs spacer on top of the QDs and wetting layer, then a layer of GaP with approximately 1 nm thickness optimized by a similar procedure as described in [106], followed by another 4 nm GaAs spacer on which to grow the next QDs. The 20 nm period used a final GaAs spacer of 12 nm. Each QDSC in this study had 10 layers of QDs in the

superlattice. QD test structures with a 5 layer superlattice and a top layer of QDs were grown in order to characterize dot size, density, photoluminescence and strain. These test structures were grown with conditions identical to the dots embedded in the cells for this study. Atomic force microscopy (AFM) images were taken of the surface layer of dots on these test structures. The density was 4.9 x 10^{10} dots/cm^3, and the average height and diameter were 1.6 and 19.4 nm, respectively. The dot size and density are consistent with previously successful studies and exhibit low coalescence which would degrade V_{oc} [12, 101]. Photoluminescence data showed a peak at 870 nm from GaAs 930 nm from the wetting layers (WL) and emission from 930 to 1053 nm from the QDs. These peaks are consistent with previous emission results from InAs dots in GaAs, both experimental and theoretical [12, 15-17, 101, 105, 106, 111, 112].

EQE measurements of the n+ip devices (referred to henceforth as "5x emitter") indicate that neither the inclusion of QDs nor anneal caused any appreciable degradation of current collection in the emitter, as shown in the inset of Figure 58. No degradation was seen in the EQE of the inverted-design nip+ QDSC, though the inverted-design QDSC with the thicker superlattice shows an increased response over the entire spectral range. This can be attributed to the fact that it is the thickest device, where none of the devices are truly optically thick. Long-wavelength EQE measurements from the four QDSC devices in this evaluation are shown in Figure 58, where 930 nm is the WL and any response above 1040 nm is the QD ground state, while response in between the WL and QD ground state are QD excited states. The integrated EQE below the GaAs band edge (880 nm) for each QDSC is quantified in Table 25. The device with the best light-IV performance on each wafer was measured. Starting with a comparison of the two thin emitter QDSCs, a slight drop in EQE of the QD ground state (around 1050 nm) is seen, but with no change in wetting layer or excited state response. This is reflected in the integrated EQE where the standard thin emitter QDSC has sub-bandgap current collection of 0.27 mA/cm^2 while the thin emitter QDSC with anneal has sub-band current of 0.25 mA/cm^2. This demonstrates anneal to have a deleterious effect on the QDs.

Table 25: SUB-BANDGAP QDSC RESPONSE

Device	Sub-880 nm Integrated EQE (mA/cm^2)
5x emitter	0.27
inverted-design	0.26
5x emitter + anneal	0.25
inverted-design & 20nm period	0.28

The inverted-design QDSC exhibited a sub-band response of 0.26 mA/cm^2 which is lower than the 5x emitter QDSC. This is consistent with the expectation that thermal budget has a slight impact on QD response, given that the inverted-design QDSC had a longer growth time at high temperature after the QDs. Lastly, the inverted-design device with increased superlattice period shows a drastic drop in QD ground state transition and a decrease in EQE of deeper excited state transitions, suggesting that carrier escape from QDs via tunneling is suppressed. However, the inverted-design device with the increased period has the greatest sub-band current 0.28 mA/cm^2, which may be due to enhanced thermal escape and could be analyzed by temperature-dependent photoluminescence.

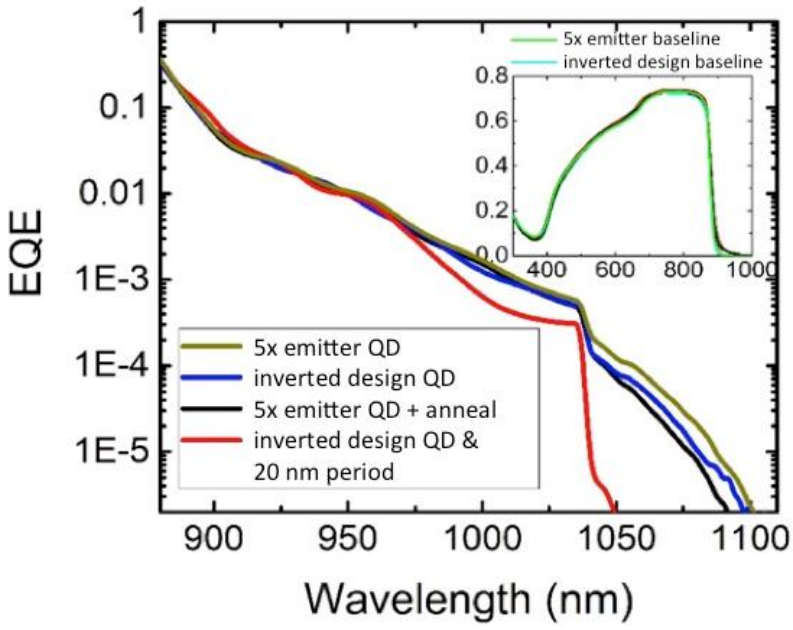

Figure 58: Sub-bandgap EQE for the QD cells in the evaluation study: inverted-design QDSC and annealed 5x emitter QDSC show similar QD response; inverted-design with thick barriers shows little to no QD response. Inset: bulk EQE similar between baselines and QDSCs.

Figure 59 shows one-sun AM0 IV characteristics from the 5x emitter devices without an anti-reflective coating (ARC). One-sun AM0 illuminated current-voltage (light I-V) measurements were performed with a two-zone TS Space Systems solar simulator with a Keithley 2440 Source Measure Unit (SMU). The control cell without QDs had a V_{OC} of 1.01 V, while the QDSC without anneal had 0.985 V, exhibiting less than a 30 mV (2.8%) drop. The QDs in the 5x emitter devices contribute a 2.5% relative enhancement in short-circuit current (J_{SC}), which is almost double the amount predicted by integrated sub-band EQE. This is slightly less than published J_{SC} enhancements around 3-3.5% for a 10 layer QDSC [12, 115]. The QDSC fill factor (FF) was slightly lower, but this is within the range seen due to process variation. The two-hour anneal, simulating the thermal budget of a longer growth, did not degrade device characteristics.

Figure 60 shows the AM0 IV results of cells grown in the inverted-design configuration without an ARC. The baseline inverted-design cell had a 30 mV higher V_{OC} than the 5x emitter baseline due to a reduction in dark current. However, the inverted-design baseline suffered from a low FF which is thought to be due to increased series resistance from variations in contact metallization rather than cell design, since both QDSCs had higher fill factors.

The inverted-design QDSC appears to be more sensitive to V_{OC} degradation even though the V_{OC} is only 10 mV lower than that of the 5x emitter QDSC, but represents a 6.9% drop as compared to the inverted-design baseline. This trend is not unsurprising given that the majority of the device is grown on top of the QD region in the inverted-design. However, increasing the superlattice period increases the V_{OC} of the device to nearly one volt, comparable with the highest reported QDSC open circuit voltages [115]. The intent of using a thicker superlattice period was to determine if it could enhance material quality in the device grown after the QD region by suppressing threading

dislocations, which occur when coalesced QDs are present [12]. Dark-IV measurements could reveal information about Shockley-Read-Hall recombination occurring from dislocations in the i-region.

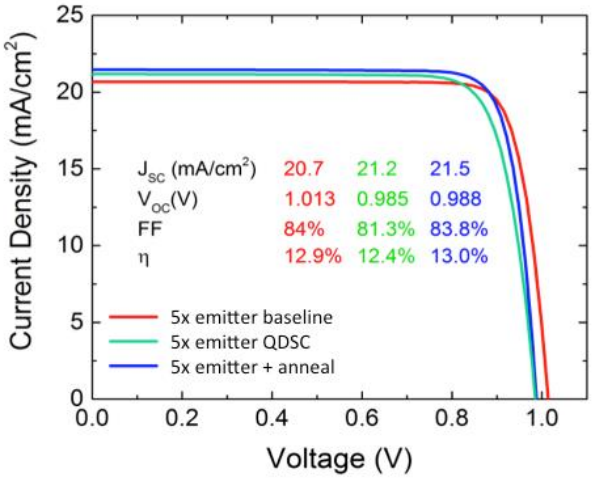

Figure 59: 1-sun AM0 light-IV of 5x emitter cells: QDSCs show a minor decrease in V_{oc} with a substantial increase in current.

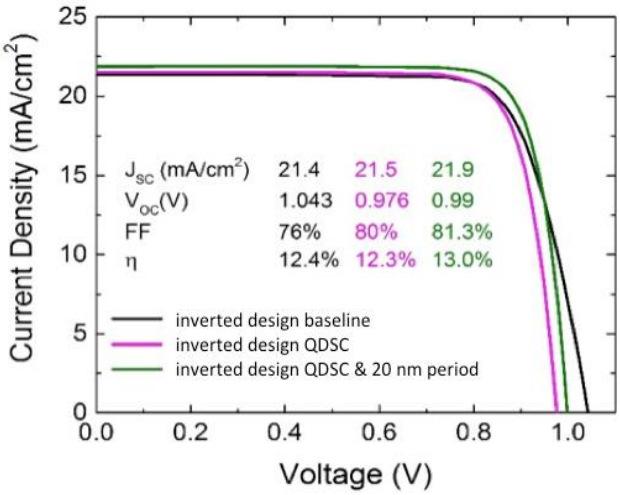

Figure 60: 1-sun AM0 light-IV of inverted-design cells: the device with thick barriers shows improvement in open-circuit voltage compared to the standard inverted-design QDSC.

The upright QDSC designs evaluated for inverted growth of ELO devices did did not expose a specific advantage for QD response in either the n+ip or nip+ configuration, though it can be concluded that anneal has a minor effect on emission from QDs and increased period thickness in the superlattice severely limits collection from QDs. The n+ip QDSC proved to be more robust in terms of V_{OC} degradation even though the nip+ control had a higher V_{OC} than the n+ip control, while the nip+ QDSC with an increased superlattice period had the highest QDSC V_{OC}.

5.4 Two-dimensional and random back surface reflectors with dielectric interlayer

5.4.1 Development of 2-D textures

The second approach used a Heidelberg DWL66+ direct write laser lithography system to write a mask directly onto AlGaAs. This provides the capacity to iteratively test multiple 2-D patterns without the need for expensive mask making. The initial patterns investigated are shown in Figure 61, which include checkerboard patterns with multiple sizes, and patterns of squares with varied spacing referred to as "alleyways". The first few rounds of exposure and development proved that squares smaller than 4 x 4 μm did not retain a uniform pattern with a significant degree of coverage, therefore only 4 μm squares were investigated going forward. Samples for pattern testing were 4 μm thick layers of $Al_{0.15}Ga_{0.85}As$, and were coated with s1827 photoresist for exposure.

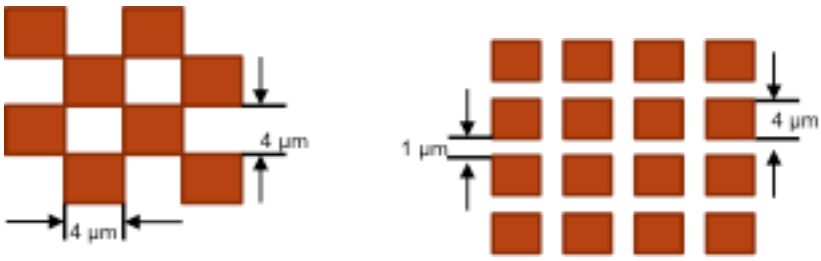

Figure 61: (left) checkerboard photoresist mask design (right) alleyway photoresist mask design

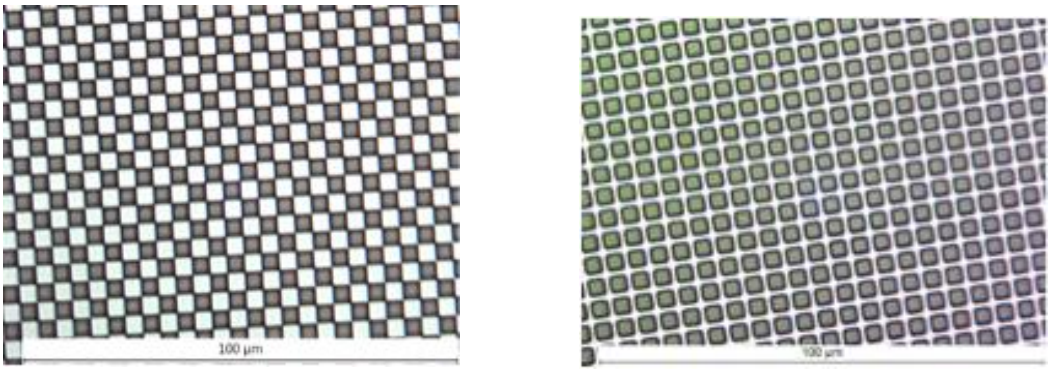

Figure 62: Nomarski contrast micrograph of photoresist patterns after exposure/develop, and before etching and photoresist strip – (left) checkerboard, (right) alleyway

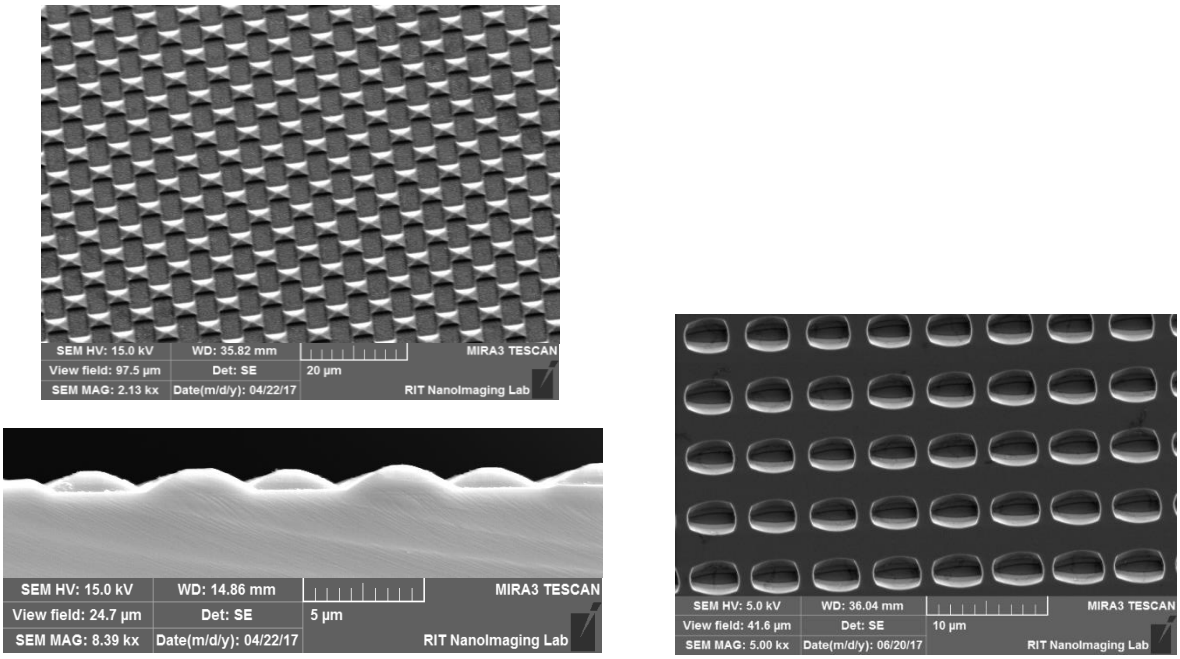

Figure 63: SEM images of (left) checkerboard pattern (including cross-section) and (right) alleyway pattern after 10-minute etch

Images of the photoresist after it was exposed and developed for each of the mask designs are shown in Figure 62. These samples were then etched in the 1:1:75 solution of $NH_4OH:H_2O_2:H_2O$ used for BSRs developed previously, and an optimal etch time of 10 minutes was determined by a separate etch-time study. SEM images of the samples after etch and photoresist removal are shown in Figure 63. Finally, reflectance measurements were taken as a function of detection angle, using an angle of incidence = 10° to normal and are shown in Figure 64. Where the angle of total internal reflection is 16.6° in GaAs, 40% of light is reflected below this angle for the checkerboard pattern while 39% is reflected below this angle for the alleyway pattern. For this reason, devices were chosen to be fabricated with the checkerboard pattern rather than the alleyway pattern.

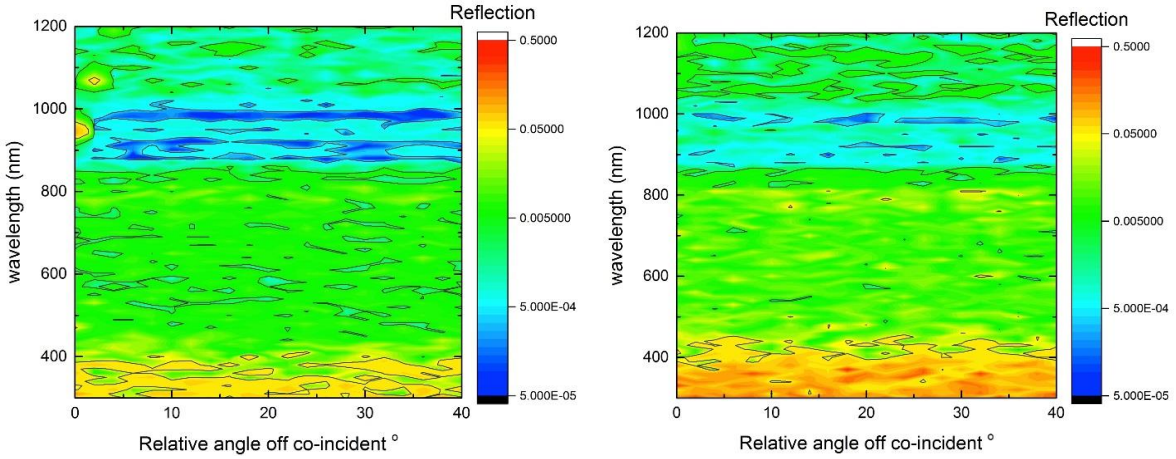

Figure 64: Angle-dependent reflectance measurements with angle-of-incidence = 10° for checkerboard pattern (left) and alleyway pattern (right)

5.4.2 Dielectric on BSR texture

In an effort to enhance the benefits of a BSR, the insertion of a dielectric between the textured back surface of GaAs cell and the reflective metal contact was simulated using the transfer matrix method and TFCalc™ software. The results are shown on the left of Figure 65, where significant benefits are observed for a textured BSR due to enhanced reflectivity of the rear metal. The insertion of a dielectric was also simulated using Synopsys® RSoft FullWAVE™ and Synopsys® Sentaurus™ TCAD for electromagnetic and device simulations, respectively. The results are shown on the right side of Figure 65, where significant benefits are observed for a textured BSR, particularly for a thinner cell. This has been experimentally demonstrated in [14]. However, due to the ELO process in this study, any oxide or dielectric could be attacked during the lift off etch. The lift off process uses hydrofluoric acid (HF) to selectively etch an AlAs layer between the substrate and the thin, inverted device. HF would attack any oxide or dielectric; and even though back-side metal is deposited on the rear of the inverted solar cell before lift-off, simply depositing the oxide before the metal would leave the oxide exposed at the edges and would laterally etch, similar to the mechanism of the AlAs release layer.

To circumvent this, a process was developed to selectively remove the oxide around the perimeter of any given sample and at regular points across the texture by protecting the oxide with photoresist, exposure using a mask with a grid of 2 mm x 2 mm squares spaced 1 cm apart, and then etching the exposed oxide in HF. The photoresist can then be removed, and metal deposited for rear contact to the devices. The metal needs to be intentionally deposited to be greater than 500 nm thick in order to protect oxide sidewalls.

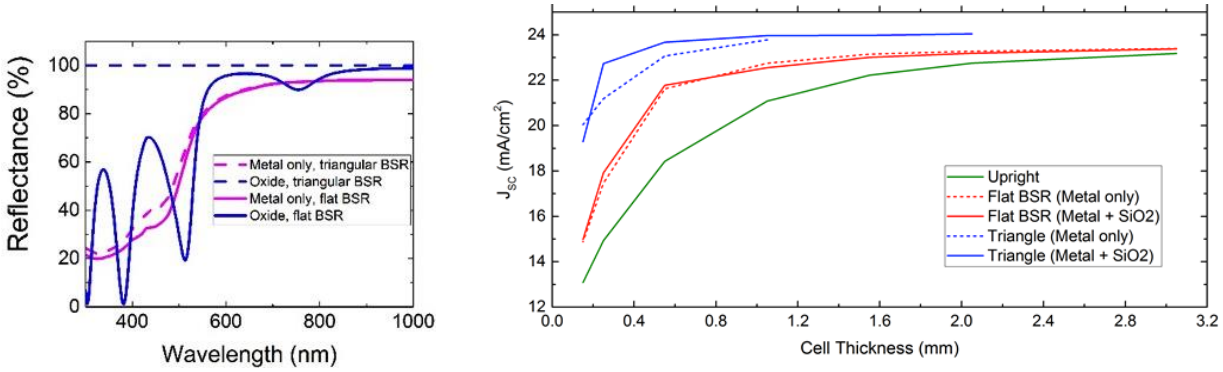

Figure 65: (left) Simulation of reflectance for different back surface configurations. Use of a dielectric significantly enhances reflectance from a textured BSR. (right) Simulation of GaAs cell performance as a function of cell thickness, for different back surface configurations. Use of a dielectric enhances cell performance with a textured BSR.

5.4.3 Device results

QDSCs were grown inverted on ELO templates, identical to the cell structure reported in Figure 53, with the exception of the 2-D back reflector texture in place of 1-D triangular or rounded textures. The set of devices in this study are shown in Figure 66. One device had a flat BSR to serve as a control, a second had the checkerboard

pattern, and the third had 450 nm of SiO_2 deposited on top of the checkerboard pattern. The oxide was then selectively removed around the perimeter of the wafer and at regular points across the texture by protecting the oxide with photoresist, exposure using a mask with a grid of 2 mm x 2 mm squares spaced 1 cm apart, and then etching the exposed oxide in HF. The photoresist was then removed, and metal was deposited for rear contact to the devices. The metal was intentionally deposited to be greater than 500 nm thick in order to protect oxide sidewalls. The devices were fabricated by collaborators in a process identical to what has been described previously in section 5.2.2.2.

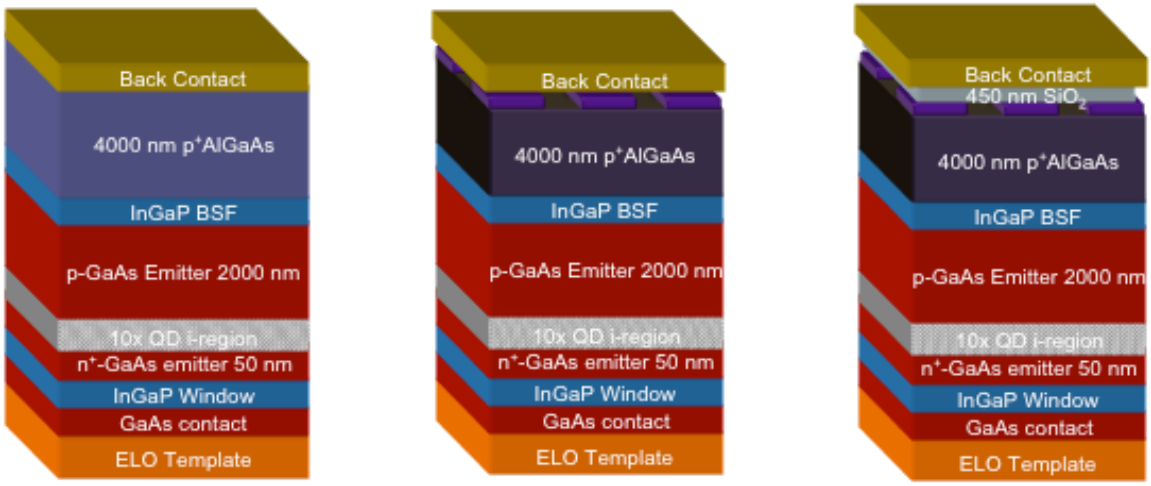

Figure 66: Schematics of QDSCs to evaluate performance of 2-D back reflector texture and dielectric interlayer

Device results are shown in Figure 67, and are overlaid with device results from section 5.2.2.2 for direct comparison. The dielectric layer in the third sample proved not to be sufficiently protected and disintegrated during the ELO process. The other two samples also disintegrated to a significant degree, but device testing was still possible. The degradation is visible in the light I-V results shown on the left in Figure 67, while sub-band EQE is shown on the right. The integrated sub-band QE current densities are reported in Table 26. The checkerboard texture not only represents a 19.6% increase over the control in this study, and also represents a sub-band current increase over the rounded BSR results from section 5.2.2.2, which follows the expectation that a BSR that varies in more than one dimension would out-perform a BSR that only varies in one dimension.

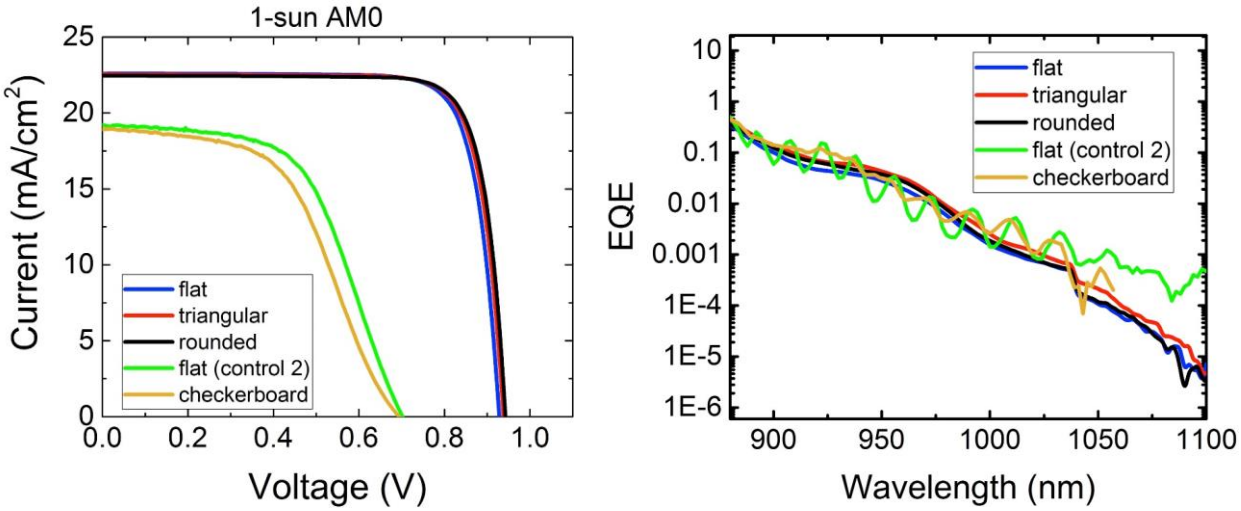

Figure 67: 2-D BSR device results (left) light I-V and (right) sub-band EQE overlaid with NIP cell results from section 5.2.2.2. "Control 2" refers to the flat BSR cell fabricated simultaneously with the checkerboard cells as a control, as compared to the flat BSR cell fabricated simultaneously with the triangular & rounded BSR cells.

Table 26: SUB-BANDGAP 2-D BSR QDSC RESPONSE

	Sub-880 nm int. QE (mA/cm^2)	**Optical Path Length**
No BSR (prior experiment)	0.26	1
Flat	0.43	2 (assumed)
Triangular	0.53	2.46
Rounded	0.60	2.79
Flat (2)	0.56	2 (assumed)
Checkerboard	0.67	2.39

5.4.4 Random texture

In order for the optical path length to approach the Lambertian limit of $4n^2$ (where n is the refractive index of the material) it will be necessary to have a back surface texture that varies in more than one direction. The theoretical maximum increase for the OPL is a factor of 36 for GaAs, which would require a more random texture than those developed previously in this section [18]. A maskless crystallographic etch to achieve a random texture has previously been demonstrated in GaAs in [102]. This texture must be replicated in AlGaAs in order to allow photon recycling in GaAs as well as QD absorption enhancement. Multiple etch times, temperatures, and concentrations were tested and resulted in little to no observable texture, with the exception of the conditions described below. This indicates that the conditions for crystallographic etch are extremely sensitive to these parameters. The etch that created the texture shown in Figure 68 was 1:4:40 NH_4OH:H_2O_2:H_2O at 2.5°C for 30 minutes, which is an

anisotropic etchant where the etch speed is dependent on the crystal orientation. This is a promising result that should be integrated into devices for testing in future work.

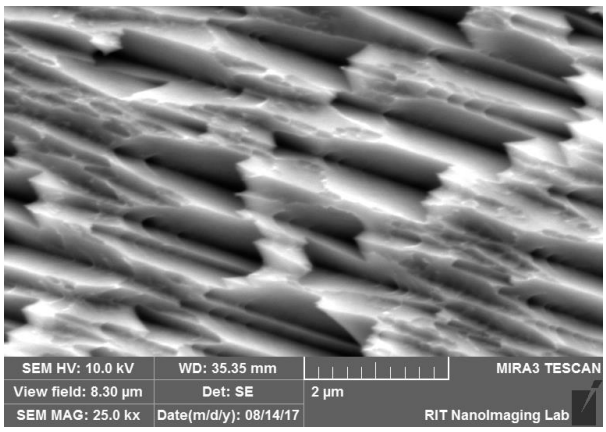

Figure 68: SEM image of random texture achieved in GaAs by maskless etch 1:4:40 $NH_4OH:H_2O_2:H_2O$ at 2.5°C

5.5 Conclusions

A texture similar to that which was executed as a back surface reflector in GaAs for quantum well solar cells [14] has been developed in $Al_{0.1}Ga_{0.9}As$ for application to quantum dot solar cells. This texture varied in one dimension across the back surface of the device and is created using a photoresist pattern and a crystallographic etchant. Variations in etch time produce slight differences in texture which decrease the proportion of light that specularly reflected and increase the proportion of light that is reflected at angles below the critical angle for total internal reflection.

In order to fabricate QDSCs with this back surface texture, devices were grown inverted on epitaxial lift off templates, the texture was applied, and then the devices were lifted off and fabricated by collaborators at Microlink Devices, Inc. who holds the intellectual property rights on the ELO process. Two sets of *pin* devices were grown in order to compare a flat back surface reflector to a textured back surface reflector (BSR). The device results show significant benefit from the use of a textured back surface reflector, where sub-bandgap absorption increased by 30% using the textured BSR as compared to a flat BSR. Interference fringes in the EQE and EL data indicate a reduced effect of destructive interference in the cavity modes when comparing the textured BSR to the flat BSR as well as a decreased effective cavity thickness.

A second round of devices were grown with optimized QD conditions and used an *nip* configuration to enable a better back contact through highly doped p-type AlGaAs. These devices compared a flat BSR to two different textures created by varying the etch time. The open circuit voltage was greater for the two sets of devices with the textured BSRs than the flat BSR, which indicates a greater degree of photon recycling. The longest etch time show the greatest sub-band current, representing a 40% increase over the flat BSR.

Upright QDSC designs intended to evaluate inverted growth of ELO devices did not expose a specific advantage for QD response in either the n+ip or nip+ configuration, though it can be concluded that anneal has a minor effect on emission from QDs and increased period thickness in the superlattice severely limits collection from QDs. The n+ip QDSC proved to be more robust in terms of V_{OC} degradation even though the nip+ control had a higher V_{OC} than the n+ip control, while the nip+ QDSC with an increased superlattice period had the highest QDSC V_{OC}.

Next, a texture that varies in two dimensions across the surface of the device was developed in order to increase the optical path length further. This texture followed a similar procedure to the one-dimensional texture described above. Additionally, a procedure for coating the texture with a dielectric (while also making contact to the device) was developed in order to increase the reflectivity of the rear contact metal. A set of QDSCs were grown inverted on ELO templates, where one was left with a flat back surface as a control, a second was textured with the two-dimensional pattern, and the third was also textured with the two-dimensional pattern and also included a dielectric interlayer. Ultimately, the ELO process destroyed the sample with the dielectric layer due to the selective ELO etchant, but the remaining two-dimensional BSR devices showed a 20% sub-band current improvement over the control devices with flat BSRs. Finally, a maskless crystallographic etch that has been studied for GaAs was optimized for AlGaAs so that a more random texture could be achieved in order to increase the optical path length even further. Characterization of this texture and testing on fabricated devices should be executed in future to further enhance the optical path length in this material system.

CHAPTER 6: Life cycle Assessment of III-V Multijunction Cells

6.1 Motivation

III-V multijunction photovoltaic cells have historically shown the highest power conversion efficiencies of any PV material or cell design [116], but are very expensive as well [3]. For space applications, the radiation tolerance and high power density of III-V photovoltaics is enough to compensate for the high material costs, given the alternative of launching a heavier payload if less efficient cells were used [117]. Terrestrially, however, III-V photovoltaics are typically only viable in concentrator applications, where less of the expensive III-V material can be used in combination with glass lenses for the same power output. This also results in a stronger overall life cycle performance, where glass and steel replace what would otherwise be larger areas of heavily engineered III-V photovoltaic material. Furthermore, cell efficiency increases with concentration, which introduces further economic and environmental benefits to system performance.

A limited number of life cycle analyses of high concentration photovoltaic (HCPV) systems containing multijunction III-V photovoltaic cells exist to date. So far, only the InGaP/InGaAs/Ge stack has been explicitly studied as part of concentrator systems [21-23, 25, 118-124]. Existing literature concludes that gains in cell efficiency will only make a stronger environmental case for the concentrator photovoltaic technology [22]. Improved life cycle performance might be achieved assuming that the cell stack stays the same and the manufacturer acquires gains in material quality. However, another option would be to deploy an alternative cell stack, such as the novel designs under development in this dissertation, or other next-generation high-efficiency designs under development for space applications.

Advanced photovoltaic designs improve cell efficiency by incorporating additional junctions or new materials like the design proposed for the work in Chapters 3 and 4, and can often require the use of additional substrates or processing techniques like the cell features investigated in Chapter 5. This implies further material and energy usage during the cell manufacturing stage as compared to the triple-junction industry standard mentioned previously. By conducting a life cycle assessment (LCA) of HCPV systems containing advanced photovoltaic designs, this study attempts to determine if there is a point at which the cell manufacturing process becomes too energy-intensive or impact-intensive such that improvements in cell efficiency no longer correlate to improvements in the overall life cycle of the HCPV system. This could manifest as a comparative increase in energy payback time, or a net increase in the greenhouse gas emissions of the HCPV system over its operational lifespan.

Previous HCPV LCAs report anywhere from >1% to up to 15% of the system's cumulative energy demand (CED) can be attributed to manufacturing the cell itself [21-23]. The tracking system manufacturing process is frequently reported as the most energy-intensive aspect of the concentrator life cycle, literature reports it is responsible for 25% to 42% of CED. In one study, this is comparable to the contribution of the heat sink to CED (26%), but in all other studies the tracking system bears the most responsibility by far. However, all of these studies employed liberal assumptions and approximations concerning the MOVPE manufacturing process, which involves specialty chemicals and components whose manufacture is proprietary in nature. Given the wide discrepancy between previously published results, this study intends to provide a more precise figure on the contribution of the

cell manufacture to the overall life cycle of the HCPV system. This is achieved by extensive data collection and process modeling of the cell growth and fabrication process, based on patents as well as empirical data in a level of detail heretofore unavailable in literature. Ultimately, the implication of this research would be to inform the community of the potential trajectory of terrestrial concentrator photovoltaics development. This study will examine a range of cell types to determine which are environmentally viable options within terrestrial concentrators. Additionally, it can inform design considerations by highlighting which aspects to focus on when attempting to improve the overall life cycle performance of HCPV.

6.2 Methods

6.2.1 Goal, Scope, and System Description

This LCA aims to accomplish two goals simultaneously: 1) provide more accurate life-cycle data for the MOVPE precursors and substrates used to create the PV cells, and 2) identify if there is a point at which III-V photovoltaic cell manufacturing becomes too energy-intensive or impact-intensive such that improvements in cell efficiency no longer correlate to improvements in the overall life cycle of a given HCPV system. This will be achieved by detailed modeling of the III-V cell growth process for a range of advanced cell types with higher efficiencies than what is commercially available today. This information would enable the photovoltaics community to not only identify which III-V cell types are environmentally viable in terrestrial applications but also to identify which aspects of the cell manufacturing process are the most impact-intensive, which could then be the focus of efforts to improve environmental performance.

The system diagram for this LCA is shown in **Figure 69**. This diagram illustrates the inputs and outputs from/to the natural world and technosphere indicated by the dashed line around the four life cycle stages that will be considered in this LCA. This LCA represents a cradle-to-use LCA, encompassing material acquisition, manufacturing, installation, and operation/maintenance. The end-of-life stage for HCPV is excluded in this study given the limited data on HCPV end-of-life scenarios, due to the long lifespan of HCPV systems and unknown disposal/recycling options for the materials in this system. The manufacture of facilities and equipment are excluded from this LCA as they are assumed to have long lifetimes such that their impacts become marginal by being distributed over large quantities of output over a long timeframe. The manufacturing stage is expanded to show the breakdown of components of the HCPV system, particularly the PV module. The PV module is expanded to illustrate the origin of the reference flow in the HCPV system, attributed to the photovoltaic cell and their corresponding maximum efficiencies that occur under 500 suns concentration. In order to compare cells of different efficiencies, the functional unit is defined as 1 kW_p of HCPV modules for a given cell type. The life cycle model has been constructed using PRé Sustainability software SimaPro, version 8.1 and the ecoinvent 3.4 database [125].

The first goal of this study seeks to provide an accurate value for cell production impacts, while the second goal aims to establish a relationship between the cell impact relative to the system impact as a function of cell type. As a result, sources of uncertainty in the LCA will impact each of these goals differently. The first goal requires that all data be as certain as possible, while also reflecting realistic variability in material production and processing steps.

With regards to the second goal, sources of uncertainty which are consistent across cell types will be less significant and can be bounded by establishing a best-case and a worst-case scenario. However, the results of the first goal will be fed into the model for second goal, so some of the same issues with uncertainty will be carried over. The methods to address each type of uncertainty for either goal are explained in the subsequent Interpretation section.

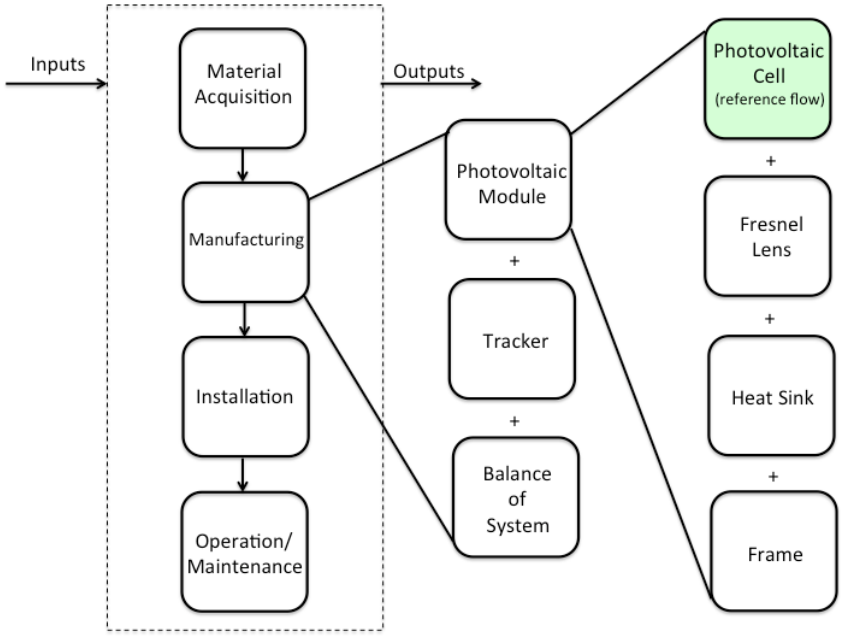

Figure 69: HCPV Life Cycle System Diagram

The cell structures that will be studied are shown in Figure 70. These cell types were chosen to represent the increases in efficiency that are possible with the addition of material and/or energy. The first cell type is the industry standard which has already been deployed on a commercial level and was introduced in Chapter 1 for illustrative purposes. The second cell is the triple-junction design that provided the basis for the research in Chapters 3 and 4. The third cell was chosen to represent the most material-intensive cell in this study, as it has five junctions that are grown on two different substrates before being bonded together. Finally, the fourth cell was chosen to represent the most energy-intensive design in this study, since it has six junctions which results in the tallest cell stack and corresponds to the longest reactor operation time.

As described previously, cell 1 is an all lattice-matched InGaP/InGaAs/Ge stack grown on a germanium substrate [2]. The module efficiency for this triple junction (3J) cell type is known to be 37% at 500 suns based on empirical data [22]. Cells 2 through 4 have yet to be commercially deployed, so certain assumptions and approximations will be made as described below. Cell 2 is the InP-based triple junction that has been the subject of prior chapters. No experimental demonstration has been achieved to date, so the theoretical figure of 52.8% efficiency under 500 suns AM1.5 will be scaled to approximate module-level efficiencies as described below. Cell 3 is a combination of two lattice-matched structures, a GaAs/AlGaAs/AlGaInP stack grown lattice-matched on a

germanium or GaAs substrate, and an InGaAsP/InGaAs stack grown lattice matched on an InP substrate. The two lattice-matched structures are bonded together at the top surface, the substrates are removed, and the structure is transferred to a support. This process is known as wafer bonding. The completed 5J structure is expected to achieve an efficiency of 46.7% under 500 suns, and has experimentally demonstrated a 1-sun AM1.5 efficiency of 37.8% [126]. Cell 4 represents an inverted metamorphic (IMM) growth technique, where the cell is grown inverted on a germanium or GaAs substrate, then substrate is removed and the stack is transferred to a support on the opposite side. The first three layers are lattice-matched to the substrate (AlGaInP/AlGaAs/GaAs) and the remaining three layers are grown on top of thick, metamorphically graded buffer layers. In this case, three active InGaAs layers are grown on top of thick InGaAs layers where the indium content gradually increases in order to expand the lattice.

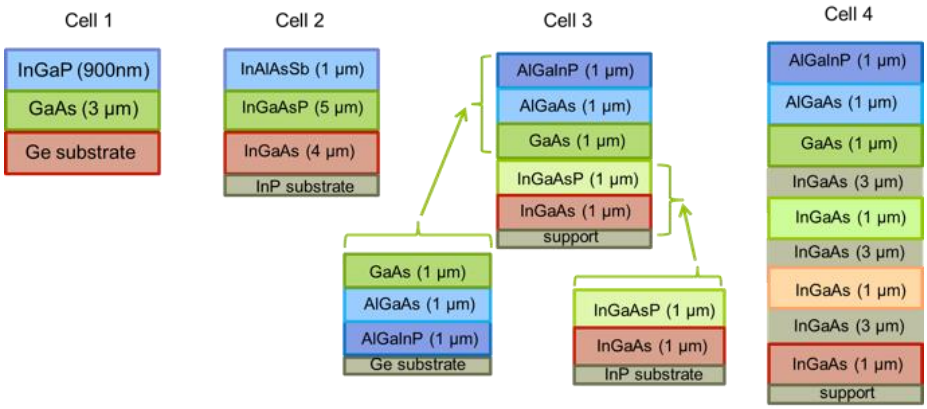

Figure 70: Photovoltaic cell designs compared within LCA. Cell 1: 3J industry standard on Ge; cell 2: novel 3J on InP; cell 3: wafer-bonded 5J; cell 4: 6J IMM.

The efficiencies and power output for each cell at its optimum concentration are reported in

Table 27. If experimental module efficiencies were unavailable, efficiencies were calculated by taking the best laboratory cell efficiency measurements (or theoretical values) and decreasing by 20% to approximate the efficiency losses observed when switching to commercial scale production of modules, and then including another 7% loss to reflect total system efficiency **[22]**.

Table 27: Cell/module/system efficiency, power output, and reference flow (cell area required for functional unit 1 kWp)

500 suns AM1.5D (50 W/cm^2)	Cell 1 **[22, 127]**			Cell 2 **[4]**			Cell 3 **[126]**			Cell 4 **[36, 128]**		
Efficiency cell, theoretical | module | system	50%	37%	30%	52.8%	42.2%	35.4%	n/a	47%	40%	n/a	50%	43%
Power (system efficiency)	15 W/cm^2			17.7 W/cm^2			20 W/cm^2			21.5 W/cm^2		
Cell area for 1 kWp (cm^2)	66.7 cm^2			56.5 cm^2			50 cm^2			46.5 cm^2		

6.2.2 Inventory

A general overview of the manufacturing differences for each cell will be presented, and then the inventory will be discussed in the order of process flow shown below in Figure 71. The life cycle inventory data in the following sections was generated based on available inputs in the ecoinvent 3.4 database [125]. If a given input was not available in the ecoinvent database, additional research was required to either model an upstream process or select an appropriate material for substitution. Manufacturing processes were initially researched by conducting a thorough patent review, and similarities between patents were identified to assess the prevalence of a given synthesis technique. Companies holding these patents were contacted to discuss further details, though dialogue was often limited due to the proprietary nature of manufacturing. In the absence of industry data, electricity demand was often estimated from power ratings of commercially available equipment (cited throughout input-output tables in the Appendix) and corroborated by existing LCAs that model similar equipment [129, 130]. Specific model values, assumptions, and sources for all inventory data are provided in the Appendix section of this dissertation.

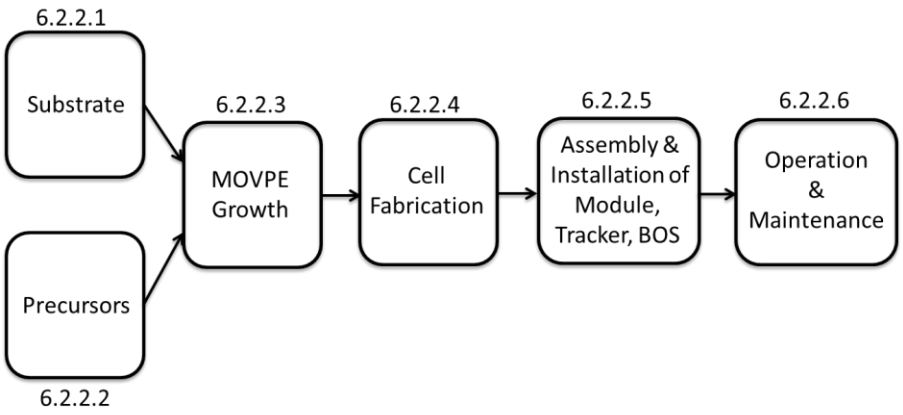

Figure 71: HCPV System Manufacturing Process Flow

Cells are grown in an MOVPE reactor, which requires a substrate and metal organic precursors for epitaxial growth as described in Chapter 2 of this dissertation. As mentioned previously, in order to achieve the first goal of the LCA, this study investigates the manufacture of metal organic precursors and III-V substrates in more detail. An inventory of the material in each cell is presented first. Based on the layer thicknesses shown in Figure 70, the total mass of each element in each cell type is reported in Table 28 as well as the total mass of the substrates consumed (assuming no substrate reuse). Given that InP substrates are only commercially available up to 4 inches (100 mm) in diameter, while GaAs and Ge are available in 6-inch (150 mm) diameter, the metrics are reported as milligrams per cm^2 to form an accurate comparison. InP and GaAs substrates larger than 2 inches (50 mm) in diameter are typically 625 μm thick, while Ge substrates are typically 175 μm thick [131].

Table 28: Material usage for each cell type, active layers and substrate listed separately

	Cell 1 (mg/cm^2)	Cell 2 (mg/cm^2)	Cell 3 (mg/cm^2)	Cell 4 (mg/cm^2)
In	0.20	2.3	0.69	1.7
Ga	0.66	3.5	1.5	2.5
Al	--	0.07	0.04	0.04
As	0.59	1.7	1.3	3.6
P	0.10	0.23	0.15	0.10
Sb	--	0.31	--	--
Ge substrate	930	--	--	--
InP substrate	--	3000	3000	--
GaAs substrate	--	--	3300	3300
SUM	**932**	**3008**	**6304**	**3308**

The substrates necessary for this study include germanium, GaAs, and InP. For cells using a germanium substrate, data from an existing LCA of germanium substrates was used [118]. Recreating this life cycle model in SimaPro (as reported in the appendix) resulted in a CED of 212 MJ/wafer, which is reasonably close to the published result of 216 MJ/wafer. No life cycle studies exist for GaAs or InP substrates to date, where previous LCAs that have included GaAs substrates used approximations based on silicon substrates [132]. Therefore, the life cycle of a GaAs substrate will be modeled in detail. The GaAs substrate's life cycle impacts determined in this study will also serve as a proxy for InP substrate impacts in cells 2 and 3, based on the similarity of manufacturing GaAs and InP substrates [133, 134].

The precursors needed for epitaxial growth are arsine, phosphine, trimethylaluminum (TMAl), trimethylgallium (TMGa), trimethylindium (TMIn), and trimethylantimony (TMSb), as well as dopants such as disilane and diethylzinc. Arsine and phosphine are the only precursors available in the ecoinvent 3.4 database [125], while previous LCAs of III-V photovoltaics have relied on chemical approximations or limited discussion with manufacturers of these compounds [21, 135]. Therefore, the life cycles of TMAl, TMGa, TMIn, and TMSb were modeled in detail, while TMGa was used as a proxy for all dopants, under the assumption that it is generally representative of metal organic production.

The amounts of precursors needed for each cell were based on the masses of individual elements reported in Table 28, which represent the material mass that ends up in the final device. However, upstream losses occur such that 250 times more mass than what is reported in Table 28 is required in some cases. To achieve high semiconductor purity, a large overpressure of group V elements is often necessary, typically 50 to 100 times greater than the group III elemental concentration. Furthermore, gas-to-solid incorporation during cell growth (essentially, material efficiency yields) is known to be between 6% to 50% for MOVPE precursors [3, 120]. A material efficiency of 20% will be assumed for this study, based on the prevalence of data in literature. Therefore, the group III molar flows corresponding to the masses in Table 28 are multiplied by a factor of 5 to account for 20% material efficiency, while the group V molar flows corresponding to the masses Table 28 are multiplied by a factor of 250 to account for both 20% material efficiency and an overpressure ratio of 50. The only exception is the InAlAsSb material, since this material does not require an overpressure of group V elements, as evidenced in Chapter 4. Furthermore, it was noted in Chapter 4 that the InAlAsSb material is best grown using tritertiarlybutylaluminum and

tertiarybutyl arsine, however this LCA will use trimethylaluminum and arsine as a proxy. Finally, dopant flows were estimated assuming an average doping of $1x10^{18}$ carriers/cm^3 throughout the device and 20% material efficiency.

A basic diagram of the cell manufacturing process is depicted in Figure 72 for each of the cell types. For cell 1, the germanium substrate forms the bottom junction of the device, so after growth in the reactor the cell proceeds directly to lithography. For cells 2 and 4, after cell growth in the reactor, the substrate can be removed by an epitaxial lift off process after the rear metal contact has been deposited, after which the cell proceeds to lithography. For cell 3, two separate substrates receive cell growth in a reactor, and are then bonded face-to-face before the substrates can be removed and the cell proceeds to lithography and metal contact deposition. After this cell-specific processing, all cells proceed through identical fabrication steps.

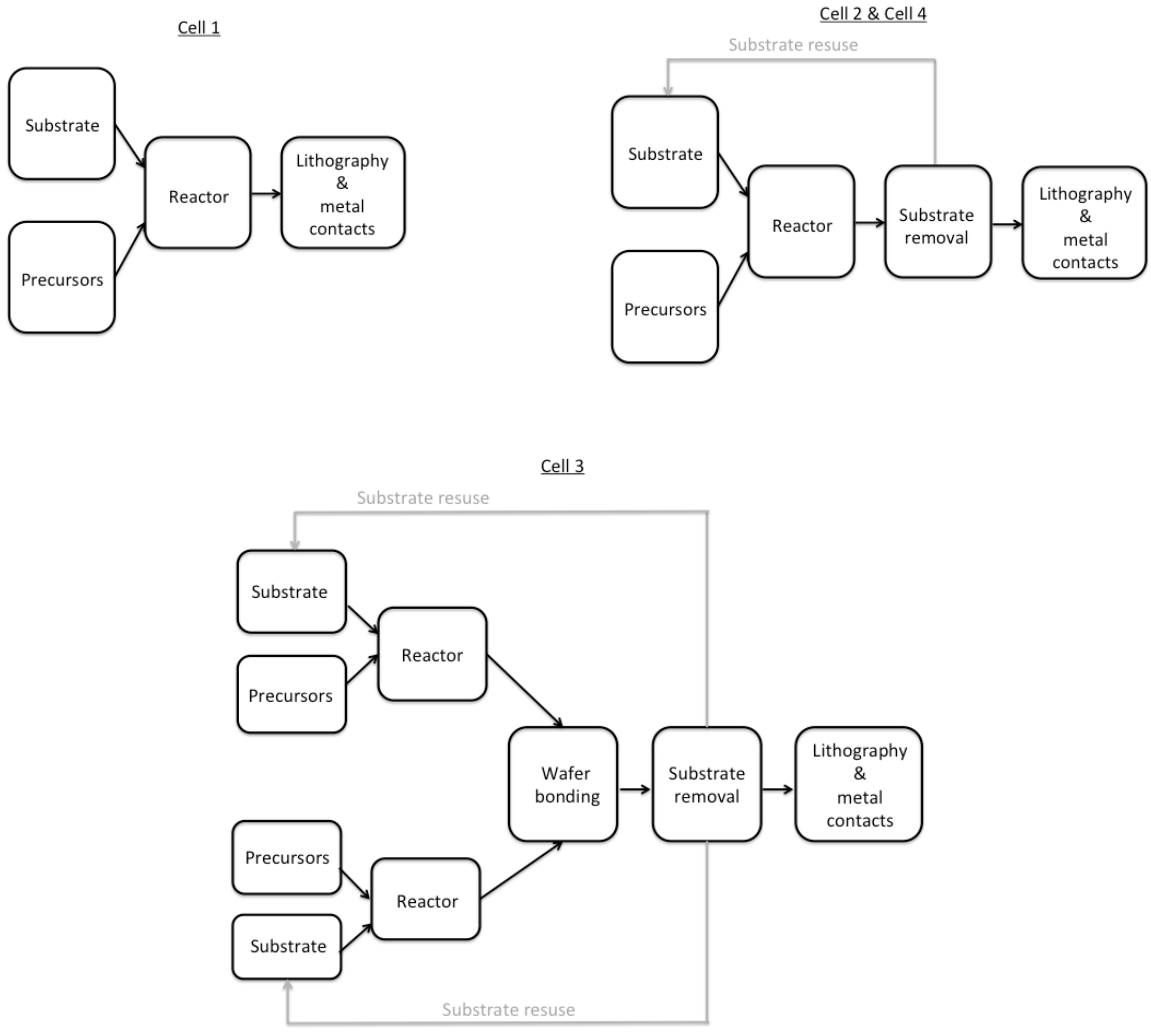

Figure 72: Photovoltaic cell growth and fabrication diagram

6.2.2.1 GaAs Substrate Inventory

As the first input to the cell manufacturing stage and the first goal of the LCA, the GaAs substrate life cycle is analyzed first. The system diagram of the GaAs substrate life cycle is shown in Figure 73. White boxes in the background system are background input flows included in the scope, while gray boxes are outputs for waste treatment that are included in the scope.

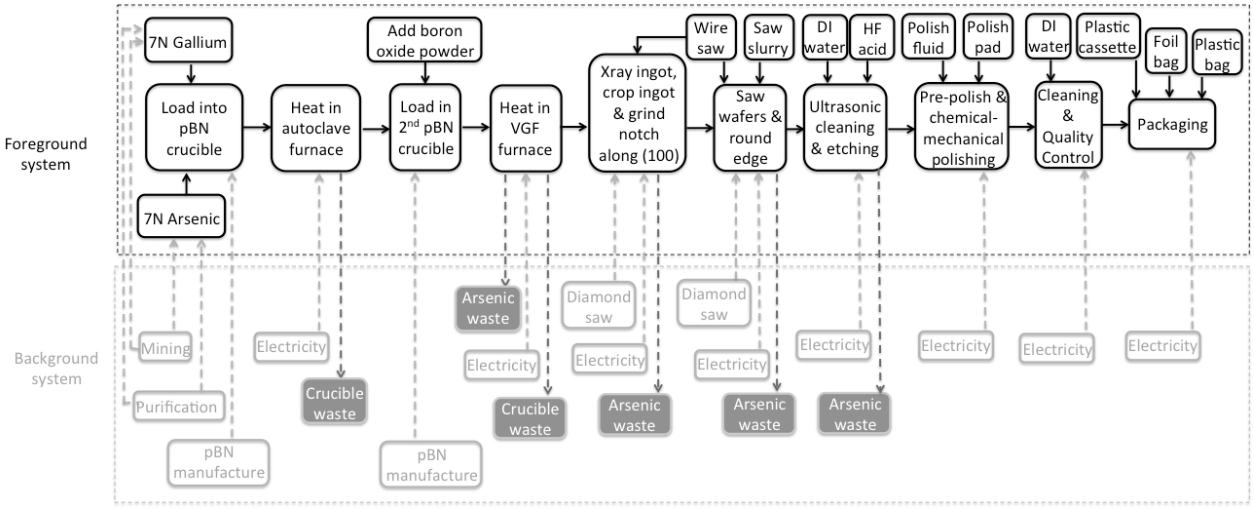

Figure 73**:** System diagram for GaAs substrate manufacturing life cycle assessment

Assumptions and details that went into these models are reported in **Appendix A.2**. Manufacturing processes were initially researched by conducting patent reviews and confirming descriptions available on vendor websites. This preliminary research established the modern GaAs substrate manufacturing technique as vertical-gradient freeze (VGF) and uses 7N gallium and arsenic metal inputs [133, 136-138]. However, the majority of detailed life cycle inventory data was gathered from personal communications with manufacturers. These communications indicated a degree of process variability that exists between manufacturers, and not all approaches are captured in this paper. The life cycle model was constructed at production scales consistent with information from manufacturers in order to in order to generate an appropriate amount of electricity demand per unit produced. Price data for inputs in the manufacturing process were either reported directly by manufacturers or by obtaining quotes from vendors of the input product at the appropriate scale. Electricity demand was estimated from power requirements of commercially available equipment or reported by manufacturers.

The manufacturing process traditionally uses 7N gallium and 7N arsenic as inputs. Semiconductor-grade gallium is available in ecoinvent at a purity of 6N. Therefore, this process was used as an input along with additional electricity input to achieve 7N purity, approximating the energy use of zone refining based on [139]. Metallic arsenic was not available as an input in ecoinvent, so a new process was created based on the metallic arsenic life cycle modeled in [140]. This model used information from the German ProBas database is used to create a system-level process in ecoinvent for metallic arsenic [141]. Based on correspondence with first author of [140], it is

assumed that the metallic arsenic reported here is 2N pure, therefore additional purification steps to generate 7N arsenic were modeled based on [142].

For one boule, approximately 12.1 kg 7N gallium and and 12.9 kg of 7N arsenic are needed. However, more than 50% of this mass is subsequently lost as waste during the substrate manufacturing process. The waste is processed to recover the gallium (the more expensive metal) which is then fed back into the system again as an input. This process supplies about half the necessary gallium inputs, such that only about 6 kg of new gallium is needed per boule. The 7N metals are first synthesized into polycrystalline GaAs before being annealed into a single crystal ingot. A polycrystalline ingot can be achieved by a number of methods, including the horizontal gradient freeze method, or methods similar to an autoclave furnace [133]. The 7N metals are placed stoichiometrically into a pyrolitic boron nitride (pBN) crucible and annealed to form a polycrystalline GaAs ingot. Boron nitride was not available in the ecoinvent database so boron carbide was selected as a substitute. The polycrystalline ingot is transferred to a second pBN crucible containing a seed crystal of desired orientation and boron oxide to protect the GaAs from the crucible walls. The crucible is then annealed in a VGF furnace to produce a single-crystal ingot.

The ingot is then analyzed by x-ray diffraction to confirm crystal orientation. Ends of the ingot are cropped using a steel wire saw and mechanical slurry, where slurry use is assumed to be negligible in this step. The ingot is then placed in a machine containing a diamond saw to grind a notch of the desired orientation. Life cycle data for diamond saws are not available in the ecoinvent database, so this was approximated by modeling the process for producing synthetic diamond, estimating a mass of steel for the core of the saw, and then normalizing for a lifetime use on 100 ingots. The ingot is then cut into wafers, again using a steel wire saw and slurry. Some manufacturers perform a wafer anneal step, but this is not considered in this study. Wafer edges are then rounded, assumed by another diamond saw, and are then cleaned and etched. Wafers are then mechanically polished using a polyurethane polishing pad and the mechanical slurry. Wafers then undergo chemical-mechanical polishing (CMP), which uses a similar polishing pad and a chemically active slurry. Wafers are cleaned again and pass through quality control before being packaged for shipment.

The amounts of GaAs that are lost during each of these steps (due to effective yield rates, sawing, polishing, etc) are quantified in **Figure 91** in the Appendix. Gallium is reclaimed from these losses but the arsenic is disposed as waste. The yield rate of the gallium recycling process is unknown, so a range of rates is assessed based on [143]. This yield rate affects the amount of new gallium needed as an input in the polycrystalline step. Since a lower gallium recycling yield provides less recycled gallium that can be re-used as an input in the polycrystalline step, this mean a greater amount (more than 6 kg) of new gallium would be required to be input instead. Again, since modeling the life cycle for GaAs substrate manufacturing supports the first goal of the LCA (achieving accurate values for cell manufacturing), the strategy for dealing with uncertainty in manufacturing parameters is discussed later in the Methods section.

6.2.2.2 Trimethyl Precursor Inventory

The second input to the cell manufacturing stage are the precursors, where a life cycle model of the trimethyl precursors is necessary to achieve to the first goal of the LCA. The trimethyl precursor life cycle diagram is shown

in **Figure 74**. This model does not include product packaging since it varies significantly depending on the volume of precursor needed, and as such it is portrayed outside the dashed border of the system boundary. Packaging should be considered in future LCAs if the scale of use is known. These precursors are sold at multiple purity levels and often require additional purification before being used to grow epitaxial films, so multiple purity levels were examined in this study but do not represent the full range of commercially available purity levels. The inventory will be determined per kilogram of the precursor when comparing between chemicals in this section, but will ultimately be fed into the 1 kWp functional unit defined above.

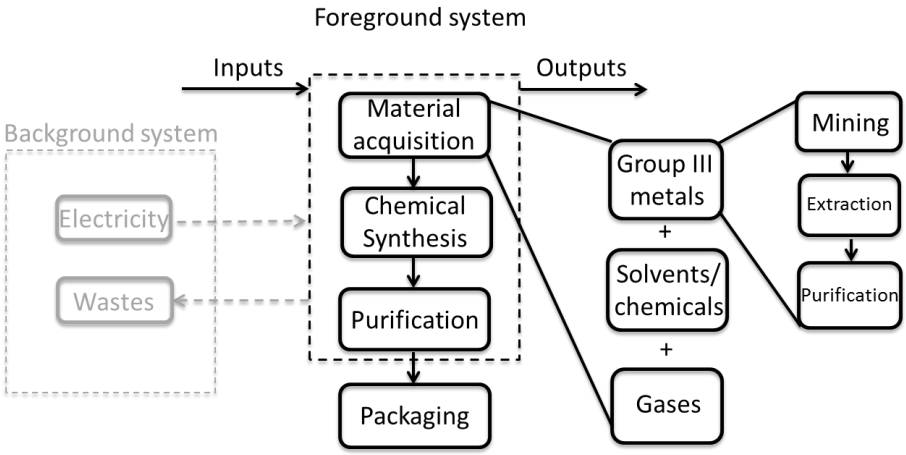

Figure 74: System diagram for group III precursor manufacturing LCA

Some process variability exists between manufacturers – for example, one supplier reported group-III metal reactants to be 99.99% pure (also known as four nines, or 4N), while another reported 5N or 6N purity [144, 145]. Suppliers consistently confirmed that TMAl is produced in the largest quantities. Annual production was reported to be roughly 1,000 MT of TMAl, 100 MT of TMGa, and 10 MT of TMIn. Similarly, TMAl was reported to be produced in 30 kg batches, while TMGa is produced in 2.5 kg batches. Synthesis was modeled at these batch scales in order to generate an appropriate amount of electricity demand per unit produced, where TMSb was assumed to use similar batch sizes as TMIn. Since modelling these compounds in detail supports the first goal of the LCA (achieving accurate values for cell manufacturing), the strategy for dealing with the uncertainty in manufacturing parameters will be discussed later in the Methods section.

6.2.2.2.1 Trimethylaluminum

Given that TMAl is used to synthesize TMGa and TMIn, TMAl was analyzed first. Of the 22 patents identified for TMAl, all were either lapsed (unpaid) or expired (life of patent), with one exception. This patent (and most others) described similar synthesis processes often referred to as the "sesquichloride" technique [146]. A schematic of this technique is shown in **Figure 75**. The white box represents the product, the gray boxes represent reactants, and black boxes represent wastes. The solvent in [146] (n-decane) was absent from ecoinvent, so mineral oil was substituted based on [147]. Since methyl aluminum sesquichloride was not available in ecoinvent, its synthesis was

modeled based on [148]. Anhydrous aluminum chloride was also unavailable in ecoinvent, so a new entry was created based on [149]. The aluminum ecoinvent entry had 4N purity, which is consistent with manufacturer descriptions of TMAl synthesis [125]. It is assumed that this synthesis route produces TMAl that is 98% to 99% pure, so an additional purification step was modeled based on [146] which simply washes the TMAl product in more sodium. Full details for this purification are reported in **Appendix A.1**.

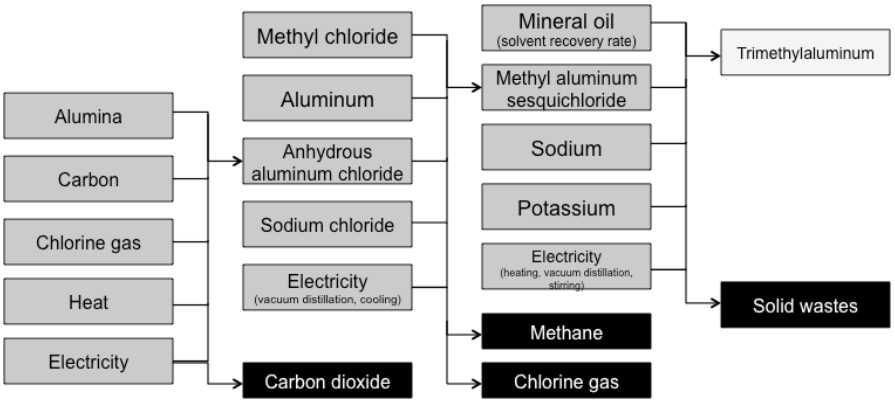

Figure 75: Sesquichloride route for TMAl synthesis

6.2.2.2.2 Trimethylgallium, Trimethylindium, Trimethylantimony

Thirty patents were identified that refer to TMGa and/or TMIn synthesis, or any group III precursor. Discussions with suppliers indicated the modern process is the "molten salt" technique described in [150]. All patents except two used gallium trichloride ($GaCl_3$) or indium trichloride ($InCl_3$) as the starting reactant, as shown in **Figure 76**. $GaCl_3$ and $InCl_3$ were both unavailable in ecoinvent, so models for these compounds were based on [151, 152]. It is assumed in this study that TMSb follows a similar production route to TMGa and TMIn, so $SbCl_3$ was modeled as well.

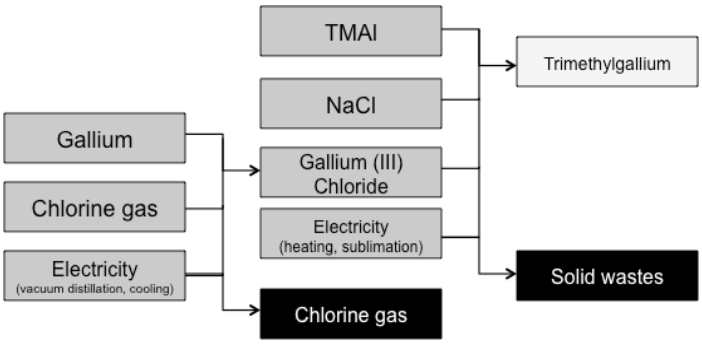

Figure 76: Trichloride route for TMGa synthesis (identical TMIn synthesis with indium)

For group III metal entries, ecoinvent had 6N gallium and 5N indium. The text associated with the ecoinvent entry for indium denotes, "This dataset is not to be used when indium is a substantial part of the system modeled,"

[125]. A more detailed study on LCA of metals has been published [140] and suggested allocation changes for indium ecoinvent entries – using these updated allocation factors decrease indium CED by 32%. Allocation changes are documented in Table 59 in **Appendix A.1.** In order to examine the effects of input metal purity on precursor impacts, the method of purifying gallium to 7N was modeled based on [139]. This was also used as an approximation to purify the 5N indium metal to 6N purity, and the 4N aluminum to 6N purity. Finally, the ecoinvent entry for antimony is assumed to have a purity of 2N since purity is not explicitly stated in the ecoinvent documentation. Therefore, antimony was modeled to be purified to 4N using the approximation from gallium purification and then used in synthesis of $SbCl_3$, or alternatively an additional purification to 6N could be performed as well. Input-output tables for all metal purification steps and precursors are available in **Appendix A.1**.

6.2.2.3 MOVPE Growth

Both the substrates and precursors are fed into an MOVPE reactor to grow the cell. Hydrogen and nitrogen use for the MOVPE reactor were assessed based on [22]. To ascertain the typical power rating of MOVPE reactors, a review of existing literature was executed to identify a consensus.

The earliest study by Meijer et al. (2003) [132] considered an Aixtron AIX3000 model which is capable of containing 96 x 2-inch wafers or 20 x 4-inch wafers. They reported a CED of 16 GJ for the MOCVD operation required to produce 4 m^2 of InGaP cells on 2-inch GaAs substrates. This would require 2,171 wafers (assuming 10% edge losses), which would require 23 batches in this reactor. This corresponds to 695 MJ per batch – however, considering the InGaP cells are 2.5 μm thick, it can be assumed that each batch only took approximately 20 minutes (including time for heating), so this corresponds to 2,087 MJ per hour of MOCVD operation for roughly 0.2 m^2 of material. This study assumed a Dutch electricity mix corresponded to an "electricity-to-CED" ratio of 0.37, which assumes that every MJ of electricity requires 2.7 MJ of primary energy. This means a CED of 2,087 MJ generated from one hour of MOVPE operation is equivalent to 772 MJ of electricity. This indicates a power rating of roughly 200 kW. Furthermore it is known that the heating unit alone corresponds to 132 kW [153].

Peharz and Dimroth (2005) [21] directly measured the electricity use for an MOVPE reactor that contained 8 x 4-inch wafers in their study. While they did not directly report the electricity use, they did report the CED of the electricity used by the MOVPE for their PV system (1700 MJ). The system in their study used 16.5 germanium wafers, which would require two batches from the reactor (the reported CED for the 4-inch germanium wafers used in the system was 5110 MJ, where one wafer had a CED of 290 MJ). It is assumed these cells require deposition of 4 μm of III-V material on the germanium substrates. It is also assumed that growth occurred at 14 μm per hour [154], which indicates the growth of one batch would take approximately half an hour (including time for heating). This implies the reactor has a CED of 1700 MJ for one hour of operation. This study assumed a German electricity mix corresponds to an "electricity-to-CED" ratio of 0.34, which means a CED of 1700 MJ is equivalent to 590 MJ of electricity consumed over an hour of MOVPE operation. This indicates a power rating of roughly 160 kW.

A study by Kim et al. (2008) [24] reported the CED for MOVPE operation to be 4,209 MJ/1000 Ge wafers when growing a typical triple junction like cell 1, though they do not specify the reactor size or wafer size. They also reported a separate figure (842 MJ) that included CED for gas scrubbing (an important part of MOVPE operation)

and "cell processing". This forms a significantly different comparison to the figure reported in [21] which empirically measured the reactor electricity usage, multiplied by an "electricity-to-CED" ratio of 0.34, and reported a CED of 850 MJ per 8 wafers. However, [24] assumes the US electricity mix has an "electricity-to-CED" ratio of 0.29, yet reports a CED of 34 MJ per 8 wafers. A subsequent study [22] by the same authors reports electricity to be 16% of the 14,562 MJ total CED for 53 kW (assumed to correspond to 150 4-inch Ge wafers), where electricity for MOVPE is assumed to be responsible for 83% of that 16%. In this study, this corresponds to a CED of 1,934 MJ for 4 μm of material on 150 substrates. Assuming that 4 μm of material takes a half hour to grow, this may have been executed in two batches of 75 wafers each, to correspond to a reactor CED of 1934 MJ for an hour of operation. This study [22] used the Cumulative Energy Demand Method 1.04 and assumed US production, which corresponds roughly to an "electricity-to-CED" ratio of 0.3, and indicates a power rating of roughly 160 kW.

A 2010 study reported on scaling MOVPE reactors up to 18 x 4-inch wafers or 8 x 6-inch wafers, which was reported to have a power rating of 150 kW [155]. MOVPE reactor technology has progressed since these reports, with commercially available reactors containing up to 48 x 6-inch wafers (or 124 x 4-inch wafers) [156]. This corresponds to 0.875 m^2 of 6-inch wafers or 1 m^2 of 4-inch wafers. This study will assume the largest reactor reported in [156] is in use, and will be estimated to have a power rating of 200 kW and a growth rate of 14 μm/hr. Given the prevalence of literature and information on MOVPE energy usage, uncertainty analysis for this particular aspect of manufacturing is less vital.

6.2.2.4 Cell Fabrication

After the cell is grown in the MOVPE reactor, it proceeds to fabrication which involves multiple steps. Substrate removal, lithography, metal deposition, and anti-reflective coating deposition require multiple chemicals and take place in a cleanroom, which has advanced air filtration systems to preserve the integrity of the electrical devices. The epitaxial lift off (ELO) process for substrate removal is described in Chapter 5, which involves bonding the top surface of the wafer to a rigid handle (such as plastic), then a selective etchant (typically hydrofluoric acid) is used to remove the substrate, after which the substrate undergoes chemical-mechanical polishing and can then be reused. A generic ELO process has been modeled for this study, details can be found in **Appendix A.3**.

Energy and material use for the remaining processes can be estimated from previous studies. References [21] and [22] report CED for fabrication inputs per a 6 kWp system and a 53 kWp system, respectively. These studies were analyzed to calculate impacts per cm^2 of cell rather than kWp, so they could be applied to cells in this study regardless of power conversion efficiency. In reference [21], the 6 kWp system contained 333 modules that housed approximately 50 cells each, corresponding to a total of 16,650 cells in the system. Each cell was reported to be 3 mm^2, which corresponds to 500 cm^2 of cells in the system. Reference [22] reports 37% efficient cells with 6.8% electric losses in the system, so this implies 15 W/cm^2 net cell power and requires 3,533 cm^2 for a 53 kWp system.

An important input that can be determined from these studies is the area of substrate required per area of cell. In reference [21], a 4-inch germanium wafer was reported to contain 1,150 cells where the size of each cell was 3mm^2. Since a 4-inch wafer is 81.1 cm^2 but 1,150 cells only occupy 34.5 cm^2, this implies 7 mm^2 of the wafer is allocated to each 3 mm^2 cell, most likely to provide room for dicing. Furthermore, 1,150 cells per wafer indicates 14.5 wafers

are necessary for the system, but a 15% loss rate was then subsequently applied to account for typical cell breakage and losses. This means 8.1 mm^2 of wafer is actually needed for each 3 mm^2 cell, or more simply each 1 cm^2 cell requires 2.75 cm^2 of wafer. Similarly, in [22] the total mass of Ge substrates required was reported as 0.9 kg for the 53 kW system. Assuming that each 4-inch Ge substrate weighs 6 grams [118], this corresponds to 150 substrates for the system. 150 substrates have a surface area of 1.2 m^2, however the system only requires 0.35 m^2 of cells. This indicates each 1 cm^2 cell requires 3.4 cm^2 of wafer, which includes 10% cell losses and likely extra area for dicing .

Table 29 shows CED values for other cell fabrication inputs from [21] and [22] both at system level and also normalized to MJ/cm^2 fabricated cell for ease of comparison. This information was used to build the life cycle model for this study by iteratively analyzing each material in SimaPro to back-calculate the masses that correspond to the reported CED. The resolution of data from references [21] and [22] was not adequate to evaluate purified water usage and antireflective coating materials. Therefore, these were estimated assuming the mass of water usage was equivalent to solvent usage, and assuming a 200 nm zinc sulfide antireflection coating.

Table 29: Cell fabrication CED values from literature

	CED (MJ/500 cm^2 of useful fabricated cells) [21]	CED (MJ/cm^2 useful fabricated cells) [21]	CED (MJ/3533 cm^2 useful fabricated cells) [22]	CED (MJ/cm^2 useful fabricated cells) [22]
Solvents	1400	0.28	7380	2.1
Acids/Bases	9	0.02	903	0.26
Lithography materials	160	0.32	--	--
Contact metals	1140	2.28	1209	0.34
Energy (cleanroom)	4170	8.34	383	0.11
Energy (other)	520	1.04	248	0.07
TOTAL		**12.28**		**2.94**

Again, since modeling cell fabrication supports the first goal of the LCA (achieving accurate values for cell manufacturing), the strategy for addressing uncertainty in fabrication parameters is discussed later in the Methods section. The major approach to mitigate uncertainty in this life cycle stage is to create a combination of values from each reference that represent the highest CED scenario as well as the lowest CED scenario for cell fabrication. CED values per cm^2 for solvents and acids/bases are higher in reference [22], but all other values are higher in reference [21], though it should be noted that reference [21] lists “lithography materials” as a separate category which could account for some of the solvent and acids/bases impacts.

6.2.2.5 Module, Tracker, and Balance of System Assembly and Installation Inventory

After the cell growth and processing steps, the photovoltaic cell is complete and ready to be inserted onto a heat sink and into the module. Again, a literature comparison was executed for the CED of module and tracker assembly and installation for HCPV systems – Table 30 summarizes the results. At this stage in the life cycle, the purpose of the LCA has shifted to the second goal outlined in the goal and scope section above, where the accuracy of the individual inputs are less important as they will be present in each of the HCPV systems being compared. However, uncertainty in this stage may still affect the overall comparison and will be discussed in more detail in the Methods section. The major approach to mitigate uncertainty in this life cycle stage was to create a combination of values

from each reference to represent the highest CED scenario as well as the lowest CED scenario for module/tracker assembly and installation. Masses were reported in reference [22] and are used where appropriate in this study once normalized to 1 cm^2 of usable fabricated cell, while masses are inferred from [21] on the basis of CED for each component.

Table 30: Module, tracker, and balance-of-system assembly and installation CED values from literature

	CED (MJ/500 cm^2 of fabricated cells) [21]	CED (MJ/cm^2 of fabricated cells) [21]	CED (MJ/3533 cm^2 of fabricated cells) [22]	CED (MJ/cm^2 of fabricated cells) [22]
Cell packaging materials	1600	3.2	--	--
Cell packaging energy	1300	2.6	--	--
Heat sink (copper / aluminum)	3500	7	440089	125
Inverter	3000	6	33395	9.5
Energy for module assembly/install	530	1.1	162	0.05
Float glass	10580	21.1	--	--
Silicone sealant	800	1.6	--	--
Fresnel lens (silicon lens array)	1680	3.36	171974	48.7
Galvanized steel (frame)	29000	58	234218	66.3
Other steel (tracker pedestal/tube, hydraulic drive)			427106 + 117972	121 + 33.4
Sensor electronics (anemometer)	220	0.4	762	0.2
Cables (AC/DC wiring)	1400	2.8	5278	1.5
Transformer (high voltage interconnection board)	2000	4	11973	3.4
Foundation (concrete)	3600	7.2	2341	0.8
Motor / controller	--	--	2056 + 8907	0.6 + 2.5
Transport to site	8000	6	61364	17.4
TOTAL		**118.5**		**412.2**

6.2.2.6 Operation and Maintenance Inventory

Finally, the operation and maintenance stage of the HCPV system was considered. A lifetime of 30 years was assumed as a best-case scenario from literature [22]. Reference [22] reported materials used for operation and maintenance, while reference [21] reported electricity usage of the tracker motor, which is assumed to be drawn from the grid. Again, at this point in the life cycle, the purpose of the LCA has shifted to the second goal outlined in the goal and scope section above, where a reasonable range has been established to determine when and if it is possible for cell impacts to outweigh system impacts. However, uncertainty in this stage may still affect the overall comparison and will be discussed in more detail in the Methods section. Given dearth of detailed literature on this stage of the HCPV life cycle, one operation and maintenance scenario was constructed, and this was evaluated for both the high and low impact scenario for module and tracker assembly and install.

6.2.3 Impact Assessment

The impacts considered in this LCA are cumulative energy demand (CED) and greenhouse gas (GHG) emissions. These impacts were selected since photovoltaics are a renewable energy source, hence it is appropriate to

evaluate the energy invested in its manufacture and the GHG emissions that its use is attempting to offset. The methods to calculate impacts provided in the SimaPro software are Cumulative Energy Demand version 1.1 and Greenhouse Gas Protocol version 1.02. Given that III-V semiconductors are composed of heavy metals including arsenic, toxicity impacts are also a concern but are not explicitly evaluated in this study since CED has been shown to correlate well with multiple toxicity impact categories and can be used as a proxy [157]. The heavier III-V elements are not abundant in the earth's crust which necessitates an assessment of HCPV impacts on resource scarcity, however a metric for evaluating this type of impact is not currently established [158]. A comparison of the consumption of these metals by the different cells will be included in the Interpretation discussion section following the Results section, based on the information in Table 28.

6.2.4 Interpretation

Interpretation of the impact assessment will require a methodical approach to the uncertainty inherent to the system model and assumptions. Since this LCA aims to accomplish two goals simultaneously, the approach to uncertainty is different for each. Namely, these are 1) provide more accurate data for MOVPE precursors and substrates, and 2) identify if there is a point at which III-V PV cell manufacturing becomes too impact-intensive such that increasing cell efficiency no longer correlates to improvements in the life cycle of the system. The first goal seeks to provide an accurate value for impacts, while the second goal aims to establish a relationship between cell impacts and system impacts as a function of cell type and efficiency. The first goal requires that all data be as certain as possible, while also reflecting realistic variability in material production and processing steps. With regards to the second goal, sources of uncertainty which are consistent across cell types can be bounded by establishing a best-case and a worst-case scenario. However, the results of the first goal will ultimately be used to achieve the second goal as well, so some of the same issues with uncertainty will be carried over. Table 31 below lists the types of uncertainty in the LCA and how it is addressed with respect to each of the two goals.

Table 31: Approach to Sources of Uncertainty

Source of Uncertainty	Goal: Accuracy	Goal: Establish Trend
Manufacturing parameters such as input amounts, yield, and scale of production	Define and analyze a range of reasonable values or substitutions, group into scenarios to represent lowest and highest impact combinations	Define and analyze a range of reasonable values, group into scenarios to represent lowest and highest impact combinations
Facilities and equipment impacts	Excluded from LCA (noted in Goal and Scope section), discuss usage over lifetime and infer scale of impact necessary to affect results	Assumed to be relatively consistent across cell types, therefore effect on trend results is minimal
Location-specific effects	Use global market LCI data from ecoinvent wherever possible, such that results represent a representative average of known manufacturing routes	Assumed to be relatively consistent across cell types, therefore effect on trend results is minimal, any potential exceptions noted (i.e. if specific cell is more dependent on electricity, etc) provide estimate for effect
Accurate market representation in ecoinvent LCI data	Noted in Methods section, provide estimate for effect	Assumed to be relatively consistent across cell types, therefore effect on trend results is minimal, any potential exceptions noted (i.e. cell with higher gallium content than other cells), provide estimate for effect

Allocation assumptions in ecoinvent LCI data	Updated allocation for known issues (specifically, indium) – otherwise noted in Methods section, provide estimate for effect	Assumed to be relatively consistent across cell types, therefore effect on trend results is minimal, any potential exceptions noted (i.e. cell with higher indium content than other cells, etc) provide estimate for effect
General uncertainty of modeling decisions in ecoinvent LCI data	Noted in Methods section, magnitude of effect unknown	Assumed to be relatively consistent across cell types, therefore effect on trend results is minimal

For the components of the LCA that aim to achieve the first goal (i.e. precursor, substrate, and cell manufacturing), ranges for uncertain manufacturing parameters will be defined later in this section. In order to define an upper and lower bound of possibilities, scenarios will be created that represent a conglomeration of the lowest-impact manufacturing parameter values as well as scenarios that represent an amalgamation of the highest-impact manufacturing parameter values. These ranges will then be fed into the subsequent life cycle stages (module/tracker/BOS install and assembly, operation and maintenance) which contribute exclusively to the second goal, therefore the uncertainty in their manufacturing parameters is addressed in less detail. For these stages, inventory data were collected directly from multiple literature sources and as such already constituted a degree of variance that provided a reasonable range for uncertainty analysis. Ultimately, a lower bound will be created by inputting the low-impact cell manufacturing scenario into the lower-impact values from literature for the subsequent life cycle stages, and an upper bound will be constructed in a similar fashion with the high impact scenario and literature values.

As mentioned previously in the goal and scope section, impacts from facility manufacture and equipment manufacture were excluded from this LCA as they are assumed to be negligible over the lifetime of the facility/equipment. Inferences regarding the magnitude at which these impacts would become significant can be deduced once the impacts of the cell manufacture are quantified. However, facility and equipment impacts of any magnitude are not expected to significantly affect the results when comparing HCPV systems with different cell types, since the impacts will be present in a similar proportion across all cell types.

Similarly, the impacts of manufacturing that vary by location (regional electricity mix, modes of transportation, water sources, etc.) is not expected to affect the comparison of HCPV systems since the impacts will be present in a similar proportion across all cell types. Notable exceptions would include cell 4 or any system using a GaAs substrate, which would require more electricity than the other cell or substrate options, and as such would be more susceptible to regional electricity mix impacts. As described in Table 31, location effects on either LCA goal in this study are moderated by using inputs that represent a weighted average of the global market for the input. Further uncertainty exists when considering if the market represented in ecoinvent LCI data is an accurate reflection of global processes. For example, indium can be extracted from either zinc or molybdenum primary ores. Ecoinvent models the majority of global indium to be extracted from zinc ores, but this may change over time. Similarly, ecoinvent assumes that all gallium is extracted from primary sources (i.e. not recycled content), but clearly as evidenced in section 6.2.2.1, some manufacturers rely on an internal recycling loop, which demonstrates there may be an economic basis for external secondary sourcing as well. Again, it is expected that this will have a minimal effect on establishing a trend between HCPV of different cell types, where differences would only exist as a result of

different gallium proportions in the cell. This affects the accuracy of results as related to the first goal of this LCA, but must be tolerated given that current and accurate market insights are difficult to obtain.

This study relies on multiple assumptions regarding the allocation of impacts between co-products or by-products of a given process, in both the ecoinvent data and the models created for this study. This is particularly relevant for III-V PV since the majority of III-V elements are extracted as by-products during mining of a more common metal such as copper or zinc. The ecoinvent database uses economic allocation for these metals, which assigns impacts based on the economic value of the outputs. This typically makes the III-V elements more impactful than if impacts were allocated by mass, since most III-V elements exist in very low concentrations in host ore [140]. Furthermore, the economic value of III-V elements tends to vary significantly since their supply is largely controlled by the demand for the host ore, which adds temporal uncertainty to the economic allocation method. A 2014 study suggested allocation changes for gallium and indium ecoinvent entries – using these updated allocation factors would increase gallium CED by 18% and decrease indium CED by 32% [140]. Given that the indium discrepancy was particularly large, the indium allocation factor was updated according to [140] and is explained earlier in the Inventory section. Fortunately, the effects of altering the allocation assumptions is not expected to significantly affect the comparison between HCPV systems of different cell types given the cells typically rely on similar materials. At most, effects might be observed in cells with proportionally greater amounts of a given element, such as the case of indium content in cell 2.

Finally, there is inherent uncertainty in all of the modeling assumptions for the data in the ecoinvent database and other life cycle databases, which is a reality within which all LCA practitioners must work.

6.2.4.1 GaAs substrate uncertainty

Uncertainty analysis was applied to parameters that were either largely unknown or had the potential to have a large effect on impacts. These included gallium recovery, electricity-dependence on location of manufacturing, and substitution of boron carbide for boron nitride. More specifically, the gallium recycling process was evaluated at 50% efficiency and 70% efficiency, based on the range of results reported in the study referenced in [143]. Since electricity is such a large input, the impacts of assuming a US electricity mix were also evaluated as an alternative to the global electricity mix used in the rest of the study. And finally, silicon carbide was evaluated as an alternative substitute for boron nitride, since it has similar material properties and hardness. The default scenario was assumed to be 70% recycling efficiency and a global electricity mix, and so a total of 4 scenarios will be considered where only one variable is modified at a time while holding all other variables at their default condition.

6.2.4.2 Trimethyl precursor uncertainty

For manufacturing assumptions that were made with significant uncertainty, sensitivity analysis was performed either by establishing a range of reasonable values based on literature, evaluating alternative materials if a substitution was made, or both. For example, solvents are commonly recycled within a chemical process, where 95% re-use represents the best case scenario [159]. However, no information on solvent recovery for precursor

synthesis was made available, so both a high and low scenario were analyzed. Furthermore, alternative solvents to mineral oil were also evaluated as substitutes for n-decane, such as toluene and xylene [160].

In order to evaluate the significance of other assumptions used in this study, several manufacturing scenarios were evaluated in order to show the effect of certain parameters. The parameters include input metal purity, solvent reclaim, additional purification after synthesis, and updated allocation factors. The scenarios are listed in Table 32, which all use mineral oil as a solvent input. The TMAl described in each scenario is then used as an input in the manufacture of the other precursors in that scenario. The first four scenarios use input metals as available in the ecoinvent database. The remaining five scenarios use the TMAl conditions from the fourth scenario, and primarily evaluate impacts from input metal purity. The impact assessments of these scenarios will be presented and compared in the results section.

Table 32: Sensitivity analysis for trimethyl precursor manufacturing

Scenario Name	Details
Low purity TMAl	No solvent reclaim, 98% pure TMAl 4N aluminum, 6N gallium, 5N indium (0.14% allocation), 2N antimony
Low purity TMAl, solvent reclaim	90% solvent reclaim, 98% pure TMAl 4N aluminum, 6N gallium, 5N indium (0.14% allocation), 2N antimony
High purity TMAl	No solvent reclaim, 99.95% pure TMAl 4N aluminum, 6N gallium, 5N indium (0.14% allocation), 2N antimony
High purity TMAl, solvent reclaim	90% solvent reclaim, 99.95% pure TMAl 4N aluminum, 6N gallium, 5N indium (0.14% allocation), 2N antimony
Higher aluminum purity	90% solvent reclaim, 99.95% pure TMAl 6N aluminum, 6N gallium, 5N indium (0.14% allocation), 2N antimony
Higher metal purities	90% solvent reclaim, 99.95% pure TMAl 6N aluminum, 7N gallium, 6N indium (0.14% allocation), 6N antimony
Updated indium allocation	90% solvent reclaim, 99.95% pure TMAl 4N aluminum, 5N indium (0.09% allocation)
Higher aluminum purity (updated allocation)	90% solvent reclaim, 99.95% pure TMAl 6N aluminum, 5N indium (0.09% allocation)
Higher metal purities (updated allocation)	90% solvent reclaim, 99.95% pure TMAl 6N aluminum, 6N indium (0.09% allocation)

6.2.4.3 Cell manufacturing uncertainty

A number of aspects of cell manufacturing are unknown but can be approximated within a reasonable range of values. For example, the optimal purity and manufacturing process of precursors for MOVPE growth of PV devices is unknown, so a number of the precursor scenarios defined in section 6.2.4.1 can be evaluated as inputs. The lowest impact scenario is the "low purity TMAl, solvent reclaim", while the highest is likely "high purity TMAl" with no solvent reclaim. The individual junction thicknesses for cells 3 and 4 are proprietary so a lower bound of 1 μm per subcell and upper bound of 2 μm per subcell will be used for the final analysis, to approximate an average subcell thickness observed in known multijunction devices. Current literature on epitaxial lift off has demonstrated that a substrate can be reused five times successfully [161], therefore a best-case scenario of 10 reuses and a worst-case scenario of 0 reuses will be considered. Given that the lattice constants of germanium and GaAs are relatively similar, these substrates can be used almost interchangeably with minor impacts on cell design and efficiency, where the germanium substrate is expected to be the lower impact option. To manage these uncertainties simultaneously, a

series of scenarios were constructed to represent the highest impact and lowest impact cases. These are reported below in Table 33.

Table 33: Sensitivity analysis for cell manufacturing

Impact	Cell growth scenario parameters
High purity & high material-usage cell growth scenario	• No substrate re-use • Precursor scenario: High purity TMAl • 2 μm subcells for cell 3 and cell 4 • Cell 3 & 4 = GaAs wafer
Mid-purity & mid material-usage cell growth scenario	• 5 substrate re-uses • Precursor scenario: High purity TMAl, solvent reclaim • 2 μm subcells for cell 3 and cell 4 • Cell 3 & 4 = Ge wafer
Low purity & low material-usage cell growth scenario	• 10 substrate re-uses • Precursor scenario: Low purity TMAl, solvent reclaim • 1 μm subcells for cell 3 and cell 4 • Cell 3 & 4 = Ge wafer

6.3 Results

6.3.1 GaAs Substrate Impact Assessment

A life cycle model of a 6-inch GaAs substrate as described in section 6.2.2.1 was analysed by the impact assessment methods Cumulative Energy Demand version 1.1 and Greenhouse Gas Protocol version 1.02. Four different manufacturing scenarios were analysed to evaluate the potential magnitude of effects associated with uncertainty in manufacturing parameters, as described in section 6.2.4.1. The parameters under consideration include the location of manufacturing, the yield rate of gallium recycling, and the appropriate substitute material for pyrolytic boron nitride. The resulting impacts from these scenarios are reported in Table 34. When evaluating a US electricity mix as an input for all steps in GaAs manufacturing (excluding metal purification and other upstream processes before polycrystalline synthesis) as compared to a global electricity mix, the CED only decreases by 1.5%. The yield rate of gallium recycling shows the largest effect: reducing the yield rate to 50% from 70% results in a CED increase of more than 8%. Finally, when evaluating potential substitutes for pyrolytic boron nitride, the CED values resulting from using boron carbide or silicon carbide were identical. The greenhouse gas emissions follow a similar trend as a function of scenario.

Table 34: CED and GHG impacts per GaAs wafer, multiple scenarios for uncertainty analysis

Scenario	70% gallium reclaim, global electricity mix, boron carbide (Default)	70% gallium reclaim, US electricity mix, boron carbide	50% gallium reclaim, global electricity mix, boron carbide	70% gallium reclaim, global electricity mix, silicon carbide
CED (MJ/wafer)	951	937	1030	951
GHG (kg-CO_2-eq/wafer)	62.4	54.7	66.7	62.4

Major contributions to CED in the default manufacturing scenario are shown in **Figure 77**. The majority of the CED (51%) is from electricity for the VGF furnace operation, which requires a week-long cycle time to transform polycrystalline material into a single crystal. The second largest contributors are the 7N gallium metal and the electricity to operate the polycrystalline furnace, which are each responsible for about 25% and 17% of the final CED, respectively. The remainder (9%) comes from multiple sources that each correspond to 2% or less of the CED. Greenhouse gas emissions also follow the general distribution as shown in **Figure 77**, where the electricity for the single-crystal furnace represents 54% of emissions, 7N gallium represents 22% of emissions, and electricity for the polycrystalline furnace represents 18% of emissions.

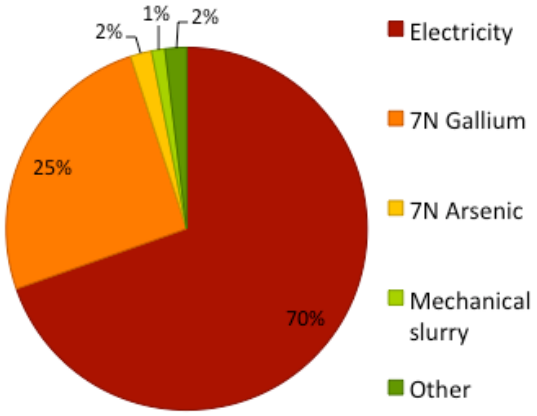

Figure 77: Largest contributions to CED for one 6-inch GaAs substrate (default scenario in **Table 34**)

6.3.2 Trimethyl precursor impact assessment

The life cycles of the trimethyl precursors described in section 6.2.2.2 were analyzed using the CED and GHG impact assessment methods defined in section 6.2.3 Impact Assessment. A set of manufacturing scenarios were constructed as previously defined in section 6.2.4.2 Trimethyl precursor uncertaintyin order to evaluate the potential effects of uncertainty regarding manufacturing parameters or allocation methods. These parameters included solvent recovery, TMAl purification, purity of input metals, and indium allocation. Table 35 reports the CED values for these precursors across all scenarios, which are also displayed graphically in **Figure 78**. Across scenarios, the CED of any given precursor varies by a factor of 2 or 3, which indicates a relative degree of precision in estimating the order of magnitude.

Aluminum metal is responsible for the majority of the impacts to methyl aluminum sesquichloride. TMAl is dominated by solvent impacts if there is no reclaim, otherwise methyl aluminum sesquichloride is the dominant contributor and the CED is approximately cut in half. For TMAl purification, the majority of the impact is attributed to the 98% pure TMAl needed as an input. This information is graphically displayed in Appendix A.1, showing input contributions to CED for methyl aluminum sesquichloride, 98% pure TMAl, and 99.95% pure TMAl for both solvent reclaim scenarios.

Though solvent reclaim reduces overall CED by about half for TMAl and TMSb, it only causes 20% reductions for TMGa and TMIn. This inelasticity results from the metal-chlorine complex being responsible for the majority of the CED in TMGa and TMIn, where the group-III metal is responsible for 87 - 99% of the chloride complex impacts. The high burden of the group-III metal is why re-allocating indium results in significant CED reductions for TMIn. The effect of metal purity is also significant – for example, 1 kg of the 7N gallium that was modelled for this study has a CED of 3830 MJ/kg, as compared to the 6N gallium CED of 2640 MJ/kg, which represents a 30% increase in CED. Input contributions to CED for TMSb, TMGa, and TMIn are graphically shown in Appendix A.1 for both low-purity TMAl scenarios.

Table 35: Production scenario analysis for trimethyl precursor CED

Scenario	TMAl (MJ/kg)	TMSb (MJ/kg)	TMGa (MJ/kg)	TMIn (MJ/kg)
Low purity TMAl	733	1180	2410	3880
Low purity TMAl, solvent reclaim	346	661	2020	3370
High purity TMAl	1250	1860	2940	4570
High purity TMAl, solvent reclaim	603	1000	2280	3710
Higher aluminum purity	790	1250	2470	3960
Higher metal purities	--	1600	3220	5260
Updated indium allocation	--	--	--	2740
Higher aluminum purity (updated allocation)	--	--	--	2990
Higher metal purities (updated allocation)	--	--	--	3880

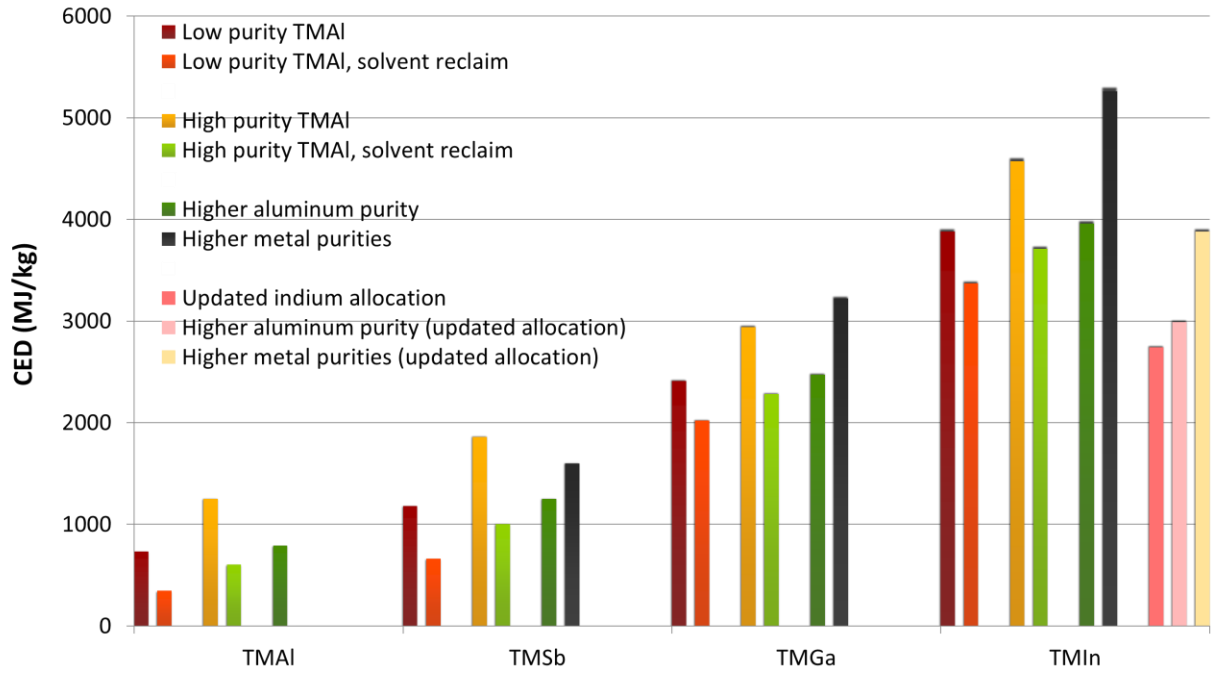

Figure 78: Precursor CED for multiple scenarios as reported in **Table 35**

Since mineral oil was assumed to be the solvent used in all the scenarios described above due to the lack of life cycle data on the preferred industry solvent (n-decane), toluene and xylene were evaluated as alternate solvent substitutes which were mentioned in older literature [160]. The impacts from these solvents are also shown in Table 36. The CED of these solvents are within 20% of mineral oil CED, however their GHG emissions are close to half that of mineral oil. More information about the production n-decane would be necessary to evaluate which of these solvents best approximates its impacts.

Table 36: Solvent substitute analysis for TMAl

	Mineral oil (no reclaim)	Toluene (no reclaim)	Xylene (no reclaim)
CED (MJ/kg TMAl)	365	301	293
GHG (kg-CO_2-eq/kg TMAl)	9.2	4.9	4

Greenhouse gas (GHG) emissions are reported in Table 37 for both low-purity TMAl scenarios. Overall GHG emissions follow the CED trends shown above, with the exception of the GHG impacts from methyl aluminum sesquichloride, which is evident in Figure 79, where GHG emissions for 98% TMAl are shown. Methyl aluminum sesquichloride was modeled with methane as a waste emission (reported in detail in Appendix A.1) which is a potent greenhouse gas. Manufacturers likely use a flare to burn methane waste so the final emission is carbon dioxide which has lower a global warming potential than methane.

Table 37: GHG emission values for TMAl, TMGa, TMIn, and TMSb in two low-purity TMAl solvent recovery scenarios

	TMAl – 98% pure		TMGa (from 98% pure TMAl)		TMIn (from 98% pure TMAl)		TMSb (from 98% pure TMAl)	
	No solvent reclaim	90% solvent reclaim	No solvent reclaim	90% solvent reclaim	No solvent reclaim	90% solvent reclaim	No solvent reclaim	90% solvent reclaim
GHG (kg-CO_2-eq/kg)	54.1	33.3	151	130	235	207	80	70

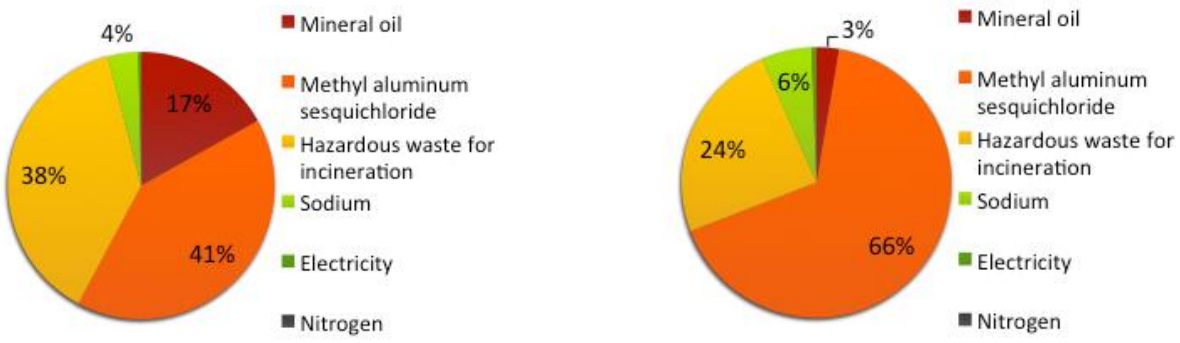

Figure 79: GHG emissions for 98% pure TMAl: (left) no solvent recovery, (right) 90% solvent recovery

6.3.3 HCPV System

6.3.3.1 Cell growth impact assessment

Impacts from cell growth were analyzed for multiple growth scenarios as defined in section 6.2.4.3. **Figure 80** compares the total CED for each cell across scenarios, while quantitative results for both CED and greenhouse gas emissions can be found in Appendix A.3. **Figure 81** breaks down contributions to CED for cells 2, 3, and 4 in each scenario and also provides a graph for cell 1 that applies in all scenarios. The impacts for cell 1 are constant over all three scenarios given that substrate re-use is not possible and minimal precursors are used. For cells 2 through 4, it is clear that substrates dominate the CED in all scenarios, and it can be inferred that most of the CED reductions are due to substrate re-use and replacement with ELO impacts. Cell 3 has the highest impacts in every scenario due to its use of multiple substrates. This is particularly pronounced in cell growth scenario 1, which assumes the use of higher impact substrates and no re-use. However, given that cell 3 needs to have at least one substrate removed in order to fabricate the cell, an assumption of no substrate re-use does not seem intuitive. This is also true for cell 4, which is grown inverted, and therefore must have the substrate removed prior to fabrication. The benefits are clear when evaluating the CED for substrate re-use: 1 cm^2 of ELO treatment is 0.98 MJ, which is almost 3 times less impactful than the equivalent area of a 4-inch germanium substrate and more than 5 times less impactful than an equivalent area of GaAs substrate.

On the other hand, the trimethyl precursors did not represent a large portion of the impacts in sections 6.3.3.1. Of all the cells, cell 4 showed the highest dependence on precursor CED given that it had the thickest cell stack, but even still only had 6% of its CED from precursors. Across all cells, the percentage of CED attributed to precursors was between 2% to 6% in scenario 1, 1% to 4% in scenario 2, and <1% to 4% in scenario 3. Even if the high-impact precursor conditions and usage (2 μm subcell thickness) used in scenario 1 were substituted in to the low-impact scenario 3, precursors would still only be responsible for 2% to 6% of CED. It is unknown what precursors purity is typically used when manufacturing III-V PV devices, as well as the effects of precursor purity on device performance. It is possible that higher purity precursors would be necessary to achieve high device efficiencies like those studied here, and would require precursors that represent a significantly larger fraction of cell CED.

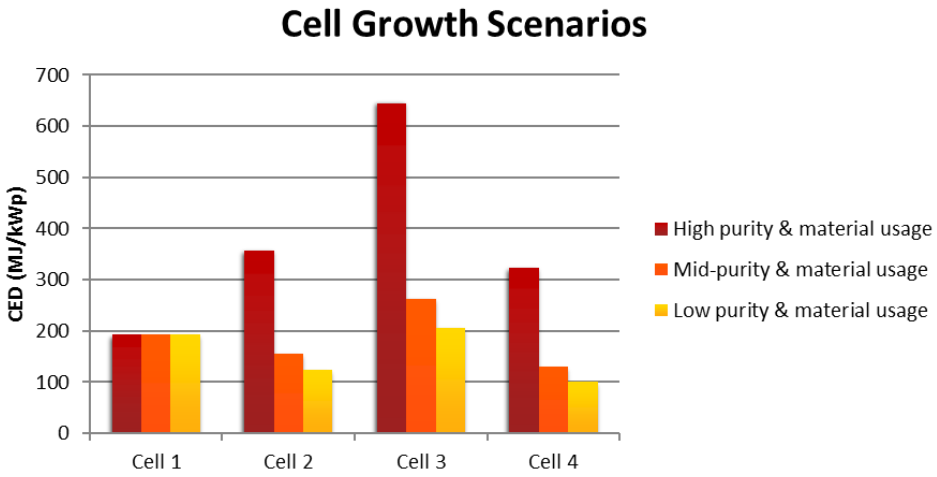

Figure 80: Cell growth CED for multiple scenarios defined in Table 84

Cell 1

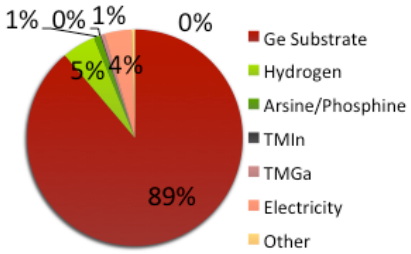

	Cell 2	Cell 3	Cell 4
High	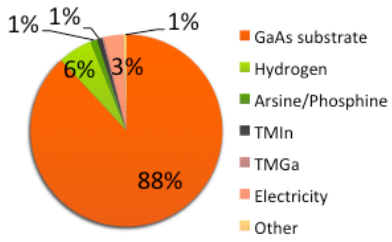	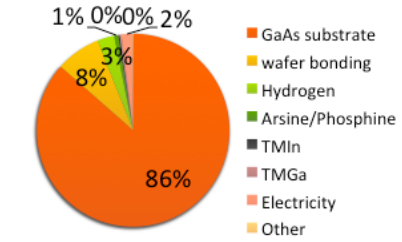	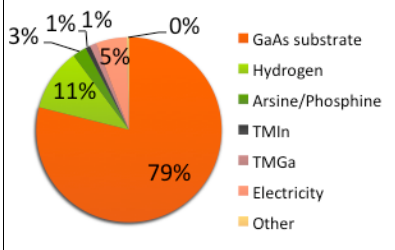
Mid	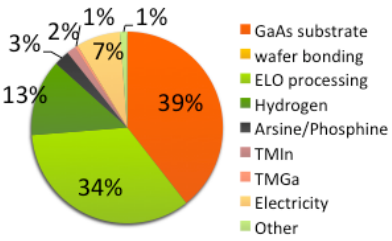	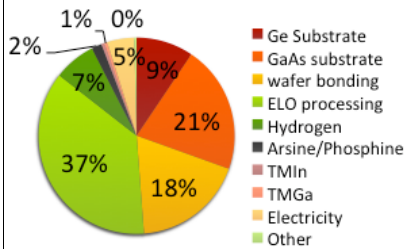	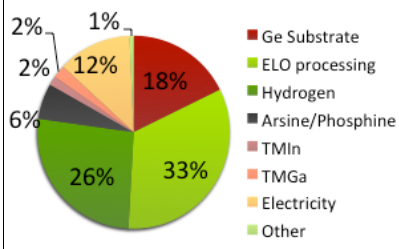
Low	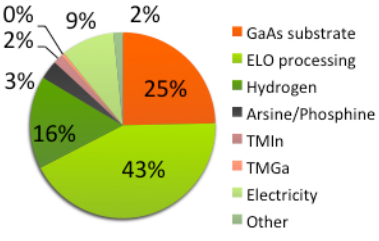	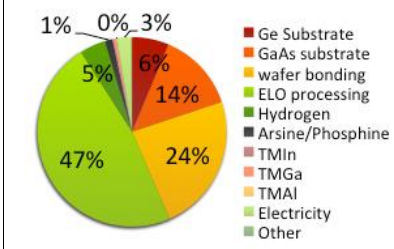	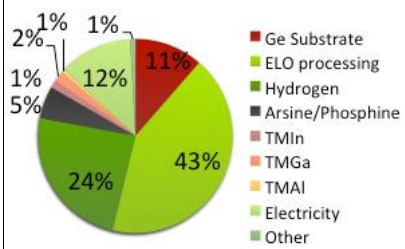

Figure 81: Input contributions to cell growth CED for all cells and scenarios reported in Table 84 in the Appendix

A comparison of the consumption of these metals by the different cells is reported in Table 38, based on the information in Table 28. This data provides a basic analysis of resource depletion associated with each cell type per functional unit. These values assume 1 um subcells where relevant (cells 3 and 4) and 10 re-uses of the substrate, with the exception of cell 1. Cell 1 is clearly the most germanium-intensive, while cell 2 is the most indium,

phosphorus, antimony, and aluminum-intensive, cell 3 is the most gallium and arsenic intensive if a GaAs substrates are employed, but cell 4 is the most gallium and arsenic-intensive if germanium substrates are employed. The substrate poses the most significant resource depletion risks, and would be even more pronounced if no re-use were assumed.

Table 38: III-V elemental demand per kWp for resource depletion analysis

	Cell 1 (mg)	Cell 2 (mg)	Cell 3 (mg) GaAs substrate	Cell 4 (mg) GaAs substrate	Cell 3 (mg) Ge substrate	Cell 4 (mg) Ge substrate
Indium	0.07	13300	11800	0.40	11800	0.40
Gallium	0.22	0.21	8000	7400	0.24	0.57
Arsenic	10	24	8600	8000	16	44
Antimony	--	0.09	--	--	--	--
Phosphorous	1.9	3600	3190	1.3	3190	1.3
Aluminum	--	0.05	0.03	0.03	0.03	0.03
Germanium	62000	--	--	--	4700	4300

6.3.3.2 Cell Fabrication Impact Assessment

The mid-impact cell growth scenario was used as an input into the cell fabrication scenarios defined in section 6.2.2.4. Numerical CED and GHG impacts from the cell fabrication step are reported in Appendix A.3. The CED values are displayed graphically in **Figure 82**. Cell 3 still shows the highest impacts in the low-impact fabrication scenario but is competitive with cell 1 in the high-impact fabrication scenario. The input contributions to cell fabrication CED are shown for each cell and fabrication scenario in **Figure 83**. The low-impact fabrication scenario is dominated by impacts from cell growth, around 92% for each cell with the exception of cell 3 at 95% which has a comparatively larger impact due to its use of multiple substrates. In the high-impact cell fabrication scenario, cell growth is still the largest contributor to CED but is assigned less than half of impacts for all cells with the exception of cell 3, which serves to highlight the outsize role that substrates play in generating cell CED.

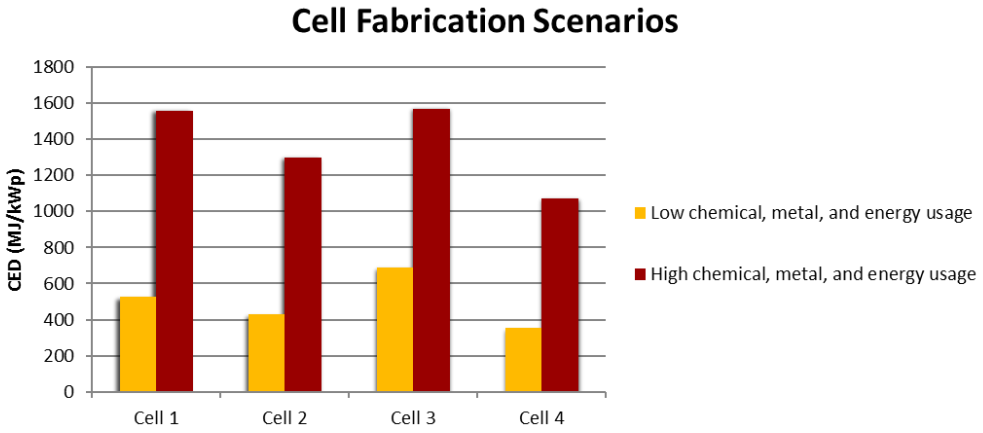

Figure 82: CED from cell fabrication scenarios reported in Table 85, assuming mid-range cell growth scenario from Figure 80

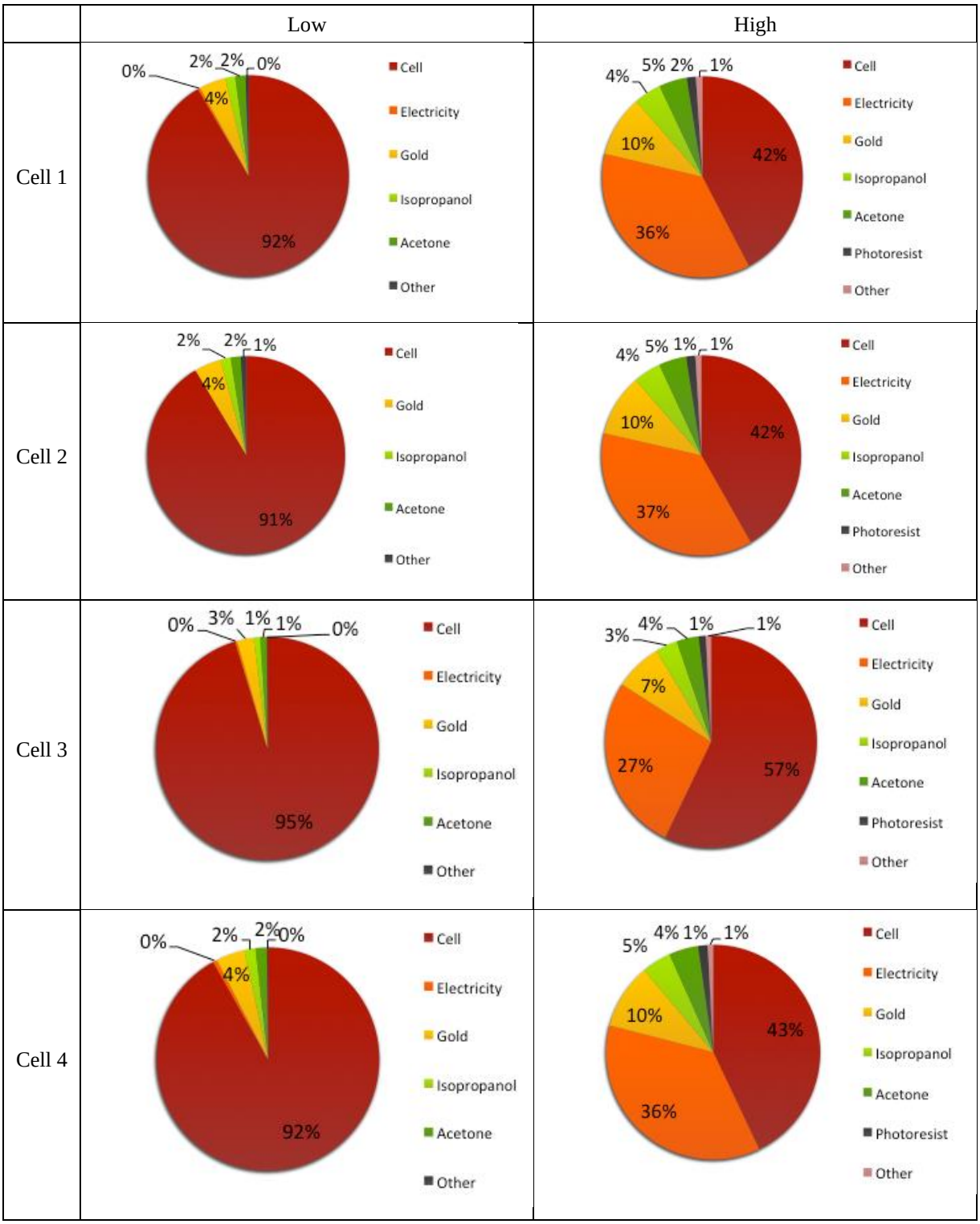

Figure 83: Input contributions to cell processing CED for all cells and scenarios reported in Table 85.

6.3.3.3 Impact Assessment of Module, Tracker, and Balance-of-System Assembly and Installation

The high-impact fabrication scenario was then used as an input into a high-impact scenario for module assembly, tracker assembly, balance-of-system (BOS) and installation. Similarly, the low-impact fabrication scenario was used as an input into a low-impact assembly/install scenario in order to provide an upper and lower range of possible impacts for the system as defined in section 6.2.2.5. A comparison of CED values for each cell and assembly/install scenario is shown in Figure **84**, while the exact CED and GHG emission values for each are reported in the Appendix. At this stage in HCPV manufacturing, the benefits of cell efficiency have become apparent. CED unequivocally decreases as cell efficiency increases. The high-impact scenarios are all approximately 4 times larger than their respective low-impact scenarios.

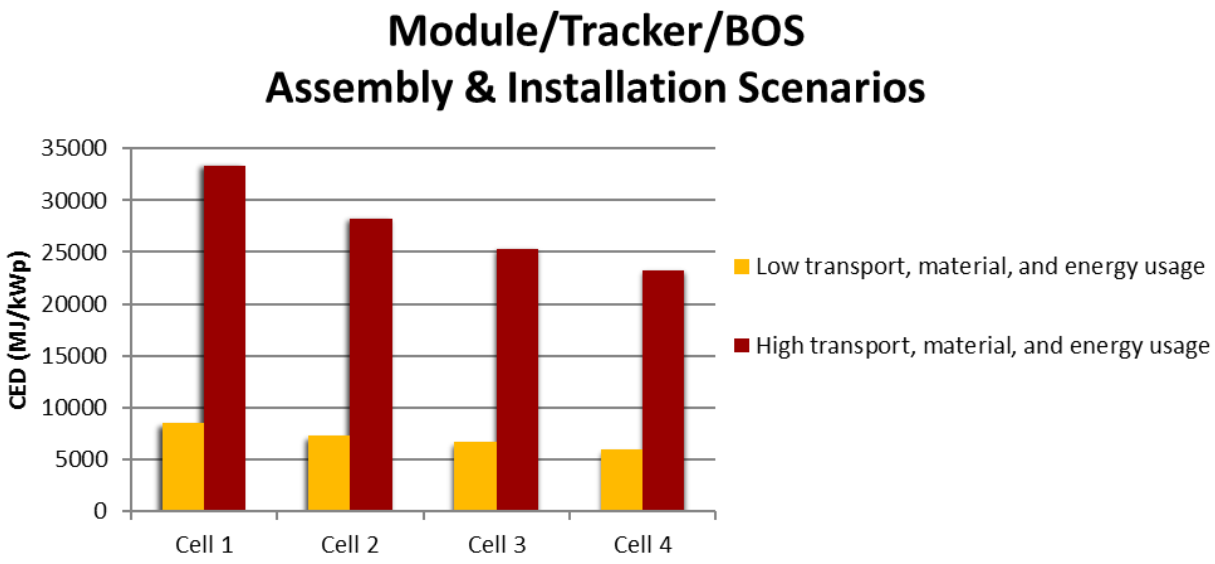

Figure 84: CED from assembly & installation scenarios reported in Table 86, assuming mid-range cell growth scenario

Individual contributions to assembly/install CED are shown in **Figure 85**. In the low-impact assembly/install scenario, the fabricated cell is typically only 6% of CED where the exception is again cell 3, representing 10% of CED. This is consistent with the comparatively large cell 3 impacts in earlier stages of the life cycle. In the high-impact assembly/install scenario this distinction is less pronounced, where cell 3 is only responsible for 6% of CED while all other cells are responsible for 5%.

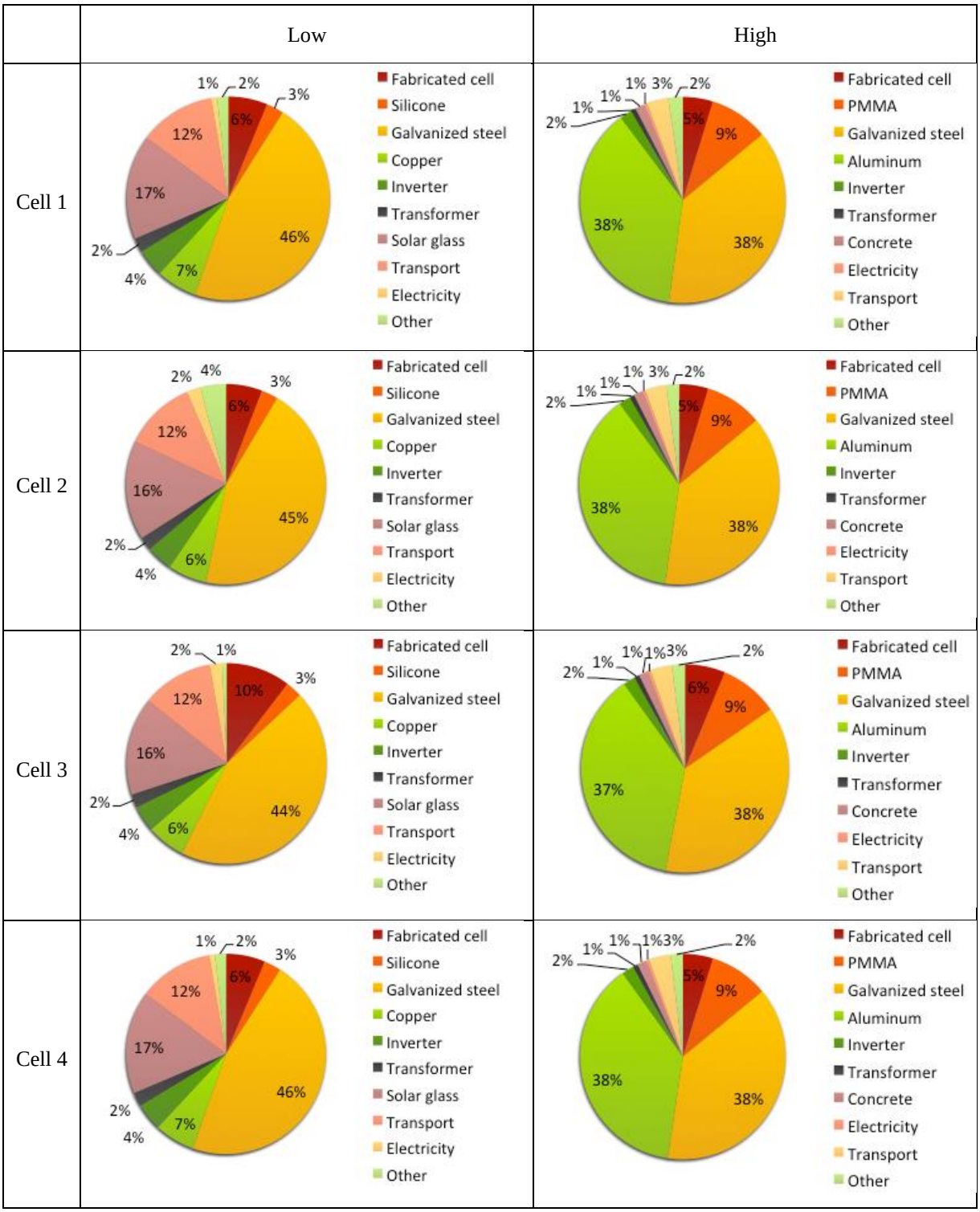

Figure 85: Input contributions to module/tracker assembly & installation CED for all cells and scenarios reported in Table 86

6.3.3.4 Operation and Maintenance Impact Assessment (Total Cradle-to-Use Impacts)

Finally, to create the lower bound for total cradle-to-use impacts, the low-impact assembly/install scenario was used as an input for the operation and maintenance (O&M) scenario as defined in section 6.2.2.6. Similarly, to create a higher bound for total cradle-to-use impacts, the high-impact assembly/install scenario was used as an input for the same O&M scenario. The upper and lower bound of CED for each cell type is displayed graphically in Figure **86**, and the data is reported quantitatively in the Appendix. This figure shows the high-impact scenario is more than twice as large as the low-impact scenario, but all impacts are on the same order of magnitude.

The percentage of CED attributed to cell growth and fabrication is shown as a part of the module CED in Figure 87, and is around 2% of the final CED for a given cell in the low scenario and around 4% in the high scenario. The combination of scenarios where the cell would represent the highest percentage of CED would use cell growth scenario 1, the high-impact cell fabrication scenario, the low impact module/tracker scenario as an input into the O&M scenario. This results in a cradle-to-use CED in which 7%, 10%, 16%, and 11% of impacts are attributed to cell growth and fabrication for cells 1 through 4, respectively. Approximately half of cell impacts are from fabrication inputs unrelated to substrates and MOVPE growth. To place these results in context, the life cycle impacts for cell 1 are most appropriate to compare to previous studies. The reports in [21, 22] assigned 15% and 0.9% of the total CED to the cell, respectively. This is partially due to the fact that [21] is a cradle-to-gate LCA and also slightly overestimates the CED of germanium substrates as compared to [118], while [22] is a cradle-to-grave LCA and severely underestimates the CED of germanium substrates as compared to [118].

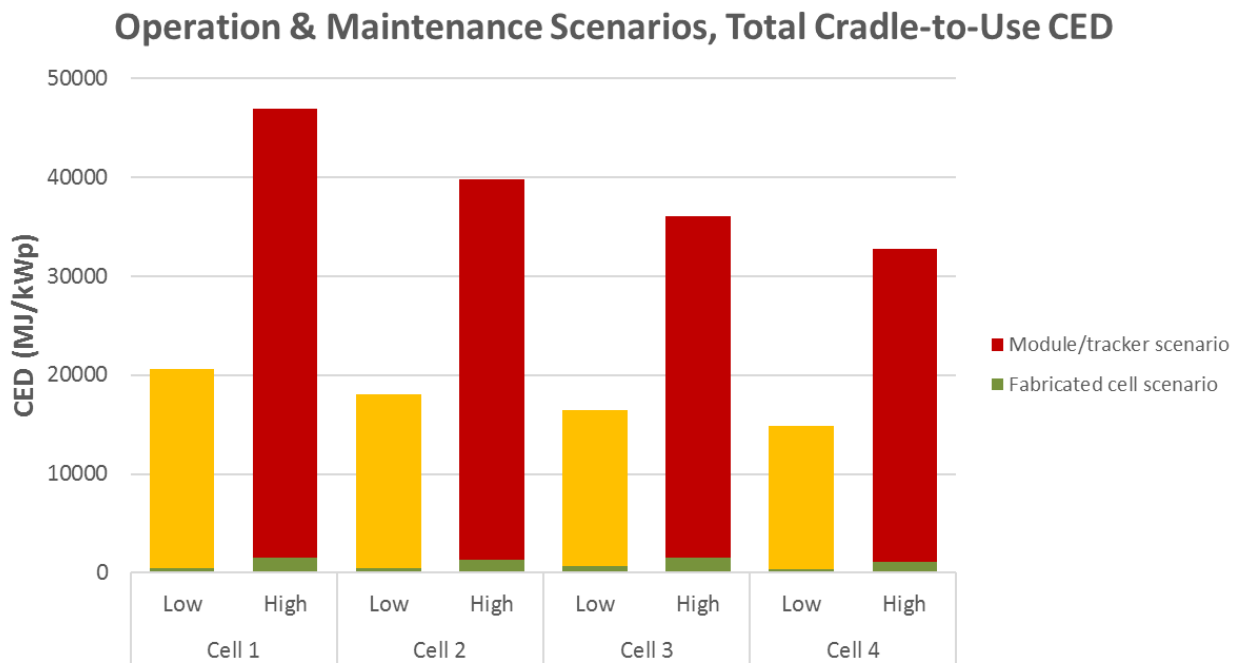

Figure 86: Total cradle-to-use CED for 1 kWp of each cell type under 500x concentration

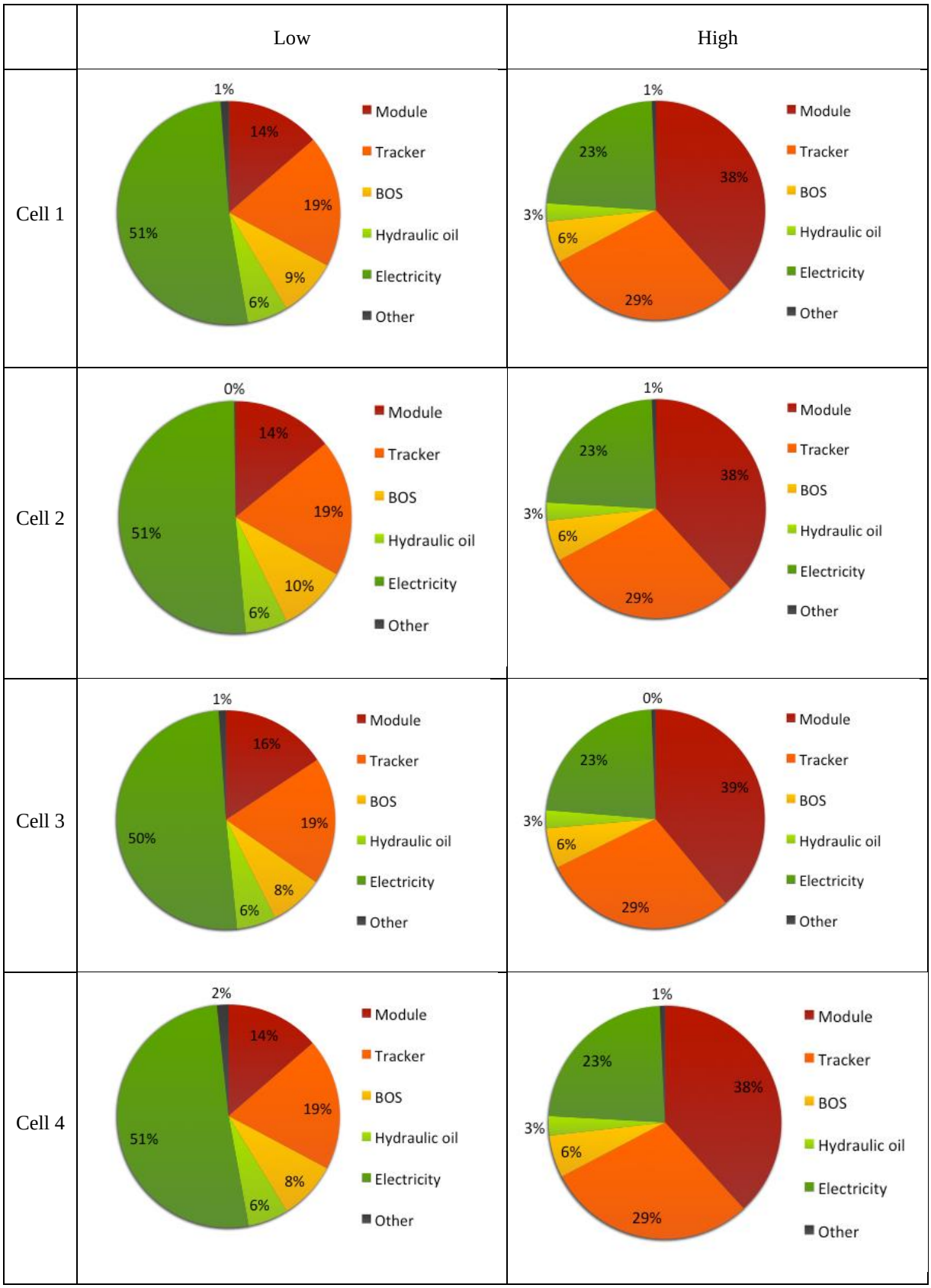

Figure 87: Input contributions to total cradle-to-use CED for all cells and scenarios

The performance of the HCPV system using cell 1 can also be compared to literature, where reference [21] assessed a 6 kWp system which was reported to have a cradle-to-gate CED of 80,266 MJ. The low scenario in this study corresponds to a cradle-to-use CED of 124,200 MJ for the 6 kWp system, while the high scenario corresponds to a cradle-to-use CED of 272,400 MJ for the 6 kWp system. Both of these values are higher than the published value since the use phase is included in the CED. Reference [22] assessed a 53 kWp system, which was reported to have a cradle-to-grave CED of 1,664,733 MJ. The low scenario in this study would generate a CED of 1,097,100 MJ for a 53 kWp system, while the high scenario would generate a CED of 2,406,200 MJ. The average of these values is approximately 1,750,000 MJ, which approximates the published value for the 53 kWp system.

When comparing a 1 kWp system employing cell 1 (in either the high or low scenario), the total CED is 15% less for a 1 kWp system using cell 2, 24% less for a 1 kWp system using cell 3, and 30% less for a 1 kWp system that uses cell 4. This scales directly with the decrease in area needed per functional unit. It should be noted that these comparisons do not address any dependence of impacts on module size, but merely represent an average of known system impacts across a given power output. For example, it may be the most materially efficient to build modules that are 10 meters by 10 meters in size, so to compare modules of the same power output would require deviation from this optimal size and therefore increase impacts. The relationship between CED and HCPV system efficiency (based on cell efficiency) is shown in **Figure 88** for both the lower and upper bound of the entire cradle-to-use life cycle. The R^2 value for a linear regression is greater than 99% which represents an adequate description of the data. Ultimately, the results of this LCA indicate that in the context of known high-efficiency cell designs under development today, improvements in cell efficiency consistently result in improvements in the overall life cycle of the HCPV system. There is no tradeoff between high-efficiency cell designs and environmental impact.

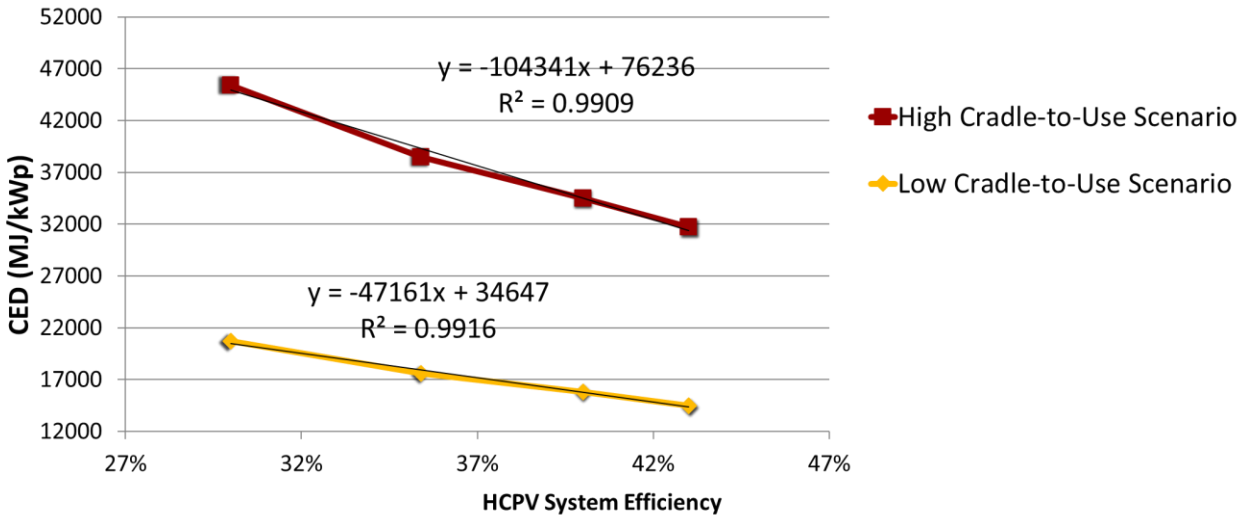

Figure 88: CED dependence on HCPV system efficiency per kWp

6.4 Interpretation

6.4.1 GaAs Substrate

The GaAs substrate life cycle impacts presented in this study were created from a detailed model of the current manufacturing technique, which has not been executed previously in literature. Therefore, this model can be expected to have produced results with a higher degree of accuracy than previous literature which relied on estimates that were not based on a detailed investigation the manufacturing process. Previous literature also relied on some parameters that have become outdated as the industry has matured, such as a smaller diameter of wafer production or use of the liquid-encapsulated Czochralski crystallization technique. As such, the unit of manufacture in this study (one 6-inch GaAs substrate) does not form a direct comparison with previous LCAs of GaAs substrates, which considered 2-inch substrates that are typically half as thick [132, 135]. To circumvent this, the CED per m^2 of GaAs wafers can be compared, and values are reported in Table 39.

Table 39: Comparison of GaAs substrate CED against literature

	6-inch GaAs (Current Study)	2-inch GaAs [132]	Germanium [118]	Silicon [125]
CED comparison (GJ/m^2)	39.1	9.6	27	3.2

This study produced a CED of 39.1 GJ/m^2 of 6-inch GaAs wafers, while [132, 135] produced a CED of approximately 9.6 GJ/m^2 of 2-inch GaAs wafers. However in [132], the majority of the CED was attributed to arsenic, and secondarily to the energy for crystallization, which is a significant departure from the results produced in this study. Creating arsenic model based on [140] corresponds to a CED of 16.5 MJ/kg, which resulted in CED of 133 MJ/kg for 7N arsenic. This is lower than previous GaAs-wafer LCAs which modeled the arsenic chloride route of purification instead, where the CED for 6N arsenic was approximately 1000 MJ/kg when using mass allocation [132], and approximately 700 MJ/kg when using economic allocation [135]. For reference, previous studies report 6N gallium to have a CED around 200 MJ/kg (which used mass allocation) [132], and 3000 MJ/kg (using economic allocation) [135], while in this study the ecoinvent 6N gallium had a CED of 2640 MJ/kg, while the modeled 7N gallium process had a CED of 3830 MJ/kg.

The implications of the larger impact result in this study highlight the benefits of substituting other substrates such as germanium where possible. As evidenced in section 6.3.3.1, substrates played a large role in the cell-level impacts for all cells in all scenarios. This was especially pronounced when a GaAs substrate was part of the cell structure. The GaAs result from this study was 1.5 times larger than the CED reported for an equivalent area of germanium substrates and 12 times larger than that of silicon wafers. A detailed analysis of a 4-inch germanium wafer reported the CED to be 216 MJ/wafer, which corresponds to 27 GJ/m^2 [118], while a 6-inch silicon wafer produced for photovoltaic applications has a CED of 78.7 MJ/wafer (or 3.2 GJ/m^2) available in ecoinvent [125]. Though the environmental performance of GaAs substrates is poor as compared to other substrates, it is mitigated by the fact that substrates are not ultimately influential in the overall CED of an HCPV system. However, this would not be the case in non-concentrator applications such as one-sun PV or LEDs. As such, the GaAs substrate impacts reported in this study will be valuable for life cycle assessments regarding such technologies in the future. These

comparisons provide additional motivation and context for current research regarding the re-use or replacement of III-V substrates, such as advanced epitaxial lift off procedures or tandem III-V devices grown on silicon substrates.

6.4.2 Trimethyl precursors

The life cycle impacts reported for trimethyl precursors in this study resulted from a detailed model of the manufacturing process for these compounds. As such, this study represents a completely new approach to reporting the impacts of these compounds whereas previously in literature, life cycle data from a "generic metal organic" was used as a substitute, or impacts from the group III metals alone were considered to be acceptable approximations. In Table 40, the impacts from this study are compared to previous literature in order to evaluate the differences between approximations versus a detailed LCA.

Table 40: Comparison of trimethyl precursor impacts against literature (where x is defined as results from this study)

CED comparison	Current Study (MJ/kg)	Reference [21] (MJ/kg)	Reference [22] (MJ/kg)
Trimethylgallium	2020 - 3420	0.1x	0.25x
Trimethylindium	2740 - 5260		

A study on the energy payback time for a terrestrial concentrator PV system reported the total CED for all metal organics used in the production of the system estimated to be 2 MJ [21]. The system required 16.5 4-inch germanium wafers, given the 5110 MJ total CED for germanium wafers, the stated electricity demand of 100 MJ for each wafer, and accounting for the "electricity-to-CED" ratio of 2.9 MJ CED/MJ of electricity. This corresponds to approximately 7.3g TMGa and 1.9g of TMIn when using basic assumptions regarding cell structure and material efficiency. Using the "high purity TMAl, solvent reclaim" scenario results from this study, the total CED of 7.3g TMGa and 1.9g of TMIn is 21.7 MJ. This is an order of magnitude larger than the original estimation, but given the total CED for the system under consideration was 80,266 MJ, it can be concluded that the estimate for the CED of metal organics in [21] was reasonable given the size of the system under study.

An LCA of a similar system and cell type in [22] used 150 4-inch germanium wafers, and reported the total CED for precursors in their system to be 160 MJ. Again, using basic assumptions regarding cell structure and material efficiency, this corresponds to 17g TMIn, 66g TMGa, 1.9 kg arsine, and 0.34 kg phosphine. Using the results from the "high purity TMAl, solvent reclaim" scenario and the ecoinvent 3.4 entries for arsine and phospine, this corresponds to a total of 550 MJ for their system. This is almost 4 times larger than their reported figure, but ultimately corresponds to less than 4% of their total reported cell impacts, which comprises less than 1% of their system impacts.

In conclusion, the increased accuracy of this study resulted in precursor impacts that are 4 to 10 times larger than previous estimates but are still typically less than 1% of the impacts from the systems under study. This implies metal organic precursors are not a strong target for environmental performance improvements within the concentrator applications that have been examined by life cycle assessments to date. However, the enhanced accuracy of the results from this study will be more significant for other products which require a larger proportion

of metal organic precursors, such as one-sun PV applications. This would be especially pronounced if such applications required precursors with higher purity levels than the ones modeled in this study.

6.4.3 HCPV System

In order to provide context for the results in this study, Table 41 summarizes the novel findings in this study and compares them to previous literature and other technologies. The results from fabricating cell 1 in this study can be compared to previous literature, where the range of cell impacts from this study falls within the range of cell impacts reported in literature. This reasonably corroborates the model in this study, since the two publications under comparison modeled a cradle-to-gate life cycle and a cradle-to-grave life cycle, respectively.

The fabricated cell impacts for all four cells can be used as an initial estimate for the impacts per kWp if these cells were under 1 sun illumination only. This results in impacts that are 12 to 23 times larger if no concentrating lenses were used and instead more cell area was used to generate an equivalent amount power (1 kWp). Furthermore, this is without assessing impacts of non-concentrator module materials and installation, which would form an even greater contrast. This indicates that III-V cells in non-concentrator applications are definitively less sustainable and more energy intensive, which validates the fact that they are only used in applications where lightweight power density is necessary, such as space and mobile applications.

Table 41: Comparison of HCPV impacts against literature

CED comparison	Current Study (GJ/kWp under 500x)	Reference [21] (GJ/kWp under 500x)	Reference [22] (GJ/kWp under 500x)
Cell 1 - fabricated	0.5 – 1.6	2	0.3

CED comparison	Current Study (GJ/kWp under 500x)	Current study, fabricated cells only (GJ/kWp under 1 sun)	Cell 1 reference [21] - [22] (GJ/kWp under 500x)	Silicon under 1-sun (GJ/kWp) [125]
Cell 1 system	20.7 – 45.4	267 - 785	13.4 – 31.4	4.2 "Photovoltaic flat-roof installation, 3kWp, single-Si, on roof {GLO}| market for | APOS"
Cell 2 system	17.6 – 38.5	220 - 655		
Cell 3 system	15.8 – 34.5	351 - 795		
Cell 4 system	14.5 – 31.7	189 - 550		

Finally, when comparing to the dominant photovoltaic technology (single crystalline silicon), the concentrator system CED values are between 3 to 11 times larger, which underscores the importance of developing III-V concentrator PV with more efficient cells and lower impact system components. Helpful design considerations can be inferred by evaluating the impacts from the module and tracker assembly in this study. For example, the use of copper for a heat sink is significantly less impactful than aluminum, although in this study it is assumed that the aluminum is from a primary source. Also, Fresnel lenses made from silicon and solar grade glass are less impactful than lenses made from PMMA. Some of these options are included in the more recent HCPV module design

published in [121], which intentionally designed a lightweight module with a goal of materials reduction. This type of HCPV design progress will be necessary in order for III-V PV to compete with silicon at a utility-scale level.

6.5 Conclusion

A cradle-to-use LCA of advanced III-V photovoltaic cell designs in high concentration applications was conducted in order to determine if there is a point at which energy and material investments in cell efficiency no longer correlate to improvements in the overall environmental performance across the life cycle of the HCPV system. Four cell designs were studied that increase in sequentially in power conversion efficiency: the first represents a control that is commercially available and has been studied previously in LCA literature, the second uses novel materials and substrates, the third uses multiple substrates, and the fourth contained the greatest mass and volume of III-V photovoltaic material.

In order to provide a more precise figure on the impact of III-V photovoltaic cell production, a detailed LCA of metal organic precursors was conducted, specifically for trimethylaluminum, trimethylgallium, trimethylindium, and trimethyl antimony. The CED of these chemicals was on the order of 1000 - 3000 MJ/kg for these chemicals, which is 4 to 10 times larger than previous approximations in literature. A detailed LCA of GaAs substrate manufacturing was also modeled to contribute to the cell designs that require alternative substrates. The resulting CED was 951 MJ/ 6-inch GaAs wafer, which is approximately 3 times the CED of an equivalent area of a germanium substrate, and approximately 12 times the CED of a 6-inch silicon wafer.

Finally, the life cycle of the four cells proposed above was modeled in four stages: cell growth, cell processing, HCPV system assembly and installation, and finally, operation and maintenance over a 30 year lifespan. The four cells were modeled using a functional unit of 1 kWp to account for differences in their power conversion efficiency. The LCAs for the precursors and substrate conducted in this study were used as inputs in the cell growth stage, along with energy and usage of other materials from literature. The remaining three stages were also estimated from literature. Multiple scenarios for each life cycle stage were modeled to represent an upper and lower bound of possible impacts based on what has been reported in literature. The substrates proved to be the most impactful component of the cell, while the precursors had a very minimal role. However, on the scale of the HCPV systems, the III-V cells only represented up to 5% of life cycle impacts. Ultimately, in either the high or low scenario, the total HCPV system CED is 15% less if cell 2 were used in place of cell 1, 23% less if cell 3 were used, and 30% less if cell 4 were used. The HCPV system with the lowest CED in this study is approximately an order of magnitude larger than the CED of a monocrystalline silicon PV system with an equivalent power rating, which indicates further optimization of III-V HCPV systems is necessary to compete with the dominant silicon PV technology.

CHAPTER 7: Summary & Future Work

III-V semiconductors have high material quality and make for highly efficient solar cells, but are expensive to produce and must be further optimized in order to be competitive with other photovoltaic materials. Mechanisms for improving III-V photovoltaic performance in this dissertation focused on development of an InAlAsSb material for a mulitjunction design with the potential of achieving 52.8% efficiency under 500 suns, and the integration of InAs quantum dots in a GaAs solar cell in conjunction with light management with the potential to increase current by 2.5 mA/cm^2, increase voltage due to photon recycling, and progress toward the intermediate band solar cell which could exceed conventional single-junction efficiency limits. Furthermore, a life cycle assessment of these technologies was performed in order to address the broader research question, which is to identify optimum conditions at which energy investments in cell performance no longer correspond to improvements in the overall life cycle performance of the PV system.

7.1 InAlAs

Development of a single-junction InAlAs cell lattice-matched to InP was executed as a preliminary goal towards the development of InAlAsSb. The cell design was developed by leveraging existing device results in literature, in-house bulk material characterization, and physics-based device simulations. This design built off of previous InAlAs solar cells in literature by incorporating a protective etch stop above the high-aluminum content window to prevent the window from oxidizing. This etch stop could then be selectively removed immediately before depositing an ARC. A material-specific etch process was developed for the proposed design. This design was then grown by MOVPE using industry-standard precursors, fabricated, and tested which resulted in an unprecedented efficiency measurement of 17.9% under 1-sun AM1.5 for the InAlAs material. Based on these extracted diffusion lengths, a further optimized device design is proposed for any future research efforts on this material.

InAlAs was also grown using alternative MOVPE precursors in order to transition to the InAlAsSb quaternary. Bulk material was grown using alternative aluminum and arsenic precursors and compared to material grown with industry-standard precursors, where the industry standards were TMAl and arsine, while the alternatives were TTBAl and TBAs. Multiple sets of samples were grown with either precursor with varying growth conditions such as growth temperature, growth rate, and V/III ratio. These bulk materials were sent out for analysis by SIMS to quantify impurity concentrations of carbon and oxygen. When comparing arsenic precursors, impurity concentrations measured by SIMS decrease as the V/III ratio increases, and as growth temperature increases. Oxygen incorporation associated with arsine is comparable to that of TBAs, whereas carbon incorporation is definitively less for arsine as compared to TBAs under the conditions studied. TMAl exhibits an inverse impurity dependence on V/III ratio while TTBAl growths did not exhibit such a dependence, impurity concentrations remained virtually constant regardless of V/III ratio. The impurity independence of TTBAl at low V/III ratios make it a desirable candidate for other alloys that may require low V/III ratios, such as antimony-containing alloys.

Finally, single-junction $In_{0.52}Al_{0.48}As$ solar cells were grown using the alternative precursors and fabricated in parallel to devices grown with the standard precursors to control for variation in fabrication runs. Three devices

were compared, the first using TMIn/TMAl/arsine, the second TMIn/TTBAl/arsine, and the third TMIn/TTBAl/TBAs. Devices grown with TMAl had a higher V_{oc}, a lower dark current, and a two diode region dark-IV curve which reflects better material quality. However, cells grown with TTBAl show enhanced J_{sc} and spectral response as compared to those grown with TMAl. Devices grown with TTBAl show exceptional carrier lifetimes throughout the device due to significant improvements in diffusion length, and would benefit from time-resolved photoluminescence measurements to empirically verify lifetimes in future work.

7.2 InAlAsSb

An extensive literature review, composition analysis, and surface characterization contributed to the development of InAlAsSb growth by MOVPE. This work informed the growth conditions necessary for compositional control and high-Sb content InAlAsSb. Specifically, this included low growth temperatures and low V/III ratios, which necessitated the use of alternative precursors with low pyrolysis temperatures to be substituted in the place of more standard industry precursors that have higher pyrolysis temperatures. Use of these alternative precursors resulted in both higher incorporation of Sb and mitigated surface morphology issues.

Multiple bandgap characterization techniques including photoluminescence, UV-Vis transmission, and photoreflectance spectroscopy were used to evaluate InAlAsSb samples. Photoreflectance proved to be the most promising technique, where spectroscopic features were consistently evident in origin. Measurements of multiple known-composition InAlAsSb samples corresponded to bandgap values predicted by a quaternary-composition dependent predictive model based on band parameters developed in [10]. Photoreflectance was used to verify a 1.82 eV bandgap on an InAlAsSb sample which approximated the target composition for the top cell in a InP-lattice-matched triple junction solar cell. Furthermore, photoreflectance was used on MBE-grown InAlAsSb from collaborators to assist in an MBE growth temperature study and informed collaborator's subsequent annealing experiments.

7.3 Back surface reflectors on quantum dot solar cells

Multiple textured back surface reflectors (BSRs) were developed for light management in quantum dot solar cells (QDSCs). These BSRs were fabricated on QDSCs by growing devices inverted on epitaxial lift-off templates and then texturing the rear surface, while cells with a flat back surface served as a control. A texture similar to that which was executed as a back surface reflector in GaAs for quantum well solar cells [14] has been developed in $Al_{0.1}Ga_{0.9}As$ for application to quantum dot solar cells. This texture varied in one dimension across the back surface of the device and is created using a photoresist pattern and a crystallographic etchant. Variations in etch time produce slight differences in texture which decrease the proportion of light that specularly reflected and increase the proportion of light that is reflected at angles below the critical angle for total internal reflection. The open circuit voltage was greater for the devices with the textured BSRs than the flat BSR, which indicates a greater degree of photon recycling. The longest etch time show the greatest sub-band current, representing a 40% increase over the flat BSR. Interference fringes in the EQE and EL data indicate a reduced effect of destructive interference in the

cavity modes when comparing the textured BSR to the flat BSR as well as a decreased effective cavity thickness. Optimization of inverted QDSC growth conditions was also performed via a cell design study, where it was concluded that anneal has a minor effect on emission from QDs and increased period thickness in the superlattice severely limits collection from QDs, while using an inverted design resulted in a higher open-circuit voltage but also a greater degree of voltage degradation with the inclusion of QDs.

Next, a texture that varies in two dimensions across the surface of the device was developed in order to increase the optical path length further. This texture followed a similar procedure to the one-dimensional texture described above. Additionally, a procedure for coating the texture with a dielectric (while also making contact to the device) was developed in order to increase the reflectivity of the rear contact metal. A set of QDSCs were grown inverted on ELO templates, where one was left with a flat back surface as a control, a second was textured with the two-dimensional pattern, and the third was also textured with the two-dimensional pattern and also included a dielectric interlayer. Ultimately, the ELO process destroyed the sample with the dielectric layer due to the selective ELO etchant, but the remaining two-dimensional BSR devices showed a 20% sub-band current improvement over the control devices with flat BSRs. Finally, a maskless crystallographic etch that has been studied for GaAs was optimized for AlGaAs so that a more random texture could be achieved in order to increase the optical path length even further. Characterization of this texture and testing on fabricated devices should be executed in future to further enhance the optical path length in this material system.

7.4 Life cycle assessment of III-V photovoltaics

A cradle-to-use LCA of advanced III-V photovoltaic cell designs in high concentration applications was conducted in order to determine if there is a point at which energy and material investments in cell efficiency no longer correlate to improvements in the overall environmental performance across the life cycle of the HCPV system. Four cell designs were studied that increase in sequentially in power conversion efficiency and required some combination of increased material inputs and increased energy inputs. In order to provide a more precise figure on the impact of III-V photovoltaic cell production, a detailed LCA of GaAs substrates and group-III metal organic precursors was conducted. The GaAs substrate CED was 951 MJ per 6-inch wafer, which was approximately 4 times greater than previous values published in literature for a similar area and typically represented more than 30% of III-V cell CED. The CED of the metal organic precursors was 4 to 10 times larger than previous approximations in LCA literature, but ultimately played a small role in III-V cell CED.

Finally, the life cycle of the four cells proposed above was modeled over a 30 year lifespan. The four cells were compared using a functional unit of 1 kWp to account for differences in their power conversion efficiency. Each stage in the life cycle was modeled to approximate an upper bound of possible impacts based on what has been reported in literature, and a second version was modeled represented a lower bound. Ultimately, in either the high or low-impact life cycle scenarios, the III-V photovoltaic cells were shown to only represent up to 5% of the total HCPV system CED. This resulted in HCPV system CED values that decreased in direct proportion to any increase in cell efficiency.

SUMMARY OF ACADEMIC ACHIEVEMENTS

Fellowships and internships

- NASA Space Technology Research Fellowship, 2015 – 2018.
- LERCIP Internship, NASA Glenn Research Center, June-August 2013

Refereed journal publications

1. **Brittany L. Smith**, Callie W. Babbitt, Kelsey A. W. Horowitz, Gabrielle Gaustad, Seth M. Hubbard, "Life Cycle Assessment of III-V Precursors for Photovoltaic and Semiconductor Applications," *MRS Advances*, *3*(25), 1399-1404 (2018). doi:10.1557/adv.2018.287
2. **Brittany L. Smith,** Zachary S. Bittner, Staffan D. Hellstroem, George T. Nelson, Michael A. Slocum, David V. Forbes, Seth M. Hubbard, "InAlAs photovoltaic cell design for high device efficiency," Progress in Photovoltaics: Research and Applications, Accepted March 2017.
3. Michael Slocum, David V. Forbes, Glen C. Hillier, **Brittany L. Smith**, Jessica G. Adams, Seth M. Hubbard, "Development of InAlAsSb growth by MOVPE," Journal of Crystal Growth, In Review Feb 2017.

Conference Proceedings

1. **Smith, B. L.,** Nelson, G. T., Dai, Y., Slocum, M. A., Wibowo, A., Tatavarti, R., Hubbard, S. M. "Development of Back Surface Texture for Light Management in Epitaxial Lift Off (ELO) Quantum Dot Solar Cells," *Proceedings of 44th IEEE Photovoltaic Specialists Conf.*, Washington, DC (2017).
2. **Smith, B. L.,** Slocum, M. A., Bittner, Z. S., Dai, Y., Nelson, G. T., Hellstroem, S. D., Tatavarti, R., Hubbard, S. M. "Inverted Growth Evaluation for Epitaxial Lift Off (ELO) Quantum Dot Solar Cell and Enhanced Absorption by Back Surface Texturing," *Proceedings of 43rd IEEE Photovoltaic Specialists Conf.*, Portland, OR, (2016).
3. Dai, Y., Hubbard, S. M., Hellstroem, S. D., **Smith, B. L**, Slocum, M. A., Forbes, D. V. "Optimization of Wide-band-gap InAs/InGaP Quantum Dot Solar Cells," *Proceedings of 43rd IEEE Photovoltaic Specialists Conf.*, Portland, OR, (2016).
4. Slocum, M. A., Nelson, G. T., Hellstroem, S. D., **Smith, B. L.,** Tatavarti, R., Hubbard, S. M. "Growth of InAs Quantum Dots in a Metamorphic InGaAs Bottom Cell of an Inverse Metamorphic Solar Cell," *Proceedings of 43rd IEEE Photovoltaic Specialists Conf.*, Portland, OR, (2016).
5. **Smith, B. L.,** Bittner, Z. S., Hellstroem, S. D., Slocum, M. A., Hubbard, S. M., Forbes, D. V. "InAlAs solar cells grown by alternative MOVPE precursors," *Proceedings of 42nd IEEE Photovoltaic Specialists Conf.*, New Orleans, LA, (2015).
6. **Smith, B. L.,** Hellstroem, S. D., Nelson, G. T., Bittner, Z. S., Slocum, M. A., Forbes, D. V., Hubbard, S. M. "Characterization of InAlAs solar cells grown by MOVPE." *Proceedings of 40th IEEE Photovoltaic Specialist Conference*, pp. 1180-1185. Denver, CO, IEEE (2014).
7. Nelson, G. T., Bittner, Z. S., **Smith, B. L.,** Forbes, D. V., Hubbard, S. M. "Study of deep levels in InAlAsSb grown via organometallic vapor phase epitaxy." *Proceedings of 40th IEEE Photovoltaic Specialist Conference*, pp. 1168-1173. Denver, CO, IEEE (2014).
8. **Smith, B. L.,** Hoven, N. M., Hillier, G., Hubbard, S. M., Forbes, D. V. "OMVPE of InAlAs Using Alternative Al and As Precursors." In *MRS Proceedings*, vol. 1635, pp. 63-68. Cambridge University Press, 2014.

Presentations (*indicates invited, underline indicates presenter)

1. Smith, B. L., Horowitz, K., Babbitt, C. W., Gaustad, G., Hubbard, S. M., "Life cycle assessment and techno-economic analysis of III-V precursors for photovoltaic and semiconductor applications," MRS Fall Meeting, Boston, MA, (2017).

2. *Smith, B. L., Horowitz, K., Heath, G., Babbitt, C. W., Hubbard, S. M., "Techno-economic analysis and life cycle assessment of GaAs substrates and MOVPE precursors," National Renewable Energy Laboratory, Golden, CO, August 2017.
3. Hubbard, S. M., Smith, B. L., Nelson, G. T., Dai, Y., Slocum, M. A., Wibowo, A., Tatavarti, R., "Development of Back Surface Texture for Light Management in Epitaxial Lift Off (ELO) Quantum Dot Solar Cells," 44th IEEE Photovoltaic Specialists Conf., Washington, DC (2017).
4. Dai, Y., Smith, B. L., Slocum, M. A., Bittner, Z. S., Kum, H., Hubbard, S. M., "Temperature and voltage bias dependent two step photon absorption in InAs/GaAs/Al0.3GaAs quantum dot in a well solar cells," 44th IEEE Photovoltaic Specialists Conf., Washington, DC (2017).
5. Smith, B. L., Nelson, G. T., Slocum, M. A., Dai, Y., Bittner, Z. S., Tatavarti, R., Hubbard, S. M., "Back surface patterning for enhanced absorption in epitaxial lift-off quantum dot solar cells," SPIE Photonics West Conference, San Francisco, CA. January, 2017.
6. Smith, B. L., Bittner, Z. S., Nelson, G. T., Slocum, M. A., Dai, Y., Tatavarti, R., Hubbard, S. M., "Sub-band Absorption Enhancement in Epitaxial Lift-Off Quantum Dot Solar Cell by Back Surface Texturing," NASA Space Photovoltaics Research and Technology Conference, Cleveland, OH, (2016).
7. Smith, B. L., Nelson, G. T., Dai, Y., Slocum, M. A., Bittner, Z. S., Hellstroem, S. D., Tatavarti, R., Hubbard, S. M., "Enhanced absorption in epitaxial lift off quantum dot solar cells by back surface texturing," 43rd IEEE Photovoltaic Specialists Conf., Portland, OR, (2016).
8. * Dai, Y., Hubbard, S. M., Hellstroem, S. D., Smith, B. L, Slocum, M. A., Forbes, D. V. "Optimization of Wide-band-gap InAs/InGaP Quantum Dot Solar Cells," 43rd IEEE Photovoltaic Specialists Conf., Portland, OR, (2016).
9. Hubbard, S. M., Smith, B. L., Slocum, M. A., Bittner, Z. S., Nelson, G. T., Forbes, D. V. "Growth of InAlAs and InAlAsSb by MOVPE for photovoltaic applications," 18th International Conference on Metal Organic Vapor Phase Epitaxy, San Diego, CA (2016).
10. Slocum, M. A., Smith, B. L., Bittner, Z. S., Tatavarti, R., Hubbard, S. M. "Development of Epitaxial Lift-off Inverted Metamorphic Quantum Dot Solar Cell," 18th International Conference on Metal Organic Vapor Phase Epitaxy, San Diego, CA (2016).
11. Smith, B. L., Bittner, Z. S., Hellstroem, S. D., Slocum, M. A., Nelson, G. T., Forbes, D. V., Hubbard, S. M., "Optical and electronic characterization of InAlAs and InAlAsSb grown by MOVPE for photovoltaic applications," SPIE Photonics West Conference, San Francisco, CA. February, 2016.
12. Bailey, C. G., Babcock, S. J., Lichty, M., Rajan, G., Ashrafee, T., Marsillac, S., McClure, E. L., Bittner, Z. S., Smith, B. L., Hubbard, S. M., Maximenko, S., Walters, R. J. "Thin-Film Vapor-Liquid-Solid Growth of III-V Materials for Photovoltaics," SPIE Photonics West Conference, San Francisco, CA. February, 2016.
13. Smith, B. L., Bittner, Z. S., Hellstroem, S. D., Slocum, M. A., Hubbard, S. M., Forbes, D. V. "InAlAs solar cells grown by alternative MOVPE precursors," 42nd IEEE Photovoltaic Specialists Conf., New Orleans, LA, (2015).
14. Smith, B. L., Bittner, Z. S., Hellstroem, S. D., Hubbard, S. M., Forbes, D. V. "Development of InAlAs solar cell towards integration as top cell in triple-junction photovoltaic designs," NASA Space Photovoltaics Research and Technology Conference, Cleveland, OH, (2014).

Awards

- Best Student Presentation Award, Area 1: Fundamentals and New Concepts for Future Technologies, IEEE Photovoltaics Specialists Conference, Portland, OR, 2016.
- Best Poster Award, Area 3: III-V on Silicon and III-V Materials for Solar Cells, IEEE Photovoltaics Specialists Conference, Denver, CO, 2014.

APPENDIX

A.1 Supporting information for life cycle of metal organic precursors

Table 42: Material input-output table for trimethylaluminum 98% pure

Input	Amount	Unit	Model source	Database entry	Assumptions
Methyl aluminum sesquichloride	82.6	kg	[160]	See **Table 44**	
4:5 Sodium/Potassium melt	27	kg	[160]	Sodium {GLO}| market for | APOS [125]	Potassium unavailable in ecoinvent, use equivalent mass of sodium
Nitrogen	825	g	[160]	Nitrogen, liquid {RoW}| market for | APOS [125]	
n-decane solvent (or xylene or mineral oil)	153.1	kg	[147, 160]	White mineral oil, at plant/RNA [162]	Estimated mass, no re-use (90% re-use = 15.3 kg)
Electricity	5.1	kWh	[160]	Electricity, low voltage, {GLO}| market group for | APOS [125]	Kept near 150°C for 7 hours, estimated from heat capacity of diethyl aluminum chloride
Electricity	82	Wh	[160]	Electricity, low voltage, {GLO}| market group for | APOS [125]	Stirring [163]
Electricity	8	Wh	[160]	Electricity, low voltage, {GLO}| market group for | APOS [125]	Vacuum distillation [130]
Output					
Trimethylaluminum 99% pure	30	kg		Created process block in SimaPro	Assumed 68% yield
Waste	**Amount**	**Unit**	**Model**	**Database entry**	**Notes**
Lost solvent	153.1	kg	estimated	Hazardous waste, for incineration {RoW}| market for hazardous waste, for incineration | APOS [125]	No re-use (90% re-use = 15.3 kg)
Un-reacted methyl aluminum sesquichloride	26	kg	estimated	Hazardous waste, for incineration {RoW}| market for hazardous waste, for incineration | APOS [125]	
Sodium chloride	48	kg	estimated	Hazardous waste, for incineration {RoW}| market for hazardous waste, for incineration | APOS [125]	Assume excess unreacted sodium is re-used

Table 43: Material input-output table for trimethylaluminum purification (99.95% pure)

Input	Amount	Unit	Model source	Database entry	Assumptions
Trimethylaluminum 98% pure	100	kg	[146]	See **Table 42**	
3N Sodium metal	20	kg	[146]	Sodium {GLO}| market for | APOS [125]	
Helium	400	g	[146]	Helium {GLO}| market for | APOS [125]	
Electricity	0.1	kWh	estimated	Electricity, low voltage, {GLO}| market group for | APOS [125]	vacuum, 50 W for 2 hours [164]
Electricity	0.46	kWh	estimated	Electricity, low voltage, {GLO}| market group for | APOS [125]	Heating/Cooling, 230W for 2 hours [165]

Output					
Trimethylaluminum, 99.95% pure	60	kg	[146]	Created process block in SimaPro	60% yield [146]
Waste	**Amount**	**Unit**	**Model**	**Database entry**	**Notes**
Sodium + unreacted trimethylaluminum	60	kg	estimated	Hazardous waste, for incineration {RoW}| market for hazardous waste, for incineration | APOS [125]	

Table 44: Material input-output table for methyl aluminum sesquichloride

Input	**Amount**	**Unit**	**Model source**	**Database entry**	**Assumptions**
Aluminum Chloride	1.62	kg	[148]	See **Table 45**	
Aluminum, 4N	26.16	kg	[148]	Aluminium, wrought alloy {GLO}| market for | APOS [125]	
Methylchloride	73.7	kg	[148]	Methylchloride {GLO}| market for | APOS [125]	
Electricity	25	Wh	[148]	Electricity, low voltage, {GLO}| market group for | APOS [125]	30 mbar vacuum, 50 W for 0.5 hours [164]
Electricity	230	Wh	[148]	Electricity, low voltage, {GLO}| market group for | APOS [125]	Heating/Cooling, 230W for 1 hour [165]
Electricity	0.03	Wh	[148]	Electricity, low voltage, {GLO}| market group for | APOS [125]	Vacuum distillation [130]
Output					
Methyl aluminum sesquichloride	100	kg	[148]	Created process block in SimaPro	100% yield by aluminum
Waste	**Amount**	**Unit**	**Model**	**Database entry**	**Notes**
methane	2.3	kg	[148]	Emissions to air [125]	
chlorine	2.3	kg	[148]	Emissions to air [125]	

Table 45: Material input-output table for anhydrous aluminum chloride

Input	**Amount**	**Unit**	**Model source**	**Database entry**	**Assumptions**
Aluminum oxide	199.4	kg	[149]	Aluminium, wrought alloy {GLO}| market for | APOS [125]	
Chlorine	199.4	g	[149]	Methylchloride {GLO}| market for | APOS [125]	
Carbon black	50	kg	[149]	Electricity, low voltage, {GLO}| market group for | APOS [125]	
Heat	1700	MJ	[149]	Electricity, low voltage, {GLO}| market group for | APOS [125]	
Electricity	103	MJ	[149]	Electricity, low voltage, {GLO}| market group for | APOS [125]	
Output					
Aluminum Chloride	1000	kg	[149]	Created process block in SimaPro	
Waste	**Amount**	**Unit**	**Model**	**Database entry**	**Notes**
Carbon dioxide	49.5	kg	estimated	Emissions to air [125]	

Table 46: Material input-output table for trimethylindium 99% pure

Input	Amount	Unit	Model source	Database entry	Assumptions
Indium Chloride	521	g	[150]	See **Table 47**	
Trimethyl aluminum (either 98% pure or 99.95% pure)	333.4	g	[150]	See **Table 42** or **Table 43**	
Sodium Chloride	269	g	[150]	Sodium chloride, powder {GLO}| market for | APOS [125]	
Electricity	230	Wh	[150]	Electricity, low voltage, {GLO}| market group for | APOS [125]	Maintain at 150ºC for one hour [165]
Electricity	50	Wh	[150]	Electricity, low voltage, {GLO}| market group for | APOS [125]	Vacuum, 50 W for one hour [164]
Output					
Trimethyl indium	250	g	[150]	Created process block in SimaPro	Assume 90% yield
Waste	**Amount**	**Unit**	**Model**	**Database entry**	**Notes**
$NaAl(CH_3)Cl_3$	550	g	estimated	Inert waste, for final disposal {RoW}| market for inert waste, for final disposal | APOS [125]	

Table 47: Material input-output table for indium (III) chloride

Input	Amount	Unit	Model source	Database entry	Assumptions
Indium	114.8	g	[151]	Indium{GLO}| market group for | APOS [125] *or* Table 57: "Indium RoW – 0.09% allocation"	
Chlorine	106.4	g	[151]	Chlorine, gaseous {RoW}| market for | APOS [125]	
Electricity	50	Wh	[151]	Electricity, low voltage, {GLO}| market group for | APOS [125]	Vacuum, 50 W for one hour [164]
Output					
Indium Chloride	221.2	kg	[151]	Created process block in SimaPro	Assumed 100% yield by indium

Table 48: Material input-output table for trimethylgallium 99% pure

Input	Amount	Unit	Model source	Database entry	Assumptions
Gallium Chloride	3.94	kg	[150]	See **Table 49**	
Trimethyl aluminum (either 98% pure or 99.95% pure)	2.53	kg	[150]	See **Table 42** or **Table 43**	
Sodium Chloride	2	kg	[150]	Sodium chloride, powder {GLO}| market for | APOS [125]	
Electricity	230	Wh	[150]	Electricity, low voltage, {GLO}| market group for | APOS [125]	Maintain at 150ºC for one hour [165]
Electricity	50	Wh	[150]	Electricity, low voltage, {GLO}| market group for | APOS [125]	Vacuum, 50 W for one hour [164]
Output					
Trimethyl gallium	2.5	kg	[150]	Created process block in SimaPro	96% yield [150]
Waste	**Amount**	**Unit**	**Model**	**Database entry**	**Notes**
$NaAl(CH_3)Cl_3$	6	kg	estimated	Inert waste, for final disposal	

				{RoW}| market for inert waste, for final disposal | APOS [125]	

Table 49: Material input-output table for gallium (III) chloride

Input	Amount	Unit	Model source	Database entry	Assumptions
Gallium	69.7	g	[152]	Gallium, semiconductor-grade{GLO}| market group for | APOS [125]	
Chlorine	106.4	g	[152]	Chlorine, gaseous {RoW}| market for | APOS [125]	
Electricity	50	Wh	[152]	Electricity, low voltage, {GLO}| market group for | APOS [125]	Vacuum, 50 W for one hour [164]
Output					
Gallium Chloride	176.1	g	[152]	Created process block in SimaPro	Assumed 100% yield

Table 50: Material input-output table for trimethylantimony 99% pure

Input	Amount	Unit	Model source	Database entry	Assumptions
Antimony Chloride	521	g	[150]	See Table 51	
Trimethyl aluminum (either 98% pure or 99.95% pure)	333.4	g	[150]	See **Table 42** or **Table 43**	
Sodium Chloride	269	g	[150]	Sodium chloride, powder {GLO}| market for | APOS [125]	
Electricity	230	Wh	[150]	Electricity, low voltage, {GLO}| market group for | APOS [125]	Maintain at 150°C for one hour [165]
Electricity	50	Wh	[150]	Electricity, low voltage, {GLO}| market group for | APOS [125]	Vacuum, 50 W for one hour [164]
Output					
Trimethyl antimony	250	g	[150]	Created process block in SimaPro	Assume 90% yield
Waste	**Amount**	**Unit**	**Model**	**Database entry**	**Notes**
$NaAl(CH_3)Cl_3$	550	g	estimated	Inert waste, for final disposal {RoW}| market for inert waste, for final disposal | APOS [125]	

Table 51: Material input-output table for antimony (III) chloride

Input	Amount	Unit	Model source	Database entry	Assumptions
4N Antimony	114.8	g	[151]	See Table 55	
Chlorine	106.4	g	[151]	Chlorine, gaseous {RoW}| market for | APOS [125]	
Electricity	50	Wh	[151]	Electricity, low voltage, {GLO}| market group for | APOS [125]	Vacuum, 50 W for one hour [164]
Output					
Antimony Chloride	221.2	kg	[151]	Created process block in SimaPro	Assumed 100% yield by antimony

Table 52: Input-output table for 7N Gallium

Input	Amount	Unit	Model source	Database entry	Assumptions
Gallium, 6N	5	kg	[139, 166]	Gallium, semiconductor-grade {GLO}| market for | APOS [125]	
Electricity	20	kWh	[139, 166]	Electricity, low voltage, {GLO}| market group for | APOS [125]	Approx 4 hours, assume 5kW system
Output					
7N Gallium	3.5	kg	[139, 166]	Created process block in SimaPro	Assumed 70% yield
Waste	**Amount**	**Unit**	**Model**	**Database entry**	**Notes**
--					

Table 53: Input-output table for 6N Indium

Input	Amount	Unit	Model source	Database entry	Assumptions
Indium, 5N	5	kg	[139, 166]	Indium{GLO}| market group for | APOS [125] *or* Table 57: "Indium RoW – 0.09% allocation"	
Electricity	20	kWh	[139, 166]	Electricity, low voltage, {GLO}| market group for | APOS [125]	Approx 4 hours, assume 5kW system
Output					
6N Indium	3.5	kg	[139, 166]	Created process block in SimaPro	Assumed 70% yield
Waste	**Amount**	**Unit**	**Model**	**Database entry**	**Notes**
--					

Table 54: Input-output table for 6N Aluminum

Input	Amount	Unit	Model source	Database entry	Assumptions
Aluminum, 4N	5	kg	[139, 166]	Aluminium, wrought alloy {GLO}| market for | APOS [125]	
Electricity	20	kWh	[139, 166]	Electricity, low voltage, {GLO}| market group for | APOS [125]	Approx 4 hours, assume 5kW system
Output					
6N Aluminum	3.5	kg	[139, 166]	Created process block in SimaPro	Assumed 70% yield
Waste	**Amount**	**Unit**	**Model**	**Database entry**	**Notes**
--					

Table 55: Input-output table for 4N Antimony

Input	Amount	Unit	Model source	Database entry	Assumptions
Antimony, 2N	5	kg	[139,	Antimony{GLO}| market group	

			166]	for | APOS [125]	
Electricity	20	kWh	[139, 166]	Electricity, low voltage, {GLO}| market group for | APOS [125]	Approx 4 hours, assume 5kW system
Output					
4N Antimony	3.5	kg	[139, 166]	Created process block in SimaPro	Assumed 70% yield
Waste	**Amount**	**Unit**	**Model**	**Database entry**	**Notes**
--					

Table 56: Input-output table for 6N Antimony

Input	**Amount**	**Unit**	**Model source**	**Database entry**	**Assumptions**
Antimony, 4N	5	kg	[139, 166]	See Table 55	
Electricity	20	kWh	[139, 166]	Electricity, low voltage, {GLO}| market group for | APOS [125]	Approx 4 hours, assume 5kW system
Output					
6N Antimony	3.5	kg	[139, 166]	Created process block in SimaPro	Assumed 70% yield
Waste	**Amount**	**Unit**	**Model**	**Database entry**	**Notes**
--					

Table 57: Changes to ecoinvent 3.4 entries to re-allocate zinc concentrate impacts for indium-rich leaching residues

Renamed	Ecoinvent entry	Original content			Updated content		
Indium leaching RoW – 0.09% allocation	Indium rich leaching residues, from zinc production {RoW} | primary zinc production from concentrate | APOS, U	*Outputs to technosphere: Products and coproducts*	*Amount*	*Allocation*	*Outputs to technosphere: Products and coproducts*	*Amount*	*Allocation*
		Indium rich leaching residues, from zinc production {RoW} | primary zinc production from concentrate | APOS, U	1 kg	100%	Indium rich leaching residues, from zinc production {RoW} | primary zinc production from concentrate | APOS, U	1 kg	64.3%
					Germanium-rich and cadmium-rich leaching residues, from zinc production	1 kg	35.7%
Indium leaching GLO – 0.09% allocation	Indium rich leaching residues, from zinc production {GLO}| market for | APOS, U	*Inputs from technosphere: materials/fuels*		*Amount*	*Inputs from technosphere: materials/fuels*		*Amount*
		Indium rich leaching residues, from zinc production {RoW} | primary zinc production from concentrate | APOS, U		0.9948 kg	Indium leaching RoW – 0.09% allocation		0.9948 kg
Indium RoW – 0.09% allocation	Indium {RoW}| production | APOS, U	*Inputs from technosphere: materials/fuels*		*Amount*	*Inputs from technosphere: materials/fuels*		*Amount*
		Indium rich leaching residues, from zinc production (nuss) {GLO}| market for | APOS, U		10,000 kg	Indium leaching GLO – 0.09% allocation		10,000 kg

	Methyl aluminum sesquichloride	TMAl – 98% pure	TMAl – 99.95% pure
No solvent reclaim	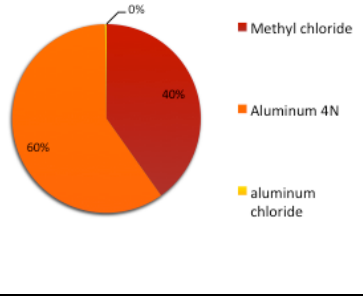	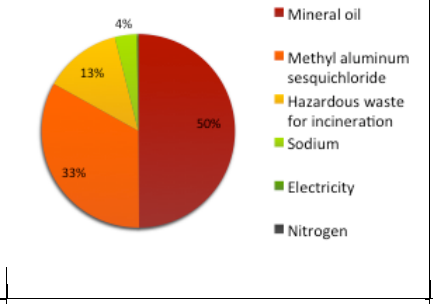	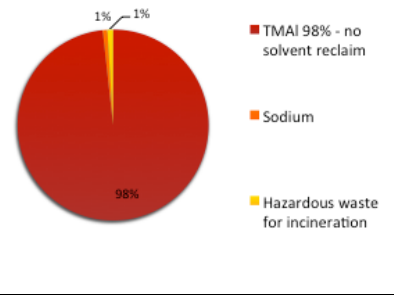
90% solvent reclaim		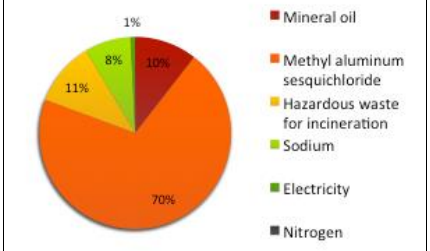	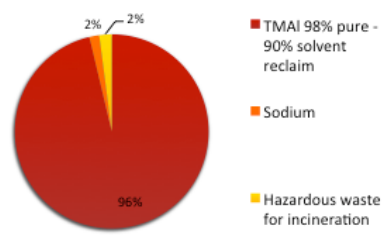

Figure 89: Input contributions to CED for methyl aluminum sesquichloride, 98% pure TMAl, and 99.95% pure TMAl

Scenario	TMGa	TMIn	TMSb
Low purity TMAl	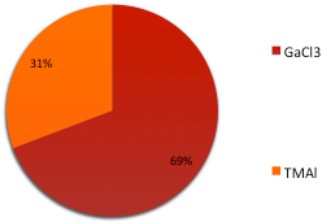	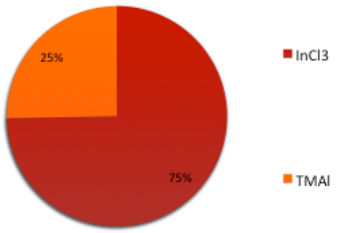	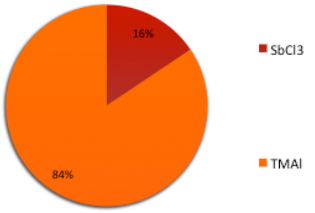
Low purity TMAl, solvent reclaim	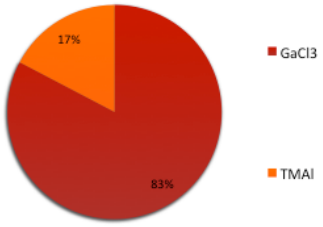	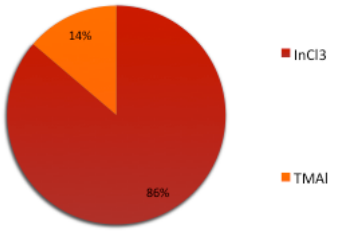	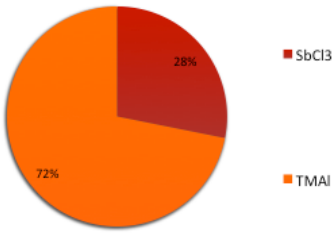

Figure 90: Input contributions to CED for TMGa, TMIn, and TMSb using low purity TMAl, with and without solvent reclaim

A.2 Supporting information for life cycle of GaAs substrate

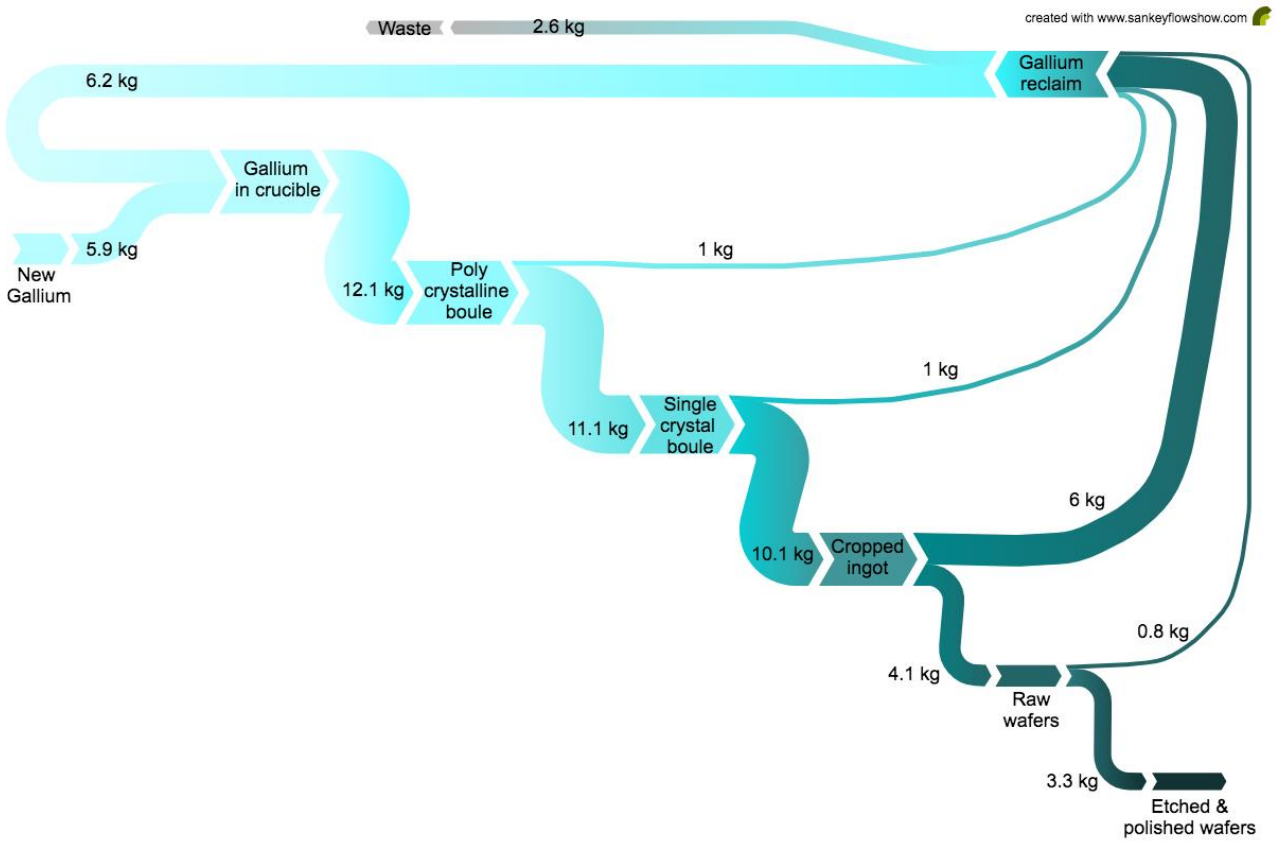

Figure 91: Gallium recycling during GaAs substrate manufacturing – process flow

Table 58: Input-output table for Polycrystalline GaAs boule

Input	Amount	Unit	Model source	Database entry	Assumptions
7N Gallium	5.9	kg	[136]	See **Table 59**	12.1 kg is initial input but half is internally recycled: see Figure 1
7N Arsenic	12.9	kg	[136]	See **Table 60** [140-142]	
pBN crucible	0.25	kg	[167]	Boron carbide {GLO}| market for | APOS [125]	1.5kg crucible, re-used 6 times
Electricity	1250	kWh	estimated	Electricity, low voltage, {GLO}| market group for | APOS [125]	25 kW furnace, 50 hour cycle
Output					
Polycrystalline GaAs boule	25	kg	Personal communication	Created process block in SimaPro	Assumed 100% yield
Waste	**Amount**	**Unit**	**Model**	**Database entry**	**Notes**
pBN crucible	0.25	kg		Hazardous waste, for underground deposit {GLO}| market for | APOS [125]	

Table 59: Input-output table for 7N Gallium

Input	Amount	Unit	Model source	Database entry	Assumptions
Gallium, 6N	5	kg	[139, 166]	Gallium, semiconductor-grade {GLO}| market for | APOS [125]	
Electricity	20	kWh	[139, 166]	Electricity, low voltage, {GLO}| market group for | APOS [125]	Approx 4 hours, assume 5kW system
Output					
7N Gallium	3.5	kg	[139, 166]	Created process block in SimaPro	Assumed 70% yield
Waste	**Amount**	**Unit**	**Model**	**Database entry**	**Notes**
--					

Table 60: Input-output table for 7N Arsenic

Input	Amount	Unit	Model source	Database entry	Assumptions
Arsenic, metallic (2N)	5	kg	[142]	[140, 141]	
Hydrogen	0.32	kg	[142]	Hydrogen, liquid {RoW}| market for | APOS [125]	
Argon	0.16	kg	[142]	Argon, liquid {GLO}| market for | APOS[125]	
Electricity	27.6	kWh	[142, 168, 169]	Electricity, low voltage, {GLO}| market group for | APOS [125]	2.5 furnace for 3 hr, two 5kW furnaces for 2 hr, 1kW vacuum for 5 minutes
Output					
7N Arsenic	3.4	kg	[142]	Created process block in SimaPro	Assumed 68% yield
Waste	**Amount**	**Unit**	**Model**	**Database entry**	**Notes**
--					

Table 61: Input-output table for single-crystal GaAs boule

Input	Amount	Unit	Model source	Database entry	Assumptions
Polycrystalline GaAs boule	27	kg	Personal communication	**Output of Table 58**	Assumed 92% yield based on failure rate
Boron oxide	0.125	kg	[167]	Boric oxide {GLO}| market for | APOS [125]	500 mg, re-used 4 times
pBN crucible	0.25	kg	[167]	Boron carbide {GLO}| market for | APOS [125]	1.5kg crucible, re-used 6 times
Electricity	4000	kWh	Personal communication	Electricity, low voltage, {GLO}| market group for | APOS [125]	25 kW furnace, 160 hour cycle
Output					
Single-crystal GaAs boule	25	kg	Personal communication	Created process block in SimaPro	Assumed 92% yield based on failure rate
Wastes	**Amount**	**Unit**	**Model**	**Database entry**	**Notes**
pBN crucible	0.25	kg		Hazardous waste, for	

				underground deposit {GLO}| market for | APOS [125]	
Boron oxide	0.125	kg		Hazardous waste, for underground deposit {GLO}| market for | APOS [125]	
7N Arsenic	1	kg		Hazardous waste, for underground deposit {GLO}| market for | APOS [125]	

Table 62: Input-output table for x-ray, cropping, and grinding notch of GaAs ingot

Input	**Amount**	**Unit**	**Model source**	**Database entry**	**Assumptions**
Single-crystal GaAs boule	25	kg	[137]	Output of **Table 61**	
Steel wire (cropping)	1.3	mg	estimated	Steel wire rod/GLO [170]	120 μm diameter, re-used 20 times
Diamond saw (notch)	0.01	piece	[137]	See **Table 63**	1 piece re-used for 100 ingots
Electricity (x-ray)	10	kWh	[137]	Electricity, low voltage, {GLO}| market group for | APOS [125]	10 kW, 10 minutes per boule
Electricity (cropping)	1.7	kWh	estimated	Electricity, low voltage, {GLO}| market group for | APOS [125]	10 kW saw, 1 hr per boule
Electricity (notch)	10	kWh	[137]	Electricity, low voltage, {GLO}| market group for | APOS [125]	10 kW saw, 1 hr per boule
Output					
Single-crystal GaAs ingot	22.75	kg	[137]	Created process block in SimaPro	Assumed 91% mass left after cropping
Wastes	**Amount**	**Unit**	**Model**	**Database entry**	**Notes**
arsenic	1.15	kg		Hazardous waste, for underground deposit {GLO}| market for | APOS [125]	

Table 63: Input-output table for diamond saw

Input	**Amount**	**Unit**	**Model source**	**Database entry**	**Assumptions**
Steel	20	g	assumed	Steel, unalloyed {GLO}| market for | APOS [125]	
Synthetic diamond	0.2	g	assumed	See **Table 64**	
Electricity	10	kWh	assumed	Electricity, low voltage, {GLO}| market group for | APOS [125]	
Output					
Diamond saw	1	piece	assumed	Created process block in SimaPro	
Wastes	**Amount**	**Unit**	**Model**	**Database entry**	**Notes**
--					

Table 64: Input-output table for synthetic diamond

Input	**Amount**	**Unit**	**Model source**	**Database entry**	**Assumptions**
methane	0.08	m3	[171]	Natural gas, high pressure	

				{GLO}| market group for | APOS [125]	
Hydrogen gas	0.2	g	[171]	Hydrogen, liquid {RoW}| market for | APOS [125]	
Electricity	6700	kWh	[171]	Electricity, low voltage, {GLO}| market group for | APOS [125]	10 kW furnace, 28 day cycle time
Output					
Synthetic diamond	5.5	g	[171]	Created process block in SimaPro	
Wastes	**Amount**	**Unit**	**Model**	**Database entry**	**Notes**
--					

Table 65: Input-output table for Wafering & Edge-rounding of GaAs substrates

Input	**Amount**	**Unit**	**Model source**	**Database entry**	**Assumptions**
Single-crystal GaAs ingot	68.25	kg	[137]	Output of **Table 62**	3 ingot = 22.75*3
Steel wire (wafering)	264	mg	[137]	Steel wire rod/GLO[170]	120 μm diameter, re-used 20 times
Sawing slurry	1.05	kg	[137]	See **Table 66**	1.56 mL/wafer
Diamond saw (edge-saw)	0.06	piece	[137]	See **Table 63**	1 piece re-used for 100 ingots
Electricity (wire saw)	10	kWh	[137]	Electricity, low voltage, {GLO}| market group for | APOS [125]	10 kW saw, 1 hr per batch (3 ingots)
Electricity (edge saw)	25	kWh	[137]	Electricity, low voltage, {GLO}| market group for | APOS [125]	10 kW saw, 2.5 hrs per 300 wafers
Output					
6-inch raw GaAs wafers	300	pieces	Personal communication	Created process block in SimaPro	Assumed 41% mass left after cutting
Wastes	**Amount**	**Unit**	**Model**	**Database entry**	**Notes**
arsenic	20.5	kg		Hazardous waste, for underground deposit {GLO}| market for | APOS [125]	**Loss from sawing**

Table 66: Input-output table for sawing slurry

Input	**Amount**	**Unit**	**Model source**	**Database entry**	**Assumptions**
Silica particles	100	g	[172]	Very fine milled silica sand d50 = 20 micrometer, production, at plant, median diameter of sand grains is 20 micrometers EU-27 S [173]	
Polyethylene glycol	100	g	[172]	Triethylene glycol {RoW}| ethylene glycol production | APOS [125]	
Output					
Sawing slurry	200	g	[172]	Created process block in SimaPro	Assumes 1:1 weight ratio
Wastes	**Amount**	**Unit**	**Model**	**Database entry**	**Notes**
--					

Table 67: Input-output table for cleaning & etching GaAs substrates

Input	Amount	Unit	Model source	Database entry	Assumptions
Raw GaAs wafers	300	Pieces	estimated	Output of **Table 65**	
Ultrapure water	300	kg	estimated	Water, ultrapure {GLO}| market for | APOS [125]	1 L/wafer
H2O2	4.35	kg	estimated	Hydrogen peroxide, without water, in 50% solution state {GLO}| market for | APOS [125]	0.01 L/wafer
HF	3.45	kg	[137]	Hydrogen fluoride {GLO}| market for | APOS [125]	0.01 L/wafer
Electricity (ultrasonic cleaning)	3.3	kWh	[137]	Electricity, low voltage, {GLO}| market group for | APOS [125]	10 kW, 20 minute cycle time
Electricity (rinse tank)	6.7	kWh	estimated	Electricity, low voltage, {GLO}| market group for | APOS [125]	10 kW saw, 40 minute cycle
Output					
6-inch etched GaAs wafers	300	pieces	estimated	Created process block in SimaPro	Assumed 100% yield
Wastes	**Amount**	**Unit**	**Model**	**Database entry**	**Notes**
Arsenic/etchant	3	kg		Hazardous waste, for underground deposit {GLO}| market for | APOS [125]	**1 kg per ingot = 3 kg**

Table 68: Input-output table for Pre-polishing of GaAs substrates

Input	Amount	Unit	Model source	Database entry	Assumptions
6-inch etched GaAs wafers	30	pieces	Estimated	**Output of** Table 67	
Polishing pad	3.14	g	[137, 174]	Polyurethane, rigid foam, {GLO}| market for | APOS [125]	3.14 g pad, 15 re-uses
Sawing slurry	10.1	kg	[137]	See **Table 66**	1.56 mL/wafer
Electricity (polishing)	3.3	kWh	Estimated	Electricity, low voltage, {GLO}| market group for | APOS [125]	10 kW machine, 20 minutes per batch
Output					
pre-polished GaAs wafers	30	pieces	estimated	Created process block in SimaPro	Assumed 100% yield
Wastes	**Amount**	**Unit**	**Model**	**Database entry**	**Notes**
arsenic	0.5	kg		Hazardous waste, for underground deposit {GLO}| market for | APOS [125]	

Table 69: Input-output table for Chemical-mechanical polishing (CMP) of GaAs substrates

Input	Amount	Unit	Model source	Database entry	Assumptions
Pre-polished GaAs wafers	6	pieces	Personal communication	Output of **Table 68**	
Polishing pad	1.26	g	[174]	Polyurethane, rigid foam, {GLO}| market for | APOS [125]	3.14 g pad, 15 re-uses

CMP slurry	1.6	kg	estimated	**See** Table 70	0.78 L/batch
Electricity (polishing)	3.3	kWh	Personal communication	Electricity, low voltage, {GLO}| market group for | APOS [125]	10 kW machine, 20 minutes per batch
Output					
Double-polished GaAs wafers	6	pieces	Personal communication	Created process block in SimaPro	Assumed 100% yield
Wastes	**Amount**	**Unit**	**Model**	**Database entry**	**Notes**
arsenic	0.5	kg		Hazardous waste, for underground deposit {GLO}| market for | APOS [125]	

Table 70: Input-output table for CMP slurry

Input	**Amount**	**Unit**	**Model source**	**Database entry**	**Assumptions**
Silica particles	100	g	[175]	Very fine milled silica sand d50 = 20 micrometer, production, at plant, median diameter of silica sand grains is 20 micrometers EU-27 S [173]	
Ultrapure water	50	g	[175]	Water, ultrapure {GLO}| market for | APOS [125]	
KOH	50	g	[175]	Potassium hydroxide {GLO}| market for | APOS [125]	
Output					
CMP slurry	200	g	[175]	Created process block in SimaPro	Assumes 1:1 weight ratio
Wastes	**Amount**	**Unit**	**Model**	**Database entry**	**Notes**
--					

Table 71: Input-output table for Cleaning, Quality Control, Packaging of GaAs substrates

Input	**Amount**	**Unit**	**Model source**	**Database entry**	**Assumptions**
Double-polished GaAs wafers	100	Pieces	estimated	Output of **Table 69**	
Ultrapure water	100	kg	estimated	Water, ultrapure {GLO}| market for | APOS [125]	1 L/wafer
KOH	6.7	kg	estimated	Potassium hydroxide {GLO}| market for | APOS [125]	0.01 L/wafer
Plastic cassette	138	g	[137]	Polyethylene terephthalate, granulate, bottle grade {GLO}| market for | APOS [125]	1 cm^3/cassette
Foil bag	1.6	g	[137]	Aluminum, primary, ingot {RoW}| market for | APOS [125]	500nm foil on PET
PET bag	200	g	[137]	Packaging film, low density polyethylene {GLO}| market for | APOS [125]	6mil thick PET film
Electricity (QC - flatness)	10	kWh	[137]	Electricity, low voltage, {GLO}| market group for | APOS [125]	10 kW, 1 hour cycle time per batch

Electricity (QC - surface)	10	kWh	[137]	Electricity, low voltage, {GLO}| market group for | APOS [125]	10 kW, 1 hour cycle time per batch
Output					
GaAs wafers	100	pieces	estimated	Created process block in SimaPro	Assumed 100% yield

A.3 Supporting information for life cycle of III-V HCPV cells

Table 72: Input-output table for 4-inch diameter, 150 μm thick germanium substrate

Input	Amount	Unit	Model source	Database entry	Assumptions
Hydrochloric acid (GeO_2 production)	0.6	kg	[118]	Hydrochloric acid, without water, in 30% solution state {RoW}| market for | APOS [125]	Total CED of GeO2 is 73 MJ, where 64 MJ is assumed to be from electricity (stated 75% of total wafer CED from electricity)
Hydrochloric acid (wafer production)	1	kg	[118]	Hydrochloric acid, without water, in 30% solution state {RoW}| market for | APOS [125]	Assumed to be majority of "auxiliaries" 21 MJ CED impacts
Nitrogen	1	kg	[118]	Nitrogen, liquid {RoW}| market for | APOS [125]	Assumed to be remainder of "auxiliaries" impact for simplicity
Natural gas, cokes, and fuel oil	0.35	kg	[118]	Petroleum coke {GLO}| market for | APOS [125]	Approximation for 3 MJ of impacts
Water	15	kg	[118]	Water, ultrapure {GLO}| market for | APOS [125]	
Electricity (GeO_2 production)	5.3	kWh	[118]	Electricity, low voltage, {GLO}| market group for | APOS [125]	
Electricity (wafer production)	8.3	kWh	[118]	Electricity, low voltage, {GLO}| market group for | APOS [125]	
Output					
Germanium wafer	81.1	cm^2	[118]	Created process block in SimaPro	Assumed 100% yield

Table 73: Input-output table for cell 1 (standard triple-junction cell on germanium)

Input	Amount	Unit	Model source	Database entry	Assumptions
Germanium substrate	1	cm^2	[118]	See **Table 72**	No substrate re-use possible
Arsine	154	mg	[127]	Arsine {GLO}| market for | APOS [125]	
Phosphine	28.2	mg	[127]	Phosphane {GLO market for | APOS [125]	
Nitrogen	0.006	g	[22]	Nitrogen, liquid {RoW}| market for | APOS [125]	
Hydrogen	1.86	g	[22]	Hydrogen, liquid {RoW}| market for | APOS [125]	
Trimethyl indium	1.39	mg	[127]	See **Table 46**	
Trimethyl gallium	5.44	mg	[127]	See **Table 48**	
Dopants	0.0007	mg	estimated	See **Table 48** or Arsine {GLO}| market for | APOS [125]	Consider TMGa or arsine for sensitivity analysis
Electricity (MOVPE)	0.01	kWh	estimated	Electricity, low voltage, {GLO}| market group for | APOS [125]	4 μm = 0.5 hours = 100 kWh per $1m^2$ / 10,000 = 0.01 kWh per cm^2

Output					
Unprocessed 3J germanium cells	1	cm^2	[127]	Created process block in SimaPro	Assumed 100% yield

Table 74: Input-output table for cell 2 (triple-junction on InP)

Input	Amount	Unit	Model source	Database entry	Assumptions
InP substrate	1	cm^2	**[4]**	Use GaAs substrate as approximation, see **Table 71**	0 substrate re-use = 1 cm^2 5 re-uses = 0.2 cm^2 10 re-uses = 0.1 cm^2
Arsine	431	mg	**[4]**	Arsine {GLO}| market for | APOS [125]	
Phosphine	63.5	mg	**[4]**	Phosphane {GLO market for | APOS [125]	
Nitrogen	0.015	g	estimated	Nitrogen, liquid {RoW}| market for | APOS [125]	Extrapolated from [22]
Hydrogen	4.65	g	estimated	Hydrogen, liquid {RoW}| market for | APOS [125]	Extrapolated from [22]
Trimethyl indium	16	mg	**[4]**	See **Table 46**	
Trimethyl gallium	6.1	mg	**[4]**	See **Table 48**	
Trimethyl aluminum	0.94	mg	**[4]**	See **Table 43**	
Trimethyl antimony	2.1	mg	**[4]**	See Table 50	
Dopants	0.0017	mg	estimated	See **Table 48** or Arsine {GLO}| market for | APOS [125]	Consider TMGa or arsine for sensitivity analysis
Electricity (MOVPE)	0.02	kWh	estimated	Electricity, low voltage, {GLO}| market group for | APOS [125]	10 μm = 1 hour = 200 kWh per $1m^2$ / 10,000 = 0.02 kWh per cm^2
Generic ELO processing	0 or 1	cm^2	estimated	See Table 79	0 cm^2 = no substrate re-use 1 cm^2 = substrate re-used
Output					
Unprocessed 3J InP cell	1	cm^2	**[4]**	Created process block in SimaPro	Assumed 100% yield

Table 75: Input-output table for cell 3 (wafer-bonded 5-junction): 1 μm subcells

Input	Amount	Unit	Model source	Database entry	Assumptions
Ge substrate	1	cm^2	**[126]**	See **Table 72**	0 substrate re-use = 1 cm^2 5 re-uses = 0.2 cm^2 10 re-uses = 0.1 cm^2
InP substrate	1	cm^2	**[126]**	Use GaAs substrate as approximation, see **Table 71**	0 substrate re-use = 1 cm^2 5 re-uses = 0.2 cm^2 10 re-uses = 0.1 cm^2
Arsine	325	mg	**[126]**	Arsine {GLO}| market for | APOS [125]	
Phosphine	40.9	mg	**[126]**	Phosphane {GLO market for | APOS [125]	
Nitrogen	0.0075	g	estimated	Nitrogen, liquid {RoW}| market for | APOS [125]	Extrapolated from [22]

Hydrogen	2.33	g	estimated	Hydrogen, liquid {RoW}| market for | APOS [125]	Extrapolated from [22]
Trimethyl indium	4.78	mg	**[126]**	See **Table 46**	
Trimethyl gallium	8.05	mg	**[126]**	See **Table 48**	
Trimethyl aluminum	0.54	mg	**[126]**	See **Table 43**	
Dopants	0.0008	mg	estimated	See **Table 48** or Arsine {GLO}| market for | APOS [125]	Consider TMGa or arsine for sensitivity analysis
Electricity (MOVPE)	0.01	kWh	estimated	Electricity, low voltage, {GLO}| market group for | APOS [125]	5 μm = ~0.5 hours = 100 kWh per 1m^2 / 10,000 = 0.01 kWh per cm^2
Electricity (wafer bonding)	0.2	Wh	[176]	Electricity, low voltage, {GLO}| market group for | APOS [125]	Rough estimate for wafer bonding
Wafer bonding materials	1	cm^2	[176]	Generic ELO processing, see Table 79	Used as estimate for CMP and "proprietary layer"
Generic ELO processing	0, 1, or 2	cm^2	estimated	See Table 79	0 cm^2 = no substrate re-use 1 cm^2 = 1 substrate re-used 2 cm^2 = both substrates re-used
Output					
Unprocessed 5J SBT cells	1	cm^2	**[126]**	Created process block in SimaPro	Assumed 100% yield

Table 76: Input-output table for cell 3 (wafer-bonded 5-junction): 2 μm subcells

Input	Amount	Unit	Model source	Database entry	Assumptions
GaAs substrate	1	cm^2	**[126]**	See **Table 71**	0 substrate re-use = 1 cm^2 5 re-uses = 0.2 cm^2 10 re-uses = 0.1 cm^2
InP substrate	1	cm^2	**[126]**	Use GaAs substrate as approximation, see **Table 71**	0 substrate re-use = 1 cm^2 5 re-uses = 0.2 cm^2 10 re-uses = 0.1 cm^2
Arsine	496	mg	**[126]**	Arsine {GLO}| market for | APOS [125]	
Phosphine	81.8	mg	**[126]**	Phosphane {GLO market for | APOS [125]	
Nitrogen	0.015	g	estimated	Nitrogen, liquid {RoW}| market for | APOS [125]	Extrapolated from [22]
Hydrogen	4.66	g	estimated	Hydrogen, liquid {RoW}| market for | APOS [125]	Extrapolated from [22]
Trimethyl indium	9.5	mg	**[126]**	See **Table 46**	
Trimethyl gallium	11.6	mg	**[126]**	See **Table 48**	
Trimethyl aluminum	1.1	mg	**[126]**	See **Table 43**	
Dopants	0.0017	mg	estimated	See **Table 48** or Arsine {GLO}| market for | APOS [125]	Consider TMGa or arsine for sensitivity analysis
Electricity (MOVPE)	0.02	kWh	estimated	Electricity, low voltage, {GLO}| market group for | APOS [125]	10 μm = 1 hour = 200 kWh per 1m^2 / 10,000 = 0.02 kWh per cm^2
Electricity (wafer bonding)	0.2	Wh	[176]	Electricity, low voltage, {GLO}| market group for | APOS [125]	Rough estimate for wafer bonding
Wafer bonding	1	cm^2	[176]	Generic ELO processing, see	Used as estimate for CMP

materials				Table 79	and "proprietary layer"
Generic ELO processing	0, 1, or 2	cm^2	estimated	See Table 79	0 cm^2 = no substrate re-use 1 cm^2 = 1 substrate re-used 2 cm^2 = both substrates re-used
Output					
Unprocessed 5J SBT cells	1	cm^2	**[126]**	Created process block in SimaPro	Assumed 100% yield

Table 77: Input-output table for cell 4 (inverted metamorphic 6-junction): 1 μm subcells

Input	Amount	Unit	Model source	Database entry	Assumptions
Germanium substrate (or GaAs substrate)	1	cm^2	**[36, 128]** [177]	See **Table 72** or **Table 71**	0 substrate re-use = 1 cm^2 5 re-uses = 0.2 cm^2 10 re-uses = 0.1 cm^2
Arsine	945	mg	[127]	Arsine {GLO}| market for | APOS [125]	
Phosphine	28.2	mg	[127]	Phosphane {GLO market for | APOS [125]	
Nitrogen	0.023	g	estimated	Nitrogen, liquid {RoW}| market for | APOS [125]	Extrapolated from [22]
Hydrogen	7	g	estimated	Hydrogen, liquid {RoW}| market for | APOS [125]	Extrapolated from [22]
Trimethyl indium	11.9	mg	[127]	See **Table 46**	
Trimethyl gallium	20.3	mg	[127]	See **Table 48**	
Trimethyl aluminum	0.59	mg	[127]	See **Table 43**	
Dopants	0.0025	mg	estimated	See **Table 48** or Arsine {GLO}| market for | APOS [125]	Consider TMGa or arsine for sensitivity analysis
Electricity (MOVPE)	0.025	kWh	estimated	Electricity, low voltage, {GLO}| market group for | APOS [125]	15 μm = 1.25 hours = 250 kWh per $1m^2$ / 10,000 = 0.025 kWh per cm^2
Generic ELO processing	0 or 1	cm^2	estimated	See Table 79	0 cm^2 = no substrate re-use 1 cm^2 = substrate re-used
Output					
Unprocessed 6J IMM cells	1	cm^2	[127]	Created process block in SimaPro	Assumed 100% yield

Table 78: Input-output table for cell 4 (inverted metamorphic 6-junction): 2 μm subcells

Input	Amount	Unit	Model source	Database entry	Assumptions
Germanium substrate (or GaAs substrate)	1	cm^2	**[36, 128]** [177]	See **Table 72** or **Table 71**	0 substrate re-use = 1 cm^2 5 re-uses = 0.2 cm^2 10 re-uses = 0.1 cm^2
Arsine	1290	mg	[127]	Arsine {GLO}| market for | APOS [125]	
Phosphine	56.4	mg	[127]	Phosphane {GLO market for | APOS [125]	
Nitrogen	0.032	g	estimated	Nitrogen, liquid {RoW}| market for | APOS [125]	Extrapolated from [22]
Hydrogen	9.8	g	estimated	Hydrogen, liquid {RoW}| market	Extrapolated from [22]

				for | APOS [125]	
Trimethyl indium	16.4	mg	[127]	See **Table 46**	
Trimethyl gallium	28	mg	[127]	See **Table 48**	
Trimethyl aluminum	1.18	mg	[127]	See **Table 43**	
Dopants	0.0035	mg	estimated	See **Table 48** or Arsine {GLO}| market for | APOS [125]	Consider TMGa or arsine for sensitivity analysis
Electricity (MOVPE)	0.035	kWh	estimated	Electricity, low voltage, {GLO}| market group for | APOS [125]	21 μm = 1.75 hours = 350 kWh per $1m^2$ / 10,000 = 0.035 kWh per cm^2
Generic ELO processing	0 or 1	cm^2	estimated	See Table 79	0 cm^2 = no substrate re-use 1 cm^2 = substrate re-used
Output					
Unprocessed 6J IMM cells	1	cm^2	[127]	Created process block in SimaPro	Assumed 100% yield

Table 79: Input-output table for generic ELO processing

Input	Amount	Unit	Model source	Database entry	Assumptions
Hydrofluoric acid	0.3	kg	estimated	Hydrogen fluoride {GLO}| market for | APOS **[125]**	0.01 L / 6-inch wafer
Acetone	0.3	kg	estimated	Acetone, liquid {GLO}| market for | APOS [125]	0.01 L / 6-inch wafer
Isopropyl alcohol	0.3	kg	estimated	Isopropanol {GLO}| market for | APOS [125]	0.01 L / 6-inch wafer
Polishing pad	3.14	g	[137, 174]	Polyurethane, rigid foam, {GLO}| market for | APOS [125]	3.14 g pad, 15 re-uses
CMP slurry	8	kg	[137]	See **Table 66**	0.78 kg / 6 x 6-inch wafers
PET handle	25.2	g	estimated	Polyethylene terephthalate, granulate, amorphous {GLO}| market for | APOS [125]	
Electricity (polishing)	4	kWh	Estimated	Electricity, low voltage, {GLO}| market group for | APOS [125]	10 kW machine, 20 minutes per batch of 30 6-inch wafers
Output					
Epi-ready ELO wafers	182.4	cm^2	estimated	Created process block in SimaPro	Estimated from GaAs substrate CMP, Assumed 100% yield

Table 80: Input-output table for generic III-V HCPV cell processing – low scenario

Input	Amount	Unit	Model source	Database entry	Assumptions
Unfabricated cell (1, 2, 3, or 4)	2.5	cm^2	[21]	**See** Table 73 **-Table 78**	
Solvents	4	g	[21]	Acetone{GLO}| market for |	2g acetone, 2g isopropanol

				APOS, Isopropanol{GLO}| market for | APOS [125]	
Acids	0.6	g	[21]	Hydrochloric acid, without water, in 30% solution state {RoW}| market for | APOS, Hydrogen fluoride{GLO} market for | APOS [125]	0.3g hydrochloric acid, 0.3g hydrogen fluoride
Contact metals	1.4	mg	[22]	Gold {GLO}| market for | APOS [125]	
Lithography materials	0.085	g	[22]	Methyl methacrylate{RoW}| market for | APOS [125]	
Water	1	g	estimated	Water, ultrapure {GLO}| market for | APOS [125]	
Antireflective coating	0.16	mg	estimated	Zinc sulfide {GLO}| market for | APOS [125]	Assume 200 nm coating, and material efficiency of 50%
Electricity (cleanroom & other)	3	Wh	[22]	Electricity, low voltage, {GLO}| market group for | APOS [125]	
Output					
Fabricated cell (1, 2, 3, or 4)	1	cm^2	[21]	Created process block in SimaPro	

Table 81: Input-output table for generic III-V HCPV cell processing – high scenario

Input	Amount	Unit	Model source	Database entry	Assumptions
Unfabricated cell (1, 2, 3, or 4)	3.4	cm^2	[22]	**See** Table 73 **-Table 78**	
Solvents	32	g	[22]	Acetone{GLO}| market for | APOS, Isopropanol{GLO}| market for | APOS [125]	16g acetone, 16g isopropanol
Acids	8	g	[22]	Hydrochloric acid, without water, in 30% solution state {RoW}| market for | APOS, Hydrogen fluoride{GLO} market for | APOS [125]	4g hydrochloric acid, 4g hydrogen fluoride
Contact metals	9.5	mg	[21]	Gold {GLO}| market for | APOS [125]	
Lithography materials	2.8	g	[21]	Methyl methacrylate{RoW}| market for | APOS [125]	
Bases	3	g	[22]	Hydrogen peroxide, without water, in 50% solution state {GLO}| market for | APOS [125]	
Water	10	g	estimated	Water, ultrapure {GLO}| market for | APOS [125]	
Antireflective coating	0.16	mg	estimated	Zinc sulfide {GLO}| market for | APOS [125]	Assume 200 nm coating, and material efficiency of 50%
Electricity (cleanroom & other)	0.7	kWh	[21]	Electricity, low voltage, {GLO}| market group for | APOS [125]	
Output					
Fabricated cell (1, 2,	1	cm^2	[22]	Created process block in	

3, or 4)				SimaPro	

Table 82: Input-output table for module/tracker assembly and installation – low scenario

Input	Amount	Unit	Model source	Database entry	Assumptions
Generic cell processing – low scenario	1	cm^2	[21, 22]	See **Table 80** or Table 81	
Heat sink	0.05	kg	[21]	Copper {GLO}| market for | APOS [125]	
Inverter	0.0015	p	[21]	Inverter, 2.5kW {GLO}| market for | APOS [125]	
Fresnel lens	0.06	kg	[21]	Silicone product {GLO}| market for | APOS, [125]	
Float glass	1.5	kg	[21]	Solar glass, low-iron {GLO}| market for | APOS [125]	
Galvanized steel	1.9	kg	[21]	Galvanized steel sheet, at plant/RNA [162]	
Sensor	0.05	g	[22]	Light emitting diode {GLO}| market for | APOS [125]	
Cables	0.01	kg	[22]	Cable, unspecified {GLO}| market for | APOS [125]	
Transformer	0.03	kg	[22]	Transformer, low voltage use {GLO}| market for | APOS [125]	
Foundation	0.8	kg	[22]	Concrete block {GLO}| market for | APOS [125]	
Electricity (other)	0.1	kWh	[22]	Electricity, low voltage, {GLO}| market group for | APOS [125]	
Transport	10	tkm	[21]	Transport, freight, lorry >32 metric ton, EURO3 {GLO}| market for | APOS [125]	
Output					
Module/tracker/BOS corresponding to cell area - low scenario	1	cm^2	[21, 22]	Created process block in SimaPro	[178]

Table 83: Input-output table for module/tracker assembly and installation – high scenario

Input	Amount	Unit	Model source	Database entry	Assumptions
Generic cell processing – high scenario	1	cm^2	[21, 22]	See **Table 80** or Table 81	
Cell packaging	0.04	kg	[21]	Ethylene vinyl acetate copolymer {GLO}| market for | APOS [125]	
Steel	4	kg	[22]	Galvanized steel sheet, at plant/RNA [162]	
Motor	0.0035	kg	[22]	Electric motor, for electric scooter {GLO}| market for | APOS [125]	

Controller	0.0035	kg	[22]	Controller, for electric scooter {GLO}| market for | APOS [125]	
Heat sink	0.9	kg	[22]	Aluminium, primary, ingot {RoW}| market for | APOS [125]	
Inverter	0.0025	p	[22]	Inverter, 2.5kW {GLO}| market for | APOS [125]	
Fresnel lens	0.32	kg	[22]	Polymethyl methacrylate, sheet {GLO}| market for | APOS [125]	
Galvanized steel	2.1	kg	[22]	Galvanized steel sheet, at plant/RNA [162]	
Sensor	0.1	g	[21]	Light emitting diode {GLO}| market for | APOS [125]	
Cables	0.019	kg	[21]	Cable, unspecified {GLO}| market for | APOS [125]	
Transformer	0.04	kg	[21]	Transformer, low voltage use {GLO}| market for | APOS [125]	
Foundation	8.4	kg	[21]	Concrete block {GLO}| market for | APOS [125]	
Electricity (other)	0.2	kWh	[21, 22]	Electricity, low voltage, {GLO}| market group for | APOS [125]	
Transport	11	tkm	[22]	Transport, freight, lorry >32 metric ton, EURO3 {GLO}| market for | APOS [125]	
Output					
Module/tracker/BOS corresponding to cell area - high scenario	1	cm^2	[21, 22]	Created process block in SimaPro	

Table 84: Input-output table for operation and maintenance over 30 year life span – low scenario

Input	Amount	Unit	Model source	Database entry	Assumptions
Module/tracker/BOS corresponding to cell area - low scenario	1	cm^2	[22]	See **Table 82**	
Demineralized water	30	kg	[22]	Water, deionised, from tap water, at user {RoW}| market for water, deionised, from tap water, at user | APOS [125]	
Hydraulic oil	0.25	kg	[22]	White mineral oil, at plant/RNA [162]	
Lubricating oil	0.007	kg	[22]	Lubricating oil {GLO}| market for | APOS [125]	
Polycarbonate	0.0008	kg	[22]	Polycarbonate {GLO}| market for | APOS [125]	
Polyester	0.017	kg	[22]	Polyester resin, unsaturated {GLO}| market for | APOS [125]	
Polyurethane	0.0025	kg	[22]	Polyurethane, flexible foam {GLO}| market for | APOS [125]	
ABS plastic	0.011	kg	[22]	Acrylonitrile-butadiene-styrene copolymer {GLO}| market for | APOS [125]	
Polyamide	0.0003	kg	[22]	Glass fibre reinforced plastic, polyamide, injection moulded {GLO}| market for | APOS [125]	
Silica gel	0.0025	kg	[22]	Silica sand {GLO}| market for |	

				APOS [125]	
Stainless steel	0.002	kg	[22]	Steel, chromium steel 18/8 {GLO}| market for | APOS [125]	
Glass fiber	0.002	kg	[22]	Glass fibre {GLO}| market for | APOS [125]	
Electricity (other)	13.1	kWh	[21]	Electricity, low voltage, {GLO}| market group for | APOS [125]	
Output					
System impacts over 30 year lifespan – low scenario	1	cm^2	[22]	Created process block in SimaPro	

Table 85: Input-output table for operation and maintenance over 30 year life span – high scenario

Input	Amount	Unit	Model source	Database entry	Assumptions
Module/tracker/BOS corresponding to cell area - low scenario	1	cm^2	[22]	See Table 83	
Demineralized water	30	kg	[22]	Water, deionised, from tap water, at user {RoW}| market for water, deionised, from tap water, at user | APOS [125]	
Hydraulic oil	0.25	kg	[22]	White mineral oil, at plant/RNA [162]	
Lubricating oil	0.007	kg	[22]	Lubricating oil {GLO}| market for | APOS [125]	
Polycarbonate	0.0008	kg	[22]	Polycarbonate {GLO}| market for | APOS [125]	
Polyester	0.017	kg	[22]	Polyester resin, unsaturated {GLO}| market for | APOS [125]	
Polyurethane	0.0025	kg	[22]	Polyurethane, flexible foam {GLO}| market for | APOS [125]	
ABS plastic	0.011	kg	[22]	Acrylonitrile-butadiene-styrene copolymer {GLO}| market for | APOS [125]	
Polyamide	0.0003	kg	[22]	Glass fibre reinforced plastic, polyamide, injection moulded {GLO}| market for | APOS [125]	
Silica gel	0.0025	kg	[22]	Silica sand {GLO}| market for | APOS [125]	
Stainless steel	0.002	kg	[22]	Steel, chromium steel 18/8 {GLO}| market for | APOS [125]	
Glass fiber	0.002	kg	[22]	Glass fibre {GLO}| market for | APOS [125]	
Electricity (other)	13.1	kWh	[21]	Electricity, low voltage, {GLO}| market group for | APOS [125]	
Output					
System impacts over 30 year lifespan – high scenario	1	cm^2	[22]	Created process block in SimaPro	

Table 86: Cell growth scenarios for 1 kWp of each cell type under 500x concentration

Cell growth scenario	Impact / kWp	Cell 1	Cell 2	Cell 3	Cell 4
High purity, high material-usage	**CED** (MJ)	196 MJ	361 MJ	650 MJ	332 MJ
	GHG (kg CO_2-eq)	12.9 kg	22.6 kg	41.2 kg	20 kg
Mid-range purity, mid-range material usage	**CED** (MJ)	195 MJ	161 MJ	267 MJ	139 MJ
	GHG (kg CO_2-eq)	12.8 kg	9.3 kg	15.8 kg	7.2 kg
Low purity, low material usage	**CED** (MJ)	195 MJ	129 MJ	207 MJ	107 MJ
	GHG(kg CO_2-eq)	12.8 kg	7.2 kg	12.3 kg	5.6 kg

Table 87: High-impact and low-impact cell fabrication scenarios for 1 kWp of each cell type under 500x concentration

Cell fabrication scenario – assuming "mid" cell growth scenario	Impact / kWp	Cell 1	Cell 2	Cell 3	Cell 4
Low chemical, metal, and energy usage	**CED** (MJ)	533 MJ	441 MJ	702 MJ	379 MJ
	GHG (kg CO_2-eq)	34.4 kg	25 kg	41.1 kg	19.5 kg
High chemical, metal, and energy usage	**CED** (MJ)	1570 MJ	1310 MJ	1590 MJ	1100 MJ
	GHG (kg CO_2-eq)	100 kg	79.4 kg	96 kg	63.9 kg

Table 88: Module/tracker/BOS assembly and install scenarios for 1 kWp of each cell type under 500x concentration

Module/Tracker/BOS assembly & install scenarios	Impact / kW_p	Cell 1	Cell 2	Cell 3	Cell 4
Low transport, material, and energy usage (including low cell fabrication scenario)	**CED** (MJ)	8570 MJ	7250 MJ	6730 MJ	5980 MJ
	GHG (kg CO_2-eq)	643 kg	542 kg	498 kg	445 kg
High transport, material, and energy usage (including high cell fabrication scenario)	**CED** (MJ)	33300 MJ	28200 MJ	25400 MJ	23200 MJ
	GHG (kg CO_2-eq)	2870 kg	2420 kg	2170 kg	1990 kg

Table 89: Operation and maintenance over 30-year lifespan for 1 kWp of each cell type under 500x concentration

Operation & Maintenance scenarios	Impact /kWp	Cell 1	Cell 2	Cell 3	Cell 4
Low module/tracker/BOS scenario input	**CED** (MJ)	20700 MJ	17600 MJ	15800 MJ	14500 MJ
	GHG (kg CO_2-eq)	1420 kg	1200 kg	1080 kg	989 kg
High module/tracker/BOS scenario input	**CED** (MJ)	45400 MJ	38500 MJ	34500 MJ	31700 MJ
	GHG (kg CO_2-eq)	3650 kg	3080 kg	2750 kg	2540 kg

REFERENCES

[1] M. A. Green, K. Emery, Y. Hishikawa, W. Warta, and E. D. Dunlop, "Solar cell efficiency tables (Version 45)," *Progress in photovoltaics: research and applications,* vol. 23, no. 1, pp. 1-9, 2015.

[2] K. Horowitz, M. Woodhouse, H. Lee, and G. Smestad, "Bottom-Up Cost Analysis of a High Concentration PV Module; NREL (National Renewable Energy Laboratory)," NREL (National Renewable Energy Laboratory (NREL), Golden, CO (United States))2015.

[3] M. Woodhouse and A. Goodrich, "A manufacturing cost analysis relevant to single-and dual-junction photovoltaic cells fabricated with III-Vs and III-Vs grown on Czochralski silicon," National Renewable Energy Laboratory2013.

[4] M. González *et al.*, "Modeling and analysis of multijunction solar cells," presented at the SPIE, the International Society for Optical Engineering, San Francisco, 2011. doi:. Available: http://dx.doi.org/10.1117/12.875757

[5] H. Yokoyama, H. Sugiyama, Y. Oda, M. Sato, N. Watanabe, and T. Kobayashi, "Metalorganic vapor phase epitaxy growth of InAlAsSb on InP," *Japanese journal of applied physics,* vol. 43, no. 8R, p. 5110, 2004.

[6] L. C. Hirst *et al.*, "Spatially indirect radiative recombination in InAlAsSb grown lattice-matched to InP by molecular beam epitaxy," *Journal of Applied Physics,* vol. 117, no. 21, p. 215704, 2015.

[7] E. R. Glaser, R. Magno, B. V. Shanabrook, and J. G. Tischler, "Optical characterization of In0.27Ga0.73Sb and InxAl1−xAsySb1−y epitaxial layers for development of 6.2-Å-based heterojunction bipolar transistors," *Journal of Vacuum Science & Technology B: Microelectronics and Nanometer Structures Processing, Measurement, and Phenomena,* vol. 24, no. 3, pp. 1604-1606, 2006.

[8] J. R. Chang, Y.-K. Su, D. H. Jaw, H. P. Shiao, and W. Lin, "Metalorganic vapor phase epitaxy (MOVPE) growth and characterization of AlInAsSb and AlInAsSb/InGaAs multiple-quantum-well structures," *Journal of crystal growth,* vol. 203, no. 4, pp. 481-485, 1999.

[9] Y.-J. Chen, Y.-W. Chen, Y.-S. Lin, C.-Y. Yeh, Y.-J. Li, and W.-C. Hsu, "An Improved In0. 34Al0. 66As0. 85Sb0. 15/InP Heterostructure Utilizing Coupled δ-Doping InP Channel," *Japanese Journal of Applied Physics,* vol. 40, no. 1A, p. L7, 2001.

[10] M. P. Lumb *et al.*, "Simulation of novel InAlAsSb solar cells," in *SPIE OPTO*, 2012, pp. 82560S-82560S-13: International Society for Optics and Photonics.

[11] C. Kerestes *et al.*, "Fabrication and analysis of multijunction solar cells with a quantum dot (In) GaAs junction," *Progress in Photovoltaics: Research and Applications,* vol. 22, no. 11, pp. 1172-1179, 2014.

[12] C. G. Bailey *et al.*, "Open-Circuit Voltage Improvement of InAs/GaAs Quantum-Dot Solar Cells Using Reduced InAs Coverage," *Photovoltaics, IEEE Journal of,* vol. 2, no. 3, pp. 269-275, 2012.

[13] G. Wei, K.-T. Shiu, N. C. Giebink, and S. R. Forrest, "Thermodynamic limits of quantum photovoltaic cell efficiency," *Applied Physics Letters,* vol. 91, no. 22, p. 223507, 2007.

[14] T. Inoue, K. Watanabe, K. Toprasertpong, H. Fujii, M. Sugiyama, and Y. Nakano, "Enhanced Light Trapping in Multiple Quantum Wells by Thin-Film Structure and Backside Grooves With Dielectric Interface," *Photovoltaics, IEEE Journal of,* vol. 5, no. 2, pp. 697-703, 2015.

[15] Y. Dai *et al.*, "Effects of electric field on thermal and tunneling carrier escape in InAs/GaAs quantum dot solar cells," in *SPIE OPTO*, 2014, pp. 898106-898106-6: International Society for Optics and Photonics.

[16] H. Jiang and J. Singh, "Strain distribution and electronic spectra of InAs/GaAs self-assembled dots: An eight-band study," *Physical Review B,* vol. 56, no. 8, pp. 4696-4701, 08/15/ 1997.

[17] O. Stier, M. Grundmann, and D. Bimberg, "Electronic and optical properties of strained quantum dots modeled by 8-band k· p theory," *Physical Review B,* vol. 59, no. 8, p. 5688, 1999.

[18] E. Yablonovitch, "Statistical ray optics," *Journal of the Optical Society of America,* vol. 72, no. 7, pp. 899-907, 1982/07/01 1982.

[19] C. Kerestes *et al.*, "Strain effects on radiation tolerance of triple-junction solar cells with InAs quantum dots in the GaAs junction," *IEEE Journal of Photovoltaics,* vol. 4, no. 1, pp. 224-232, 2014.

[20] C. Keavney, R. Walters, and P. Drevinsky, "Optimizing the radiation resistance of InP solar cells: Effect of dopant density and cell thickness," *Journal of applied physics,* vol. 73, no. 1, pp. 60-70, 1993.

[21] G. Peharz and F. Dimroth, "Energy payback time of the high-concentration PV system FLATCON®," *Progress in Photovoltaics: Research and Applications,* vol. 13, no. 7, pp. 627-634, 2005.

[22] V. M. Fthenakis and H. C. Kim, "Life cycle assessment of high-concentration photovoltaic systems," *Progress in Photovoltaics: Research and Applications,* vol. 21, no. 3, pp. 379-388, 2013.

[23] A. Nishimura *et al.*, "Life cycle assessment and evaluation of energy payback time on high-concentration photovoltaic power generation system," *Applied Energy,* vol. 87, no. 9, pp. 2797-2807, 9// 2010.

[24] H. C. Kim, K. G. Knight, N. Krishnan, and V. M. Fthenakis, "Life cycle analysis of two new concentrator PV systems," pp. 909-913.
[25] C. Reich-Weiser, T. Fletcher, D. A. Dornfeld, and S. Horne, "Development of the supply chain optimization and planning for the environment (SCOPE) tool-applied to solar energy," pp. 1-6: IEEE.
[26] F. Dimroth, C. Agert, and A. W. Bett, "Growth of Sb-based materials by MOVPE," *Journal of Crystal Growth*, vol. 248, no. 0, pp. 265-273, 2// 2003.
[27] Inductiveload. (2008, May 6, 2018). *File:Brillouin Zone (1st, FCC).svg*.
[28] J. S. Blakemore, "Semiconducting and other major properties of gallium arsenide," *Journal of Applied Physics*, vol. 53, no. 10, pp. R123-R181, 1982.
[29] F. H. Yang, "2 - Modern metal-organic chemical vapor deposition (MOCVD) reactors and growing nitride-based materials," in *Nitride Semiconductor Light-Emitting Diodes (LEDs)*: Woodhead Publishing, 2014, pp. 27-65.
[30] M. Ohring, *Materials science of thin films*. Academic press, 2001.
[31] G. B. Stringfellow, *Organometallic vapor-phase epitaxy: theory and practice*. Elsevier, 1999.
[32] U. W. Pohl, *Epitaxy of Semiconductors: Introduction to Physical Principles*. Springer Science & Business Media, 2013.
[33] W. Shockley and H. J. Queisser, "Detailed balance limit of efficiency of p-n junction solar cells," *Journal of applied physics*, vol. 32, no. 3, pp. 510-519, 1961.
[34] M. A. Green, Y. Hishikawa, E. D. Dunlop, D. H. Levi, J. Hohl-Ebinger, and A. W. Y. Ho-Baillie, "Solar cell efficiency tables (version 51)," *Progress in Photovoltaics: Research and Applications*, vol. 26, no. 1, pp. 3-12, 2018.
[35] J. Nelson, *The physics of solar cells*. World Scientific Publishing Co Inc, 2003.
[36] R. R. King *et al.*, "Band gap-voltage offset and energy production in next-generation multijunction solar cells," *Progress in Photovoltaics: Research and Applications*, vol. 19, no. 7, pp. 797-812, 2011/11/01 2010.
[37] S. Fujita, T. Noda, C. Nozaki, and Y. Ashizawa, "InGaAs/InAlAs HEMT with a strained InGaP Schottky contact layer," *Electron Device Letters, IEEE*, vol. 14, no. 5, pp. 259-261, 1993.
[38] C. Lenox *et al.*, "Resonant-cavity InGaAs-InAlAs avalanche photodiodes with gain-bandwidth product of 290 GHz," *Photonics Technology Letters, IEEE*, vol. 11, no. 9, pp. 1162-1164, 1999.
[39] I. Mathews *et al.*, "InAlAs solar cell on a GaAs substrate employing a graded InxGa1− xAs–InP metamorphic buffer layer," *Applied Physics Letters*, vol. 102, no. 3, p. 033906, 2013.
[40] M. S. Leite, R. L. Woo, W. D. Hong, D. C. Law, and H. A. Atwater, "Wide-band-gap InAlAs solar cell for an alternative multijunction approach," *Applied Physics Letters*, vol. 98, no. 9, p. 093502, 2011.
[41] M. S. Leite, E. C. Warmann, G. M. Kimball, S. P. Burgos, D. M. Callahan, and H. A. Atwater, "Wafer-Scale Strain Engineering of Ultrathin Semiconductor Crystalline Layers," *Advanced Materials*, vol. 23, no. 33, pp. 3801-3807, 2011.
[42] B. L. Smith *et al.*, "Characterization of InAlAs solar cells grown by MOVPE," in *Photovoltaic Specialist Conference*, Denver, CO, 2014, pp. 1180-1185: IEEE.
[43] B. Wakefield, M. A. G. Halliwell, T. Kerr, D. A. Andrews, G. J. Davies, and D. R. Wood, "Direct energy gap of Al1−xInxAs lattice matched to InP," *Applied Physics Letters*, vol. 44, no. 3, pp. 341-343, 1984.
[44] I. Vurgaftman, J. Meyer, and L. Ram-Mohan, "Band parameters for III–V compound semiconductors and their alloys," *Journal of applied physics*, vol. 89, no. 11, pp. 5815-5875, 2001.
[45] M. S. Leite *et al.*, "Towards an optimized all lattice-matched InAlAs/InGaAsP/InGaAs multijunction solar cell with efficiency> 50%," *Applied Physics Letters*, vol. 102, no. 3, p. 033901, 2013.
[46] C. Gelderloos, K. Miller, R. Walters, G. Summers, and S. Messenger, "Low intensity low temperature performance of advanced solar cells," in *Photovoltaic Specialists Conference, 2002. Conference Record of the Twenty-Ninth IEEE*, 2002, pp. 804-807: IEEE.
[47] P. Jenkins, D. Scheiman, D. Brinker, and J. Appelbaum, "Low intensity low temperature (LILT) measurements and coefficients on new photovoltaic structures," in *Photovoltaic Specialists Conference, 1996., Conference Record of the Twenty Fifth IEEE*, 1996, pp. 317-320: IEEE.
[48] R. Walters, "A review of radiation effects in InP solar cells," in *Indium Phosphide and Related Materials, 1994. Conference Proceedings., Sixth International Conference on*, 1994, pp. 275-279: IEEE.
[49] H. Hovel, "The effect of depletion region recombination currents on the efficiencies of Si and GaAs solar cells," in *Photovoltaic Specialists Conference*, Palo Alto, CA, 1974, pp. 34-39.
[50] H. Dinges, H. Burkhard, R. Lösch, H. Nickel, and W. Schlapp, "Refractive indices of InAlAs and InGaAs/InP from 250 to 1900 nm determined by spectroscopic ellipsometry," *Applied Surface Science*, vol. 54, pp. 477-481, 1992.

[51] M. K. Yakes *et al.*, "Evaluation of strained InAlAs as a window layer for wide bandgap materials lattice matched to InP," in *Photovoltaic Specialist Conference (PVSC), 2015 IEEE 42nd*, 2015, pp. 1-4: IEEE.
[52] J. Matthews and A. Blakeslee, "Defects in epitaxial multilayers: I. Misfit dislocations," *Journal of Crystal Growth,* vol. 27, pp. 118-125, 1974.
[53] M. S. Leite, R. L. Woo, W. D. Hong, D. C. Law, and H. A. Atwater, "InAlAs epitaxial growth for wide band gap solar cells," in *IEEE Photovoltaic Specialists Conference*, 2011, pp. 000780-000783: IEEE.
[54] D. Olego, T. Chang, E. Silberg, E. Caridi, and A. Pinczuk, "Compositional dependence of band-gap energy and conduction-band effective mass of In1− x− yGaxAlyAs lattice matched to InP," *Applied Physics Letters,* vol. 41, no. 5, pp. 476-478, 1982.
[55] H. K. Cho, J. Y. Lee, M. S. Kwon, B. Lee, J. H. Baek, and W. S. Han, "Observation of phase separation and ordering in the InAlAs epilayer grown on InP at the low temperature," *Materials Science and Engineering: B,* vol. 64, no. 3, pp. 174-179, 10/15/ 1999.
[56] B. L. Smith *et al.*, "InAlAs photovoltaic cell design for high device efficiency," *Progress in Photovoltaics: Research and Applications,* vol. 25, no. 8, pp. 706-713, 2017.
[57] M. Wolf and H. Rauschenbach, "Series resistance effects on solar cell measurements," *Advanced Energy Conversion,* vol. 3, no. 2, pp. 455-479, 1963/04/01 1963.
[58] B. M. Kayes *et al.*, "27.6% Conversion efficiency, a new record for single-junction solar cells under 1 sun illumination," in *2011 37th IEEE Photovoltaic Specialists Conference*, 2011, pp. 000004-000008.
[59] H. Kakinuma, M. Mohri, and M. Akiyama, "Characterization of oxygen and carbon in undoped AlGaAs grown by organometallic vapor-phase epitaxy," *Japanese journal of applied physics,* vol. 36, no. 1R, p. 23, 1997.
[60] N. I. Buchan, T. F. Kuech, G. Scilla, and F. Cardone, "Carbon incorporation in metalorganic vapor phase epitaxy grown GaAs using CHyX4− y, TMG and AsH3," *Journal of crystal growth,* vol. 110, no. 3, pp. 405-414, 1991.
[61] T. F. Kuech and R. Potemski, "Reduction of background doping in metalorganic vapor phase epitaxy of GaAs using triethylgallium at low reactor pressures," *Applied physics letters,* vol. 47, no. 8, pp. 821-823, 1985.
[62] T. F. Kuech, E. Veuhoff, T. S. Kuan, V. Deline, and R. Potemski, "The influence of growth chemistry on the MOVPE growth of GaAs and AlxGa1− xAs layers and heterostructures," *Journal of Crystal Growth,* vol. 77, no. 1-3, pp. 257-271, 1986.
[63] W. S. Hobson and M. Geva, "Alternative Group V Precursors for the Growth of Al-Based III-V Epitaxial Layers by OMVPE," vol. 282, p. 93: Cambridge Univ Press.
[64] R. M. Biefeld, "The metal-organic chemical vapor deposition and properties of III–V antimony-based semiconductor materials," *Materials Science and Engineering: R: Reports,* vol. 36, no. 4, pp. 105-142, 2002.
[65] C. Agert, F. Dimroth, U. Schubert, A. W. Bett, S. Leu, and W. Stolz, "High-efficiency (AlGa)As/GaAs solar cells grown by MOVPE using TBAs at low-temperatures and low V/III-ratios," *Solar Energy Materials and Solar Cells,* vol. 66, no. 1-4, pp. 637-644, Feb 2001.
[66] R. M. Biefeld, A. A. Allerman, and K. C. Baucom, "Method of making AlInSb by metal-organic chemical vapor deposition," ed: Google Patents, 2000.
[67] P. Velling, M. Agethen, W. Prost, and F. J. Tegude, "InAlAs/InGaAs/InP heterostructures for RTD and HBT device applications grown by LP-MOVPE using non-gaseous sources," *Journal of crystal growth,* vol. 221, no. 1, pp. 722-729, 2000.
[68] S. Neumann, W. Prost, and F. J. Tegude, "Growth of carbon-doped LP-MOVPE InAlAs using non-gaseous sources," *Journal of crystal growth,* vol. 248, pp. 130-133, 2003.
[69] S. Leu, F. Höhnsdorf, W. Stolz, R. Becker, A. Salzmann, and A. Greiling, "C-and O-incorporation in (AlGa) As epitaxial layers grown by MOVPE using TBAs," *Journal of crystal growth,* vol. 195, no. 1, pp. 98-104, 1998.
[70] C. Wang, S. Salimand, K. Jensen, and A. Jones, "Low oxygen and carbon incorporation in AIGaAs using tritertiarybutylaluminum in organometallic vapor phase epitaxy," *Journal of electronic materials,* vol. 25, no. 5, pp. 771-774, 1996.
[71] C. A. Wang, M. C. Finn, S. Salim, K. F. Jensen, and A. C. Jones, "Tritertiarybutylaluminum as an organometallic source for epitaxial growth of AlGaSb," *Applied physics letters,* vol. 67, no. 10, pp. 1384-1386, 1995.
[72] C. A. Larsen, N. I. Buchan, S. H. Li, and G. B. Stringfellow, "Decomposition Mechanisms of Tertiarybutylarsine," (in English), *Journal of Crystal Growth,* vol. 94, no. 3, pp. 663-672, Mar 1989.

[73] C. Giesen, M. Beerbom, X. Xu, and K. Heime, "MOVPE of AlAsSb using tritertiarybutylaluminum," *Journal of crystal growth*, vol. 195, no. 1, pp. 85-90, 1998.
[74] R. Dittrich and W. Schroeder, "Empirical pseudopotential band structure of In 0.53 Ga 0.47 As and In 0.52 Al 0.48 As," *Solid-State Electronics*, vol. 43, no. 2, pp. 403-407, 1999.
[75] J. Boisvert *et al.*, "Development of space solar cells at Spectrolab," in *Photovoltaic Specialists Conference (PVSC), 2011 37th IEEE*, 2011, pp. 001528-001531.
[76] H. W. J. Brandhorst, *InP (Indium Phosphide): Into the future*. 1989, p. Medium: X; Size: Pages: (10 p).
[77] M. Slocum, D. V. Forbes, G. C. Hillier, B. L. Smith, J. G. Adams, and S. M. Hubbard, "Development of InAlAsSb growth by MOVPE," *Submitted*, 2016.
[78] C. Giesen, M. M. Beerbom, X. G. Xu, and K. Heime, "MOVPE of AlAsSb using tritertiarybutylaluminum," *Journal of crystal growth*, vol. 195, no. 1, pp. 85-90, 1998.
[79] C. A. Wang, "Organometallic vapor phase epitaxial growth of AlSb-based alloys," *Journal of crystal growth*, vol. 170, no. 1, pp. 725-731, 1997.
[80] A. A. Allerman, R. M. Biefeld, and S. R. Kurtz, "InAsSb-based mid-infrared lasers (3.8–3.9 μm) and light-emitting diodes with AlAsSb claddings and semimetal electron injection, grown by metalorganic chemical vapor deposition," *Applied physics letters*, vol. 69, no. 4, pp. 465-467, 1996.
[81] R. M. Biefeld, A. A. Allerman, and S. R. Kurtz, "The growth of mid-infrared lasers and AlAs x Sb 1− x by MOCVD," *Journal of crystal growth*, vol. 174, no. 1, pp. 593-598, 1997.
[82] R. M. Biefeld, A. A. Allerman, and S. R. Kurtz, "The growth and doping of Al (As) Sb by metal-organic chemical vapor deposition," vol. 421, p. 33: Cambridge Univ Press.
[83] R. M. Biefeld, A. A. Allerman, and M. W. Pelczynski, "Growth of n-and p-type Al (As) Sb by metalorganic chemical vapor deposition," *Applied physics letters*, vol. 68, no. 7, pp. 932-934, 1996.
[84] W.-K. Chen, J. Ou, and C.-H. Hsu, "Effects of growth temperature on solid incorporation of AlAs1-xSbx using tertiarybutylarsine as arsenic source precursor," *Japanese journal of applied physics*, vol. 35, no. 10A, p. L1234, 1996.
[85] R. M. Biefeld, S. R. Kurtz, and A. A. Allerman, "The metalorganic chemical vapor deposition growth of AlAsSb and InAsSb/lnAs using novel source materials for Infrared Emitters," *Journal of electronic materials*, vol. 26, no. 8, pp. 903-909, 1997.
[86] J. Ou and W.-K. Chen, "Composition control in the growth of AlAs 1-x Sb x alloys," pp. 157-160: IEEE.
[87] S. Polly, "Photoluminescence: photoluminescence fitting," ed. github.com, 2015.
[88] W. J. Turner, W. E. Reese, and G. D. Pettit, "Exciton Absorption and Emission in InP," *Physical Review*, vol. 136, no. 5A, pp. A1467-A1470, 11/30/ 1964.
[89] A. Fahrenbruch and R. Bube, *Fundamentals of solar cells: photovoltaic solar energy conversion*. Elsevier, 2012.
[90] T. K. S. Wong, *Semiconductor strain metrology: principles and applications*. Bentham Science Publishers, 2012.
[91] D. E. Aspnes, "Third-derivative modulation spectroscopy with low-field electroreflectance," *Surface Science*, vol. 37, pp. 418-442, 1973.
[92] F. H. Pollak and H. Shen, "Modulation spectroscopy of semiconductors: bulk/thin film, microstructures, surfaces/interfaces and devices," *Materials Science and Engineering: R: Reports*, vol. 10, no. 7, pp. xv-374, 1993/10/01 1993.
[93] S. Polly, "Photoreflectance: photoreflectance fitting," ed. github.com, 2015.
[94] C. M. Herzinger, P. G. Snyder, B. Johs, and J. A. Woollam, "InP optical constants between 0.75 and 5.0 eV determined by variable-angle spectroscopic ellipsometry," *Journal of applied physics*, vol. 77, no. 4, pp. 1715-1724, 1995.
[95] H. Lipsanen and V. Airaksinen, "Interference effects in photoreflectance of epitaxial layers grown on semi-insulating substrates," *Applied physics letters*, vol. 63, no. 21, pp. 2863-2865, 1993.
[96] D. J. Hall, T. J. C. Hosea, and D. Lancefield, "Airy function analysis of Franz–Keldysh oscillations in the photoreflectance spectra of In1−xGaxAsyP1−y layers," *Journal of Applied Physics*, vol. 82, no. 6, pp. 3092-3099, 1997.
[97] W. Zhou *et al.*, "Investigation of near interface properties in semi-insulating InP substrates with epitaxial grown InGaAs and InAlAs by photoreflectance," *Journal of applied physics*, vol. 73, no. 3, pp. 1266-1271, 1993.
[98] Y. Okada *et al.*, "Intermediate band solar cells: Recent progress and future directions," *Applied physics reviews*, vol. 2, no. 2, p. 021302, 2015.

[99] R. Tatavarti *et al.*, "Lightweight, low cost InGaP/GaAs dual-junction solar cells on 100 mm epitaxial liftoff (ELO) wafers," in *Photovoltaic Specialists Conference (PVSC), 2009 34th IEEE*, 2009, pp. 002065-002067: IEEE.
[100] H. F. Lu, S. Mokkapati, L. Fu, G. Jolley, H. H. Tan, and C. Jagadish, "Plasmonic quantum dot solar cells for enhanced infrared response," *Applied Physics Letters*, vol. 100, no. 10, p. 103505, 2012.
[101] M. F. Bennett *et al.*, "Epitaxial lift-off of quantum dot enhanced GaAs single junction solar cells," *Applied Physics Letters*, vol. 103, no. 21, p. 213902, 2013.
[102] K. Watanabe, T. Inoue, H. Sodabanlu, M. Sugiyama, and Y. Nakano, "Self-organized texture of GaAs by wet etching for light trapping in MQWS solar cells," in *31st European Photovoltaic Solar Energy Conference*, Hamburg, Germany, 2015, pp. 181-184.
[103] D. Bimberg, M. Grundmann, and N. N. Ledentsov, *Quantum dot heterostructures*. John Wiley & Sons, 1999.
[104] D. Leonard, K. Pond, and P. M. Petroff, "Critical layer thickness for self-assembled InAs islands on GaAs," *Physical Review B*, vol. 50, no. 16, pp. 11687-11692, 10/15/ 1994.
[105] S. M. Hubbard, A. Podell, C. Mackos, S. Polly, C. G. Bailey, and D. V. Forbes, "Effect of vicinal substrates on the growth and device performance of quantum dot solar cells," *Solar Energy Materials and Solar Cells*, vol. 108, pp. 256-262, 1// 2013.
[106] C. G. Bailey, S. M. Hubbard, D. V. Forbes, and R. P. Raffaelle, "Evaluation of strain balancing layer thickness for InAs/GaAs quantum dot arrays using high resolution x-ray diffraction and photoluminescence," *Applied Physics Letters*, vol. 95, no. 20, p. 203110, 2009.
[107] R. E. Williams, "GaAs processing techniques," *Artech House*, pp. 85-122, 1984.
[108] S. Adachi and K. Oe, "Chemical etching characteristics of (001) GaAs," *Journal of The Electrochemical Society*, vol. 130, no. 12, pp. 2427-2435, 1983.
[109] S. H. Jones and D. K. Walker, "Highly anisotropic wet chemical etching of GaAs using NH 4 OH: H 2 O 2: H 2 O," *Journal of the Electrochemical Society*, vol. 137, no. 5, pp. 1653-1654, 1990.
[110] B. L. Smith *et al.*, "Inverted growth evaluation for epitaxial lift off (ELO) quantum dot solar cell and enhanced absorption by back surface texturing," pp. 1276-1281: IEEE.
[111] N. López, A. Martí, A. Luque, C. Stanley, C. Farmer, and P. Diaz, "Experimental Analysis of the Operation of Quantum Dot Intermediate Band Solar Cells," *Journal of Solar Energy Engineering*, vol. 129, no. 3, pp. 319-322, 2006.
[112] S. M. Hubbard, M. Bennett, A. Podell, and D. V. Forbes, "Optimization of growth and device performance for InAs quantum dot solar cells," in *Photovoltaic Specialists Conference (PVSC), 2012 38th IEEE*, 2012, pp. 001788-001793.
[113] K. Watanabe *et al.*, "Optical analysis of the photon recycling effect in InGaAs/GaAsP multiple quantum well solar cell with light trapping structure," in *2016 IEEE 43rd Photovoltaic Specialists Conference (PVSC)*, 2016, pp. 1268-1272.
[114] Z. S. Bittner *et al.*, "Characterization of InGaP heterojunction emitter quantum dot solar cells," in *Photovoltaic Specialists Conference (PVSC), 2012 38th IEEE*, 2012, pp. 003158-003161: IEEE.
[115] C. G. Bailey, D. V. Forbes, R. P. Raffaelle, and S. M. Hubbard, "Near 1 V open circuit voltage InAs/GaAs quantum dot solar cells," *Applied Physics Letters*, vol. 98, no. 16, p. 163105, 2011.
[116] (2018). *Best Research-Cell Efficiencies*. Available: https://www.nrel.gov/pv/assets/images/efficiency-chart-20180716.jpg
[117] A. W. Bett *et al.*, "Overview about technology perspectives for high efficiency solar cells for space and terrestrial applications," in *Proceedings of the 28th European Photovoltaic Solar Energy Conference and Exhibition, Paris, France, EU PVSEC, München, Germany*, 2013, p. 1AP.
[118] P. Swart, J. Dewulf, H. Van Langenhove, K. Moonens, K. Dessein, and C. Quaeyhaegens, "Assessment of the overall resource consumption of germanium wafer production for high concentration photovoltaics," *Resources, Conservation and Recycling*, vol. 55, no. 12, pp. 1119-1128, 10// 2011.
[119] B. Corona, L. Escudero, G. Quéméré, I. Luque-Heredia, and G. San Miguel, "Energy and environmental life cycle assessment of a high concentration photovoltaic power plant in Morocco," *The International Journal of Life Cycle Assessment*, vol. 22, no. 3, pp. 364-373, 2017/03/01 2017.
[120] G. Timò, "Results of the APOLLON Project and Concentrating Photovoltaic Perspective," *Milan (IT)*, 2014.
[121] P. Sandwell, G. Duggan, J. Nelson, and N. Ekins-Daukes, "The environmental impact of lightweight HCPV modules: efficient design and effective deployment," *Progress in Photovoltaics: Research and Applications*, vol. 24, no. 11, pp. 1458-1472, 2016/11/01 2016.

[122] A. Hu *et al.*, "Assessment of the Carbon Footprint, Social Benefit of Carbon Reduction, and Energy Payback Time of a High-Concentration Photovoltaic System," *Sustainability*, vol. 9, no. 1, p. 27, 2017.
[123] C. Reich-Weiser, D. A. Dornfeld, and S. Horne, "Environmental assessment and metrics for solar: Case study of SolFocus solar concentrator systems," in *Photovoltaic Specialists Conference, 2008. PVSC '08. 33rd IEEE*, 2008, pp. 1-4.
[124] M. de Wild-Scholten, "Environmental sustainability of concentrator PV systems: preliminary LCA results of the Apollon project," in *25th European Photovoltaic Solar Energy Conference and Exhibition Valencia, Spain*, 2010, pp. 6-10.
[125] G. Wernet, C. Bauer, B. Steubing, J. Reinhard, E. Moreno-Ruiz, and B. Weidema, "The ecoinvent database version 3 (part I): overview and methodology," *The International Journal of Life Cycle Assessment*, journal article vol. 21, no. 9, pp. 1218-1230, 2016.
[126] P. T. Chiu *et al.*, "Direct Semiconductor Bonded 5J Cell for Space and Terrestrial Applications," *IEEE Journal of Photovoltaics*, vol. 4, no. 1, pp. 493-497, 2014.
[127] F. Dimroth, C. Baur, A. W. Bett, M. Meusel, and G. Strobl, "3-6 junction photovoltaic cells for space and terrestrial concentrator applications," in *Photovoltaic Specialists Conference, 2005. Conference Record of the Thirty-first IEEE*, 2005, pp. 525-529.
[128] R. R. King *et al.*, "Solar cell generations over 40% efficiency," *Progress in Photovoltaics: Research and Applications*, vol. 20, no. 6, pp. 801-815, 2012.
[129] C. Jiménez-González, S. Kim, and M. R. Overcash, "Methodology for developing gate-to-gate life cycle inventory information," *The International Journal of Life Cycle Assessment*, vol. 5, no. 3, pp. 153-159, 2000.
[130] R. L. McGinnis and M. Elimelech, "Energy requirements of ammonia–carbon dioxide forward osmosis desalination," *Desalination*, vol. 207, no. 1, pp. 370-382, 2007/03/10/ 2007.
[131] (February 27). *AXT, Inc. Product Specifications*. Available: http://www.axt.com/site/index.php?q=taxonomy/term/3
[132] A. Meijer, M. A. J. Huijbregts, J. J. Schermer, and L. Reijnders, "Life-cycle assessment of photovoltaic modules: Comparison of mc-Si, InGaP and InGaP/mc-Si solar modules," *Progress in Photovoltaics*, vol. 11, no. 4, pp. 275-287, Jun 2003.
[133] (2010, April 18, 2018). *Growth - Crystal Growth Technology: Wafer Technology*. Available: http://www.wafertech.co.uk/growth.htm
[134] K. Okita, "Indium phosphide substrate manufacturing method, epitaxial wafer manufacturing method indium phosphide substrate, and epitaxial wafer," ed: Google Patents, 2013.
[135] N. J. Mohr, J. J. Schermer, M. A. J. Huijbregts, A. Meijer, and L. Reijnders, "Life cycle assessment of thin-film GaAs and GaInP/GaAs solar modules," (in English), *Progress in Photovoltaics*, Article vol. 15, no. 2, pp. 163-179, Mar 2007.
[136] W. Liu, M. S. Young, and M. H. Badawi, "Low etch pit density (EPD) semi-insulating III-V wafers," ed: Google Patents, 2013.
[137] *GaAs Wafer Technology*. Available: http://www.fcm-germany.com/en/technology/
[138] AXT. (April 24, 2018). *VGF Technology | AXT Inc.* Available: http://www.axt.com/site/index.php?q=node/2
[139] K. Ghosh, "Production of ultra pure gallium by zone refining and liquid phase epitaxial growth of related III V layered structures and their characterization," Department of Electronic Science, University of Calcutta, Shodhganga, 2009.
[140] P. Nuss and M. J. Eckelman, "Life cycle assessment of metals: a scientific synthesis," *PLoS One*, vol. 9, no. 7, p. e101298, 2014.
[141] G. F. E. Agency, "ProBas: Arsenic," ed. http://www.probas.umweltbundesamt.de/php/prozessdetails.php?id={F457A261-DEC5-42B7-9F5E-383B3F840C1D}, 2004.
[142] H. Yang, "Production method for high-purity arsenic and its equipment " China, 2009. Available: https://patents.google.com/patent/CN100482819C/en.
[143] F. Lu *et al.*, "Resources and extraction of gallium: A review," *Hydrometallurgy*, vol. 174, pp. 105-115, 2017/12/01/ 2017.
[144] J. Koch, "Budget estimate for increased III-V solar production," ed: Dock Chemicals, Chief Marketing Officer, 2017.
[145] L. Gibson, "Technical questions regarding MO purchase," B. Smith, Ed., ed: Business Development Manager, SAFC Hitech Inc, 2017.
[146] T. Tsudera, S. Tanaka, D. Iwai, H. Nishiwaki, and T. Honma, "High-purity trimethylaluminum and purification method of crude trimethylaluminum," ed: Google Patents, 2007.

[147] N. H. Tran, D. L. Deavenport, and C. W. Post, "Preparation of trimethylaluminum," ed: Google Patents, 1991.
[148] V. F. Hnizda and C. A. Kraus, "Preparation of Methylaluminum Chlorides," *Journal of the American Chemical Society*, vol. 60, no. 9, pp. 2276-2276, 1938/09/01 1938.
[149] S. Kim and M. Overcash, "Energy in chemical manufacturing processes: gate-to-gate information for life cycle assessment," *Journal of Chemical Technology and Biotechnology*, vol. 78, no. 9, pp. 995-1005, 2003.
[150] N. Maggiarosa, A. Preetz, and D. J. Sikora, "Preparation of tri-alkyl gallium or tri-alkyl indium compounds," ed: Google Patents, 2013.
[151] A. J. Carty and D. G. Tuck, "Co-ordination compounds of indium. Part IV. Adducts of indium(III) chloride, bromide, and iodide with neutral donors," *Journal of the Chemical Society A: Inorganic, Physical, Theoretical*, 10.1039/J19660001081 no. 0, pp. 1081-1087, 1966.
[152] A. W. Laubengayer and F. B. Schirmer, "The chlorides of gallium," *Journal of the American Chemical Society*, vol. 62, no. 6, pp. 1578-1583, 1940.
[153] (https://caeonline.com/buy/reactors/aixtron-aix-3000/9080733). *Aixtron Aix 3000 for sale (used, price)*. Available: https://caeonline.com/buy/reactors/aixtron-aix-3000/9080733
[154] K. J. Schmieder *et al.*, "Analysis of GaAs solar cells at High MOCVD growth rates," in *2014 IEEE 40th Photovoltaic Specialist Conference (PVSC)*, 2014, pp. 2130-2133.
[155] C. S. Kim, J. Hong, J. Shim, Y. Won, and Y. I. Kwon, "Multiphysics modeling and design of ultralarge multiwafer MOVPE reactor for group III-nitride light emitting diodes," in *2010 11th International Thermal, Mechanical & Multi-Physics Simulation, and Experiments in Microelectronics and Microsystems (EuroSimE)*, 2010, pp. 1-7.
[156] Veeco. (2017, May 22, 2018). *Veeco | Technologies & Products | MOCVD Systems | TurboDisc EPIK 868 MOCVD System for LED Production*. Available: http://www.veeco.com/products/turbodisc-epik-868-mocvd-system-for-led-production
[157] M. A. J. Huijbregts *et al.*, "Is Cumulative Fossil Energy Demand a Useful Indicator for the Environmental Performance of Products?," *Environmental Science & Technology*, vol. 40, no. 3, pp. 641-648, 2006/02/01 2006.
[158] M. L. C. M. Henckens, P. P. J. Driessen, and E. Worrell, "Metal scarcity and sustainability, analyzing the necessity to reduce the extraction of scarce metals," *Resources, Conservation and Recycling*, vol. 93, pp. 1-8, 2014/12/01/ 2014.
[159] G. Geisler, T. B. Hofstetter, and K. Hungerbühler, "Production of fine and speciality chemicals: procedure for the estimation of LCIs," *The International Journal of Life Cycle Assessment*, vol. 9, no. 2, pp. 101-113, 2004.
[160] S. Pasynkiewicz and M. Boleslawski, "Synthesis of trimethylaluminium," *Journal of Organometallic Chemistry*, vol. 25, no. 1, pp. 29-32, 1970.
[161] J. Adams *et al.*, "Demonstration of Multiple Substrate Reuses for Inverted Metamorphic Solar Cells," *Photovoltaics, IEEE Journal of*, vol. 3, no. 2, pp. 899-903, 2013.
[162] N. R. E. Laboratory, "U.S. Life Cycle Inventory Database," N. R. E. Laboratory, Ed., ed. https://www.lcacommons.gov/nrel/search, 2012.
[163] (November 10, 2017). *Advanced Large Capacity Stirrers*. Available: font: 12.0px 'Lucida Grande'}Available: https://stirrers.net/collections/magnetic-stirrers/products/advanced-large-capacity-stirrers
[164] (November 10 2017). *Diaphragm-type Dry Vacuum Pump*. Available: https://www.lesker.com/newweb/vacuum_pumps/pdf/manuals/dtc-22_usermanual.pdf
[165] (November 10, 2017). *Versatile Cold/Hot Plate*.
[166] *Zone Refining Unit*. Available: http://barc.gov.in/technologies/zru/zru_br.html
[167] P. Bhattacharya, R. Fornari, and H. Kamimura, *Comprehensive Semiconductor Science and Technology* (no. v. 1). Elsevier Science, 2011.
[168] C. Gero. (May 1, 2018). *Compact Vertical Split Tube Furnace*. Available: https://www.carbolite-gero.com/products/tube-furnace-range/split-tube-furnaces/evt-evz/models/
[169] C. Gero. (May 1 2018). *Rotating Horizontal Split Tube Furnace*. Available: https://www.carbolite-gero.com/api/?action=product_pdf&productId=347&id=2374085&L=0&userId=&site=carbolite&print_language=0&print_info=1&print_image=1&print_advantages=1&print_features=1
[170] "Industry data 2.0," ed. Data can be accessed through www.ecoinvent.org, 2000.
[171] BrilliantEarth.com. (2017, April 2, 2018). *How Lab Created Diamonds Are Made*. Available: https://www.brilliantearth.com/news/how-lab-created-diamonds-are-made/

[172] AlmatecSolar.com. (April 18, 2018). *What Is "Slurry?" | Almatec Pumps in Solar PV Manufacturing*. Available: http://www.almatecsolar.com/index.php?option=com_content&view=article&id=201&Itemid=205⟨=en
[173] "European Life Cycle Database - ELCDv3," ed. http://eplca.jrc.ec.europa.eu/ELCD3/.
[174] (April 18, 2018). *Eminess | Polishing Pads - OPC6350*.
[175] N. T. U. o. Technology, "Chapter 12 - Chemical Mechanical Polishing," ed. http://www.me.ntut.edu.tw/introduction/teacher/lu/IC%20fabrication_GA/IC_%20Chp%2012.pdf.
[176] D. Bhusari *et al.*, "Direct Semiconductor Bonding Technology (SBT) for high efficiency III-V multi-junction solar cells," in *2011 37th IEEE Photovoltaic Specialists Conference*, 2011, pp. 001937-001940.
[177] P. Patel *et al.*, "Initial results of the monolithically grown six-junction inverted metamorphic multi-junction solar cell," in *Photovoltaic Specialists Conference (PVSC), Volume 2, 2012 IEEE 38th*, 2012, pp. 1-4.
[178] H. C. Kim, K. G. Knight, N. Krishnan, and V. M. Fthenakis, "Life cycle analysis of two new concentrator PV systems," 2008, pp. 909-913.